MEDNARODNA PODIPLOMSKA ŠOLA JOŽEFA STEFANA
JOŽEF STEFAN INTERNATIONAL POSTGRADUATE SCHOOL

MIHA DEŽMAN

APPLICATION OF PASSIVE AND MECHANICALLY VARIABLE STIFFNESS ELEMENTS IN WEARABLE ROBOTIC MECHANISMS

DOCTORAL DISSERTATION

LJUBLJANA, MAY 2020

APPLICATION OF PASSIVE AND MECHANICALLY VARIABLE STIFFNESS ELEMENTS IN WEARABLE ROBOTIC MECHANISMS

Miha Dežman

Doctoral Dissertation
Jožef Stefan International Postgraduate School
Ljubljana, Slovenia

Supervisor: Asst. Prof. Andrej Gams, Jožef Stefan Institute, Ljubljana, Slovenia

Evaluation Board:
Prof. Dr. Aleš Ude, Chair, Jožef Stefan Institute, Ljubljana, Slovenia
Prof. Dr. Jan Babić, Member, Jožef Stefan Institute, Ljubljana, Slovenia
Prof. Dr. Tamim Asfour, Member, Karlsruhe Institute of Technology, Karlsruhe, Germany

MEDNARODNA PODIPLOMSKA ŠOLA JOŽEFA STEFANA
JOŽEF STEFAN INTERNATIONAL POSTGRADUATE SCHOOL



Miha Dežman

APPLICATION OF PASSIVE AND MECHANICALLY VARIABLE STIFFNESS ELEMENTS IN WEARABLE ROBOTIC MECHANISMS

Doctoral Dissertation

UPORABA PASIVNIH IN MEHANSKO VARIABILNO PODAJNIH ELEMENTOV V OBTELESNIH ROBOTSKIH MEHANIZMIH

Doktorska disertacija

Supervisor: Asst. Prof. Andrej Gams

Ljubljana, Slovenia, May 2020

To my parents and my grandmother. The first reason for what I have accomplished.

Acknowledgments

First of all, I would like to thank my mechanical engineering colleagues, with whom I have discussed and solved many mechanical design and overall world problems. I would like to thank my firefighting colleague Rok Pahič for the daily meetings and discussions about many new research ideas. I thank my supervisor Andrej for sharing his knowledge with me and for giving me positive encouragement when I was about to give up. The completion of this research would not have been possible without the support of department head Prof. Dr. Aleš Ude.

Finally, I would also like to thank my other office colleagues and the rest of the E1 department of the Jožef Stefan Institute for their positive company and all the support I received.

This research would not have been possible without the funding from the Slovenian Research Agency (ARRS, Research Core Funding No. PR-06812). My thanks also go to the German Academic Exchange Service (DAAD), which financed my short research stay at the Karlsruhe Institute of Technology (KIT). Finally, my thanks go to the H^2T laboratory team of Prof. Dr. Tamim Asfour for hosting my short research stay, for sharing their knowledge and for supporting me during my stay.

Abstract

Assistive robot technologies are devices such as exoskeletons and prostheses that provide movement assistance, support, can augment users or even replace their limbs. Currently commercially available devices have limited performance and power capacity, and are expensive. The focus of this thesis is on the integration and use of compliant actuation technologies that combine motors and passive elastic elements to enable superior performance of exoskeleton devices. Their integration can resolve the above-listed issues with features like mechanical adaptivity, energy efficiency, increased safety and reduced costs. The thesis revolves around their integration and is divided into three parts.

In the first part, a quasi-passive ankle exoskeleton is evaluated. The exoskeleton features a passive elastic element and clutch assembly that is placed in parallel to the human calf muscles. Through correct clutch activation timing and proper stiffness of the elastic element, the strain on the calf muscles is reduced without the use of heavy motors, resulting in easier walking. The prototype and its effects are evaluated through two pilot studies and analysed. One study assesses its physiological effect through measurements of oxygen consumption, EMG muscle activity and hearth-rate and the other assesses the user's subjective perception of the exoskeleton use with a questionnaire.

Part two shows the development of a novel, more efficient way of stiffness variation that could be used to replace the process of manual spring exchange in the passive ankle exoskeleton. The new principle combines characteristics of a cam mechanism and a variable lever mechanism. A compact structure, a nearly linear torque-deflection characteristics and fast, energy-efficient stiffness adaptation are the main properties of the pseudo-linear variable lever variable stiffness actuator (PLVL-VSA). The research includes a mathematical model, a fully-functional prototype, an elbow exoskeleton device featuring the proposed mechanism, extensive evaluation and analysis of the proposed concept, and finally a technique for parameter optimization of its components.

The third part focuses on the development of a mechanically compliant exoskeleton device. Integration of mechanical compliance despite its additional weight and complexity is possible through the use of modular design techniques and by moving all the heavy components onto the user's back. Bowden cable transmission allows the transfer of power from the user's back to the exoskeleton joints to retain a light frame with minimal inertia. This research analyses the power loss and control performance degradation due to Bowden cable friction and resolves it through mathematical modelling and the use of sensor fusion methods. The focus lies on the external torque estimation in light of high levels of friction by combining the signals from an integrated load cell and Bowden cable stretch measurements. The methods are evaluated on a new upper-limb exoskeleton prototype, which is at the end prepared for a possible integration with variable stiffness components.

Povzetek

Obtelesni robotski mehanizmi in proteze spadajo med asistenčne robotske tehnologije, ki nudijo pomoč pri gibanju, podporo, lahko ojačajo uporabnikove zmogljivosti ali nadomestijo izgubljeno okončino. Trenutne tržno dostopne naprave imajo omejene zmogljivosti delovanja in baterij ter zelo visoko nabavno ceno. Uporaba mehansko podajnih tehnologij lahko poveča zmogljivost robotskih pogonov z združitvijo klasičnih pogonskih komponent s pasivnimi elastičnimi elementi. Združitev obeh tehnologij ponuja rešitve za zgoraj omenjene težave z lastnostmi, kot so mehanska prilagodljivost, energetska učinkovitost, povečana varnost in nižja cena končnega izdelka. Disertacija se osredotoča na integracijo obeh tehnologij in je razdeljena na tri dele.

Prvi del opisuje razvoj kvazi-pasivnega gleženjskega eksoskeleta. Glavna komponenta eksoskeleta je sestav sklopke in vzmeti, ki je nameščen vzporedno z mišicami v človekovih mečih. S pravilnim vklopom sklopke in z uporabo elastičnega elementa pravilne togosti lahko naprava razbremeni delovanje mišic in zmanjša napor hoje. Eksoskelet izboljša učinkovitost gibanja uporabnika brez uporabe težkih motorjev in baterij. Učinki prototipa na uporabnika so ovrednoteni z dvema raziskavama. Prva ovrednoti fiziološki učinek z meritvami porabe kisika, mišične aktivnosti in frekvence srčnega utripa in druga uporabnikovo subjektivno zaznavanje uporabe eksoskeleta s pomočjo vprašalnika.

Drugi del prikazuje razvoj novega učinkovitega samodejnega mehanskega načina za spreminjanje podajnosti, ki lahko nadomesti trenutno ročno menjavo vzmeti v pasivnem gleženjskem eksoskeletu. Predlagani princip združuje značilnosti odmičnega mehanizma in ročičnega mehanizma s spremenljivo dolžino ročice. Kompaktna zgradba, psevdo-linearna navorno odmična karakteristika ter hitra in energetsko učinkovita adaptacija podajnosti so glavne značilnosti psevdo-linearnega spremenljivo ročičnega spremenljivo podajnega aktuatorja (ang.: pseudo-linear variable lever variable stiffness actuator, PLVL-VSA). Raziskave vključujejo matematični model, polno delujoč prototip, komolčni eksoskelet z eno aktivno prostostno stopnjo gibanja, obsežna testiranja in analize predlagane zasnove ter tehniko optimiranja parametrov podajnega aktuatorja.

Tretji del predstavlja razvoj mehansko podajnega nosljivega robota. Za uspešno združitev tehnologij mora načrtovanje eksoskeleta upoštevati večjo zapletenost in dodatno maso kot posledici integracije mehanske podajnosti. Eden od načinov za uspešno združitev je ločitev motorjev ter baterij in njihov premik iz sklepov eksoskeletnega ogrodja na uporabnikov hrbet. To je mogoče z uporabo bovden prenosa, s čimer eksoskeletno ogrodje ostane lahko in ima majhno vztrajnost. Enaka strategija se uporabi za montažo komponent s spremenljivo podajnostjo, kjer je težava dodatna masa. Ta raziskava analizira izgubo moči ter poslabšanje zmogljivosti krmiljenja zaradi trenja bovden prenosa. Rešitev je mogoča preko matematičnega modeliranja trenja in uporabe senzorskih metod zlivanja. Omenjene metode izboljšajo oceno zunanjega navora s pomočjo združevanja signala iz vgrajene merilne celice ter preko meritve raztezka bovden žice. Vse meritve so opravljene na novem nosljivem robotu, ki je na koncu pripravljen za vgradnjo komponent s spremenljivo podajnostjo.

Contents

List of Figures **xv**

List of Tables **xxv**

1 Introduction **1**
1.1 Purpose of the Dissertation . . . 5
1.2 Goals of the Dissertation . . . 6
1.3 Hypothesis . . . 7
1.4 Outline of the Thesis . . . 8

2 Literature Review **9**
2.1 Compliant Actuation . . . 9
2.1.1 Human & Animal Physiology . . . 9
2.1.2 Compliant Actuators . . . 13
2.1.3 Variable Stiffness . . . 16
2.2 Exoskeletons . . . 22
2.2.1 Rigid Exoskeletons & Compliant Actuation . . . 23
2.2.2 Soft Exoskeletons & Bowden-Cable . . . 27
2.2.3 Passive & Quasi-Passive Exoskeletons . . . 29
2.2.4 Control of Exoskeletons & Compliant Actuators . . . 33

3 Use of Passive Elements in Exoskeleton Devices: Passive Ankle Exoskeleton **37**
3.1 Design & Mechanics of the Passive Ankle Exoskeleton . . . 37
3.2 Metabolic Cost Measurement Study Design . . . 40
3.2.1 Results . . . 42
3.3 Mechanics & Operation of the Quasi-Passive Ankle Exoskeleton . . . 46
3.4 Experimental Design & Protocol . . . 49
3.4.1 Results . . . 51
3.5 Chapter Conclusion . . . 53

4 Mechanically Compliant Actuator With Efficient Stiffness Variation **55**
4.1 Operation Principle . . . 56
4.2 Mathematical Model . . . 57
4.3 Theoretical Analysis . . . 59
4.4 PLVL-VSA Prototype . . . 62
4.4.1 Internal/External Mechanism . . . 63
4.4.2 Experimental Setup . . . 64
4.4.3 Control Algorithms . . . 66
4.4.4 Results . . . 68
4.4.4.1 Internal Mechanism Torque . . . 68
4.4.4.2 External Mechanism Torque . . . 69

4.4.4.3 Stiffness variation speed . . . 71
4.5 Discussion PLVL-VSA . . . 72
4.5.1 Comparison to other VSAs . . . 72
4.5.2 PLVL-VSA Analysis & Discussion . . . 73
4.6 Elbow Exoskeleton . . . 75
4.7 PLVL-VSA Modification & Parameter Optimization . . . 77
4.7.1 Torque/Deflection Space . . . 77
4.7.2 Proposed Modification & a New Mathematical Model . . . 79
4.7.3 Parameter Optimization . . . 82
4.7.3.1 Optimization Goal & Cost Function . . . 82
4.7.3.2 Cost Function Evaluation . . . 84
4.7.3.3 Linear Stiffness Approximation . . . 85
4.7.4 Analysis and Discussion . . . 88
4.8 Chapter Conclusion . . . 91

5 Upper-Limb Exoskeleton 93
5.1 Design Goals and Parameters . . . 94
5.2 Mechanical Design of the Exoskeleton . . . 96
5.3 Design of Actuator Mechanics & Mechatronics . . . 99
5.4 Control Design . . . 106
5.4.1 Position Controller . . . 106
5.4.2 Torque Controller . . . 106
5.4.3 Stribeck+Coulomb Friction Model . . . 107
5.4.4 Experimental System . . . 109
5.4.5 Friction Modelling & Compensation . . . 111
5.5 Experimental Results . . . 121
5.5.1 Signal Comparison & Sensor Fusion . . . 121
5.5.2 Final Algorithm Implementation . . . 123
5.6 Mechanically Compliant Exoskeleton . . . 126
5.7 Chapter Conclusion . . . 127

6 Future Work and Conclusion 129

References 131

Bibliography 145

Biography 147

List of Figures

Figure 1.1: **Demographic pyramid of Slovenia** for the age above 50 years [3]. . 2
Figure 1.2: **Soft exoskeleton** example from [29]. 4

Figure 2.1: **The pogo stick principle.** A pneumatic jumping robot [33] shown in **a**, tendons spanning the animal leg in **b** and tendons spanning the human ankle joint in **c**. All three figures are adapted from [33]. 10
Figure 2.2: **Return spring principle.** The simplified schematics is shown in **a**. A potential example of a return spring from the animal kingdom **b**. Both figures are adapted from [33]. 11
Figure 2.3: **Fatty pads** in animal **a** and human feet **b** [72]. Figure **a** is adapted from *www.shutterstock.com* and **b** is adapted from [72]. 11
Figure 2.4: **Hill musculo-tendon contraction model**. The model consists of a muscle contractile element in series and parallel with elastic elements. The muscle has a scaled force-length and force-velocity relation dependent on activation, as shown in graphs **a** and **b**. Value a stands for the amount of muscle activation. A tendon extension/force model is shown in **c**. Figure is adapted from [73]. 12
Figure 2.5: **Two antagonistic muscle pairs in humans.** The flexion and extension of the elbow joint and its biceps/triceps antagonistic pair is shown in the *left* image. The quadriceps/hamstring antagonistic pair is shown in the *right* image. 13
Figure 2.6: **Compliant actuation architectures - part I**; **a** stiff actuator, **b** series elastic actuator. 14
Figure 2.7: **A collaborative robot**; KUKA LWR (Light Weight Robot) [85] is shown *left* and its mechatronic joint design, including actuation, electronics, and sensing is shown *right*. Figures are adapted from [85] and [31]. 14
Figure 2.8: **Compliant actuation architectures - part II**; **a** parallel elastic actuator and **b** series-parallel elastic actuator. 15
Figure 2.9: **Compliant actuation architectures - part III**; **a** variable stiffness actuator, **b** variable impedance actuator. 16
Figure 2.10: **The working principle of the MACCEPA actuator** is shown in **a**. **b** and **c** show the working principle of the novel MACCEPA 2.0, in an equilibrium position and in a deflected position. A prototype of the actual MACCEPA actuator system is shown in **d**. Images **a**, **b** and **c** are adapted from [104] and **d** is adapted from [105]. 18
Figure 2.11: **AwAS stiffness variation principle.** **a** shows the operational principle of the AwAS actuator, where a lever deflection is opposed by linear springs. A computer model of the actuator is shown in **b**. The second version, AwAS-II, is shown in **c** and its physical prototype in **d**. Images **a** and **b** are adapted from [97] and **c** and **d** is adapted from [109]. . . . 19

Figure 2.12: **Perpendicular and parallel force application analogy.** **a** shows the parallel force application and **b** shows the perpendicular force application. . . . 20

Figure 2.13: **The VS-Joint mechanism** is shown in **a** and its principle of operation is shown in **b**. Both **a** and **b** are adapted from [110]. . . . 20

Figure 2.14: **The FS-Joint** is shown in **a**, with its principle of operation in **b**. The final prototype implementation is shown in **c**. Images **a**, **b** and **c** are adapted from [96]. . . . 21

Figure 2.15: **Small and large pressure angle α.** The difference between a small pressure angle *left* and a large pressure angle *right*. . . . 21

Figure 2.16: **Exoskeletons and advanced sensors.** The hard exo-suit is shown **left** and its soft counterpart **right**. Figure is adapted from [114]. . . . 22

Figure 2.17: **HARMONY exoskeleton** shown in **a**. A user performing a complicated exoskeleton motion is shown in **b**. Figure is adapted from [127]. . . . 24

Figure 2.18: **The NEUROexos exoskeleton** prototype is shown in **a**. A mechanically compliant shell is shown in **b**. It is used to attach the exoskeleton onto the user and offers comfort and adaptability. Its compliant actuator is shown in **c**. Figure is adapted from [91]. . . . 25

Figure 2.19: **The VariLeg exoskeleton** with its important features is shown in **a**. The schematic of the underlying compliant actuation system is shown in **b**. Figure is adapted from [124]. . . . 26

Figure 2.20: **Lower limb exoskeletons; a** ReWalk^{TM} 6.0 [129], **b** Indego^{TM} [130], **c** Ekso GT^{TM} [131]. Figures are adapted from the respective sources. . 26

Figure 2.21: **Soft exo-suits.** A lightweight exoskeleton for the rehabilitation and assistance of a paretic ankle shown in **a**. Image **b** shows a lightweight exoskeleton with pneumatic actuation. A hip-actuated soft-suit exoskeleton with multi-articular actuation aiding in ankle plantar-flexion and hip flexion is shown in **c**. Image **a** is adapted from [134]; **b** and **c** are adapted from [29]. . . . 28

Figure 2.22: **Soft exo-suit actuator units.** Images **a** and **b** show a waist belt from a hip exoskeleton [29] with arrows indicating the force paths through the garment. Graph in **c** shows the results from force/strain testing of three different textile materials. A compact actuator unit for a soft-suit ankle exoskeleton is shown in **d**. Images **a**, **b** and **c** are adapted from [29]; and **d** is adapted from [134]. . . . 29

Figure 2.23: **Bowden-cable properties.** Image **a** shows a flat out representation of a steel cable in a Bowden sheet. As shown in **b**, the efficiency of force transmission, i.e., friction characteristics, change based on the sheath bending angle. **c** shows the transmission efficiency based on the bending angle for several friction coefficients. Images **a** and **b** are adapted from [138]; image **c** is adapted from [139]. . . . 30

Figure 2.24: **The types of mechanical locking devices** with **a** a latch with one locking position, **b** a latch with multiple locking positions, **c** a ratchet, **d** a dog clutch, **e** a cam-based locking device: cam follower, **f** a cam-based locking device: mutilated gears, **g** a cam-based locking device: Geneva mechanism, and **h** a hydraulic lock. Figure is adapted from [142]. 30

Figure 2.25: **The types of friction-based locking devices** with **a** a bistable brake, **b** an overrunning clutch, **c** a piezo-actuated brake, **d** a statically balanced brake, **e** a worm wheel, **f** a self-engaging brake, **g** a thermic lock, **h** a self-engaging pinion-gear mechanism, and **i** a capstan. Figure is adapted from [142]. 31
Figure 2.26: **The types of singularity locking devices.** The types of singularity locking devices with **a** and **b** the two different four-bar mechanisms and **c** a nonlinear spring mechanism. Figure is adapted from [142]. 31
Figure 2.27: **Passive exoskeletons part 1.** PAEXO exoskeleton is shown in **a** with its components. A user wearing the exoskeleton is shown in **b**. Spinal exoskeleton from the SPEXOR project is shown in **c**, **d**. **e** shows the passive joints that are used to adapt the exoskeleton to different users. The main passive-elastic mechanism is shown in **f**. Image **a** is adapted from [149]; **b** is adapted from [152]; **c**, **d**, **e** and **f** are adapted from [13]. 32
Figure 2.28: **Passive exoskeletons part 2.** The schematics of the passive ankle exoskeleton is shown in **a**. Its mechanical clutch is shown in **b**. An image of the actual prototype is shown in **c**. Image **d** shows a prototype of a clutch-spring knee exoskeleton for running with its basic functions shown in **e**. Images **a**, **b** and **c** are adapted from [53]; **d** and **e** are adapted from [145, 153]. 33
Figure 2.29: **Three exoskeleton control methods.** τ_{h} denotes the human torque, τ is the device torque, and q is the actual knee joint angle. *Left*: Gravity compensation approach control scheme. *Middle:* Oscillator-based approach. $\hat{q}$ is the estimated knee joint angle. *Right:* Position control approach control scheme. Note the control loop with the referential joint angle q_{d}. Figure is adapted from [21]. 34
Figure 2.30: **Human-in-the-loop optimization.** Measurements of human performance are used to update device control to improve the performance of the human portion of the system, as seen in **a**. A method for minimization of the energy cost of human walking is shown in **b**. Figure is adapted from [23]. 35
Figure 2.31: **Control architecture** for stable and accurate force control. Figure is adapted from [40]. 35

Figure 3.1: **The passive exoskeleton operation.** Figure is adapted from [53]. . 38
Figure 3.2: **The unpowered ankle exoskeleton** built at the Jožef Stefan Institute. 38
Figure 3.3: **Mechanical clutch**. Its relevant components are marked in a dissembled state (*left*) and in the assembled state (*right*). 39
Figure 3.4: **Insole design process**. **a** shows a 3D sheet-metal model, which was used to construct a paper version shown in **b**. The insole was built out of aluminium using a laser-cutting process and folded into a proper shape in **c**. Finally, the insole shown in **d** was created by using the aluminium insole as a template. 40
Figure 3.5: **Passive exoskeleton measurement system.** The left picture shows the measuring setup consisting of a treadmill, the Optotrak measuring system and the Cosmed VO_2 breathing apparatus. The picture on the right shows a participant during the tests while wearing the prototype of the exoskeleton with the attached sensors. 41
Figure 3.6: **Surface electrode SX230** with an integrated signal amplifier (Biometrics Ltd.) 42

Figure 3.7: **Average of the maximum oxygen consumption** (VO_2) and its standard deviation for the first pair, second pair and for all participants. 43

Figure 3.8: **Soleus muscle activity.** Average and standard deviation of EMG activity for the Soleus muscle of the first pair, second pair and all participants. 43

Figure 3.9: **Vastus muscle activity.** Average and standard deviation of EMG activity for the Vastus Medialis muscle of the first pair, second pair and all participants. 44

Figure 3.10: **Heart-rate measurements.** Average and standard deviation of heart rate for the first pair, second pair and all participants. 45

Figure 3.11: **The user carrying the exoskeleton** is shown in the image on the *left*. The CAD model of the exoskeleton is shown on the *right*. 46

Figure 3.12: **The quasi-passive ankle exoskeleton.** A side photo of the new clutch in the *left* picture, and a photo of the backside in the *right* picture. 47

Figure 3.13: **The ratchet and pawl** are shown *left*. The disassembled clutch and its components are shown *right*. 47

Figure 3.14: **Exoskeleton angle measurements and clutch activation.** Average angle (*in black*) and its standard deviation (*in gray*) measured at the exoskeleton joint in relation to the gait phase. Heel-switch activation probability is shown *in blue* and is calculated for 100 steps. 48

Figure 3.15: **The questionnaire.** The red number markings were added during the analysis of the results for easier reference. 50

Figure 3.16: **A graphical representation of the results of the questionnaire.** The histogram in *blue* represents the standard deviation. The colours from the legend represent the average values. 51

Figure 3.17: **A summarized representation of the results.** A more compact graphical representation of the questionnaire results with mean values and standard deviations. 52

Figure 3.18: **Several foot postures** are shown *left* with markings of discomfort. The markings are then transferred to a picture of the insole on the *right* side. 53

Figure 4.1: **PLVL-VS actuator functional principle: a** equilibrium position, **b** deflection under external torque and **c** stiffness variation. 56

Figure 4.2: **Rotational-based PLVL-VSA variable lever stiffness variation principle.** The figure shows the derivation of PLVL-VSA in comparison to AwAS, i.e., the transition from the linear stiffness variation principle using a ball-screw (AwAS) towards a rotational-based stiffness variation principle (PLVL-VSA). 57

Figure 4.3: **The flat-out simplified view of the proposed mechanism with its relevant parameters** is shown in **a**. The deflection of the mechanism rotates the curved lever (*circle 1*), i.e., the arc profile in **b**. The red line in **c** is perpendicular to the deflected arc (*circle 2*) and goes through the center of the arc. From its inclination (δ), the pressure angle (α) can be calculated. 58

Figure 4.4: **The torque/deflection properties of the proposed mechanism.** The torque required for the deflection of the mechanism is shown in **a**. Its derivation or stiffness is shown in **b**. The torque required to maintain a given stiffness resulting from the tangential force is shown in **c**. The line colors represent a specific stiffness setup angle. The **black** and **red dashed lines** represent the nominal and peak torque for both motors. Additional **red dashed lines** represent the torque limits for stronger stiffness variation motors. The **blue**, **red** and **yellow areas** represent the below nominal, below peak and above actuator peak torque operation regions. Under the assumption that the position motor can be backdriven at loads above its current limit (gearbox peak torque), the **white areas** in **a** and **b** are theoretically not reachable. . . 60

Figure 4.5: **The pseudo-linear property of the mechanism.** The external torque required to deflect the mechanism is shown in **a** for different cam follower angles. Its derivative, i.e., mechanism stiffness, is shown in **b**. The **black** and **red dotted lines** show the torque limits of both motors. The **black dashed lines** in **a** and **b** show the results of the linear regression. Based on the regression result, a relation between the cam follower angle and the resulting mechanism stiffness approximation can be constructed, shown in **c**. The **gray area** represents the linear regression error variance (scaled 1000x). 61

Figure 4.6: **Proof-of-concept PLVL-VSA prototype** from [63]. Some of its more important components are marked. 62

Figure 4.7: **Several representations of the PLVL-VS mechanism.** The flat-out representation of the internal mechanical components is shown in **a**. The compression motion is represented in **b** with a marked cam follower angle (φ_s) and a deflection angle (φ_d). A more detailed representation of the bidirectional VSA mechanism is shown in **c**. The CAD model of the VSA with dimensions is shown in **d** with its internal view in **e**. . . 64

Figure 4.8: **Cable transmission in-depth.** A classic cable transmission is tensioned by increasing the distance between the pulleys, as shown in **a**. The prototype cable system is connected with both its ends onto the same side of the pulley (*pulley 1*), see **b**. Classic tensioning is therefore not possible and the internal bending moment in the rope also affects the mechanism load. The proposed tension solution is shown in **c**. The cable is tensioned by a spring connected to the mechanical housing. A CAD model representation of the actual prototype solution is shown in **d**. 65

Figure 4.9: **Exploded CAD model view of the experimental actuator** is shown in **a**. Its actual implementation is shown in **b**. The experimental system where the external link is fixed to allow measurement of internal actuator properties is shown in **c**. 66

Figure 4.10: **System electronics.** The electronic system is subdivided into several units, among them: power supply unit, control unit and compliant actuator unit. 66

Figure 4.11: **Position control block scheme.** Block diagram of the position-based control for the position motor and for the stiffness variation motor. The position motor controller uses a PD regulator with a feedforward term. Both motor drivers accept speed as input. 67

Figure 4.12: **Torque control block scheme.** Torque controller with feed-forward and compensation terms for the position motor. The stiffness variation motor employs a position-based controller with a feedforward term. The position motor driver accepts the motor current as input. 68

Figure 4.13: **The measured relation between the torque and the deflection of the curved lever** shown in **a** represents the internal mechanical properties for different follower angles. In **b** the theoretical model **dashed red** and a linear regression of the measurements **dashed black** are added to the initial measurements. The torque required to maintain a given stiffness, calculated on the basis of the motor current measurement, is in **c** compared to its theoretical model **(black line)**. 69

Figure 4.14: **The torque required to deflect the VSA**, i.e., the external mechanism, is represented in **a**. In **b**, the theoretical model **(red dashed lines)** and the linear regression lines **(black dashed lines)** are added to the measurements. The approximate resulting stiffness with respect to the cam follower angle is shown in **c** for different stages of the mechanism. These include the ideal theoretical relation, the internal mechanism and the external mechanism. The colored areas represent the linear regression error variance (scaled 100x). 70

Figure 4.15: **The stiffness variation response.** The stiffness variation motor is commanded to perform a stiffness jump from 27 to 46 Nm/rad in **a** under various external loads. The equivalent follower angle is shown on the right axis. In **b** the corresponding external torque is displayed. The torque required to perform the jump on the velocity-based position-controlled motor is shown in **c**. The electric current of the motor is used to estimate its torque. 71

Figure 4.16: **The modular exoskeleton system.** The CAD model of the exoskeleton system is shown in **a**. A picture of the actual exoskeleton prototype in **b**. Image **c** shows a schematic representation of the exoskeleton where all its separate modules are marked. 75

Figure 4.17: **The elbow exoskeleton frame** is split into the upper and lower exoskeleton frame. *Left* image shows the 3D rendered image. *Right* image shows the actual implementation. 76

Figure 4.18: **Torque-deflection characteristic** shown in the *left* graph. The *middle* graph shows the corresponding derivative, i.e., the stiffness. The torque required to hold the follower at an angle is shown *right*. The BLUE region represents the below peak operation space of both motors. On the other hand, the RED region represents the area with the stiffness holding motor torques above its peak torque limit. The solid lines correspond to different follower angles as seen in the legend. The black and red dashed lines represent the nominal and peak torques of the position and stiffness varying motor gearboxes. 77

Figure 4.19: **Flat view of the original mechanism** with the essential parameters describing it in **a** and the modified one in **b**. 80

Figure 4.20: **Flat view of the mechanism** with parameters in **a** and model vectors for the calculation of $\tau_{\mathrm{d,F2}}$ and $\tau_{\mathrm{s,F2}}$ in **b**. The unloaded spring F2 is shown in **c**. 81

Figure 4.21: **Theoretical torque/deflection space** (*left*) and a low resolution numerical representation (*right*). 83

Figure 4.22: **BLUE (left) and RED (right) area sizes** for different $k_{\text{int,F2}}$ and L_1 parameter combinations. 84
Figure 4.23: **Parameter combinations and results.** The cost at different $k_{\text{int,F2}}$ and L_1 parameter combinations for different n values. 85
Figure 4.24: **Torque/deflection working space change** for different values of n. 86
Figure 4.25: **The torque-deflection graph of the modified mechanism** (*left*) and its corresponding stiffness (*right*). 86
Figure 4.26: **The linear approximation of the modified mechanism** (*left*) and the stiffness map between both cases (*right*). 87
Figure 4.27: **Difference between the actual stiffness and the linear approximation** for pre- (*left*) and post- (*right*) modification. 87
Figure 4.28: **The increase of the deflection torque** (*left*) and the resulting stiffness helping torque (*right*). 88
Figure 4.29: **The difference between the two mechanical cases for the follower torque**, i.e., the torque required to change the stiffness (*left*) and the energy required for this (E_{s}) (*right*). 89
Figure 4.30: **Comparison of the torque-deflection graph for different stiffness settings** (*left*) and the torque required to maintain the given stiffness (*right*), for original and modified mechanisms. The solid lines represent the original mechanism and the dashed lines represent the modified mechanism. 90
Figure 4.31: **Graphs showing the elastic energy storage capacity** (*left*) before and (*right*) after modification. 90

Figure 5.1: **Exoskeleton range of movement**. The first actuated movement shown in **a** is marked as *active movement 1* and includes the shoulder flexion and extension. **b** shows the *active movement 2*, which is the second actuated joint and comprises the elbow flexion and extension. Finally, shown in **c**, the mechanism allows horizontal abduction and adduction movement of the *passive* shoulder joint. 94
Figure 5.2: **Exoskeleton device and its components** shown in several perspectives. 96
Figure 5.3: **Bowden cable transmission and Bowden joint module**. Figure **a** shows the cable routing at the actuator, while **b** shows the cable routing at the Bowden joint module. The cable routing direction is marked with *blue* and *green* arrows. 97
Figure 5.4: **Shoulder passive joint of the exoskeleton** is shown from different views and some of its movement directions are marked. The upper-limb exoskeleton frame is grounded using a carbon fibre-rod that is attached to the side of the hip orthosis using a passive ball joint. 98
Figure 5.5: **Actual exoskeleton prototype** shown *left* and a user wearing it shown *right*. 99
Figure 5.6: **The actuator transmission system.** **a** shows the operating unit with various cuts made to expose its inner workings. Several bearings that support the ball screw are shown. **b** shows the integrated load cell and the mechanism that prevents torque loads on the cell and **c** shows the timing belt transmission and its belt tensioning system. 100
Figure 5.7: **A schematic diagram of the mechanical system**. The schematic shows different components and a simplified insight into the sensor placement, load cell integration and operation of the actuator transmission system. 101

Figure 5.8: **Actuator unit prototype.** The back of the unit is shown *left* and its front is shown *right*. 102
Figure 5.9: **The cooling system**. Picture **a** shows the implemented hardware cooling consisting of a cooling system for electronics and a cooling system for the motor. Figure **b** shows the separate *Motor module* and its cooling system. 103
Figure 5.10: **Electronic hardware schematics.** The figure shows the electronic components and the corresponding communication interfaces. *IE1* and *IE2* stand for the incremental encoders. *AE1*, *AE2* and *AE3* stand for the absolute encoders. 105
Figure 5.11: **Upper-limb exoskeleton position controller.** The schematic shows the position controller of the proposed system. It is built with a combination of the internal Odrive position controller and the trajectory mode. The diagram is partly adapted from [180] and [181]. 106
Figure 5.12: **Torque control of the Series-Elastic Actuator.** The friction due to the use of Bowden cables has been integrated into the SEA model. *FC1, FC2* and *FC3* blocks represent the place of mathematical friction compensation. Similarly, the *Complementary Filter* block shows the location where the two signals are blended together. 107
Figure 5.13: **Stribeck+Coulomb friction model.** The diagram shows the frictional force as a function of velocity. The friction model is composed of static, Coulomb and viscous friction. 108
Figure 5.14: **Experimental system.** The Bowden joint module was removed from the exoskeleton's frame and mounted on an aluminium stand. A lever and a weight were mounted on the joint to allow the generation of an external torque. An additional torque sensor is used to validate the system. 109
Figure 5.15: **Position trajectory data**, which shows the desired position of the motor and the actual motor position. The data is divided into several regions with vertical lines, indicating that the data represents multiple measurements. 110
Figure 5.16: **External torque data** showing the actual external torque during each measurement. 111
Figure 5.17: **Motor velocity data** showing the velocity of the motor. 111
Figure 5.18: **Experimental data plots.** **a** shows the motor current in relation to external torque and motor velocity. **b** shows the external torque measurement in relation to load cell reading and motor velocity. **c** shows the external torque in relation to cable elongation and motor velocity. The black points at the bottom present the sampling grid that was used to create the filtered surface plot. Black dots are not drawn in areas without the data. The data is also projected onto the side plane, where blue dots stand for positive velocity data and negative velocity data. 113
Figure 5.19: **The respective symmetric Stribeck+Coulomb friction curves and the scale parameters.** **a** shows the symmetric Stribeck+Coulomb friction curves $F_{\mathrm{sSCm,FF,i}}$,*left* and the parameter $k_{\mathrm{a,i}}$,*right*. **b** shows the symmetric Stribeck+Coulomb friction curves $F_{\mathrm{sSCm,LC,i}}$,*left* and the parameter $n_{\mathrm{lc,i}}$,*right*. **c** shows the symmetric Stribeck+Coulomb friction curves $F_{\mathrm{sSCm,CE,i}}$,*left* and the parameter $K_{\mathrm{ce,i}}$,*right*. 116

Figure 5.20: **Values of the symmetric Stribeck+Coulomb friction model for each discrete value of external torque.** For Fig. 5.19a,*left* in **a**, for Fig. 5.19b,*left* in **b** and Fig. 5.19c,*left* in **c**. 118
Figure 5.21: **Values of the nonsymmetric Stribeck+Coulomb friction models.** **a** shows $F_{\mathrm{nSCm,FF,i}}$, **b** shows $F_{\mathrm{nSCm,LC,i}}$ and **c** shows $F_{\mathrm{nSCm,CE,i}}$ models. 119
Figure 5.22: **Stribeck+Coulomb curves for the nonsymmetric model.** Curves for $F_{\mathrm{nSCm,FF,i}}$ are shown in **a**, for $F_{\mathrm{nSCm,LC,i}}$ are shown in **b** and for $F_{\mathrm{nSCm,CE,i}}$ in **c**. **a**, **b** and **c** show the bare curves in the *left* figure. Transparent surface data from Fig. 5.18 is added on top of the curves in the *right* figure. 120
Figure 5.23: **Calibration of the complementary filter and comparison between sensor signals**. *Left* image shows the MSE values from Eq. (5.45) for different p values and also marks the optimal ratio. *Right* image gathers the MSE values for the above sensors. It shows the load cell-based signal and the effect of friction compensation (LC+FC) next to it. Cable stretch-based external torque estimation and the effect of friction compensation (CS+FC) is shown besides it. Finally, the MSE of the complementary filter is shown. 122
Figure 5.24: **Comparison between the complementary signal and actual external torque measurements.** Both signals are shown on the same graph. Two enlarged views are added for a clearer representation. . . . 122
Figure 5.25: **Final algorithm test.** The graph shows the desired torque curve and the actual external torque for the three best cases (no. 12, 16 and 20) from Table 5.6. 125
Figure 5.26: **A schematic diagram of a novel actuator with variable stiffness.** The proposed actuator unit of the upper limb exoskeleton remains the same. A variable stiffness unit is added above it to allow for mechanical compliance with stiffness variation. 126
Figure 5.27: **Analysis of MACCEPA actuator.** The actual prototype is shown *left* and its schematic representation *right*. The original figures are adapted from [105]. 127

List of Tables

Table 3.1: Baseline of the participant characteristics of the first study. 41
Table 3.2: Baseline of the participant characteristics of the second study. 49
Table 3.3: Questionnaire results. 51

Table 4.1: Mathematical model parameters. 59
Table 4.2: Actuator components. 65
Table 4.3: Control algorithms. 67
Table 4.4: Actuator comparison - part I - performance. 72
Table 4.5: Actuator comparison - part II - components. 72
Table 4.6: Actuator comparison - part III - geometry. 73
Table 4.7: Calculation parameters. 78

Table 5.1: Human motion parameters. 95
Table 5.2: Mechanical components list. 101
Table 5.3: List of electronic components. 104
Table 5.4: Position controller parameters. 106
Table 5.5: Controller parameters. 123
Table 5.6: Controller performance. 124

Abbreviations

4Q	...	four-quadrant
A/D	...	analog to digital
ABI	...	pulsed encoder signal with index
AG	...	Aktiengesellschaft
ARRS	...	Slovenian Research Agency
AwAS	...	actuator with adjustable stiffness
BBB	...	BeagleBone Black development platform
CAD	...	computer-aided design
CAGR	...	compound annual growth rate
Co.	...	company, single owner or partners
D/A	...	digital to analog
DAAD	...	German Academic Exchange Service
DoF	...	kinematic degree of freedom
EMG	...	electromyography
EU	...	European Union
EU42	...	European shoe size 42
FC	...	friction compensation
GmBH	...	Gesellschaft mit beschränkter Haftung
GPIO	...	general-purpose input/output
H^2T	...	High Performance Humanoid Technologies Lab
HRI	...	human-robot interface
I^2C	...	inter-integrated circuit communication
IC	...	integrated circuit
ICA	...	miniature analogue in cell amplifiers
IIT	...	Istituto Italiano di Tecnologia
Inc.	...	incorporated, shareholder owners (business)
IPS	...	International Postgraduate School
JSI	...	Jožef Stefan Institute
KIT	...	Karlsruhe Institute of Technology
LC	...	low cost
LiPo	...	lithium-polymer battery
LLC	...	Limited Liability Corporation (Britain)
Ltd.	...	Limited, Inc.
LWR	...	Light-Weight-Robot
MACCEPA	...	mechanically adjustable compliance and controllable equilibrium position actuator
MSE	...	mean-squared error
NNETEC	...	neural-network-enhanced torque estimation controller
PEA	...	parallel elastic actuator
PID	...	proportional–integral–derivative controller
PLVL	...	pseudo-linear variable-lever

SEA	...	serial elastic actuator
sEMG	...	surface electromyography
SPEA	...	serial-parallel elastic actuator
SPI	...	serial peripheral interface
UART	...	universal asynchronous receiver-transmitter
USB	...	Universal Serial Bus
VIA	...	variable impedance actuator
VO2	...	oxygen consumption or oxygen uptake
VS	...	variable stiffness
VSA	...	variable stiffness actuator

Chapter 1

Introduction

If you are young, healthy and busy with daily activities and stress, you will not notice the daily routine tasks like sitting, getting up, walking, turning a door handle or climbing stairs. The loss of the ability to perform any of the above makes these simple tasks a demanding ordeal, leading to a decline in the quality of life and a loss of social independence. Disabilities that prevent voluntary body movements can be the result of diseases such as Parkinson's disease, multiple sclerosis or stroke, and can lead to a weakening of muscles and neuronal damage. Furthermore, progress in technology and medicine has enabled people to considerably prolong their lives, however, the human body still deteriorates with age. The result are many age-related difficulties, which manifest in reduced muscle strength, reduced physical working capacity, etc. Other causes of movement disabilities are typically mechanical in nature and occur as joint wear or tear of tendons and muscles as a result of an accident or overuse.

The above-mentioned difficulties are quite common with many individuals today. In the EU, a large part of the population suffers from small basic activity difficulties [1]. One person in seven reports such difficulties, which corresponds to about 73 million people. These basic activities include lifting and carrying, walking, bending, sitting or standing, seeing, remembering, concentrating and hearing. The task of lifting and carrying is the most common among them. Affected patients reduce their activity, which has a negative effect on their recovery and is unhealthy for them in the long term.

However, while the present difficulties are manageable, a more pressing matter is the phenomenon of population ageing, which will affect the population structure of the post-industrial societies. The future society structure will be, should the current trend continue, accompanied by a shrinkage of the working-age population and will have a larger number of older and very old people [2]. These people will require healthcare provided by a sufficient number of trained health workers. The numbers show that in 2018, the over-55s represented almost one third of the EU population (32.8%). By 2050, the 55-year-olds and older will represent almost half of the population (47.1%) [2]. Slovenia's demographic structure, shown in Fig. 1.1, follows the trends of the EU [3], which means that in 20-40 years, half of our population will be over 50 and more than half of that over 70. The shrinking of working-age population will force the policy makers to encourage older people to stay actively working for as long as possible. This will have an impact on health expenditure and the economic structure in the future. Thus, the age-related difficulties will be amplified through a postponed retirement, and will be combined with more prominent orthopaedic disorders that will only increase due to the expected lack of caregivers [4, 5].

In addition to the elderly population, the number of other patients with disabilities is growing in line with advances in healthcare and medicine. One example of this is the increase in stroke survivability and a growing number of patients suffering from a chronic

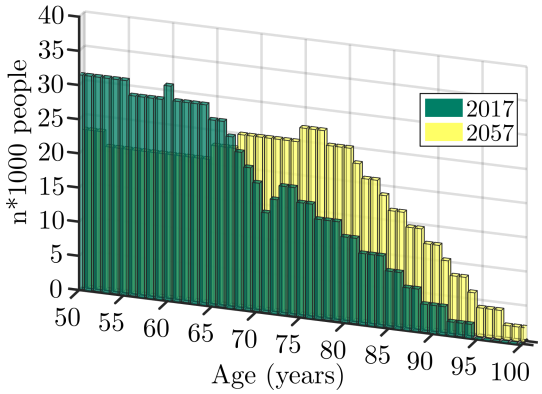


Figure 1.1: Demographic pyramid of Slovenia for the age above 50 years [3].

disease after a stroke. Their number was 3.7 million in 2015 and is estimated to reach 4.6 million [6] by 2035. Similar to the ageing of the population, the growing number of stroke patients will require sufficient rehabilitation capacities, which will be difficult to achieve with a shortage of care-givers.

This socio-economic prognosis is a great motivation for the introduction of wearable robotic devices into everyday life, in order to give people back some of what they have lost. Exoskeletons or wearable robotic devices are robots that can enhance, extend and restore human performance and mobility for both upper and lower extremities [7–11]. Patients can use exoskeletons or wearable robotic assistants in order to compensate for the lack of trained care-givers and to achieve/provide long-term benefits for both the user and the society.

More specifically, in a rehabilitation scenario, a doctor/physician can demonstrate certain movements and the exoskeleton records them. Later, the exoskeleton guides the patient's limbs according to the previously recorded movements instead of the physician moving the patient's limbs. The physician can use the extra time to reduce his workload or to focus on other patients. State-of-the-art rehabilitation exoskeletons also allow monitoring of physiological data and an overview of rehabilitation progress [12]. Ideally, an affordable and fully portable exoskeleton device would provide additional rehabilitation training in a home environment and achieve the best recovery rate for the patient. When home use is combined with sessions in health centres, the overall number of sessions increases, which leads to better recovery results.

Rehabilitation to recover from injuries caused by overwork or overuse is a corrective activity, as assistance is provided after the injury. Contrary to that, however, just as we use shoes to protect our feet, we could use exoskeleton devices as a preventive measure to reduce wear and tear on our bodies. One example are exoskeletons for lifting tasks that reduce the strain on the user's body parts, such as back muscles and spine [13]. Many manufacturing facilities already rely on the handling of tools with exoskeletons, motorized gloves and body-powered suits to reduce fatigue during long periods of work and often repeated tasks [14]. The aim is to improve productivity, reduce the user/worker stress and prevent injuries. There are also other sectors that could benefit, such as search and rescue services, space, sports and leisure activities, and the military.

It is not surprising that market analysts are forecasting positive market growth for such technologies in the coming years. The increasing population with movement disorders will accelerate the market share of the exoskeleton and drive the growth of the industry. According to Global Market Insight, Inc., the exoskeleton market is expected to reach

$3.4 billion by 2024 [15]. Similarly, ResearchAndMarkets.com [16] estimates a CAGR (Compound Annual Growth Rate) of 46.1% and also publishes some major exoskeleton developers such as Lockheed Martin Corporation, Parker Hannifin, Honda Motor Co. Ltd. etc.

The exoskeleton research field is extensive and many different prototypes exist. Some devices have already been developed to the point where they are available for everyday end-users. The website Exoskeleton Report [17] gathers a comprehensive list of exoskeletons. However, there are still many problems, which hold back the successful commercialization of such devices. With prices ranging to several 10,000€, they are not yet practical for domestic use, are not widely affordable and currently meet market requirements only to a limited extent. Exoskeleton product development costs are high due to the variability of human users, which also makes it difficult to bring a final exoskeleton device to the market. The integration of several sensors and motors into the exoskeleton contributes significantly to the increase of the total product cost. In addition, research into the merging of suitable software and hardware for calibration and customer-specific applications further increases the costs. There are also several open research questions that make successful commercialization and wider use difficult. These include versatility, robustness, portability, energy consumption, social constraints and very high cost of these devices [18]. The prospect of making a difference and taking a share of the emerging market is driving the research community to look for solutions to these problems.

The following list summarizes some of the challenging areas in exoskeleton research:

- lack of proper control techniques,
- use of learning methods to achieve exoskeleton personalization,
- adaptability to the human body for superior comfort combined with proper ergonomic design,
- reduction of high manufacture costs and long development times,
- reduction of exoskeleton mass and weight/strength optimization,
- intrinsically safe mechanical design and robust operation, etc.

Control: At the control level, the exoskeleton must predict the user's actions in order to provide proper support at the right time. Various control methods and strategies have been studied and proposed to achieve such behaviour [19, 20]. It has been shown that the chosen control strategy has a great influence on the results of the assistance effectiveness [19, 21]. Use of wrong methods leads to suboptimal results and/or hinders the user instead of providing help. Iterative learning methods [20] can compensate for the uncertainty in the human-robot system. Other information about the state of the human user can be gathered from biofeedback. In this case, feedback control based on myoelectricity, i.e., reading the electrical activation potential of the muscles, has some distinctive advantages over other types of control [22]. However, the myoelectric method is often cumbersome due to the sensor setup and tends to cause difficulties during prolonged use due to user sweating, cross-muscle activation signals, noise, sensor movement, etc. The approximation of metabolic expenditure by analysing human respiratory gases is another way to obtain biofeedback. If this metabolic expenditure can be measured in pseudo-real time, advanced control techniques can be created that allow personalization of the exoskeleton control [23, 24]. Such a device can optimize its control for a specific user and achieve the best possible results. However, these methods are currently highly dependent on laboratory equipment and require some time to set up and adapt to the user.

Personalization and Adaptation: The human body is a very difficult system to model. The effects of exoskeleton action on the user often deviate from expectations. One example is the hip exoskeleton [11], which is only supposed to help at the user's hip, but also affects the ankle joint when tested. Human body adapts other muscles on other joints, apart from

the one that is actuated with the use of an exoskeleton, which then significantly reduces muscular activity in all leg muscles. In a study by Galle et al. [25], it was shown that the metabolic reduction gets better with practice because of neuromotor adaptation. The control boundary conditions change, leading to exoskeleton-user cross-adaptation. In addition, the control strategy may also influence such human adaptation [26]. The complexity of the human body makes it difficult to predict the actual effects of the exoskeleton on the user without human-oriented studies. Involving the user in the development process increases the development time, costs and slows down the market progress of these devices.

Manufacturing and Mechanics: On the mechanical side, the exoskeleton robot goes beyond the design requirements of a classic robot. As the device is attached to the user, e.g., at the limb, its frame design must match the user's body structure to reduce any unwanted/parasitic forces/moments and not interfere with the user's kinematics. Since the body shapes of human users differ, the exoskeleton must either be mechanically adaptable to a variety of body shapes or individually designed/fitted. Note that changing the frame shape also affects the control parameters. The traditional rigid frame [27] may even be removed to create completely soft exoskeletons [28] to minimize the kinematic obstructions and to reduce the weight of the device. See Fig. 1.2 for an example of a soft exoskeleton. However, these systems can only be operated in one direction ("pull" action), as the system

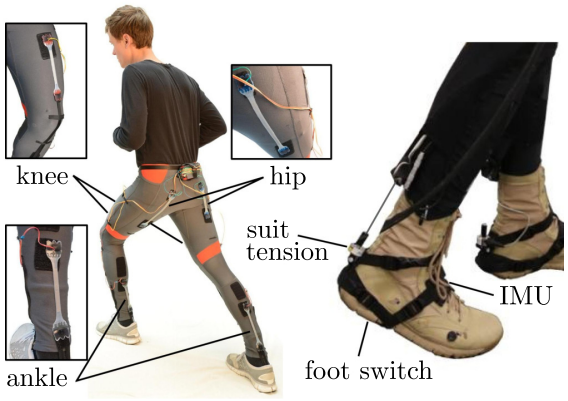


Figure 1.2: Soft exoskeleton example from [29].

typically uses a Bowden cable transmission. It relies on human bones and the garment interface to transfer the loads as there is no traditional rigid frame.

Safe and Robust Design: A solution that possibly combines the benefits of exoskeletons supported through a rigid frame and those based on soft fabric materials, is the exoskeleton driven by mechanically compliant actuators. Such actuators are attracting much attention in research [30, 31] and clearly the research is shifting towards such actuation [32]. The goal is to overcome the main drawbacks of rigid exoskeleton in terms of adaptability, comfort, safety and efficiency. The main inspiration for their design comes from animal and human physiology. Biologically evolved human and animal musculoskeletal systems [33] still surpass most of the current actuators used in robots. The majority of today's robots move by using a classic drive system consisting of an electric motor in combination with a gearbox. Muscles and their architectures around the joints in combination with tendons act as springs and feature a higher energetic efficiency [34], increased safety, robustness, and adaptability, or mechanical error compensation through compliance regulation [35]. The results are some amazing features of humans and animals like efficient walking [36], jumping [37], marathon running [38] and throwing [39].

Compliant actuation can transfer some of the capabilities of the human body to wear-

able devices or humanoid robots [40, 41]. Furthermore, through the integration of mechanical compliance, the performance requirements of existing components could also be reduced, thereby simplifying control and mechanical design. More specific benefits of such compliant actuation can be:

- intrinsically safe industrial robots that can work in close proximity to humans [42],
- toys with natural movement that are less susceptible to damage [43],
- rehabilitation robots that use mechanical compliance to achieve different levels of assistance and thereby improve patient recovery [42, 44],
- adaptation of natural dynamics [45],
- balance control through stiffness variation [46, 47],
- enabling the design of more efficient robotic prostheses [48],
- design of high-performance and efficient humanoid robots [49]
- jumping robots [37, 50], etc.

The devices that use compliant actuation allow the use of position transducers to estimate loads by spring deflection instead of the expensive load cells, and can reduce the cost and weight of the exoskeleton [51, 52]. Furthermore, the use of mechanical compliance can serve as a mechanical error buffer and allow the use of more robust, but less precise control methods and thus facilitate the design of higher-level control.

There is no doubt in the potential of such a compliant technology, yet the actuator prototypes or exoskeleton prototypes needed to investigate the positive features are not commercially available, so to explore the field, one needs to design and manufacture their own. It is also true that the additional mechanical complexity of compliant actuation introduces an additional layer of design complexity on top of the exoskeleton design. However, with careful planning, such difficulties can be mitigated. In this dissertation, several solutions to the above challenges are explored either through the integration of mechanically compliant elements or by novel mechanical design techniques. The final result of this research are three exoskeleton prototypes.

1.1 Purpose of the Dissertation

The purpose of this dissertation is to advance the field of *exoskeletons* and *compliant actuation* technology, and bring forth a fully autonomous mechanically compliant exoskeleton device. The research and the developed exoskeletons *do not target a single specific application*, such as rehabilitation, but instead focus on the *development of the underlying technology*. The technology can then be used to improve any device that targets a more specific application.

The above-stated purpose necessitates availability of proper hardware. In order to evaluate the advancement of compliant actuation within the field of wearable robotics, several prototypes were built within the scope of the research. Design techniques like modularization and combination of classical manufacturing and 3D additive technologies were used to speed up the development and reduce the costs of component manufacturing.

The final prototypes stand to be adopted by the research group and provide the possibility to evaluate some of the existing high-level control algorithms. Even more importantly, they will enable research of completely novel control algorithms that can be fully evaluated only on the actual prototypes and user-oriented studies.

1.2 Goals of the Dissertation

The goals of the dissertation are:

G1: Evaluate the use of passive elements in exoskeleton devices

Exoskeleton devices that do not use active elements, but only passive elements, such as springs, are not a complete novelty. While some such devices exist [53], their evaluations emphasize positive aspects and are not specific on the potential mechanical difficulties and the benefits they could bring to devices that combine passive elements and actuators.

To evaluate these aspects, we designed and built a passive ankle exoskeleton device inspired by [53] that employs passive elements, conducted user studies and upgraded the device.

The following list summarizes the research effort:

- Design and construct a passive ankle exoskeleton that employs passive elastic elements.
- Evaluate the exoskeleton performance and measure user biofeedback in the form of heart-rate, kinematics, VO2 and muscle EMG.
- Find potential faults of the prototype and improve its performance through a mechanical upgrade.
- Perform a quality-oriented user study with the upgraded exoskeleton and gather subjective user feedback.

G2: Develop an efficient stiffness variation principle suitable for an exoskeleton application

The passive ankle exoskeleton emphasized the need for a variable stiffness mechanism that would enable automatic stiffness modulation to achieve appropriate stiffness for each user without manual intervention. The currently used passive elements had to be manually adjusted/replaced to change the mechanism stiffness, which posed many difficulties and a source or unreliability during application and examinations. The literature on compliant actuation offers a broad perspective of such mechanisms [42, 54, 55], but only a few are intended for use on an exoskeleton and provide the desired properties only to a limited extent.

To meet the requirements for more efficient stiffness variation and reduced weight influence of such mechanisms, a novel design architecture for stiffness variation is proposed. The proposed concept was evaluated using two actuator prototypes and an elbow exoskeleton device.

The following list summarizes the research effort:

- Develop a new mechanical stiffness variation principle and its underlying mathematical model.
- Design and build a prototype with a performance close to the requirements of the final application, i.e., an elbow exoskeleton.
- Perform extensive performance evaluation of the actuator prototype. Identify any faults of the proposed variable stiffness mechanism and theoretically analyse them.
- Develop an optimization method to achieve maximum utilization of the torque-deflection workspace of the variable stiffness actuator given the torque limits of the geared motor.

G3: Develop an exoskeleton device that exploits the benefits of variable stiffness actuation

An exoskeleton structure should be lightweight and mechanically adaptive to various user shapes to allow for seemingly unobstructive movement. The lightweight structure adds minimal additional weight onto the user and minimally increases the existing inertia of the user's limbs. While mechanically compliant actuation enables and contributes to mechanical adaptivity of such devices, it inadvertently also introduces additional weight and increases inertia.

To reduce the negative effects of the integration of stiffness variation mechanisms, a new exoskeleton device was developed. The exoskeleton prototype was built, evaluated and developed to the point where it supports the integration of a variable stiffness mechanism.

The following list summarizes the research effort:

- Develop a new exoskeleton prototype which has a light-weight frame, is fully-wearable and has its own battery power supply that allows for full autonomy. The light-weight frame structure is enabled by relocation of exoskeleton actuators onto the user's back using a Bowden cable transmission.
- Investigate the quality and feasibility of different torque sensing methods:
  - ◇ Use mathematical modelling and sensor fusion tools to mitigate the effects of Bowden cable static and dynamic friction.
  - ◇ Integrate a load cell that can measure the tension of the Bowden cable.
  - ◇ Investigate external torque estimation methods based on Bowden cable stretch measurements.
- Develop a concept for compact integration of the previously developed variable stiffness mechanism (PLVL-VSA).

1.3 Hypothesis

The hypotheses can be summarized as:

H1 Making a passive exoskeleton device into a quasi-passive one can improve its overall operation robustness.

Wearable devices based on purely passive elements can augment human users. Being based on mechanical principles and only passive elements has made such devices complex and not extremely robust. The outcome is that such devices have not made a breakthrough in the field of exoskeletons and have not progressed to end-users. We hypothesize that small improvements, such as incorporating small motors, which make them quasi-passive, can significantly improve the overall operation robustness.

H2 An efficient variable stiffness actuator that favourably conforms to factors such as mechanism's weight, volume and efficiency of stiffness variation can be designed using a novel architecture.

Variable stiffness mechanism research has been the focus of the research community since the last decade. The field is vast and entails many device architectures, however, they often culminate in heavy and mechanically complex devices, and are application dependent. Learning from the available literature and the underlying mechanical principles, improvements or combinations of existing architectures allow for creation of novel stiffness variation principles that introduce beneficial features while retaining a relatively low mechanical complexity. We hypothesize that a more energy-efficient and compact variable stiffness mechanism structure exists.

H3 An upper body exoskeleton design that conforms with the integration of variable stiffness compliant actuators (VSA) is possible.

Compared to classical actuators, VSAs suffer from a higher mechanical complexity and additional weight, which does not conform well with the exoskeleton requirements for a lighter-frame and structure. Soft exoskeleton devices [29] exploit the light-weight textile supportive structures and Bowden cable transmission for a superior fit to the user's anatomical shape and high ergonomics. Furthermore, using such a mechanical transmission increases the design flexibility and allows for designs, where variable stiffness actuators are integrated outside of the users joints, thereby reducing the weight impact and inertia of the exoskeleton frame. We hypothesize that an exoskeleton device can be designed so that it allows for the integration of variable stiffness actuation. This can be achieved through, for example, the use of Bowden cable transmission, which can also be exploited for torque sensing.

1.4 Outline of the Thesis

The thesis outline is summarized as:

Chapter 2 contains a literature review of topics relevant to this work. The presented interdisciplinary nature of the research ranges from human and animal physiology to robotics and control. In the first part, Section 2.1, *compliant actuation technology* is introduced and some basic biological compliance principles found in nature and their mechanical equivalents are explained. The second part, Section 2.2, focuses on the *exoskeleton technology* and gives examples of mechanical compliance already implemented in these devices and concludes with a brief explanation of the relevant control techniques.

Chapter 3 presents the development of a quasi-passive exoskeleton device in relation to goal **G1** and hypothesis **H1**. The first part of the chapter, Section 3.1, starts with the presentation of the unpowered passive ankle exoskeleton mechanical prototype and continues with the experimental design and study results. In the second part, Section 3.3, the clutch modification that improved the performance and robustness of the exoskeleton operation is presented and analysed. The chapter continues with the experimental design and the results of the second pilot study. The quasi-passive ankle exoskeleton research is published in [56–59](conference papers) and [60, 61](abstracts with oral presentation).

Chapter 4 introduces the novel variable stiffness mechanism and is associated to goal **G2** and hypothesis **H2**. **PLVL-VSA** mechanism is presented in Section 4.4, which introduces an advanced, higher performance prototype that is rigorously tested and finally integrated into an elbow exoskeleton prototype. Its research findings have been published in [62](journal paper) and [63, 64](conference papers). Next, Section 4.7 introduces a theoretical prototype that improves on the disadvantages of the previous prototype with an updated architecture, a new optimization method, and finally, by a comprehensive analysis. The research results of the modified mechanism are published in [65](journal paper), [66, 67](conference papers) and [68](abstracts with oral presentation).

Chapter 5 presents the development of a new upper-limb exoskeleton device and is associated with goal **G3** and hypothesis **H3**. The first part, Section 5.1, begins with the presentation of the design goals and the new mechanical prototype. This is followed by Section 5.3, which introduces the mechatronic and electrical components. The control aspects of the device are presented in Section 5.4. The experimental design and results are shown in Section 5.5. Finally, in Section 5.6, the concept for the integration of mechanically compliant elements into the existing exoskeleton device is presented. The upper arm exoskeleton was presented in [69, 70] (abstracts with oral presentation).

Chapter 6 presents future work, summarizes and concludes the thesis.

Chapter 2

Literature Review

The literature review in this chapter covers the fields of compliant actuators and exoskeleton technology. **Section 2.1** starts with an introduction of compliant actuation and continues with a brief overview of human and animal physiology (Subsection 2.1.1) where several evolutionary features evolved and depend on the passive elasticity of muscles and tendons. Subsection 2.1.2 continues the review of mechanical compliant actuation and analyses its advantages and disadvantages. The focus is shifted towards mechanically compliant actuators with variable stiffness in Subsection 2.1.3.

Section 2.2 explores the exoskeleton technologies. The review starts with an analysis of rigid exoskeleton technologies with compliant actuation (Subsection 2.2.1) and continues with soft exoskeleton technologies (Subsection 2.2.2). Next, Subsection 2.2.3 introduces the passive and quasi-passive exoskeleton technology. Finally, Subsection 2.2.4 gives a short overview of the control of both exoskeletons and compliant actuators and concludes the literature review.

2.1 Compliant Actuation

2.1.1 Human & Animal Physiology

Research shows that elastic/compliant mechanisms are essential for the effective function of the muscle motors that power human and animal movement [71]. Awareness of these mechanisms can serve both as inspiration and motivation to strive for more efficient robot systems. For this reason, this section examines some characteristics of animal and human muscles and explains some principles for more efficient movement.

The simple effect of elastic elements or springs is that they stretch and store elastic strain energy when the force is applied to them, and spring back to release the energy when the force is released. Proper use of these springs offers the following advantages:

- conservation of metabolic energy,
- amplification of muscle power output,
- attenuation of muscle power input,
- rapid mechanical feedback that may aid in stability.

Human and animal muscles are associated with springy tissue, both within the muscle and in connective elements such as tendons. Paraphrasing from [33], a wheeled vehicle moving on level ground has a constant potential and a constant kinetic energy. To continue its movement, the vehicle only has to overcome the friction between the moving parts and the air resistance. The situation is not necessarily the same when using legs and other limbs instead of wheels. Yet, even in legged systems, animals and humans have developed three different ways of using passive elements to store lost mechanical energy and make

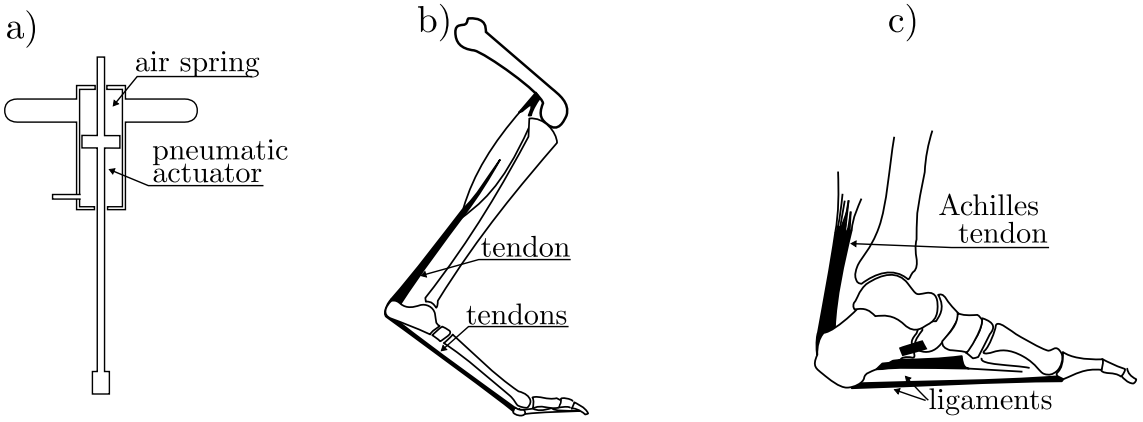


Figure 2.1: The pogo stick principle. A pneumatic jumping robot [33] shown in **a**, tendons spanning the animal leg in **b** and tendons spanning the human ankle joint in **c**. All three figures are adapted from [33].

movements more efficient [33].

To explain them, the author of [33] divides the energy of a mass system between the *external* and *internal* energy. The *external energy* of a body (external kinetic plus potential energy) is related to the motion of its center of mass. In contrast, the *internal energy* is related to the movement of parts relative to the center of mass. When moving with legs, the fluctuations of the external kinetic energy can be avoided by using springs in the legs. A concrete example is the pogo stick, see Fig. 2.1a. This pogo stick principle is the *first mechanism* to increase the efficiency of leg movement and deals with the fluctuation of external energy.

The serial elasticity built into a pogo stick makes it possible to store the external energy of a body when the foot touches the ground and then return it to preserve the energy of the system. The same is realized in animals and humans, i.e., jumping on springs when running (pogo stick principle) by using monoarticular (across one joint) and multi-articular muscles and tendons (across multiple joints). The energy is temporarily stored in the spring as strain energy, and no work is required for the actuators (except for overcoming energy losses in the spring plus friction and resistance). The pogo stick principle is used by quadrupeds, see Fig. 2.1b and by two-legged mammals, including kangaroos and humans, see Fig. 2.1c.

The human/animal body loses and regains its kinetic and potential energy when walking/running while the foot is on the ground.

The difference compared to a mechanical system is that the springs are replaced by tendons of the leg muscles and ligaments in the foot. The tendons have good elastic properties with an efficiency of up to 93% [33], which means that 93% of the stored energy can be returned and the rest is dissipated. Article [33] also argues that, when running, different speeds require different stiffness, which is an argument for actuators with variable stiffness. For the human counterpart, Sawicki et al. [34] outlined the significance of tendons in human walking, see Fig. 2.1c. These tendons improve the efficiency of the ankle's joint work by storing and releasing elastic energy in the Achilles tendon during each step.

While the *external energy* is associated with the movement of the mass-centre of the system, the fluctuations of the *internal kinetic energy* are a consequence of the reciprocal actions of parts. If, for example, the back and forth swung legs are accelerated or decelerated by inelastic actuators, the kinetic energy given to them at the beginning/end of each swing is dissipated as heat at the end. Energy is saved if the legs can be stopped

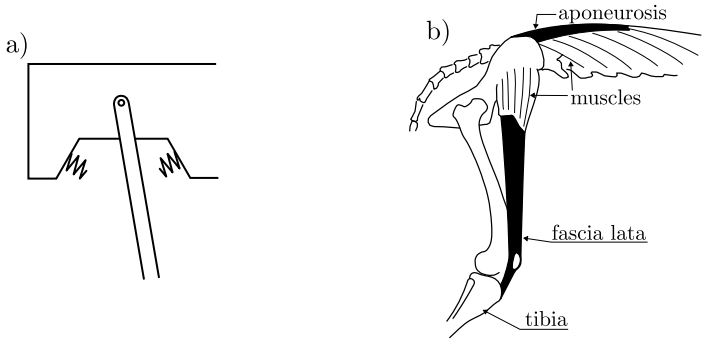


Figure 2.2: Return spring principle. The simplified schematics is shown in **a**. A potential example of a return spring from the animal kingdom **b**. Both figures are adapted from [33].

and re-accelerated by springs, see Fig. 2.2a. This is the *second principle* for increasing the efficiency of leg movement using return springs.

For a concrete example, the *Fascia lata* from the animal kingdom can be thought of as a return spring for the hind legs, see Fig. 2.2b. It runs down the front of the thigh and connects to the tibia. While it appears to function as a return spring in quadruped mammals, it does not have the same function in humans, as it runs along the side of the thigh and not at the front as in animals. Another tendon that stores strain energy is the *Longissimus aponeurosis*, see Fig. 2.2b. It serves as a tendon of the main extensor muscle of the back. Rough calculations [33] indicate that a substantial part of the internal kinetic energy that is lost can be stored in it as elastic energy. Most of this energy is taken from the front legs and returned to the back legs.

The *third type* of passive elements used in animals and humans is foot padding. A rigid foot that lands on a rigid floor would be slowed down very quickly and experience large peaks of force. Some form of padding is required to prevent excessive impact forces. The feet should be light in order to keep the fluctuations of the external kinetic energy low, but they must also have a certain mass to provide support for the entire system. Most

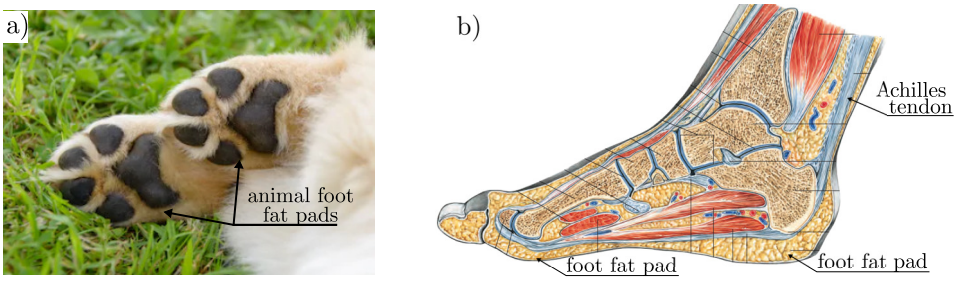


Figure 2.3: Fatty pads in animal **a** and human feet **b** [72]. Figure **a** is adapted from *www.shutterstock.com* and **b** is adapted from [72].

mammals (e.g., dogs) have padding on their paws, see Fig. 2.3a. Humans have fat pads under the skin of the sole of their feet and use additional padding (in the form of shoes) when walking and running, see Fig. 2.3b.

The use of the passive elasticity of human and animal muscles offers another important advantage, namely the adjustment of stiffness. It is an important feature of both humans and animals for successful operation in unstructured environments. However, in order to understand it, we first introduce the mathematical modelling of muscles. The human

body is highly nonlinear, but muscles can be approximated by smaller functional blocks acting as contractile units, i.e., motors, and other blocks acting as passive elements, i.e., springs. A famous example is the Hill muscle-tendon model [73, 74], see Fig. 2.4. It is important because its structure is analogous to the structure of various compliant actuators presented in Section 2.1.2. It also gives an insight into the functioning of muscle and

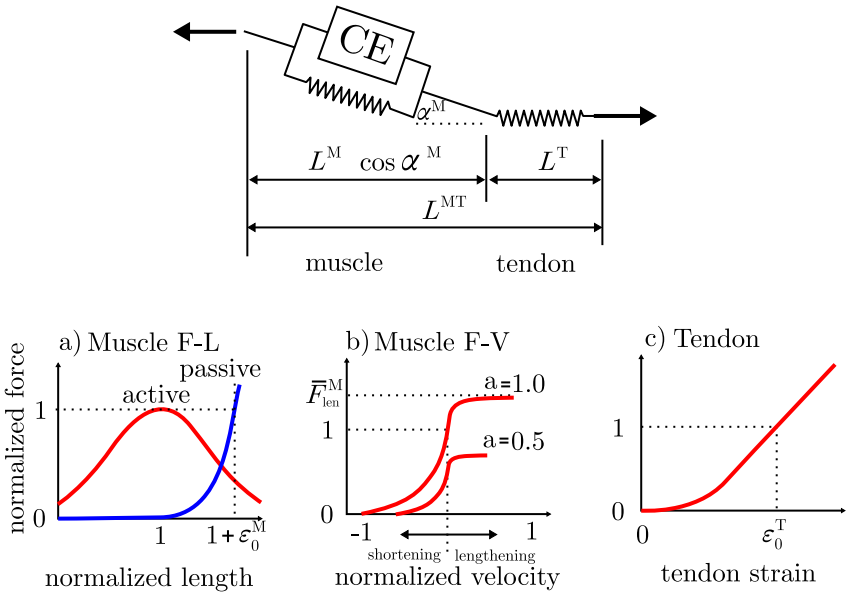


Figure 2.4: Hill musculo-tendon contraction model. The model consists of a muscle contractile element in series and parallel with elastic elements. The muscle has a scaled force-length and force-velocity relation dependent on activation, as shown in graphs **a** and **b**. Value a stands for the amount of muscle activation. A tendon extension/force model is shown in **c**. Figure is adapted from [73].

muscle systems. To better approximate the actual nonlinear muscle behavior, force-length and force-velocity relationships are introduced, since the muscle has biological/mechanical limits. The maximum force exerted depends on the muscle length, see Fig. 2.4a and is combined with additional passive elastic behaviour. Likewise, the exerted force is also dependent on the contraction speed and leads to a muscle force-velocity relationship 2.4b. Finally, the tendon spring effect is modelled as an exponential, see 2.4c. The value a in Fig. 2.4b stands for muscle activation and captures the muscle input command.

The human muscle is only able to generate a force when it contracts. The bidirectional movement of a human joint is then made possible by muscles that work in an antagonistic architecture [75]. This combination of agonist-antagonist pairs leads to an adjustment of the stiffness. The active muscle is called the agonist and the opposing muscle is called the antagonist. There are several agonist-antagonist muscle pairs in the human body, see Fig. 2.5 for the arm and leg muscles. The agonist-antagonist action occurs when one of the two pairs of muscles, or sometimes a group of muscles, flexes around an articulation while the other muscle expands. Co-contraction is the simultaneous activation of both muscles of the pair. It serves as a means of controlling the force exerted or the speed of movement of the limb.

As for the strategy of stiffness adjustment, research shows that humans reduce the stiffness of their arm when they expect a collision or when working in contact with the environment, or they increase the stiffness for higher precision [76]. A safe motion is ensured when all kinetic energy is absorbed in elastic deformations. This is possible due

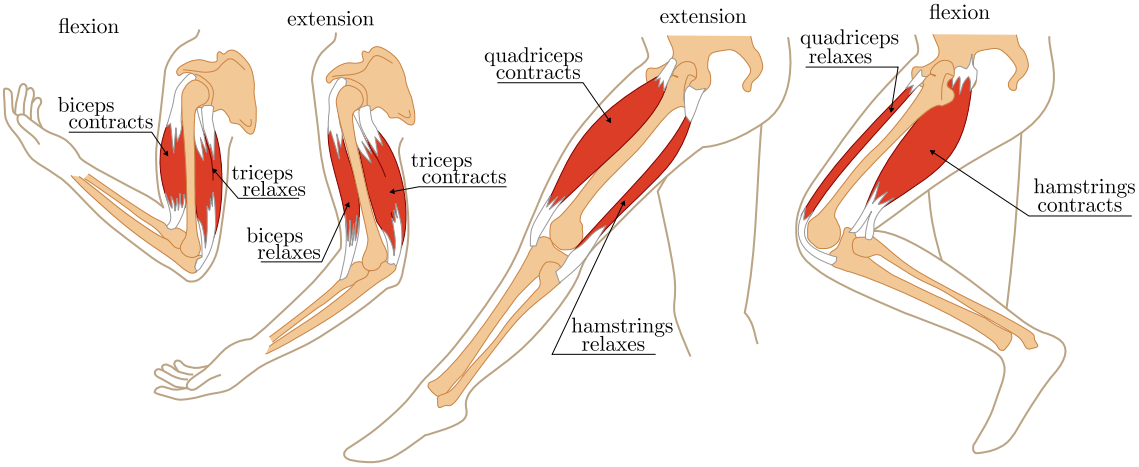


Figure 2.5: Two antagonistic muscle pairs in humans. The flexion and extension of the elbow joint and its biceps/triceps antagonistic pair is shown in the *left* image. The quadriceps/hamstring antagonistic pair is shown in the *right* image.

to the decoupled inertia and a lower mass/inertia of the human limb or robot arm. The decoupled inertia allows faster movements, while the risk of injury remains low [77]. It should be noted that this maintaining and altering of human joint stiffness by coactivated antagonistic muscles is metabolically expensive, even when the muscles do not perform any net mechanical work. In theory, effective human augmentation is possible through actuators that operate in parallel with human joints, even if these only supplement joint stiffness without performing net mechanical work [78].

To achieve stability in classical feedback control, high mechanical impedance, high sensor resolution and high control bandwidth are required [79]. The human body has a long signal transmission delay, which makes it physically inferior to artificial systems in terms of feedback control performance [80]. Nevertheless, humans can achieve not only a stable, but also a robust and adaptive control capability. A significant contribution to this performance is highlighted as feed-forward control. Humans may utilize joint stiffness to compensate for the inverse dynamics model uncertainty [80].

Sometimes, the stiffness is modulated to maximize the amount of kinetic energy that is transferred from the human limb onto an object, like throwing [81] or kicking [82]. Here the stiffness modulation is adapted to store the maximum amount of elastic energy into one's tendons or elastic elements and then this stored energy is released to amplify a specific movement. This opens the field of energy-aware motion planning [83]. Through proper stiffness adaptation, the external link is able to move much faster and transfer more kinetic energy into the desired object.

As seen above, mechanical stiffness and the ability to modulate it are two very important characteristics of the human and animal body. Not surprisingly, the research community is moving towards compliant robotic actuation, which is why the next overview section focuses on this.

2.1.2 Compliant Actuators

The classic electric motor-gearbox combination is considered a stiff actuator. See Fig. 2.6a for the component architecture diagram. Robots that use such actuators, e. g., industrial robots, strive for strength, precision and repeatability. However, such actuators are not suitable for working in an unstructured environment. Due to a high inertia, a lot of energy

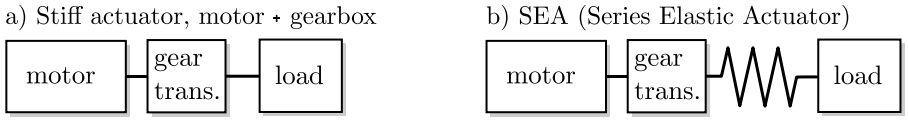


Figure 2.6: Compliant actuation architectures - part I; **a** stiff actuator, **b** series elastic actuator.

is dissipated in each unpredicted collision, which makes such robots unsuitable for force-oriented applications with many contacts and collisions [84].

However, this does not mean that such robots are unable to perform such tasks. They can be programmed to simulate compliant behavior in order to work reasonably well in force-oriented tasks [31]. Such software-based compliance is called *active compliance*. The compliance simulation is possible by high frequency torque feedback loops based on the output of integrated torque transducers. The robot detects the external disturbance through torque sensing and responds to it. The drive elements of such robots are very compact with highly integrated sensor technology and high-quality speed reducers, see Fig. 2.7(right). To increase safety, the robot joints are designed to be lightweight, which in turn reduces impact forces. A very famous robot built this way is the Kuka LWR (Light Weight Arm) series, see Fig. 2.7(left). The Kuka LWR employs compact drives and lightweight robot links.

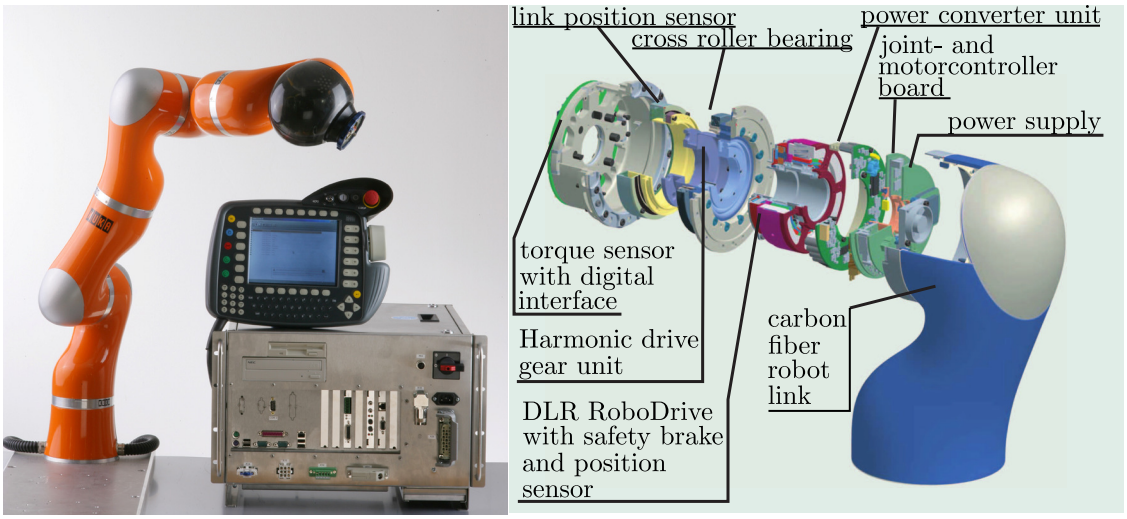


Figure 2.7: A collaborative robot; KUKA LWR (Light Weight Robot) [85] is shown *left* and its mechatronic joint design, including actuation, electronics, and sensing is shown *right*. Figures are adapted from [85] and [31].

Although such robots can perform force-oriented applications, they essentially function on the same technological principle as rigid robots. In order to meet the true performance criteria for force-oriented applications, mechanically compliant actuators are required [40]. Hardware with mechanical compliance has several advantages for robotic applications, both from the robot's and user's point of view. These include safer human-robot interaction and better energy efficiency of motion [31]. The compliant element acts as a low-pass filter that reduces peak forces [40]; it therefore protects the mechanical components of the device, e.g., gears, bearings etc. Improved force accuracy with higher stability is another

advantage. The simplest version of a compliant actuator is a series elastic actuator or SEA, see Fig. 2.6b. The elastic element decouples the external link inertia from the motor and allows for external link speeds that are higher than the motor's limits allow [84]. The decoupled inertia ensures intrinsic safety [77] and allows for higher speeds while retaining a low risk of injury.
Further advantages are [51]:

- lower cost and weight of the drive units, as it allows the use of smaller and lower precision components,
- replacement of expensive load cells with a simple spring and a position sensor measurement,
- force measurements that are less prone to chatter and noise,
- use of components with higher impedance and higher stiction is not disadvantageous.

Besides the series configuration, the elastic elements can also be used in other architectures, such as the parallel motor/spring architecture (parallel elastic actuator – PEA), see Fig. 2.8a. Such an actuator can generate torques above its motor operating limits [84]. Through the use of mechanical switches, the elastic elements can also operate in a discrete manner. By successive recruitment of parallel elastic elements using a low-power actuator, adaptive load compensation can be achieved in a passive way [86]. A combination of both cases is

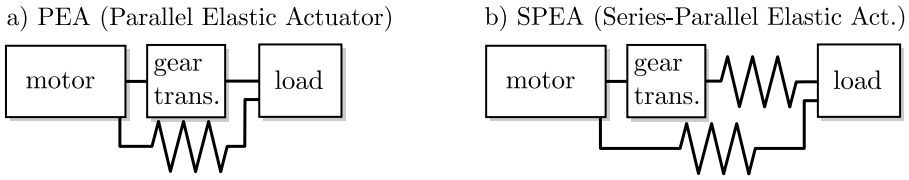


Figure 2.8: Compliant actuation architectures - part II; **a** parallel elastic actuator and **b** series-parallel elastic actuator.

also possible to achieve a parallel/serial structure and combine the advantages of both, see Fig. 2.8b as an example.

Besides the electric motor and elastic element combination, there are also other types of actuation that exhibit a mechanically compliant nature, such as:

- motors and springs in an antagonistic architecture,
- pneumatic cylinders or pneumatic muscles, since air is a compressible medium,
- hydraulics in combination with passive elements.

The above principles have their own advantages and disadvantages, and different controller designs [87]. They often require the use of completely different technologies, such as pneumatics or hydraulics, which adds additional layers to the design complexity of the system. The aspects of mechanical design include the selection and properties of actuators that can critically determine the intended use. This has been demonstrated in the design of various robot mechanisms, e.g., in humanoid robots [88–90] and jumping robots [37, 50], but also in wearable devices [44, 91, 92].

The last interesting actuation principle is called one-to-many. Normally the size, weight, and power consumption of wearable robots rapidly scales with their number of active degrees of freedom. Thus, a simple solution to keep the devices lightweight is to simply reduce the number of motors used to run the device. This can be achieved using many underactuation strategies. However, another paradigm is to independently control multiple degrees of freedom using a set of modular components, all tapping power from a single motor [93]. For example, the exosuit powered by the one-to-many scheme in [93] reduces the biological torque required to move by an average of 46.2%, compared to the unpowered

condition.

Compliant actuation brings advantages and disadvantages. One of the main difficulties is a higher mechanical complexity, which is higher than in classical plain geared motors, making the use and implementation of such technology more difficult and costly. Researchers are concentrating on the development of novel device architectures and the production of prototypes, also due to the commercial unavailability of such devices. There are many possibilities for mechanical simplification and for control design research [41]. The result are different types of compliant mechanisms in the literature with different advantages and disadvantages [42, 54, 55].

2.1.3 Variable Stiffness

Mechanically compliant actuators can prove to be superior to their rigid counterparts in force-oriented applications, even when using a fixed elastic compliance. However, to achieve truly efficient movements, the mechanical stiffness must be right. In Section 2.1.1, an argument was presented where the optimal stiffness for the most efficient motion depends on the speed of the motion. As is shown later in Section 2.2, the possibility to adjust the mechanical stiffness can be advantageous in such situations.

It should be noted that the SEA (Series Elastic Actuator) typically uses an elastic element with a fixed compliance, but with appropriate software it can render a virtual variable compliance including near zero stiffness and high stiffness up to the inherent mechanical stiffness [94]. Such a virtual variable compliance represents a best-of-both worlds scenario in which the actuator has the advantages of a mechanical compliance actuator and can simulate a virtual variable stiffness for applications that require it. Mechanical compliance through the use of the SEA approach is less complicated than the complexity of a variable stiffness actuator. Simulated compliance variability of mechanically compliant SEA can be classified somewhere between the *active* and *passive* compliance. However, in such systems, the inherent system dynamics remains the same regardless of the control method.

Advanced VSAs (Variable Stiffness Actuators) are based on a special mechanism that can manipulate the elastic element or modify the internal transmission to change the stiffness of the whole mechanism, see Fig. 2.9a. They use a second motor to add the capability of true mechanical compliance adjustment. Typically, the first motor is larger and is used to move the system to the desired position, while the smaller one changes the stiffness of the mechanism. Such technology may be suitable not only for exoskeleton

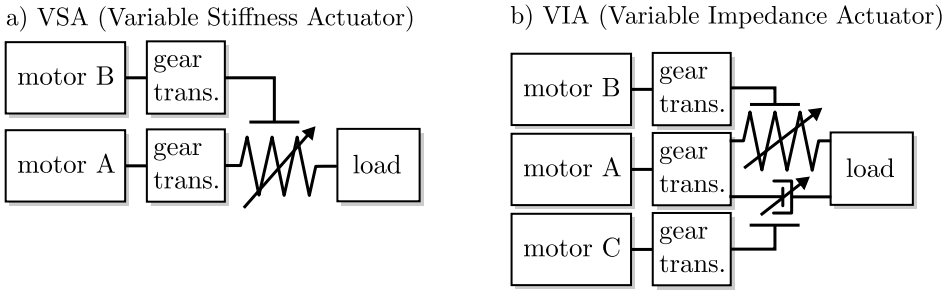


Figure 2.9: Compliant actuation architectures - part III; **a** variable stiffness actuator, **b** variable impedance actuator.

actuation, since exoskeleton devices work synchronously with humans and must be highly adaptable, but also for devices based on the use of passive or quasi-passive elastic elements

that require certain stiffness characteristics.
Stiffness variability adds additional advantages to the systems using it:

- modulation of natural dynamics [45],
- adaptation of stiffness to achieve different levels of assistance in a rehabilitation task depending on the patient's progress [42],
- ability to perform precise slow movements with higher stiffness and fast motion in a low stiffness setup [95].
- possible balance aid through stiffness modulation [46].

However, such technology is not without disadvantages. As the community strives for ever lighter robots with increased safety, such advanced mechanisms require additional weight, resulting in much more challenging lightweight design.
The disadvantages can be summarized as:

- intricate variable stiffness mechanisms are mechanically complex and entail a higher number of components,
- higher mechanical complexity results in more complex and costly manufacturing,
- higher mechanical complexity can increase the system weight and inertia,
- the system is prone to oscillations, due to its compliant nature,
- dealing with oscillations requires control algorithms with a higher complexity.

The above-mentioned disadvantages often hinder the use of these devices. However, on the other hand, this creates the opportunity for simplification and cost reduction [52], and with a proper mechanical design the disadvantages can be mitigated. A logical step beyond the VSA is to add a motorized damper as a third element, as shown in Fig. 2.9b, to produce a VIA (Variable Impedance Actuator), but due to the very high mechanical complexity, its use is often not justified even when compared to the VSA.

Despite the higher mechanical complexity, the amount of research in the field of variable stiffness actuators is constantly increasing, leading to predictions that the next generation of robots will use variable compliance hardware [30]. The favorable properties made possible by mechanical compliance and the infinite possibilities to implement elastic elements into the actuator geometry led to a large number of devices with various architectures and variants, each with its own advantages and disadvantages [96–98]. A broad overview of different types of compliance, e.g., emulated active compliance, fixed inherent mechanical compliance (SEA) or actuators with mechanically varied compliance (VSA) and different technologies that make this possible is presented in [42, 54, 55]. These papers focus on the description of different architecture types and principles of different mechanisms, thus providing a broader framework for research. The paper [42] also describes potential applications that may benefit from variable compliance actuators. Examples include safe industrial robots that can work in close proximity to humans, naturally moving toys that are less susceptible to damage, rehabilitation robots that use compliance to achieve different levels of support to improve patient recovery, robotic prostheses, walking and running robots, etc. All the applications listed depend on the characteristics of the variable stiffness actuators used.

One can exploit the advantages of both fixed compliance actuators (SEAs) and variable stiffness actuators (VSAs). Considering a gait-assistance device, both SEA and VSA find suitable applications [99]. In many situations, the use of a VSA would offer minimal benefits while unnecessarily increasing complexity and weight. However, a suitable fixed compliance is often not immediately clear, so in research situations a variable stiffness device is advantageous as it allows fast and practical stiffness adjustments. Overall, VSAs are defined by a wider range of parameters than classical actuators or SEAs, e.g., the deflection range, the stored energy, the speed of stiffness change, etc. These variables are nicely presented in [30] and [41].

Some actual examples of compliant actuators with mechanically variable stiffness from literature are presented in the short overview that follows. The reader should note that these examples represent only a small part of the available compliant technologies. In addition to the design properties under the aspect of achieving variable stiffness, the VSAs are considered in the scope of wearable devices. Here, energy efficiency can mean a longer battery time and a lighter and smaller actuator can reduce the additional weight influence and the amount of kinematic obstructions on the user. The suitability of such actuators is correlated with the desired application or task, which also makes comparison between them difficult. Some of the analysed actuators aim at wearable applications, while others aim at a humanoid robot application.

Three VSA actuator types have significantly influenced the field and the present dissertation. These are the MACCEPA-type VSAs, the DLR (German Aerospace Center) actuators, and the AwAS-type actuators. They have easily distinguishable operation principles and a high amount of available literature data. There are also many other VSA variants [100–103], but they often use a much larger number of non-standard parts, which increases not only their complexity but also the complexity of their comparison.

MACCEPA is the first interesting stiffness variation mechanism to be analysed. It is a well established VSA principle [98] and has a uniquely simple and straightforward method of stiffness variation. It is presented in Fig. 2.10.

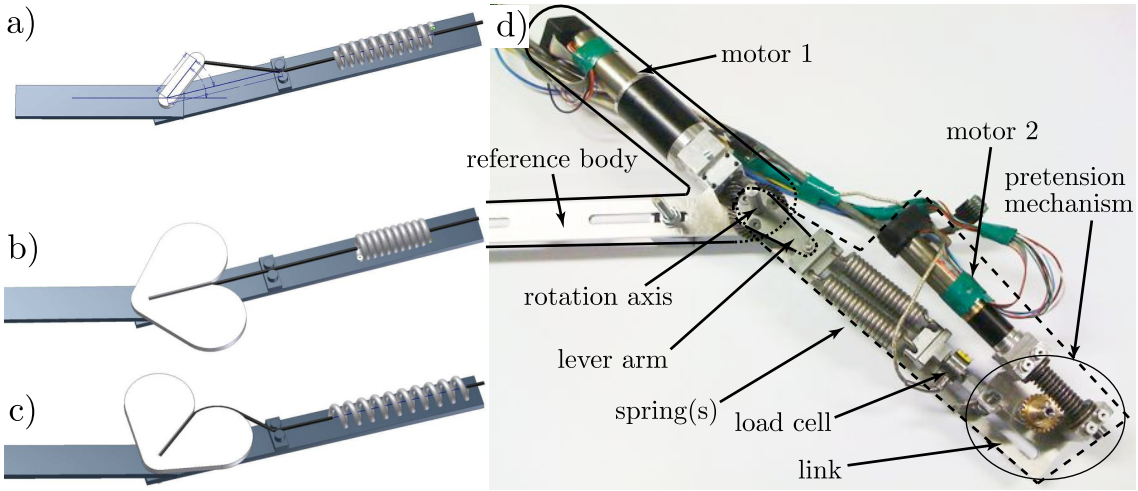


Figure 2.10: The working principle of the MACCEPA actuator is shown in **a**. **b** and **c** show the working principle of the novel MACCEPA 2.0, in an equilibrium position and in a deflected position. A prototype of the actual MACCEPA actuator system is shown in **d**. Images **a**, **b** and **c** are adapted from [104] and **d** is adapted from [105].

Its compliance is achieved by a third link which deflects and pulls on a steel cable connected to a linear spring, see Fig. 2.10a. The relative position of the external link to the third link determines the equilibrium position. To change the stiffness, a second motor can preload the elastic element, see Fig. 2.10b,c. Overall, the MACCEPA is known for a large deflection range and its ability to store more potential energy than other actuators [106]. Its flat and long structure is suitable for portable applications, as the hardware is kept close to the limbs, however, the same feature also makes it difficult to design compact units.

Over the years, further versions of the MACCEPA VSA have been released. A pulley upgrade in MACCEPA 2.0 [107] enabled a task-related modification of the actuator torque/deflection characteristics. The use of extension springs in WHEELED MACCEPA

increased the robustness of the actuator, which allowed for implementation in the ALTACRO exoskeleton [105]. Recently, the use of a torsion spring in the TORSION MACCEPA version enabled a very compact actuator structure [108]. However, none of these versions solved the difficulties of the preload-based system for stiffness variation. In the case of MACCEPA, the force required to change the spring preload is applied parallel to the load. The stiffness motor must also overcome the force in the elastic element, which makes the stiffness variation less efficient. Consequently, the MACCEPA mechanism provides slower rates of stiffness change, e.g., stiffness variation time of 2.6s from 3% to 97% stiffness was reported in [105]. Of course, a stronger motor can always be used to speed up the stiffness variation, but this costs extra weight. The MACCEPA mechanism is therefore suitable for less dynamic stiffness change scenarios.

Another interesting variable stiffness actuator principle comes from the Italian Institute of Technology (IIT). Their actuators are called AwAS-I [97] (Fig 2.11a,b) and AwAS-II [109] (Fig 2.11c,d).

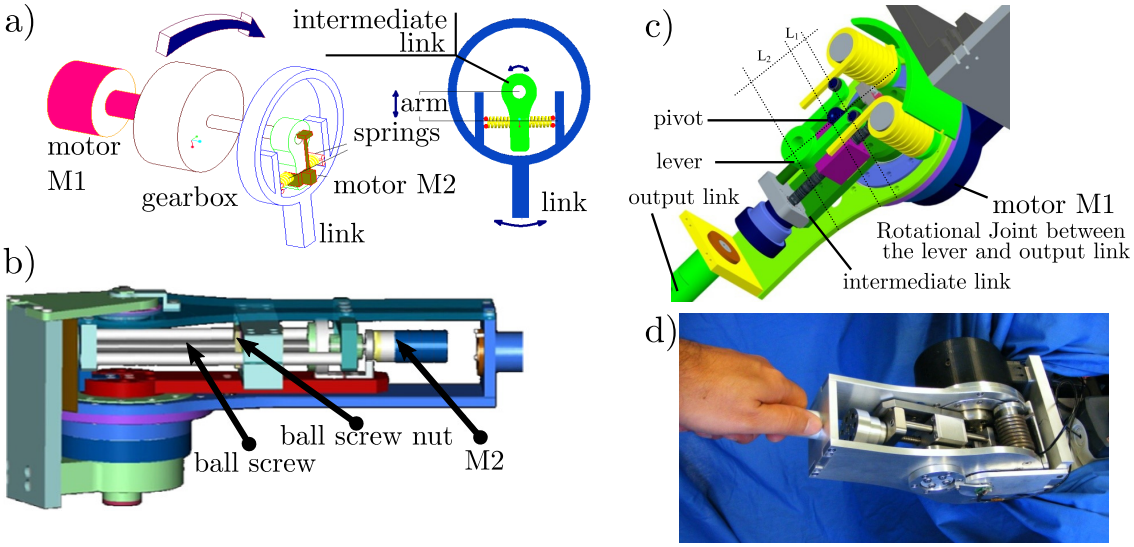


Figure 2.11: AwAS stiffness variation principle. **a** shows the operational principle of the AwAS actuator, where a lever deflection is opposed by linear springs. A computer model of the actuator is shown in **b**. The second version, AwAS-II, is shown in **c** and its physical prototype in **d**. Images **a** and **b** are adapted from [97] and **c** and **d** is adapted from [109].

The actuator functions as shown in Fig. 2.11a, where a rotary lever is placed between two linear compression springs. The deflection torque is generated when the lever arm compresses the linear spring. A screw mechanism can move the spring linearly to change the length of the lever, which determines the torque required to compress the spring. A longer lever length results in a higher stiffness. In terms of performance, the AwAS has a clear advantage because its mechanical design varies the stiffness perpendicular to the spring load. Most of the spring load is transmitted through the mechanical structure of the actuator and through the stiffness variation motor. The stiffness motor only has to overcome the friction in the bearings and the inertia of the linear stiffness variation mechanism. This property can be exploited in favour of either a faster stiffness variation or a lower stiffness variation torque and therefore a less powerful stiffness variation motor. A potential disadvantage of this system is that it requires a relatively rigid structure. The use of linear guides can be problematic because they must be able to withstand the whole

force of the spring without mechanical deformations. This increases the required size and weight of this design. However, some of these problems have been improved in the second version AwAS-II [109] by using torsion springs, see Fig. 2.11c,d.

Before continuing onto the last VSA example, the parallel and perpendicular application of force is further clarified in Fig. 2.12, which shows a load hanging on a thread. The task is to lift the load higher. There are two ways to apply a force. One can be applied in parallel to the load and another force can act perpendicular to the load. Note that, as the

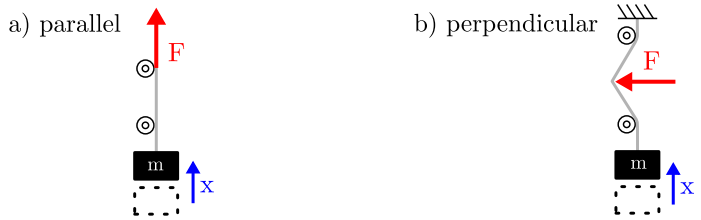


Figure 2.12: Perpendicular and parallel force application analogy. **a** shows the parallel force application and **b** shows the perpendicular force application.

perpendicular force continues to move the cable, it is becoming less perpendicular to the load. Technically, it is perfectly perpendicular only at the beginning and as soon as the cable routing changes its geometry, the perpendicular feature is lost. The system essentially differs in the manner of mechanical force transmission, where the second perpendicular force application system relies on mechanical singularity.

Another group of actuators, namely the DLR actuator VS-Joint [110] and its second version DLR FSJ [96] have a very compact structure, which is made possible through the use of the cam mechanism principle. The deflection is achieved by the rotation of a cam disc, which compresses a spring-loaded follower, see Fig. 2.13b. Higher stiffness is achieved

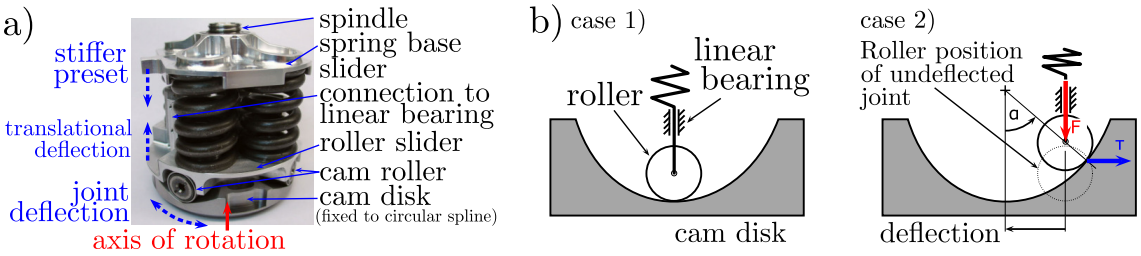


Figure 2.13: The VS-Joint mechanism is shown in **a** and its principle of operation is shown in **b**. Both **a** and **b** are adapted from [110].

via spring pretension, see Fig. 2.13a. Both version use a variable spring preload principle to change the stiffness of the mechanism and a cam mechanism to deflect the spring. The second version differs slightly in its operation, but is still based on the cam mechanism, see Fig. 2.14a,c. The compactness was also demonstrated in the implementation of DLR's [49] Hand Arm System, in which all joints are mechanically compliant. See the highly compact actuator in Fig. 2.14b.

While the cam mechanism offers a convenient way of converting the rotary motion into a linear deflection, the transmission of force is less effective due to the pressure angle. One of the more important properties of cam mechanisms is the pressure angle α (see Fig. 2.15). It is defined as the angle between the follower direction of motion (up-down, green arrow in Fig. 2.15) and the normal at the contact point between the follower and the cam surface (see Fig. 2.15). The value of the contact angle is important as it determines the

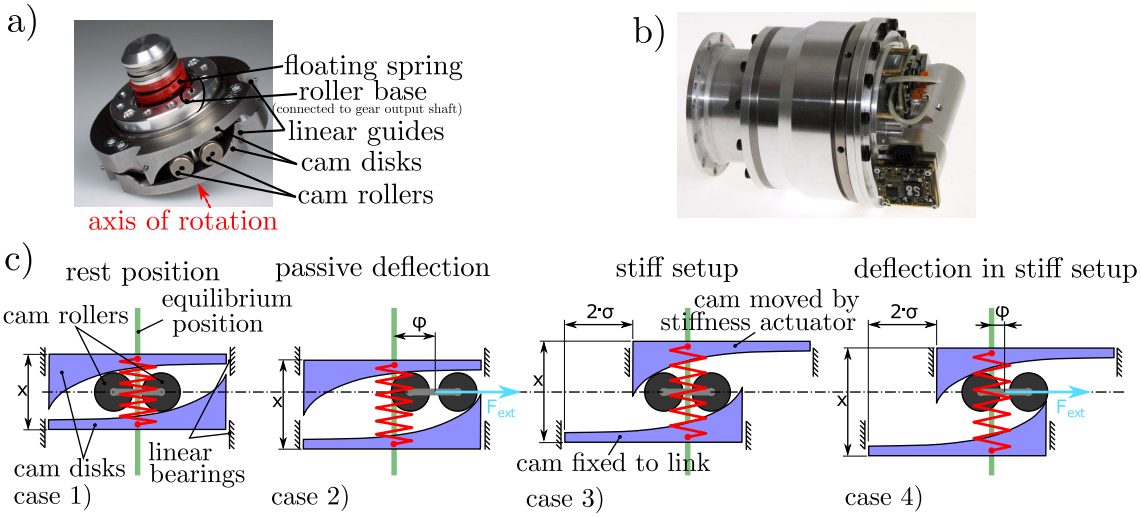


Figure 2.14: The FS-Joint is shown in **a**, with its principle of operation in **b**. The final prototype implementation is shown in **c**. Images **a**, **b** and **c** are adapted from [96].

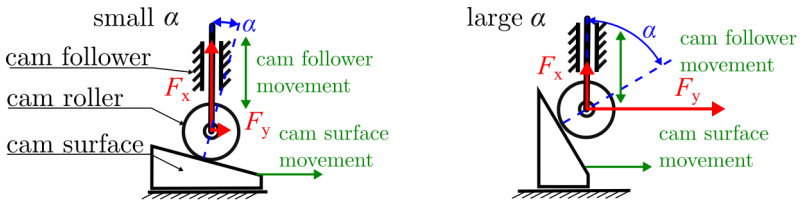


Figure 2.15: Small and large pressure angle α. The difference between a small pressure angle *left* and a large pressure angle *right*.

forces acting on the cam follower. If the angle is greater than 30° [111], the side thrust acting on the follower becomes large enough to completely prevent it from moving.

On the other hand, a smaller angle requires a greater force on the driver to turn the cam, which requires a very stiff compression spring (e.g., 908 N/mm for VS-Joint [110]). This also influences the achievable deflection angle, the torque and the maximum storable energy. Relatively high spring forces and spring preloads require a very stiff structure, which in turn is heavier and more difficult to manufacture. The actuator therefore uses a very stiff spring and requires large forces to generate a compression torque comparable to other actuators.

This is a significant limitation when weight reduction and efficiency of the VSA actuator are the primary concerns and is also the reason why this is not preferred in an exoskeleton application. Consequently, the actuator structure must be stronger and very stiff to withstand the spring force, which increases the complexity and weight of the actuator. The cylindrical shape can be advantageous, when considering the right application [49]. In terms of a wearable application, the cylindrical shape is inconvenient due to the volume expansion along the joint axis. However, a flatter shape based on a cam mechanism is also possible, e.g., the MESTRAN actuator [112].

Finally, with the exception of AwAS-I and AwAS-II, the mechanisms listed above have a highly non-linear torque-deflection response, resulting either from the mechanism principle itself or from mechanism non-linearities, or from both at the same time. A progressive torque-deflection response is often considered desirable because a stiffening effect helps the

actuator to avoid reaching the mechanical end stops when low stiffness is set [41]. While progressive stiffening prevents the mechanical end stop from being reached earlier than a linear stiffening mechanism, it is mathematically more challenging to model and thus makes it more difficult to implement control.

2.2 Exoskeletons

Wearable devices, such as exoskeletons or exo-suits, shown in Fig. 2.16, have progressed to the stage where they can efficiently provide assistance and even augment user performance [7, 9, 113]. They can augment users or serve as prostheses for missing limbs to extend, supplement, replace or improve human functions and abilities, and they can empower or replace human limbs [114].

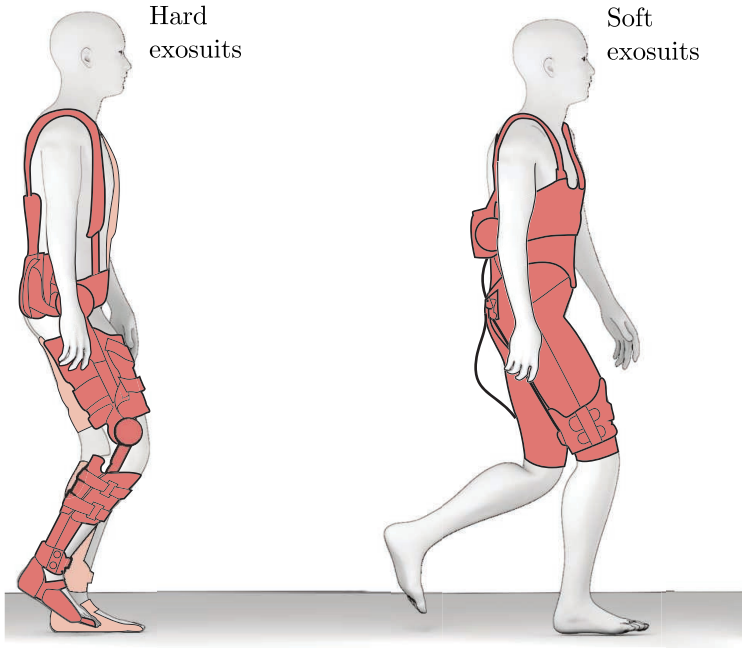


Figure 2.16: Exoskeletons and advanced sensors. The hard exo-suit is shown **left** and its soft counterpart **right**. Figure is adapted from [114].

Recent advances in actuators, sensors, materials, batteries and computer processors have intensified the development of wearable technology [8]. However, there are still many problems that stand in the way of successful commercialization and wider use, such as portability, energy consumption, social constraints and the high cost of these devices. Two big problems are also the lack of established terminology and benchmarking [32]. The high prices result from the complicated mechanics, actuators, sensors, complicated controls, electronics and the need for batteries. The difficulties differ between the spectrum of possible applications, which is wide and ranges from measuring devices to industrial and home support, rehabilitation, support and extension of movement of patients with disabilities, stress relief of users/workers, elderly and even healthy people [18]. The above outlines just some of the challenges of exoskeleton devices and justifies further research.

The exoskeleton devices can be classified in many ways. The first is *by type of construction material* used for the construction of exoskeletons [114]. In this aspect, we distinguish between *hard exoskeletons* and *soft exoskeletons*, see Fig. 2.16. Rigid exoskeletons have a strong and durable frame capable of transferring large forces or torques onto the user

or from the user towards the ground. The frame is actuated by motors directly at the respective joints. These exoskeletons are strong and stable, but also relatively heavy and can potentially hinder the kinematics of the user if the anatomical and artificial joints are misaligned. They are further presented in Subsection 2.2.1.

The more ergonomic alternative are the soft-exoskeletons, or textile exoskeletons. These exoskeletons naturally fit to the user's anatomical shape and are very ergonomic. Often, the heavy motors and power-supply components are placed away from the limbs, and combined with their flexible and light frame, the inertial characteristics of the body segments remain almost unchanged. The soft exo-suits rely on the user's bones to transfer the forces and torques, as they do not have any rigid shape, which could transfer the exoskeleton's weight to the ground. Subsection 2.2.2 is dedicated to the soft-exoskeletons.

The second way to classify the different exoskeleton is *by actuation type*, i.e., *active exoskeletons* or *passive exoskeletons*. Active ones are driven or actuated, and channel the motor power from the actuators to the user's joint or remove it. And the *passive exoskeletons* use passive elements to store kinetic or potential energy into elastic energy and return it in the next phase of movement. The *quasi-passive exoskeleton* group is similar to the passive group, but uses small motors or actuators to activate mechanical switches such as couplings and clutches, thereby activating passive elements. Section 2.2.3 is dedicated to such passive and quasi-passive exoskeletons.

Other classifications also exist, which are, however, less relevant for this dissertation. They are; e.g., *by area of assistance*, i.e., upper-body [115, 116] and lower-body exoskeletons [117]; *by intended application* [118], i.e., medicine, military, etc.; *by manner of construction geometry*, i.e., whether they assist in parallel to the human limbs, or whether they assist in a serial connection [119].

Finally, the last Subsection 2.2.4 is devoted to a brief overview of exoskeleton control and control of compliant devices. It should be noted that the control of both exoskeletons and compliant actuators have active communities and a wide field of research that goes far beyond the present dissertation, which focuses more on the mechanical aspect of exoskeleton design. Therefore, only minimal levels of control are used in this thesis, enough to allow performance testing of the built prototypes. The design of a more sophisticated control system at a higher level will be a part of future work.

2.2.1 Rigid Exoskeletons & Compliant Actuation

Exoskeletons with compliant actuators usually have rigid structures consisting of mechanical links and transmission mechanisms that are parallel to the user's limbs. *Hard* or *rigid* types are all exoskeletons that have a rigid support structure [32]. Implementation of mechanical compliance adds an additional complexity on top of the existing exoskeleton design, consequently, such devices that exploit compliant technology are less common in research than other types of exoskeletons. While initially exoskeletons were designed with stiff actuators, current research is clearly moving towards the inclusion of compliant elements [32] (i.e., actuators, structure, etc.) as a way to overcome the main disadvantage of the rigid exoskeleton in terms of adaptability, comfort, safety and efficiency. The developers select these actuators to achieve improved safety for human-robot interaction [120]. The other reason is the exploitation of the intrinsic dynamics during the motion cycle [121]. More concretely, the advantages of exoskeleton with a supportive rigid structure are:

- possible transfer of high torques, tension and compression forces onto the user's joints,
- high control bandwidth due to a very rigid frame,
- use of the exoskeleton frame to support the user and transfer the supportive forces directly to the ground.

The exoskeletons are also accompanied by several challenges:

- complex mechanical design requirements to achieve compactness and mechanical inter-person adaptability,
- complex control requirements such as intent-prediction, etc.,
- high manufacturing costs due to the complex shape of parts,
- energy requirements, efficiency and battery life.

The challenge of exoskeleton design is that motorized rigid exoskeletons can quickly increase the metabolic costs of the user due to their added weight and kinematic constraints. For example, changing the mass distribution of the legs via the addition of motors and heavy links has a detrimental effect on the cost of transportation [122] or the metabolic cost of walking [123]. Rigid exoskeletons often culminate in a heavy final device, since the exoskeleton weight is amplified through all the additional frame linkage. Furthermore, this linkage must be designed to adapt to the shape of the user's body so that the anatomical and exoskeleton joints are joined together. These mechanical requirements further increase the weight and mechanical complexity. The introduction of mechanical compliance, while beneficial, can introduce further design complexities and increase the weight.

There are several mechanically compliant exoskeletons that, despite their higher mechanical complexity, are used to study the positive properties of mechanically compliant technology [91, 105, 120, 121, 124–126]. This overview analyses a few of them. While many exoskeletons exploit the mechanical compliant actuation, many commercially available exoskeletons rely on the traditional stiff actuators, as they are a proven technology. The reader is referred to several additional review articles to get a more detailed overall view of various exoskeleton devices [17, 32].

The first interesting exoskeleton is called **Harmony** [127]. See it in Fig. 2.17a. The

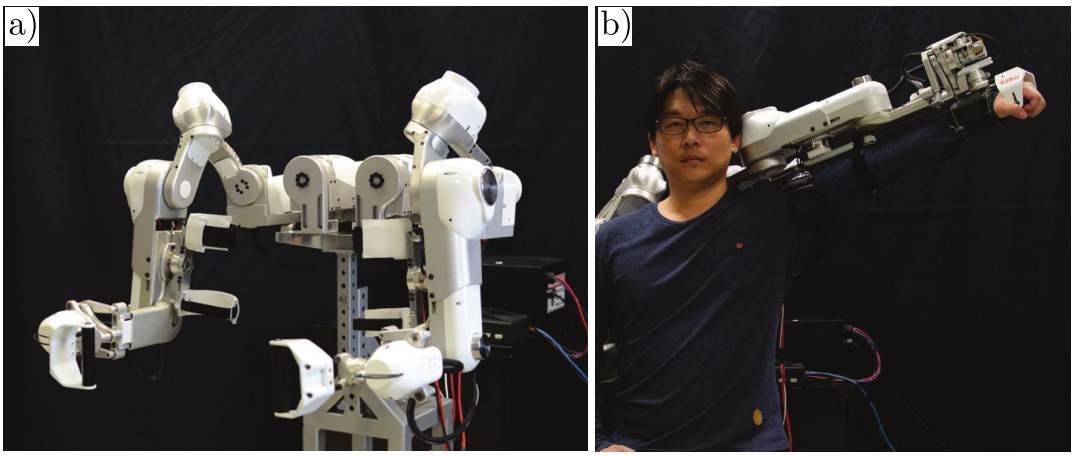


Figure 2.17: HARMONY exoskeleton shown in **a**. A user performing a complicated exoskeleton motion is shown in **b**. Figure is adapted from [127].

Harmony research group has invested a lot of effort in ergonomic and anatomically correct design. A special feature of Harmony is the anatomical shoulder mechanism with possible five degrees of freedom motion. See Fig. 2.17b for a complex motion example. This advanced upper body exoskeleton for rehabilitation offers natural, coordinated movements of the shoulder with a wide range of motion as well as force and impedance control. In addition, there is one degree of freedom at the elbow and a second one at the wrist. The exoskeleton is driven by series elastic actuators and is mechanically compliant. The results show that the exoskeleton has a good kinematic compatibility with the human body with a wide range of motion, and performs task-space force and impedance control behaviors reliably.

The second advanced exoskeleton is called **NEUROexos** [91] and is also a rigid exoskeleton driven by mechanically compliant actuation; see Fig. 2.18a. This experimental

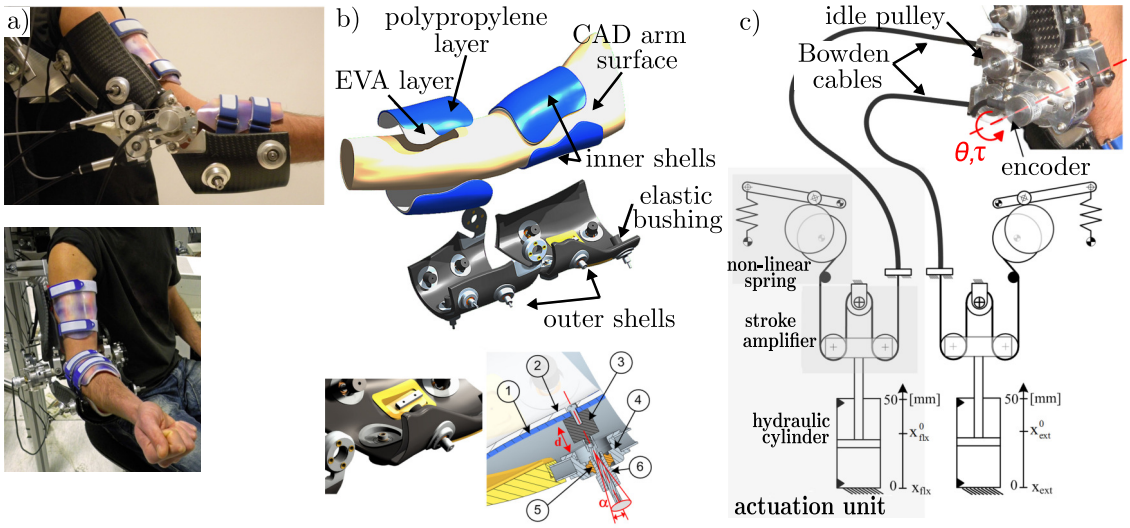


Figure 2.18: The NEUROexos exoskeleton prototype is shown in **a**. A mechanically compliant shell is shown in **b**. It is used to attach the exoskeleton onto the user and offers comfort and adaptability. Its compliant actuator is shown in **c**. Figure is adapted from [91].

exoskeleton has three solutions that allow its use for physical rehabilitation after a stroke. Firstly, the specially designed double-shelled links allow an ergonomic physical interface and a comfortable interaction between the human and the robot; see Fig. 2.18b. Secondly, a passive mechanism with four degrees of freedom embedded in the joint allows the user's elbow and robot axes to be constantly aligned during movement. While the movement of the elbow is often approximated as a wedge joint, the actual joint axis rotates during flexion of the elbow [91]. The proposed exoskeleton allows a passive rotation of the elbow axis on the frontal and horizontal planes 30° and 40°, respectively, and also a translation of the horizontal plane by 30 mm. Finally, the system is driven by an antagonistic actuation system with variable impedance. The variable stiffness actuators allow two control strategies: independent control of joint position and stiffness for the robot-in-charge rehabilitation mode; and near-zero impedance torque control for the patient-in-charge rehabilitation mode. The research shows that NEUROexos achieves greater comfort for the user because the device can adapt to the rotation of the elbow's axis and reduces pressure peaks on the user's skin through specially shaped inner shells. Development later continued towards a 4-degree of freedom exoskeleton [128], which also features self-aligning joints, but uses series elastic actuators instead of actuators with a variable stiffness.

Another interesting exoskeleton that we expose is called **VariLeg** [124]. It assists lower extremities and utilizes variable stiffness actuators in its joints. It is a novel powered lower limb exoskeleton that enables adjustments to the compliance in the leg with the objective of improving the robustness of walking on uneven terrain. This is achieved by an actuation system with variable mechanical stiffness in the knee joint, which was validated through test bench experiments, see Fig. 2.19b. The feasibility and usability of the exoskeleton was tested with two paraplegic users with motor complete thoracic lesions at Th4 and Th12. The interesting part of this exoskeleton is that it also participated in the CYBATHLON 2016 competition, which served as a field test for the usability of the exoskeleton. Research shows that during training with the exoskeleton, both users acquired



Figure 2.19: The VariLeg exoskeleton with its important features is shown in **a**. The schematic of the underlying compliant actuation system is shown in **b**. Figure is adapted from [124].

proficient skills in basic balancing, walking and slalom walking. In advanced mobility tasks, such as climbing ramps and stairs, only basic (needing support) to intermediate (able to perform task independently in 25% of the attempts) skill levels were achieved. Test bench evaluation of the variable stiffness actuation system demonstrates that the stiffness could be rendered with an error lower than 30 Nm/rad. After 4 months of training, one user competed at the CYBATHLON 2016 and was able to perform 3 (stand-sit-stand, slalom and tilted path) out of 6 obstacles of the track.

The last group of exoskeletons presented in this overview is important due to their medical certification. In 2014, the US Food and Drug Administration approved marketing of the ReWalk™ Personal Exoskeleton as a class II medical device with special controls. Since then Indego™ and Ekso™ have also received regulatory approval. All three devices can be seen in Fig. 2.20. This type of exoskeleton is most commonly used to help at the hip and knee. For example Ekso GT™ uses 4 actuators, which are placed at the hip and knee joints. The ankle joint uses a passive joint solution. The design goal is always to

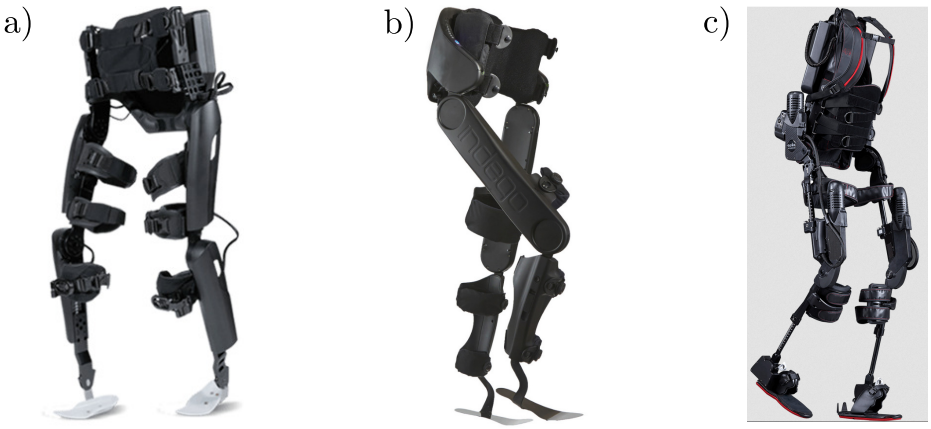


Figure 2.20: Lower limb exoskeletons; a ReWalk™ 6.0 [129], **b** Indego™ [130], **c** Ekso GT™ [131]. Figures are adapted from the respective sources.

use a minimal number of actuators that still allow a good enough tasks execution. Each additional actuator increases the complexity of the device, weight and cost.

The software of these devices offers many operating modes. In its most basic form, the first mode is intended to give the therapist control over the initiation of the patient's movements. After sufficient training, another mode can be used to transfer this movement initiation to the patient. In both cases the software tracks and monitors the patient's movements and progress.

The above lower-limb exoskeletons ReWalk^{TM} 6.0, Indego^{TM} and Ekso GT^{TM} are already deployed to the market. However, companies had/have to overcome many challenges. Authors in [132] examine some of the difficulties between the industry and regulation. It is a topic that is much discussed, since the industry is expected to grow rapidly and since, on the other hand, the regulatory science of powered exoskeletons is still developing. In addition, the nature and extent of the likely risks are not yet understood and industry standards still need to be developed.

2.2.2 Soft Exoskeletons & Bowden-Cable

Contrary to the rigid exoskeleton technology, soft or textile exo-suits [29] do not entail any support frames and are more similar to clothes than to robots. The primary building materials are fabric and flexible materials. Due to their flexibility, they are ergonomic and do not require any need for collocation of the human and exoskeleton joints. There is no need for any rigid links, and as a result, the final device has a lower overall weight, minimally contributes to the human limb inertia and imposes minimal additional kinematic constraints on the user. The exoskeleton relies on the skeletal structure to support compressive forces and provide assistance [133]. The final result is a lightweight, portable, and compliant wearable system [29]. With continuous refinement, this technology may even achieve a sufficiently low profile to fit under a wearer's existing clothing. One consequence of using fabric is that it can only transfer tensile forces and therefore the assistance is often only in one direction and has a much lower maximum support moment.

Quite a few soft exoskeletons already exist in the literature, for example Bae et al. [134] developed a soft exosuit that can improve forward propulsion symmetry and ground clearance in walking of users suffering from a paretic ankle, and ultimately reduces the metabolic cost of walking. The soft exosuit for paretic knee is also shown in Fig. 2.21a.

Soft fabric technologies require completely different materials than traditional robotics. The primary material becomes the textile, which requires completely different manufacturing, assembly and design techniques. A challenging example is the attachment of the actuating cables on the wraps, i.e., position of anchor points. The designer must be aware of how the forces are transmitted via the fabric and must therefore orient and align the materials accordingly. See Fig. 2.22a, b. Since the textile is locally much weaker than metallic materials, some stronger materials must be used in combination to distribute the force over a larger area. See Fig. 2.22c for some properties of different kinds of fabric.

The immediate advantage of this soft fabric is that it is not necessary to align it precisely with the biological joints. This alignment and adjustability are two key features of exosuits. Wearing the exoskeleton has literally no effect on the original human gait kinematics, due to the kinematic transparency [135]. A potential drawback can be the slippage of the suit, since these suits do not have a rigid support. The frame of rigid exoskeletons often spans from the user's limbs to the ground, and thus has its own connection to the ground and can prevent potential slippage of the frame/attachments in relation to the user's limbs. To prevent the soft exoskeleton from slipping, the suit must use conically shaped body parts for support or be fitted to the users shoulder in order to comfortably transfer the weight onto the user. Contrary to the rigid exoskeletons, due to the compliant suit and human

exo-interface, the bandwidth of the system is much lower. Furthermore, the fabric can transmit lower amounts of force/torque, as compared to the rigid exoskeleton counterpart. The torques are limited to about 0.1-1 times the biological nominal torques [135].

A special feature of the soft-suit exoskeletons are the specialized compact actuator units. See the compact actuator unit from [134] in Fig. 2.22d. These actuator units come with highly integrated electronics and cooling systems. Sufficient cooling allows them to optimally exploit the operational area of motors [29, 136]. Such cooling systems are much easier to implement in an actuator unit where all its components are gathered on the user's back and all the components that require cooling are in close proximity. In the case of hard exoskeletons actuation, each exoskeleton joint normally entails its own actuator unit, which would require its own cooling system. If the actuator is allocated away from the actuated joints, it requires a long-distance power transmission mechanism. Often, Bowden cable transmission is used to transfer the torques/forces from the actuator unit to the desired straps [136, 137]. It is a widely employed solution in most of the aforementioned applications, due to advantages in durability, enabled lightweight design, increased safety, and increased flexibility [135]. The major advantages of soft assistive devices driven by Bowden-cable transmissions can be identified in the superior ergonomics and wearability, allowing users to freely move as the actuation stages are allocated far from the end-effector. However, friction along the Bowden-cable transmission degenerates control performance unless it is properly compensated [138, 139]. One of the main reasons is the static and dynamic friction that occurs between the cables and the Bowden sheaths. Two other reasons are backlash and hysteresis [135]. The friction of a Bowden cable is dependent on its bend angle, see Fig. 2.23a. Fig. 2.23b shows the input and output force relation of the Bowden cable for different bending angle configurations. As seen in Fig. 2.23c, in theory, the efficiency of the force transmission quickly falls with the increasing Bowden sheath bending angle.

For soft exoskeletons many research and development challenges still remain in actu-

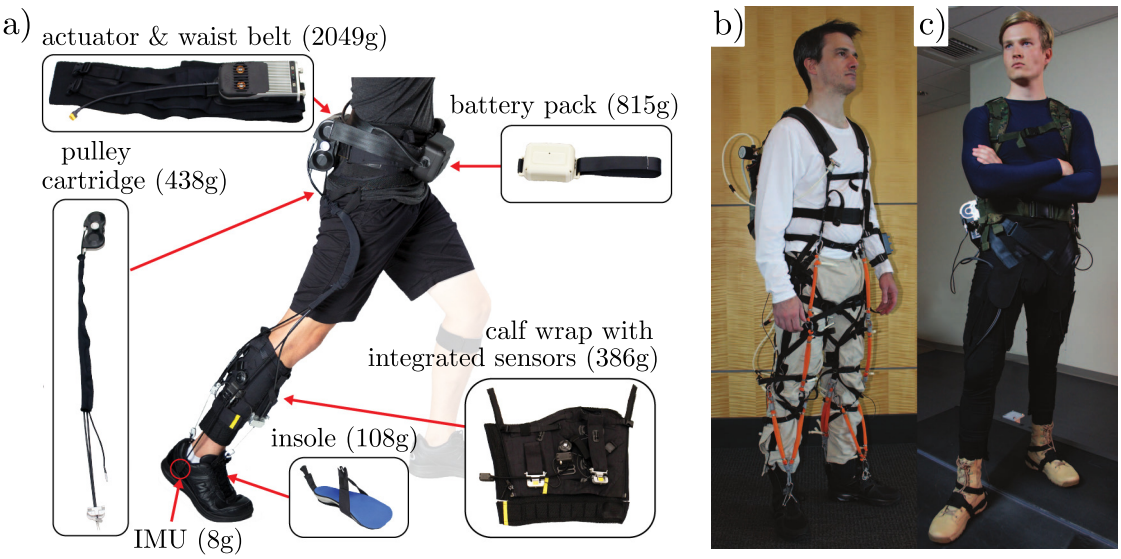


Figure 2.21: Soft exo-suits. A lightweight exoskeleton for the rehabilitation and assistance of a paretic ankle shown in **a**. Image **b** shows a lightweight exoskeleton with pneumatic actuation. A hip-actuated soft-suit exoskeleton with multi-articular actuation aiding in ankle plantar-flexion and hip flexion is shown in **c**. Image **a** is adapted from [134]; **b** and **c** are adapted from [29].

ator development, textile innovation, soft sensor development, human-machine interface (control), biomechanics, and physiology [29].

2.2.3 Passive & Quasi-Passive Exoskeletons

The group of exoskeletons based on passive or quasi-passive technologies forms a bridge between classical exoskeletons and novel compliant actuator technologies. They are not actuated in the normal sense, but may nevertheless reduce the effort required to carry out human activities. One of the main advantages of passive solutions over active solutions is a much lower weight, due to the absence of big motors or batteries. Passive exoskeletons can be lighter, easier to operate and consequently cheaper. Because of this, they possess better chances at market deployment and end-user acceptance. The reader should keep in mind that this passive technology also extends towards the design of advanced and efficient prostheses [140].

These devices are considered as passive because they use passive elements like springs to store energy passively instead of using motors and batteries to actively input power into human joints. In contrast, quasi-passive exoskeletons use motor power to activate a brake, a clutch or other passive components. However, they still primarily use passive technology, in the same way as completely passive exoskeletons, and do not introduce additional power into the user's joints. One of the goals of passive actuation is to try and reduce the amount of lost mechanical energy. An example is the pneumatic foot pad exoskeleton developed

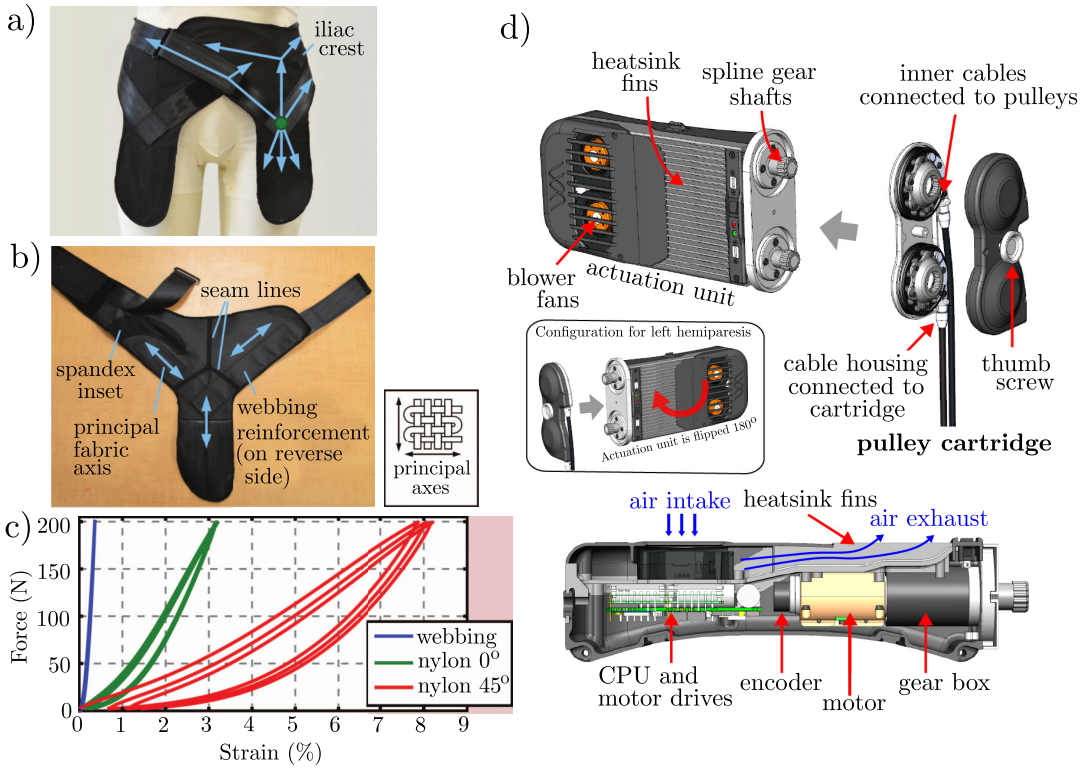


Figure 2.22: Soft exo-suit actuator units. Images **a** and **b** show a waist belt from a hip exoskeleton [29] with arrows indicating the force paths through the garment. Graph in **c** shows the results from force/strain testing of three different textile materials. A compact actuator unit for a soft-suit ankle exoskeleton is shown in **d**. Images **a**, **b** and **c** are adapted from [29]; and **d** is adapted from [134].

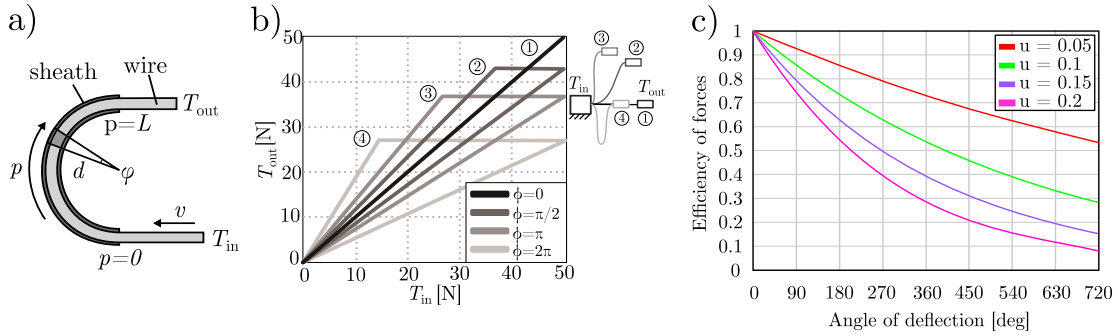


Figure 2.23: Bowden-cable properties. Image **a** shows a flat out representation of a steel cable in a Bowden sheet. As shown in **b**, the efficiency of force transmission, i.e., friction characteristics, change based on the sheath bending angle. **c** shows the transmission efficiency based on the bending angle for several friction coefficients. Images **a** and **b** are adapted from [138]; image **c** is adapted from [139].

by Chin et al. [141] that is able to harvest the power of a foot drop. By means of a clutch, i.e., a mechanical switch [142, 143], the passive elastic elements can be activated at will, whereby the elastic energy is stored in one phase and released in the other phase of the movement. Besides walking, there are passive exoskeletons that can support the user while running [144–146]. Another fine example is adaptive load cancellation [86], which can be achieved by successive recruitment of several parallel elastic elements.

The locking mechanisms are an important component of the passive exoskeleton technology. The two main reasons for their use are either energy management or reconfiguration. Locking devices are in general frequently used in robotics, e.g., to lock springs and joints or to reconfigure robots. In [142], locking devices are divided into three main categories based on different locking principles: 1) mechanical locking, 2) friction-based locking, and 3) singularity locking. The different locking devices in each category can be passive or active.

The locking devices based on a mechanical lock are shown in Fig. 2.24. They all use

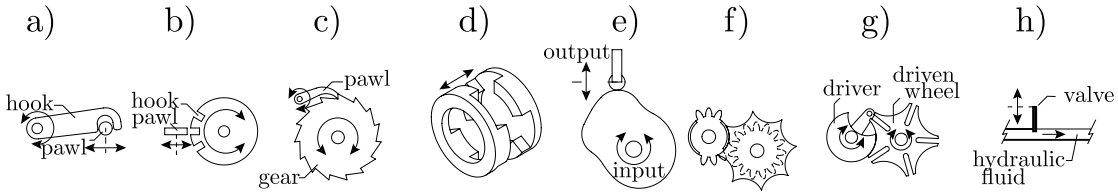


Figure 2.24: The types of mechanical locking devices with **a** a latch with one locking position, **b** a latch with multiple locking positions, **c** a ratchet, **d** a dog clutch, **e** a cam-based locking device: cam follower, **f** a cam-based locking device: mutilated gears, **g** a cam-based locking device: Geneva mechanism, and **h** a hydraulic lock. Figure is adapted from [142].

some kind of obstruction of a part by another part. The different types range from latches, ratchet gears, clutches, cam-based mechanisms to hydraulic locks. Due to the mechanical locking, they offer the highest maximum locking torque. They are, however, only able to lock the system at specific positions.

The second group are friction-based locking devices. These depend on friction to prevent motion between two parts. The friction force can be created using various mechanisms

such as disk brakes, drum brakes, cone brakes and band brakes. See Fig. 2.25 for different friction-based locking devices. Because the amount of friction between two parts is limited

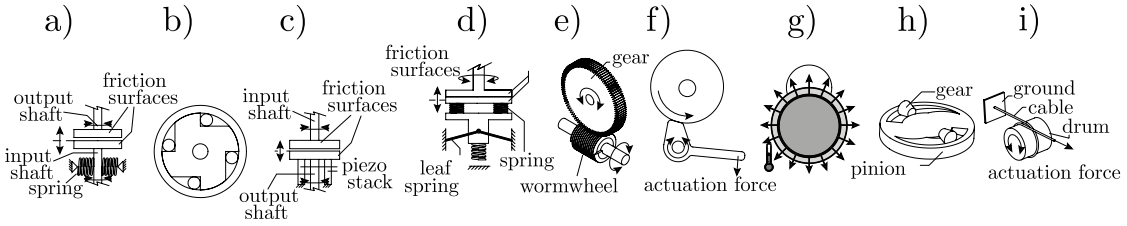


Figure 2.25: The types of friction-based locking devices with **a** a bistable brake, **b** an overrunning clutch, **c** a piezo-actuated brake, **d** a statically balanced brake, **e** a worm wheel, **f** a self-engaging brake, **g** a thermic lock, **h** a self-engaging pinion-gear mechanism, and **i** a capstan. Figure is adapted from [142].

by the normal force, the friction-based devices generally have a limited maximum locking torque. As an advantage, they can lock at every position.

The last group of locking devices are the singularity locking devices. They are characterized by a position-dependent transfer ratio. In their singular position, such locking devices have an infinitely high transfer ratio, featuring an infinitely high locking torque. Some of these mechanisms are shown in Fig. 2.26.

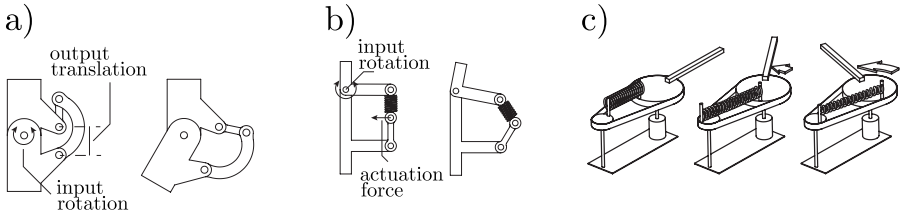


Figure 2.26: The types of singularity locking devices. The types of singularity locking devices with **a** and **b** the two different four-bar mechanisms and **c** a nonlinear spring mechanism. Figure is adapted from [142].

Many passive exoskeletons exist in the literature. The most basic implementation is a passive exoskeleton that can reduce the metabolic consumption of people carrying heavy loads by transferring some of the carried weight directly to the ground [27]. This solution, however, does not reduce metabolic consumption compared to normal walking. A similar type of exoskeletons are the passive tool-holding exoskeletons. The Ekso Works exoskeleton [147], developed by Exo Bionics, balances a workers tool that is fixed on a pre-tensioned spring-arm mechanism that transfers the tool's weight to the ground. This way, the work load of the tool on the user is reduced. Lockheed Martin developed its own version called Fortis [148].

An example of recent success are the passive exoskeletons that are designed to help with overhead industrial work [149–151]. For example, the PAEXO, which is shown in Fig. 2.27a, consists of a stabilizing structure attached to the participant and a supporting structure that transfers part of the arm's weight from the upper arm straps to the hip belt. Another type of a passive exoskeleton aims to prevent lower back pain. The passive lower-back support exoskeleton from the SPEXOR project addresses the problem of lower back pain [13]. The spinal exoskeleton developed within the project is shown in Fig. 2.27c,d. A passive-elastic mechanism stores potential energy when the user leans forward to pick up an object. Several passive joints are used to adapt the exoskeleton to different user shapes,

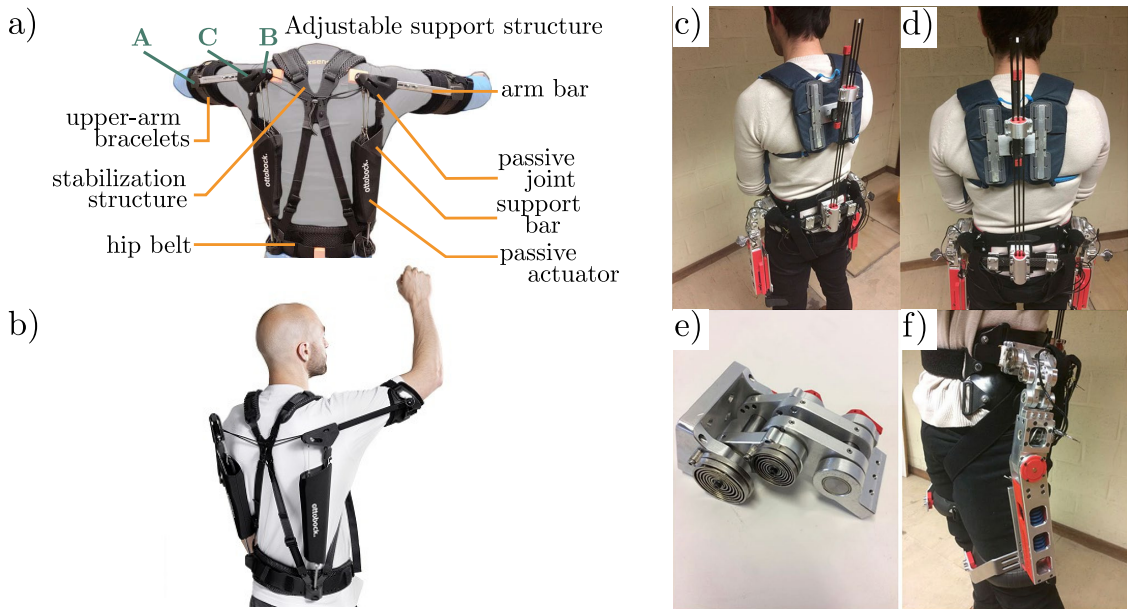


Figure 2.27: Passive exoskeletons part 1. PAEXO exoskeleton is shown in **a** with its components. A user wearing the exoskeleton is shown in **b**. Spinal exoskeleton from the SPEXOR project is shown in **c**, **d**. **e** shows the passive joints that are used to adapt the exoskeleton to different users. The main passive-elastic mechanism is shown in **f**. Image **a** is adapted from [149]; **b** is adapted from [152]; **c**, **d**, **e** and **f** are adapted from [13].

see Fig. 2.27e. The passive-elastic mechanism stores the potential energy of the user's trunk as he/she bends forward to pick up an object. Part of the potential energy is stored in the flexible spine and another part in the passive mechanism positioned at the hip. The hip mechanism is shown in Fig. 2.27f. The electromechanical coupling deactivates the passive mechanism, so that the user can walk unhindered.

Yet another group of passive exoskeleton devices uses the passive elements to store energy during one part of the task in order to release it in another part. Collins et al. [53] presented an un-powered exoskeleton that achieved metabolic cost reduction of human walking with a completely passive device. The light elastic device acts parallel to the user's calf muscles and relieves the muscular strength, thus reducing the metabolic energy used during walking; see Fig. 2.28a. The device uses a mechanical clutch to hold a spring while it is stretched and relaxed by ankle movements when the foot is on the ground, helping to fulfil a function of the calf muscles and the Achilles tendon. The mechanical clutch is shown in Fig. 2.28b.

The spring, which is operated by a passive mechanical clutch, is able to store and return energy to the ankle at correct times and thus reduce the effort of human walking for an average of 7.2%. Since the original publication, the research group proposed several modifications, including an even more light-weight electroadhesive clutch and spring [143]. Besides the reduced weight, the advantage of using an active electroadhesive clutch is in the increased reliability of locking.

A parallel-elastic exoskeleton, shown in 2.28d, provides assistance when running. It is known that the leg exhibits springlike behavior during the stance phase of running [145]. To this end, the exoskeleton introduces a clutch to disengage the parallel leg-spring and thereby does not constrain the swing-phase movements of the biological leg. The XPED, developed by Dijk et al. [146, 154], is an exoskeleton aiming to achieve a similar effect with artificial multi-articular tendons for lower limbs. It was built to experimentally evaluate

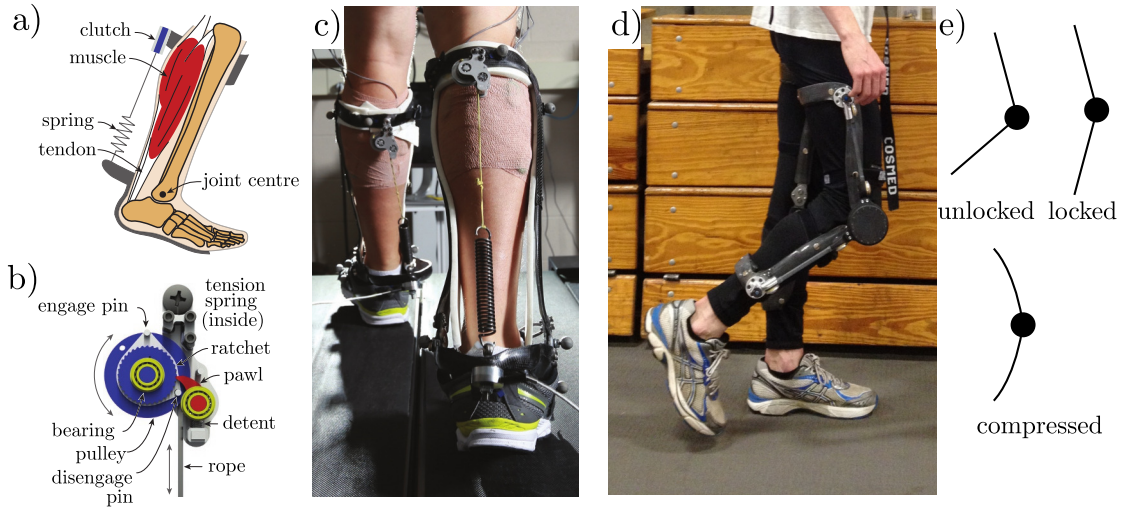


Figure 2.28: Passive exoskeletons part 2. The schematics of the passive ankle exoskeleton is shown in **a**. Its mechanical clutch is shown in **b**. An image of the actual prototype is shown in **c**. Image **d** shows a prototype of a clutch-spring knee exoskeleton for running with its basic functions shown in **e**. Images **a**, **b** and **c** are adapted from [53]; **d** and **e** are adapted from [145, 153].

the exo-tendon concept of the [155]. In this concept, long elastic cables span several joints. The cables can temporarily store and transfer the energy between the joints. In simulation, the average absolute joint moment can be reduced by as much as 71%.

Passive devices offer many possibilities for variable stiffness mechanism technology that allows one to adapt the stiffness and intrinsic dynamics. An example is the stiffness of the overhead-work exoskeletons, where the stiffness could be varied based on the user's arm posture or the weight of different hand-tools used. Through this, the device could completely passively compensate for the loads. It can be seen that not only the development of compliant actuators is important, but the development of underlying compliant mechanisms is just as equally important.

2.2.4 Control of Exoskeletons & Compliant Actuators

Regardless of the technology used to actuate the device, proper control is very important. The chosen control strategy has an effect on the human adaptation to the exoskeleton [26]. This section provides a brief overview of some relevant control methods that can be found in the literature. Note that the number of exoskeleton control methods is enormous and that this work does not seek for the best control method, but rather one that allows testing and evaluation of prototype devices.

Research shows that proper exoskeleton control is important. For example, Gams et al. [21] analysed the effect of several control methods for an active knee exoskeleton to see the effect on the energy expenditure of the user during squatting. The three control methods were gravity compensation, position-based approach, and a novel oscillator-based approach. They can be seen in Fig. 2.29. The novel oscillator-based control approach showed promise, because the controller ensures synchronization of the device and the user. Both oscillator-based and gravity compensation control approaches induced similar responses. The adaptive non-linear oscillators are one method that is capable of human-exoskeleton synchronization in cyclic tasks. There are also other works that exploit this feature [156, 157].

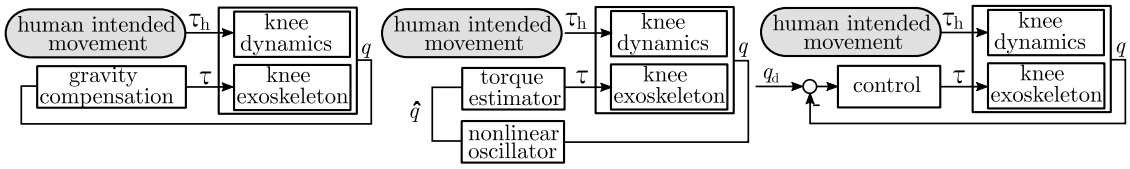


Figure 2.29: Three exoskeleton control methods. τ_h denotes the human torque, τ is the device torque, and q is the actual knee joint angle. *Left*: Gravity compensation approach control scheme. *Middle:* Oscillator-based approach. $\hat{q}$ is the estimated knee joint angle. *Right:* Position control approach control scheme. Note the control loop with the referential joint angle q_d. Figure is adapted from [21].

Bio-feedback is important when the task is unknown and for implementation of machine learning techniques. Proportional myoelectric control [22, 158, 159] is one of bio-feedback-based methods. The method considers that the EMG is a linear measure of muscle activity and tries to provide assistance to reduce it. The muscle EMG signal is typically high-pass filtered to remove motion artefacts, then full wave rectified and finally low-pass filtered to smoothen the signal. The proportional myoelectric control defines a low threshold to eliminate the electrical background noise. Above this threshold, the control signal is directly proportional to the EMG signal up to the saturation level. This method establishes a direct connection between the user's nervous system and the exoskeleton torque, albeit a nonlinear one. Often, EMG data is used to estimate the torque on the selected joint, which is not as straightforward as one would expect [160]. One of the challenges of this approach is the variability of EMG signals due to factors such as electrode positioning and conditions of the subject at the time of recording. Nevertheless, there is evidence that proportional myoelectric control may have significant advantages over other types of control of robotic exoskeletons in basic research and rehabilitation [22]. In individuals with incomplete spinal cord injury, it has been shown that muscle recruitment patterns change rapidly when practicing walking with the ankle exoskeletons. To accommodate uncertain dynamics of the human-robot system, iterative learning can prove to be very effective in learning of control of cyclic tasks [20]. The desired controller model can be learned in an iterative manner, which suits the repeating nature of patient's task through therapeutic process and also guarantees the transient performance of the robot [161].

Different generalization techniques can be used to fuse data from several sensors and generate a proper input. In [162], a neural-network-enhanced torque estimation controller (NNETEC) is proposed for a soft wearable elbow assistance exoskeleton with a compliant tendon-sheath actuator. The method fused the feedback signals from surface electromyography (sEMG) sensors, inertial measurement units, force sensors, and motor encoder. It consists of a joint torque estimation module that identifies the elbow torque of the wearer with a Kalman filter, a neural-network adjustment module to recognize human motion intention, and a proportional-integral-derivative controller with hybrid position/torque feedbacks.

A very advanced control method is the human-in-the-loop optimization. Research group of Zhang et al. [23] developed a method for identifying the exoskeleton assistance that minimizes human energy cost during walking. The method and the corresponding control algorithm can be seen in Fig. 2.30. The proposed method optimized the properties of the control based on the measured human performance. During the optimization, different control laws are applied and the metabolic rate for each one is quickly estimated. Next, the costs are compared, and by using evolutionary strategies, a new set of control laws is prepared to be tested while walking. Optimized torque patterns of the exoskeleton

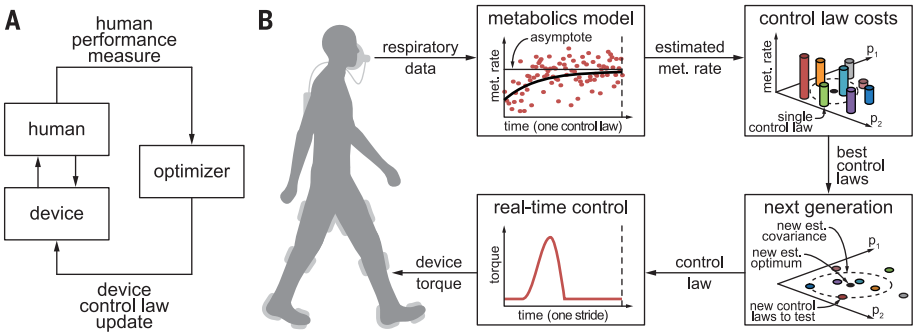


Figure 2.30: Human-in-the-loop optimization. Measurements of human performance are used to update device control to improve the performance of the human portion of the system, as seen in **a**. A method for minimization of the energy cost of human walking is shown in **b**. Figure is adapted from [23].

reduced metabolic energy consumption by 24.2 ± 7.4% as compared to the no torque case. The approach was effective in exoskeletons worn at one or both ankles during a variety of walking conditions while walking, when running and or when optimizing muscle activity. Optimization methods with these features can significantly improve the performance of exoskeleton devices. On the other hand, the method also requires a good, pseudo real-time bio-feedback loop, in this case the VO_2 measurements, which is sometimes difficult to achieve.

Many other tasks and control methods have also been studied in literature. A review on different control methods for robotic ankle systems is available in [19], while an experimental comparison between different torque methods for ankle exoskeletons is presented in [20]. Further reviews on control strategies for upper-limb exoskeleton can be found in [163, 164].

The control method from the [40] should be mentioned here, since it was adapted and used for direct control of the prototypes built in the context of this thesis. Its control architecture is shown in Fig. 2.31. The SEA model is simplified and consists of the inertia

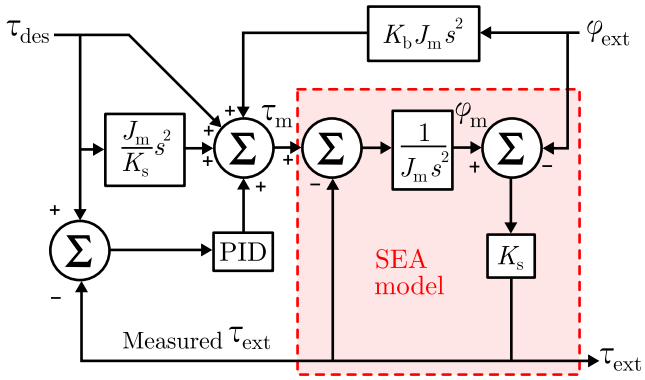


Figure 2.31: Control architecture for stable and accurate force control. Figure is adapted from [40].

J_m and an elastic feedback connection to the actuator torque of the stiffness K_s.

The control architecture includes both forward and feedback paths and ensures stable and accurate force control of the elastic actuator. The block $K_b J_m s^2$ represents the acceleration feedback. The desired torque τ_{des} is fed into the system as a feed-forward

signal. And the term $J_m/K_s s^2$ represents the force required to accelerate the mass of the motor to change the deformation of the elastic element. Finally, a PID controller corrects any discrepancies between the desired and the external measurement of torque. A more detailed analysis and derivation of the proposed algorithm can be found in [40]. If the controlled device is a variable stiffness actuator, the value of K_s can be changed according to the current mechanical stiffness of the system.

Chapter 3

Use of Passive Elements in Exoskeleton Devices: Passive Ankle Exoskeleton

This chapter presents the research directed towards goal **G1** and hypothesis **H1** of the thesis, which both address the use of passive elements in exoskeleton devices. The research is focused on the use of an implemented ankle exoskeleton device. The exoskeleton can be used by any user that is able to walk and would like to walk with less effort. The concept could potentially be extended to other human joints, instead of only the ankle, which could result in novel types of exoskeletons that work in a hybrid unpowered and powered combination to achieve greater energy efficiency and performance.

The implemented ankle exoskeleton device was inspired by the work of the research group of Collins et al. [53]. They developed a passive, non-powered exoskeleton capable of reducing the metabolic cost of walking on flat terrain for an able-bodied user. While the functional principle of the implemented ankle exoskeleton device used in our research is the same as in [53], different materials with design changes were applied to achieve more cost-effective manufacturing and easier assembly.

In the context of the dissertation, the difficulties arising from the use of a fixed spring design in the exoskeleton prototype exposed the need for mechanically adaptable compliant mechanisms, which motivated the designs in the research that followed.
The following list summarizes the research effort:

- ◇ Design and construct a passive ankle exoskeleton that employs only passive elastic elements.
- ◇ Evaluate the exoskeleton performance and measure user biofeedback in the form of heart-rate, kinematics, VO2 and muscle EMG.
- ◇ Find potential faults of the prototype and improve its performance through a mechanical upgrade.
- ◇ Perform a quality-oriented user study with the upgraded exoskeleton and gather subjective user feedback.

3.1 Design & Mechanics of the Passive Ankle Exoskeleton

The operation of the passive exoskeleton is shown in Fig. 3.1. The mechanical clutch of the device locks at the heel-strike phase of walking. Next, the forward movement through the stance phase stretches the spring and accumulates elastic energy. At the end of the stance phase, when the user lifts the heel, the spring recoils and returns the energy until

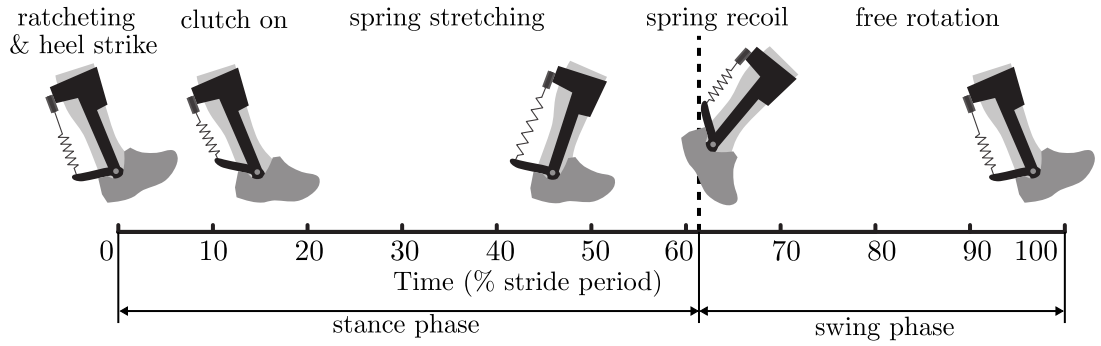


Figure 3.1: The passive exoskeleton operation. Figure is adapted from [53].

the user lifts-off the toe. During the swing phase, the clutch deactivates to allow for free rotation of the ankle.

The prototype implementation is shown in Fig. 3.2. Overall, a faster development cycle was given priority. The goal was to achieve a working prototype in as few iterations as possible. Through structural changes and use of different materials, the manufacturing was faster, cheaper and more convenient. The underlying basic function remained unchanged from the exoskeleton in [53]. In total, two exoskeletons were made, one for each leg. The two separate exoskeletons were mirrored for ergonomic purposes.

The device comprises of an insole part, a simple hinge joint, a stainless steel frame, a strap for attachment, a mechanical clutch and a linear tension spring. All components are marked in Fig. 3.2. Its frame and the clutch are discussed separately.

The *frame* of the exoskeleton is connected to the insole with a simple hinge joint which allows for a one degree of freedom movement at the ankle. Users can don-on and tighten the exoskeleton by tightening the fastening strap. The frame is made of stainless steel, which is rigid and light. It was not optimized for minimal weight in order to facilitate faster prototyping. Even so, the prototype still weighs only 0.8 kg and the weight could be further reduced in additional iterations of the design and with the use of materials with a larger strength/weight ratio.

Plastic material was used to construct the insole part using a heat-forming process. Through additional reinforcement with components made of stainless steel, the strength

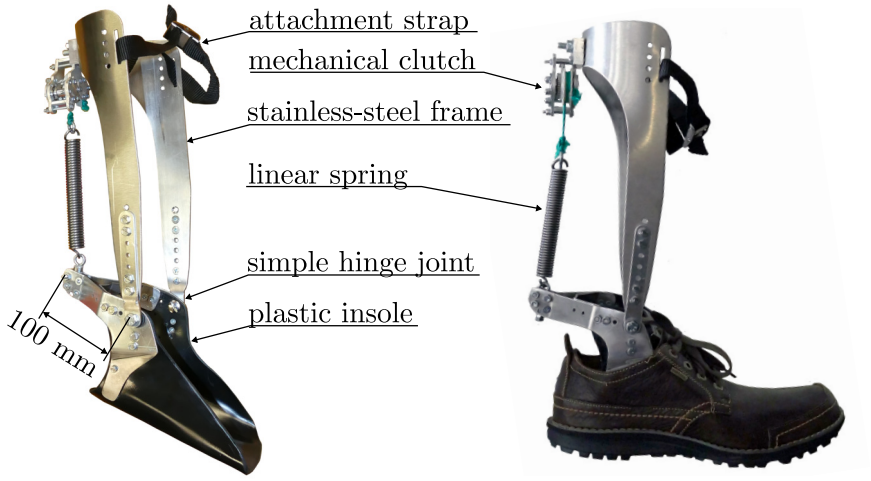


Figure 3.2: The unpowered ankle exoskeleton built at the Jožef Stefan Institute.

of the insole was increased. The insole shape was designed to be comfortable and to still fit into an average adult male shoe. Thus, the users could use their own shoes for the exoskeleton evaluations.

The mechanical clutch, shown in Fig. 3.3, is largely based on the original [53] with some modifications to make production and assembly more convenient. The clutch components are made of aluminum, stainless steel and plastic using laser cutting and 3D additive technologies.

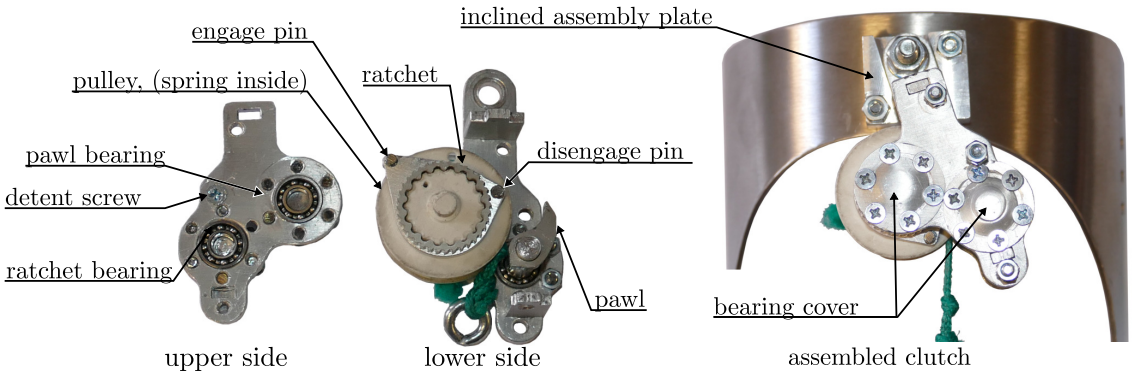


Figure 3.3: Mechanical clutch. Its relevant components are marked in a dissembled state (*left*) and in the assembled state (*right*).

Several design changes were made to increase the robustness of the clutch operation. The first problem is the robust function of the pawl, which disengages and engages and is an important factor for proper operation. During the pre-stance phase, the successful locking of the pawl depends on gravity. Since the pawl is small, the effect of the gravity is not large and therefore the function of the clutch is not robust. The friction in the pawl bearing may be large enough to prevent the correct locking of the pawl. To take this into account, we designed the shaft to sit loosely on the bearing as a post-design modification. This eliminates the need for a rolling bearing. To aid the effect of gravity on the movement of the pawl, we mounted the mechanical clutch at an angle to the exoskeleton frame. This was realised with an inclined mounting plate and helped to increase the reliability of the clutch operation.

The size of the ratchet teeth is a design choice. The one in our prototype had the same size as in the [53] version. Larger teeth of the ratchet result in a safer locking of the clutch, but reduce resolution and efficiency of the clutch. The ratcheting introduces small peak forces on the pawl, which can be strong enough to disengage it and deactivate the clutch. Optimizing the tooth size would prevent unwanted disengagement of the pawl during walking, which is problematic as it affects the walking kinematics. The user who relies on the pawl to engage can stumble because he does not expect the exoskeleton support to be suddenly released.

The timing of the clutch actuation is important. It is determined by the positions of the engagement and disengagement pins and also depends on the length of the rope connecting the spring and the clutch.

If the outer diameter of the spring and the thickness of the spring-wire remain the same, the springs need a different length to achieve a different stiffness. This problem is partially alleviated by compensating the differences in spring length with additional wire coupling elements. However, additional couplings introduce additional design parameters and raise the overall mechanical complexity. Above all, the rope must be tied to a certain length, which can prove to be difficult. The original exoskeleton of [53] had a system that

could adjust the length of the rope with a screw to account for springs of different lengths. Although useful, it is not very practical, especially when the spring needs to be changed very quickly.

The insole was manufactured of plastic using a heat forming process and then reinforced with stainless steel. Since the foot has to fit into the shoe, into the exoskeleton and be ergonomic at the same time, the design of such an insole is not an easy task. The target is an average men's shoe size of EU42. To ensure a good fit, similar to [165], the user's foot can be 3D scanned to produce a cloud-point model of the foot. However, a lot of time is required to prepare the 3D scanned data, to model a correctly shaped insole using surface modelling techniques and lastly to manufacture it. To accelerate the development cycle, we chose a more empirical approach, adapted to our manufacturing capabilities. The process consisted of four main steps, as shown in 3.4. The resulting insole would not burden the

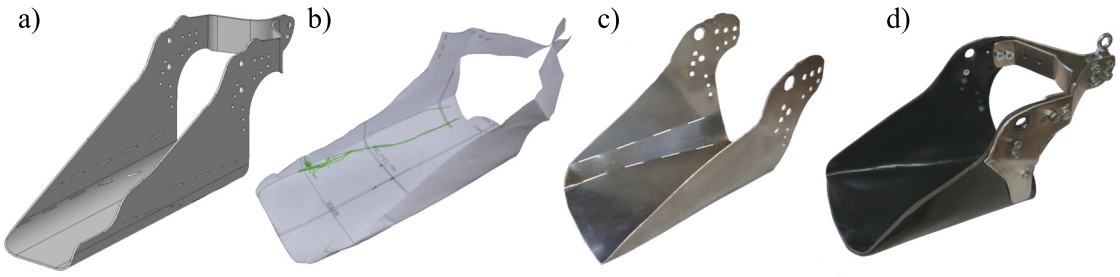


Figure 3.4: Insole design process. **a** shows a 3D sheet-metal model, which was used to construct a paper version shown in **b**. The insole was built out of aluminium using a laser-cutting process and folded into a proper shape in **c**. Finally, the insole shown in **d** was created by using the aluminium insole as a template.

user for the required experiments.

To design a comfortable insole, we first designed an approximate 3D sheet-metal model (Fig. 3.4a), which we then flattened and printed on a sheet of paper. The paper insole (Fig. 3.4b) was inserted into a shoe to estimate the positions where the aluminum version would fold. The folding positions were integrated into the 3D model in the form of rectangular holes. Next, an aluminium insole was manufactured using laser cutting and then folded into the final shape (Fig. 3.4c). A plastic sheet was heated and formed over the aluminium insole. Finally, the insole was reinforced using a stainless steel frame (Fig. 3.4d).

3.2 Metabolic Cost Measurement Study Design

A randomized crossover study was performed to evaluate the efficiency of the passive ankle exoskeleton. Four healthy young men (23-37 years old, 71-81 kg heavy, 175-181 cm tall) voluntarily participated in the study. The baseline of the participant characteristics is shown in Table 3.1.

After being informed about the procedure and giving a free consent form, participants were asked to take a series of 10-minute walks on a treadmill at a speed of 4km/h. Between the walks, the participants rested on a chair for at least 10 minutes. The five series consisted of a referential (exoskeleton-free) walk; a walk with a springless exoskeleton and three walks with a spring of different characteristics (5 N/mm, 12 N/mm and 20 N/mm). A pair of exoskeletons was used, one on each leg. The order of the sessions was randomly determined for each participant.

The influence of exoskeletons on the user was analysed through VO_2 measurements and

Table 3.1: Baseline of the participant characteristics of the first study.

	Mean	Standard Deviation
Age (years)	30	7
Weight (kg)	76	5
Height (cm)	178	3
Body Mass Index (kg/m^2)	24	1

the recordings of electrical activity of muscles (EMG). The whole measurement system is shown in Fig. 3.5,*left* and a participant during a walking session in Fig. 3.5,*right*. VO_2

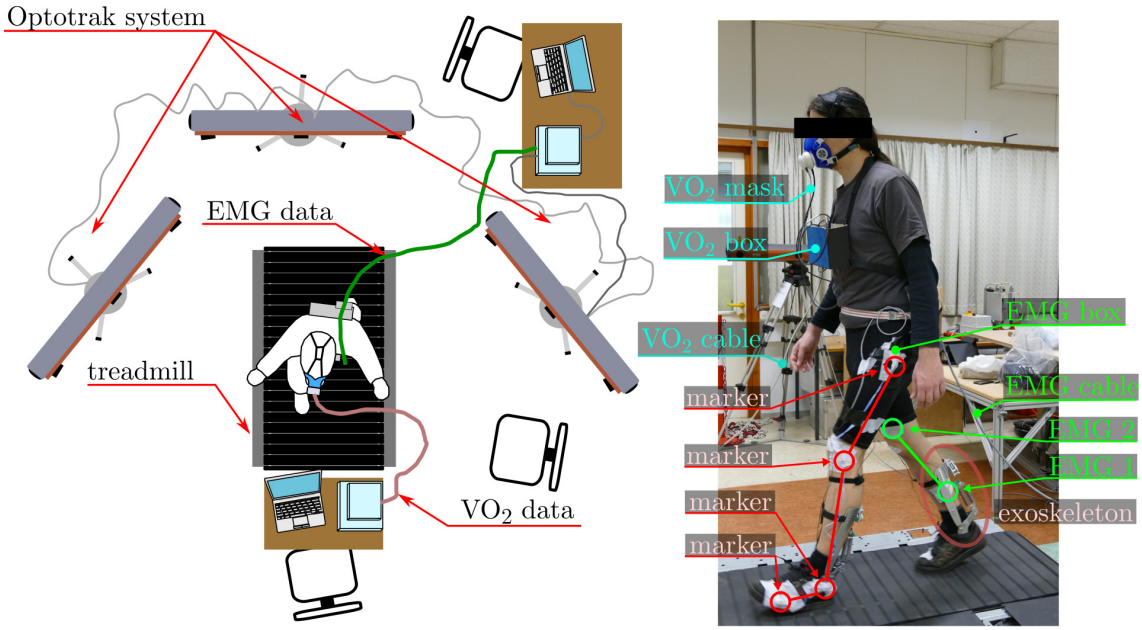


Figure 3.5: Passive exoskeleton measurement system. The left picture shows the measuring setup consisting of a treadmill, the Optotrak measuring system and the Cosmed VO_2 breathing apparatus. The picture on the right shows a participant during the tests while wearing the prototype of the exoskeleton with the attached sensors.

serves as a basis for assessing the change in average user oxygen consumption to determine the reduction or increase in metabolic costs of walking. The VO_2 of each user was measured with a portable metabolic cart $K4b^2$ from Cosmed, Italy.

In order to assess an approximation of the total muscle load during walking, we also measured the EMG activity of the Vastus Medialis and Soleus muscle on each participant's right leg. The signals were rectified and integrated for 7 minutes from a 10-minute walk sample to exclude start and end discrepancies, and then normalized to the normal walk value as shown in Eq. (3.1).

$$E_{\mathrm{ki}} = \int_{1.5\ \mathrm{min}}^{8.5\ \mathrm{min}} |U_{\mathrm{ki}}(t)|\,dt \Big/ \int_{1.5\ \mathrm{min}}^{8.5\ \mathrm{min}} |U_{\mathrm{kn}}(t)|\,dt \cdot 100\%, \tag{3.1}$$

where E_{ki} is the integrated EMG response. $U_{\mathrm{kn}}(\mathrm{t})$ is the EMG voltage with respect to

time, where n is the normal walking measurement for a particular participant k and i is the respective walking measurement for the five different boundary conditions.

The EMG signals were recorded with the SX230 surface electrodes (see Fig. 3.6) from Biometrics Ltd. with an integrated 1000x amplifier. The signals were recorded with the DataLog (Biometrics Ltd.) data acquisition device. Oxygen consumption and EMG



Figure 3.6: Surface electrode SX230 with an integrated signal amplifier (Biometrics Ltd.)

activity were compared between participant groups and different boundary conditions using mean Eq. (3.2) and sample standard deviation Eq. (3.3) for all four participants:

$$\bar{E}_{\mathrm{i}} = \frac{1}{4}\sum_{\mathrm{k}=1}^{4} E_{\mathrm{ki}}, \qquad (3.2) \qquad S_{\mathrm{Ei}} = \sqrt{\frac{1}{3}((E_{\mathrm{ki}}) - \bar{E}_{\mathrm{i}})^2}, \qquad (3.3)$$

where again k represents a participant and i represents the selected boundary condition. Additionally, the users wore a heart-rate belt to measure the changes in their heart-rate. The kinematic data gathered through the Optotrak system was not analysed in the scope of the thesis.

3.2.1 Results

As shown in Fig. 3.5, the experiment allowed us to collect the VO_2 data, the EMG activity of the Soleus and Vastus Medialis muscles of the participant's right leg, and their heart rate. The following figures show the measurements divided between the averages for the first pair, the second pair and then for all four participants. VO_2 is the first measured parameter and is shown in Fig. 3.7.

For participants 1 and 2, as shown in Fig. 3.7, a decrease in average metabolic cost (-11%) compared to normal walking can be observed when using the exoskeleton with a spring of 5 N/mm stiffness. The reduction of average metabolic costs by springs of other stiffness can also be observed, but is not so obvious. Assuming that the VO_2 measurements are the most representative, we can limit the range of appropriate spring stiffness to less than 12 N/mm and close to 5 N/mm, based on the collected results. The exoskeleton without a spring created some strain or constriction for the user, as the metabolic costs increased compared to normal walking (+8%). The main cause is attributed to the increase in weight due to the exoskeleton (0.8 kg) and the introduced kinematic restrictions, as the exoskeleton allows only 1 degree-of-freedom in the ankle.

For participants 3 and 4, i.e., the second pair, as shown in Fig. 3.7, the mechanism shows less promising results. With the use of the exoskeleton, the average metabolic costs have increased in each series. The increase in metabolic costs is attributed to the faults of the current exoskeleton prototype. During the course of the measurements, the exoskeleton performance degraded with each new participant. Most of the screws loosened and the rope

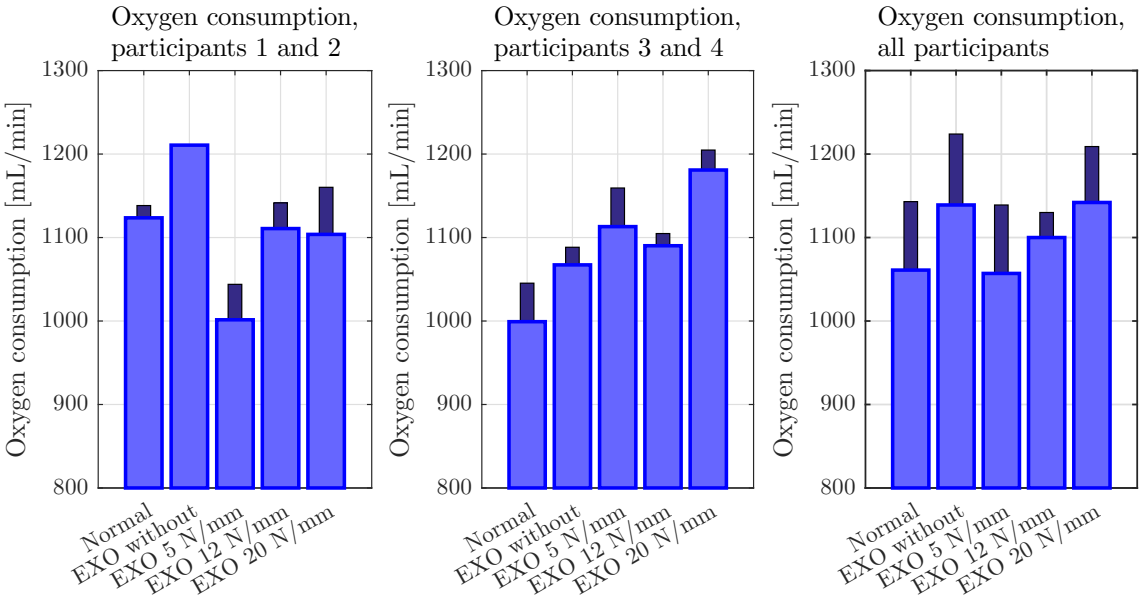


Figure 3.7: Average of the maximum oxygen consumption (VO_2) and its standard deviation for the first pair, second pair and for all participants.

became a little longer, since it tightened at its two ends, due to the high load. Between the second and third participants, the rope on one of the exoskeletons also snapped due to wear and was then replaced. Care was taken to keep the rope length of the exoskeleton constant, but this proved difficult and impractical when replacing the springs. As there was no proper feedback, there was no certain way to keep the rope length constant.

The main reason for a result change between the first pair and the second pair is due to the wrong timing setting as a result of the longer rope length. This points at the importance of the timing of the engaging and disengaging of the mechanical clutch. To ascertain the

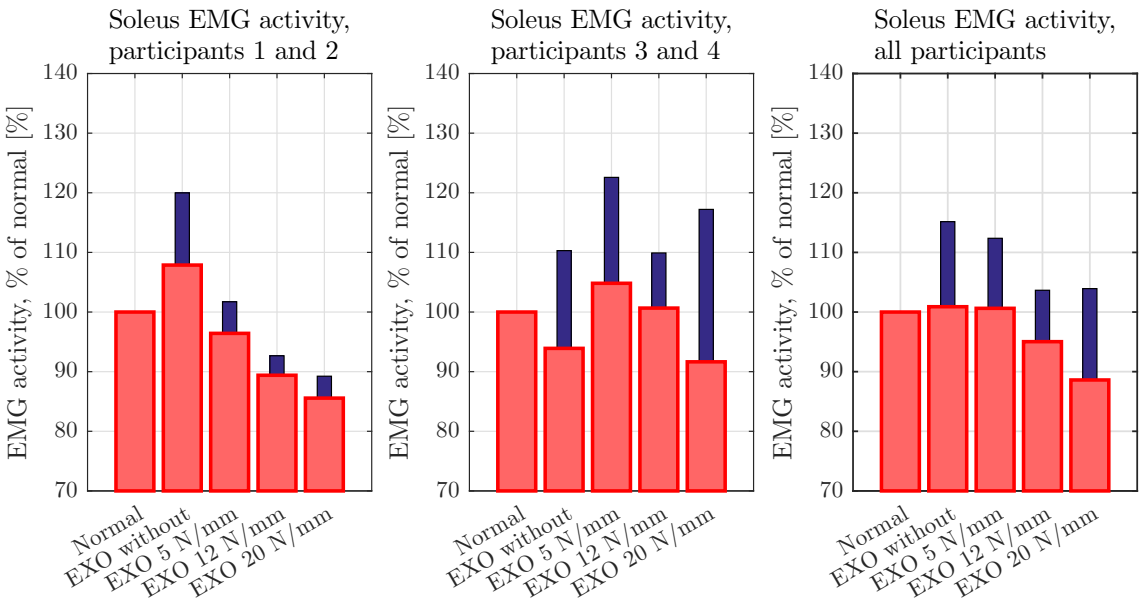


Figure 3.8: Soleus muscle activity. Average and standard deviation of EMG activity for the Soleus muscle of the first pair, second pair and all participants.

above reasoning, the exoskeleton should be equipped with additional sensors that can determine the engagement of the clutch and the force in the spring. However, this would increase the prototype mechanical complexity and require a more complex experiment. The average metabolic costs for all participants are shown in the last diagram in Fig. 3.7. A reduction in metabolic costs can be observed when walking with the exoskeleton with the 5 N/mm spring. However, the reduction is not large compared to normal walking.

EMG measurements are used to estimate the effort of two muscles on each participant's right leg. The results for the Soleus and Vastus Medialis muscles are shown in Fig. 3.8 and Fig. 3.9. The results are again grouped as for the VO_2 measurements.

Unexpectedly, the EMG measurement results do not directly correspond to those of the average oxygen consumption. For participants 1 and 2, as shown in the first diagram in Fig. 3.8, exoskeleton use without the spring increases muscle activity as expected. Soleus EMG activity decreases when springs with higher stiffness are introduced for the first pair. The activity is lowest with stiffness of 20 N/mm and not with 5 N/mm, in contrast to the average oxygen consumption results. The same is true for the second pair, but it is not as profound. A certain decrease in EMG activity can be observed, but this effect is shifted to springs with higher stiffness. The third graph, which shows the average of all participants, again shows the decrease in Soleus muscle activity.

The trend for the EMG activity of the Vastus Medialis muscle from Fig. 3.9 is similar to the Soleus muscles. The muscle activity of Vastus Medialis seems to decrease compared

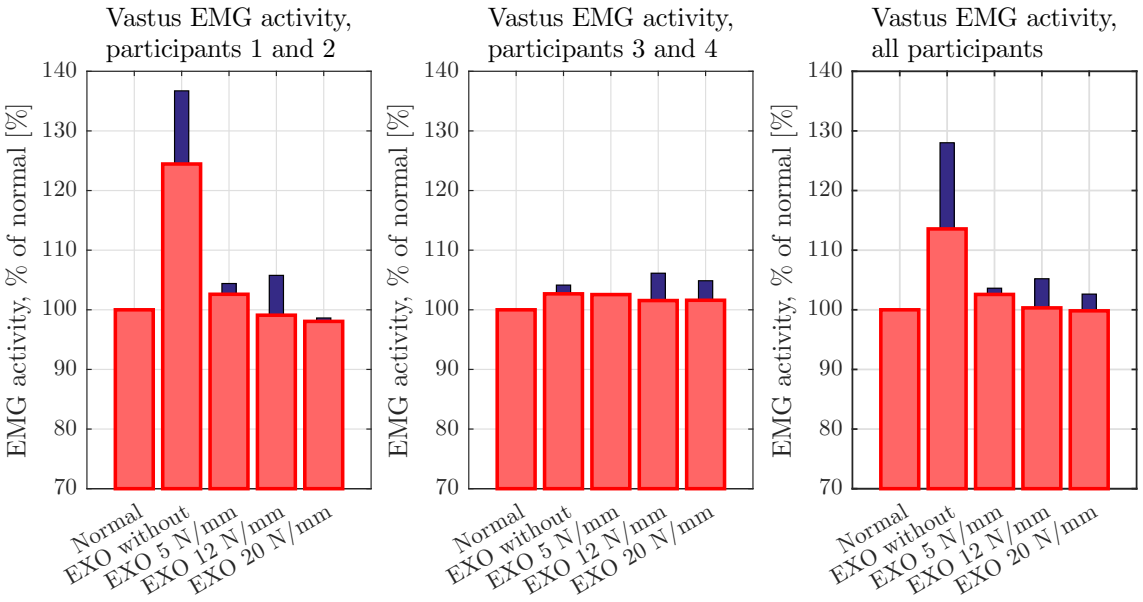


Figure 3.9: Vastus muscle activity. Average and standard deviation of EMG activity for the Vastus Medialis muscle of the first pair, second pair and all participants.

to the activity of walking with a springless exoskeleton, but compared to the activity of normal walking the reduction is not as profound. For the first pair the EMG activity is lowest at the stiffness of the 20 N/mm spring. However, the second pair shows an increase in EMG activity beyond normal case. It appears that the reduced oxygen consumption is also due to other muscles apart from the Soleus and Vastus medialis muscles, which may explain the discrepancy between average oxygen consumption and average muscle activity.

The average heart rate is shown in Fig. 3.10 and grouped as in the previous results. In the first pair, the heart rate decreases with increasing spring stiffness. The heart rate is the smallest for the spring of 12 N/mm and 20 N/mm. However, the second pair

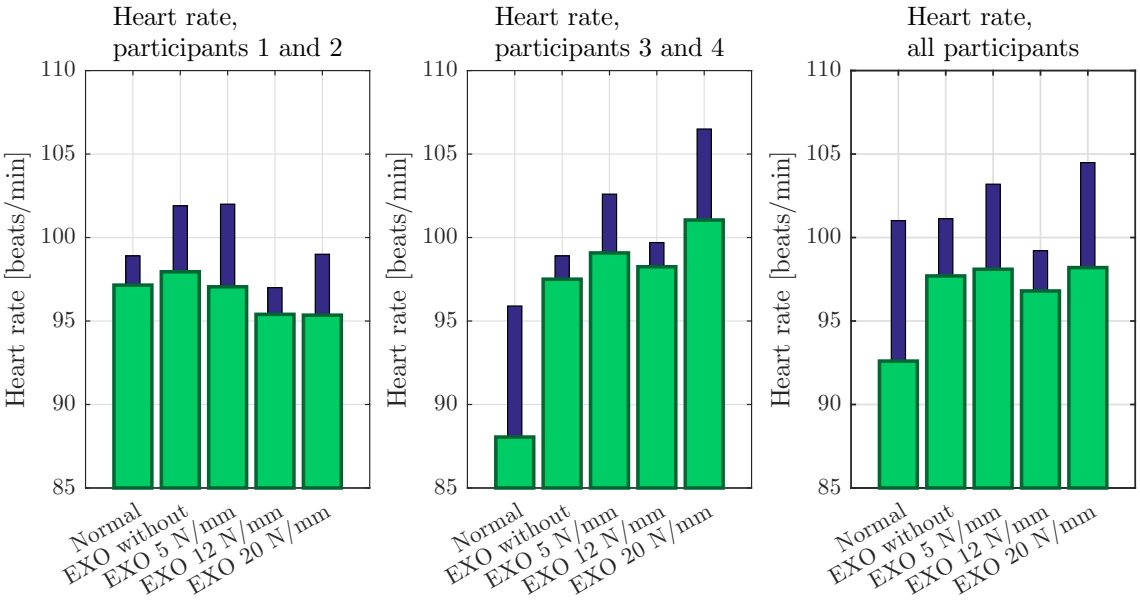


Figure 3.10: Heart-rate measurements. Average and standard deviation of heart rate for the first pair, second pair and all participants.

reacted completely differently. The same applies to the average over the entire group. This reinforces the conclusion that the exoskeleton did not work properly for the second user pair. The use of exoskeleton led to additional kinematic limitations on the user, which were not compensated by the function of the device. The human body had to increase its efforts to compensate for the additional weight of the device and the new kinematic limitations, which led to an increase in heart rate.

The heart rate is relatively straightforward to measure when compared to EMG or VO_2 max measurements. The VO_2 max requires a complex respirator device, which is also expensive and impractical as it is mounted on the user's face. The EMG requires accurate attachment of the sensors to the user's skin, which can easily move or fall off the skin during exercise. As an advantage, heart rate can be measured using a sports watch. Such a measurement can be carried out in real time and with minimal user disruption. As can be seen from the first two participants, the heart rate contains some information that could be identified in a larger study, and be later used as potential bio-feedback. However, it is also important to know that heart rate measurement alone may not be sufficient to estimate the user's condition. Heart rate can be strongly influenced by various other factors such as stress or the user's mental state [166].

In general, in all cases the introduction of the exoskeleton without the spring increases the metabolic costs of the user. This is due to the increased weight (0.8 kg) and the introduced kinematic limitations. These aspects of the exoskeleton can be improved in the next iteration of the design. When using a spring, the average metabolic costs are in some cases lower than with normal walking, which is promising for the device. The metabolic cost reduction could be more pronounced if the exoskeleton becomes more ergonomic. Otherwise, it seems that the most appropriate spring stiffness is around 5 N/mm.

The results differ greatly from subject to subject, which is reflected in relatively large standard deviations from the average. The current group size of 4 persons is not sufficient to come up with strong arguments. Nevertheless, the metabolic cost reduction is affected by the quality of the clutch actuation, the ergonomic design and comfort of the exoskeleton and its weight as well as the introduced kinematic limitations. All this should be taken into account when designing the exoskeleton.

3.3 Mechanics & Operation of the Quasi-Passive Ankle Exoskeleton

The passive ankle exoskeleton uses a fully mechanical clutch (inspired by the device in [53]). It was previously tested in a quantitatively-oriented crossover study with 4 young people. Each participant performed 5 walks of 10 minutes under 5 different boundary conditions in different order. One was the referential normal walk without the exoskeleton, the second was a walk with an exoskeleton but without the spring. Each of the other three walks used a spring with a stiffness of 5 N/mm, 12 N/mm or 20 N/mm.

These last three walks also served as stress tests, i.e., the exoskeleton worked for 2 hours under high load (3 x 10 minutes x 4 participants). It has been determined that the clutch engagement is one of the faults of the purely mechanical clutch which must be corrected. A drawback of the passive device is that the design of the clutch depends on the foot/ground contact to mechanically engage the pawl and lock the clutch. Furthermore, reliable engagement and disengagement was reported by many test subjects as one of the main problems with the device. One possible solution to this problem is to use a small motor to activate the clutch.

Subsequently, a new actuated clutch was designed and integrated into the previous exoskeleton device. The new improved device was evaluated in a quality-oriented study with 7 users. After the experiment, each user gave feedback through a questionnaire focused on the comfort of the exoskeleton and its durability. The upgraded device is shown in Fig. 3.11.

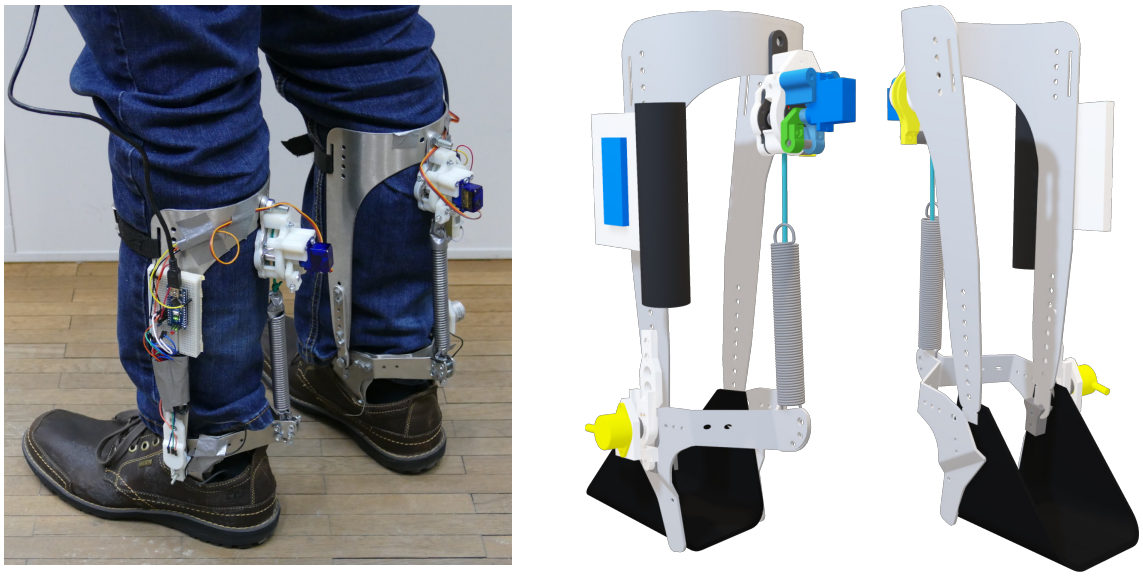


Figure 3.11: The user carrying the exoskeleton is shown in the image on the *left*. The CAD model of the exoskeleton is shown on the *right*.

The actuated clutch makes the new exoskeleton a quasi-passive device, as the actuator does not introduce any energy into the user's joint. The new clutch also solves the reliability problem of engaging and disengaging, which is critical to the proper operation of the device. Not only that, it also solves the timing difficulties. Previously, the original passive ankle exoskeleton was heavily dependent on the preset clutch activation time. The timing depends on the position of the locking pins and the length of the rope connecting the clutch to the spring. The timing varies from person to person and even changes for a person's walking style, speed and stride length.

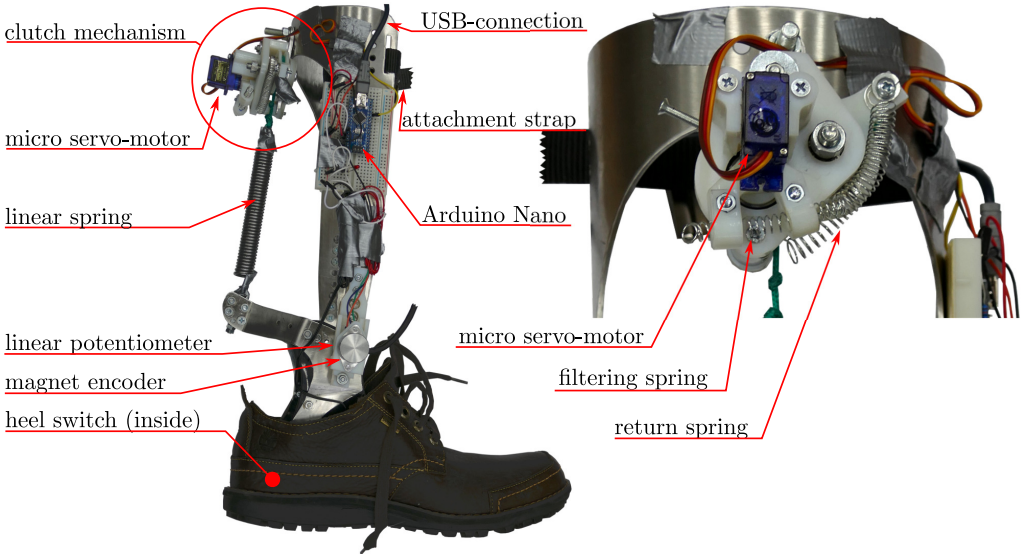


Figure 3.12: The quasi-passive ankle exoskeleton. A side photo of the new clutch in the *left* picture, and a photo of the backside in the *right* picture.

The clutch operation was unreliable and difficult to adjust, which also prevented the unit from operating at full potential. Using an electric clutch solves these problems. To operate the clutch, a small servo motor was integrated to move and lock the pawl. The clutch was triggered by a heel switch, placed at the bottom of the device insole. With all the additional components, including the microcontroller and a power bank battery, the total weight of the device increased by only 280 grams. The complete exoskeleton device is shown in Fig. 3.12. The small additional mass does not introduce any noticeable additional effort on the part of the user. Since the pawl only needs low forces to engage and disengage, the actuator can be small and of low-power with very low energy consumption. The additional small motor makes the passive exoskeleton quasi-passive. The exoskeleton now also features a foot switch on the heel and the additional option of data acquisition.

The clutch assembly is shown in Fig. 3.13. The micro servomotor is attached to the

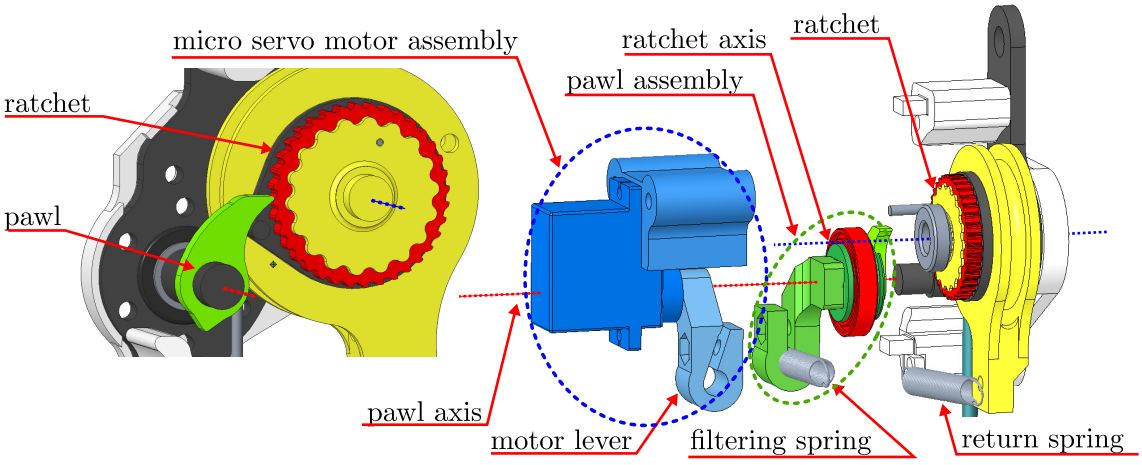


Figure 3.13: The ratchet and pawl are shown *left*. The disassembled clutch and its components are shown *right*.

clutch above the pawl. A small spring is added between the servomotor arm and the pawl to act as a shock absorber and filter out the shock loads resulting from engaging and disengaging the pawl. The shock absorber protects the plastic gears inside the micro servomotor. Without it, the plastic gears will be damaged in a short time.

The exoskeleton allows only one degree of freedom of motion, ankle plantar flexion and dorsiflexion. In order to measure its angle, a magnetic rotor encoder is integrated into the exoskeleton joint axis. In all other aspects, the exoskeleton functions and influences the user in the same way as the previous passive ankle exoskeleton. A linear spring is attached between the foot frame and the upper calf frame, which is connected to the clutch via a rope.

When the clutch is closed, the linear spring is extended by the movement of the ankle joint. And when the clutch is open, the linear spring does not affect the movement of the exoskeleton. A smaller return spring connects the pulley system to the clutch frame and prevents the cable connecting the linear spring to the coupling system from sagging.

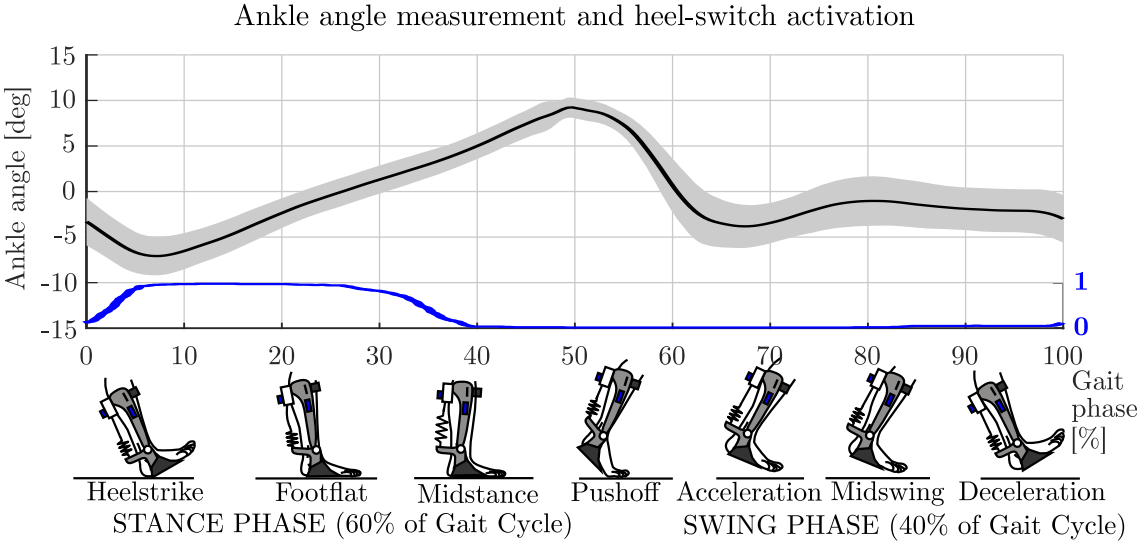


Figure 3.14: Exoskeleton angle measurements and clutch activation. Average angle (*in black*) and its standard deviation (*in gray*) measured at the exoskeleton joint in relation to the gait phase. Heel-switch activation probability is shown *in blue* and is calculated for 100 steps.

Both the left and the right leg exoskeletons independently house an Arduino Nano, which also independently controls its respective exoskeleton. The Arduino is used for sensor data acquisition and for controlling the micro-servo motor. In this study, the USB cable connection from the Arduino to a laptop served as both a power and communication port. A laptop was placed in a backpack so that the subjects could carry the system around with them during data collection. The ankle angle and the heel switch value (open, closed) at both ankles were logged during the experiments. Later, a power bank battery was added to make the device autonomous.

The algorithm running on the Arduino is designed to run endlessly and send the data to the laptop on request. The internal control algorithm of the Arduino ran at a frequency of 1000Hz, while the laptop received the data at 100Hz. During operation, the Arduino detects the heel strike and instructs the servomotor to close the clutch. Next, when the heel switch is released, the servo receives a command to open the clutch. However, because the pawl is under load, the servo cannot open it due to its low power. This keeps the clutch

closed until the linear spring is unloaded, which exactly matches the desired behavior of the spring. The energy stored in the tension spring is returned during the push-off phase. At this phase, the spring is completely unloaded, which means that the motor can open the clutch. The entire functional principle of the exoskeleton is shown in Fig. 3.14. The figure also shows the actual activation of the heel switch and the corresponding exoskeleton angle.

The small servo motor integrated in the clutch makes it easier to engage and disengage the spring and also solves the timing problem. The timing is now determined by a press on the heel down switch and is irrelevant of the walking style, speed or stride length as long as the heel-strike presses the switch.

3.4 Experimental Design & Protocol

To evaluate the exoskeleton, we conducted a pilot study with three 4-minute walks under different conditions. Seven healthy young individuals were asked to participate in the study. Their baseline characteristics are shown in Table 3.2. The trial's prime focus was on the

Table 3.2: Baseline of the participant characteristics of the second study.

	Mean	SD
Age (years)	27.1	3.48
Weight (kg)	75.9	9.48
Height (cm)	176.9	5.17
Shoe size (/)	42.5	0.99

operation of the quasi-passive clutch. From the user's point of view, no time-consuming experimental preparation was necessary before the trials. The users put on the exoskeleton and began to walk. The three operating conditions tested were as follows: First was the reference walk with the exoskeleton and without the linear spring. The second used the exoskeleton and 100% clutch probability of clutch activation and a 5 N/mm spring. The 5 N/mm spring is chosen based on the results of the previous study. In the third case, the exoskeleton used the same spring, but with only 80% probability of clutch engagement, which means that the clutch would randomly not close 20 times in 100 steps. The opening and closing of the clutch was defined in the algorithm running on the microcontroller. A defective clutch was simulated to reproduce observations from the first prototype.

The three walk sessions were not performed in random order to simplify the experimental protocol. In order to obtain unbiased questionnaire responses, the users were not informed about the difference between the walks or the simulation of the defective clutch. The walks took place in the laboratory corridor in the form of a 15x10m square path. This means that the users also had to make 4 sharp corner turns using the exoskeleton. All the necessary data was collected with a portable computer in the backpack of the user.

The user was asked to complete a questionnaire at the end of each walk. The questionnaire gave feedback on the ergonomics and comfort of the exoskeleton, the smoothness of the clutch operation and the user's feeling for the exoskeleton effects. It is shown in Fig. 3.15. Each question had four possible answers ranging from 1 to 4, one being given as the worst and four as the best. Other general operating or equipment comments were also collected in the last section of the questionnaire. Finally, a foot image was added in different positions so that users could mark any areas of discomfort.

Name: Weight:

Age: Height:

Feet (shoe) size:

	Questions:	1. walk	2. walk	3. walk				
(Q1)	Is it comfortable to walk in the exoskeleton?				**1** - very uncomfortable	**2** - uncomfortable	**3** - comfortable	**4** - very comfortable
(Q2)	How comfortable is the left leg?							
(Q3)	How comfortable is the right leg?							
(Q4)	How much walking effort was needed in the left leg compared to normal walking?				1 - a lot more effort compared to normal walking	2 - slightly more effort compared to normal walking	3 - slightly less effort compared to normal walking	4 - a lot less effort compared to normal walking
(Q5)	How much walking effort was needed in the right leg compared to normal walking?							
(Q6)	Does your left leg feel less fatigue compared to normal walking?				1 - a lot more fatigued than normal walking	2 - more fatigued than normal walking	3 - less fatigued than normal walking	4 - a lot less fatigued than normal walking
(Q7)	Does your right leg feel less fatigue compared to normal walking?							
(Q8)	Was the operation of the left exoskeleton smooth?				1 - not smooth at all	2 - not smooth	3 - almost completely smooth	4 - operates smoothly
(Q9)	Was the operation of the right exoskeleton smooth?							
(Q10)	Were there malfunctions on the left exoskeleton?				1 - does not work at all	2 - many malfunctions	3 - few malfunctions	4 - no malfunctions
(Q11)	Were there malfunctions on the left exoskeleton?							
(Q12)	Did you feel any effort decrease after dooning off the exoskeleton?				1 - a lot heavier legs	2 - heavier legs	3 - lighter legs	4 - a lot lighter legs
(Q13)	How do you think the exoskeleton affected you during walking (physiologically)?				1 -I used a lot more energy to walk than without	2 - I used more energy to walk than without	3 - I used less energy to walk than without	4 - I used a lot less energy to walk than without

(Q14) Considering, the exoskeleton reduces your walking effort for 10%. (same as taking off a 5 kg backpack) How much would you be prepared to pay for an improved version? (it would, of course, be more comfortable, lighter, better looking than the one in testing)

Other operation or device improvement remarks:

Did the exoskeleton feel tight or hurt anywhere? Please mark

Right foot



Left foot



Figure 3.15: The questionnaire. The red number markings were added during the analysis of the results for easier reference.

3.4.1 Results

For easier evaluation, the results of the questionnaire are divided into walks 1, 2 and 3. The questions are grouped into three topics as follows:

- comfort and ergonomics (Q1, Q2, Q3),
- walking effort reduction (Q4, Q5, Q6, Q7),
- smooth clutch operation (Q8, Q9, Q10, Q11).

The questions in the questionnaire shown in Fig. 3.15 are numbered with a *red* font. For each question group, the mean and standard deviation are calculated over the selected questions of all users. For example, for "Comfort and Ergonomics", the mean of questions Q1, Q2 and Q3 of all users is calculated. Table 3.3 summarizes the average values of the questionnaire answers.

Table 3.3: Questionnaire results.

	1st walk mean (SD) (no spring)	2nd walk mean (SD) (100% rate)	3rd walk mean (SD) (80% rate)
comfort, ergonomics	2.6/4 (0.6)	2.7/4 (0.6)	2.6/4 (0.5)
walking effort reduction	2.0/4 (0)	2.7/4 (0.6)	2.6/4 (0.7)
smooth operation	3.8/4 (0.4)	3.1/4 (0.5)	3.3/4 (0.6)

However, for an easier presentation, the results are shown graphically in Fig. 3.16. The "Comfort and Ergonomics" evaluation collects user feedback on the comfort and ergonomics of the device. Since the springless exoskeleton causes some discomfort, kinematic constraints and additional weight, users reflected this with a slightly lower score for the first walk. Although the difference is not great, the "Comfort and Ergonomics" rating improved in the second walk after adding the spring and activating it. Comfort and effort were expected to decrease when simulating the clutch failure in the third step.

The "Walking effort reduction" rating assesses whether the user felt a reduction in walking performance. The users observed a reduction in effort at the transition from the

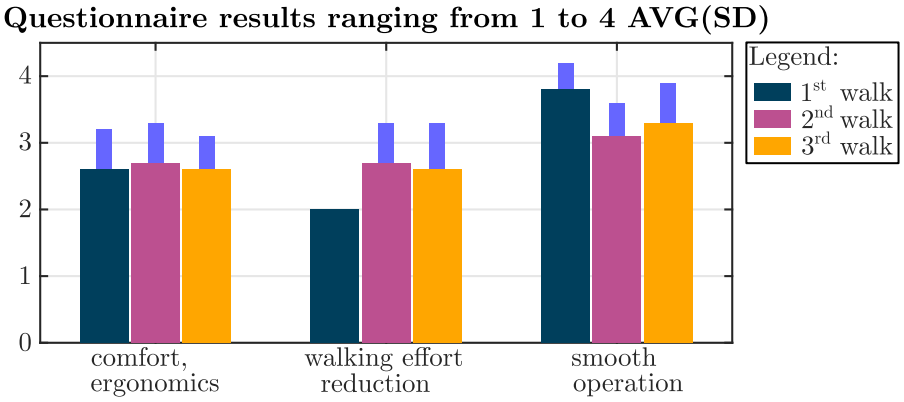


Figure 3.16: A graphical representation of the results of the questionnaire. The histogram in *blue* represents the standard deviation. The colours from the legend represent the average values.

1st to the 2nd step, i.e., from no spring to a 100% spring of 5N/mm. The third walk shows a lower observed effort decrease than the second walk, which was to be expected due to the clutch malfunction simulation. An intensive study beyond this pilot evaluation is necessary to scientifically evaluate the above effort reduction claims, and remove the human subjective factor.

The "Smooth operation" topic rates the reliability of the clutch. As the clutch does not operate quietly, the users interpreted the clutch noises as malfunctions and represented this in the questionnaire as non-smooth operation. The questionnaire shows the smoothest clutch operation for the first walk, when the clutch was not used. Both the second and the third walk have a decreased smoothness due to the clutch noises. The third walk has an increased clutch operation as compared to the second one, since the clutch did operate less frequently. However, once the sounds of the clutch actuation were explained after the study, some users were of the opinion that the clutch in the 80% run actually had a malfunction, as simulated. Unfortunately, they could not strongly reflect their observations in the questionnaire.

The results of the collected questionnaires are very subjective and should be analysed with great caution. The standard deviation is fairly large in all cases, which points towards a large diversity between users and supports the above caution. Nevertheless, the results also contain some valuable information about the use of the exoskeleton from the user's point of view.

It was found that the differences in user physiology (foot size and shape) and walking behaviour have a rather large influence on the function of the exoskeleton. Although a heel switch was integrated into the insole, sometimes the clutch was not activated because the heel impact of the user was not strong enough to activate the switch. This could be resolved by using either a more sensitive switch or by using angle data and an observer to predict the clutch activation, i.e., adaptive frequency oscillators similar to torque activation in [21].

To summarize the data, Fig. 3.17 shows the average of all three topics over all three walks. Users described the comfort level between 2 and 3 (of 4), indicating that the exoskeleton provides enough comfort for short walks. However, ergonomics and comfort need to be improved to allow for a prolonged exoskeleton use.

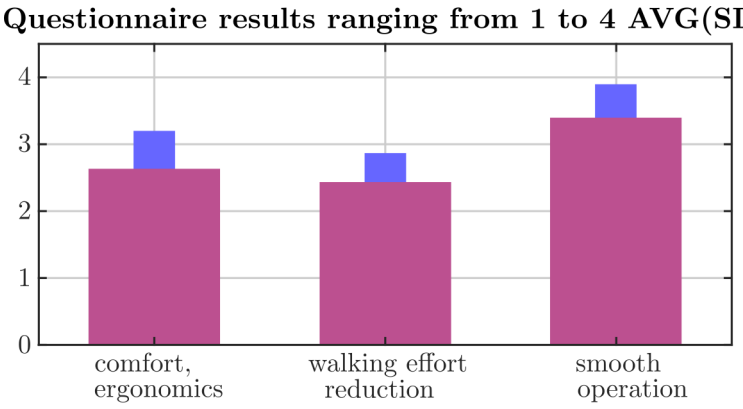


Figure 3.17: A summarized representation of the results. A more compact graphical representation of the questionnaire results with mean values and standard deviations.

The questionnaires contained several foot pictures where they could mark their areas of discomfort. The markings were collected across all the questionnaires and can be seen in Fig. 3.18. This data points at areas of the foot insole, which require more attention in ergonomic design.

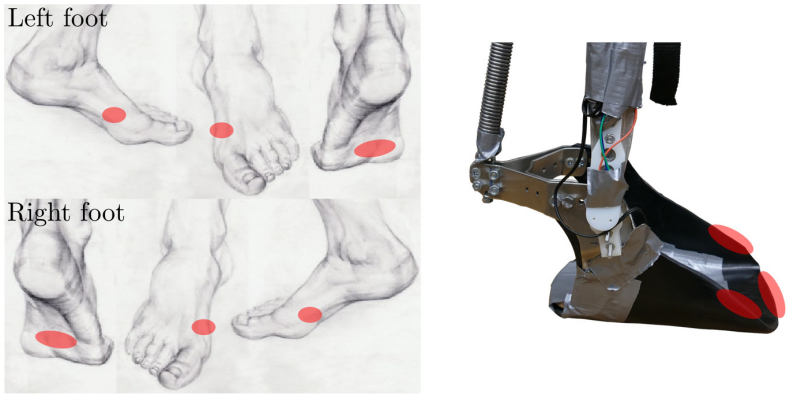


Figure 3.18: Several foot postures are shown *left* with markings of discomfort. The markings are then transferred to a picture of the insole on the *right* side.

Many users marked areas where the skin is relatively thin and the bones are closer to the surface. This results in higher pressure on the bones, as there is not much skin to absorb shocks. The exoskeleton insole material should be softer and not hard in these areas. However, the current prototype has uniform material properties and has the same material toughness everywhere. Discomfort had a negative effect on the user's feeling of reducing effort.

Some users also pointed out the introduced restriction of movement resulting from the only degree of freedom of movement of the exoskeleton. For this reason, it is difficult to make sharp corner turns. To perform a 90° rotation, the user must walk in a radius with a distance that is not negligible. Therefore, a frame with a higher number of degrees of motion is desired to reduce the motion restrictions of the proposed exoskeleton. These difficulties were already observed in the initial 4-people study, presented in Section 3.2.

3.5 Chapter Conclusion

The data collected show that the addition of a spring with appropriate stiffness leads to a reduction in metabolic costs, but differs greatly from subject to subject. A clear path to improvement is open when the added kinematic restrictions for the user and the weight of the exoskeleton are minimized. Based on the results, the appropriate spring stiffness appears to be less than 12 N/mm and close to 5 N/mm. The clutch mechanism has some weaknesses that affect the overall robustness of the clutch function, however, these difficulties were addressed in the follow-up design of the quasi-passive clutch.

The second prototype was tested in a qualitative oriented study with 7 persons. Each user used the exoskeleton for a certain period of time under different conditions and expressed his observations in a quality-oriented questionnaire. This represented a relatively short-term use of the exoskeleton, but is sufficient to obtain feedback from users. The users assessed the operation of the exoskeleton positively and showed that the majority seemed to feel a reduction in effort, but they also pointed out the ergonomics and comfort of the exoskeletons, which are not high enough yet. One way to improve the current design is with weight reduction as the exoskeleton with the additional clutch actuation now weighs around 1.09kg (without shoes). The weight comes mainly from the stainless steel frame.

Throughout the construction process and the study, we have found that the following aspects of exoskeleton construction need to be considered:

– In order to maximise effectiveness, economic value and potential user acceptance, the

exoskeleton should be as simple as possible.
- The possibility of wearing your own shoes and pulling the clothes over the exoskeleton gives the impression that the exoskeleton is easy to use. It gives a feeling of simplicity and trust.
- The exoskeleton should be easy to put on and take off.
- Ergonomic design is an important factor for comfort and safety. The lack of proper ergonomics, the discomfort, extra weight and introduced kinematic limitations can hide the feeling of reduced walking performance. It has a big impact on user acceptance, as seen in the questionnaire results.
- The exoskeleton should not hinder the user, i.e., its kinematic obstruction should be minimal. The insole should not be too thick and should have a suitable overall width when used in the user's shoes. A too wide frame would prevent the user from walking normally.
- It follows that the exoskeleton should have a sufficient size and kinematic degrees of freedom. The exoskeleton allows only one degree of movement, ankle flexion/extension, which proved to be insufficient and a limiting factor.
- In addition, it should be light in weight and have minimal inertia, yet robust enough for the intended task.

It is not clear to what extent the above observations affect the walking performance, and further research is needed to realize the full potential of the device. The concept could potentially be extended to other human joints, instead of only the ankle, which could result in novel types of exoskeletons that work in a hybrid unpowered and powered combination to achieve greater energy efficiency and performance.

On the positive side, the quasi-passive exoskeleton upgrade has led to a more reliable performance of the device with virtually no clutch problems when walking. The research showed that passive elastic elements have an important role in assistance mechanisms, however it is still unknown what is the optimal spring stiffness for a specific user. In order to find a suitable stiffness, a device is required that allows an immediate adjustment of the spring stiffness. Such devices are called variable stiffness mechanisms and are the focus of the second part of this research.

The development of, and research with the passive and quasi-passive exoskeletons were critical steps in achieving goal **G1: Evaluate the use of passive elements in exoskeleton devices** and confirming hypothesis **H1: Making a passive exoskeleton device into a quasi-passive one can improve its overall operation robustness**. Goal G1 and hypothesis H1 were reached and confirmed, respectively.

Chapter 4

Mechanically Compliant Actuator With Efficient Stiffness Variation

This chapter presents the research directed towards goal **G2** and hypothesis **H2** of the thesis, which address the development of a novel principle for efficient stiffness variation. The motivation originates from passive ankle exoskeleton research from Chapter 3, which emphasised the need for passive components that allow automatized stiffness adaptation.

One of the biggest challenges of these variable stiffness mechanisms is their mechanical complexity, which is why they can quickly lead to heavy and bulky final devices. This additional complexity and weight do not conform well with the requirements of exoskeleton devices, which should be light, comfortable, ergonomic, energy-efficient and cost-effective. As shown in the literature review in Section 2.1.3, these devices function on several principles with various degrees of mechanical efficiency. The characteristics of the chosen architecture have a direct impact on the final device where better performance of the mechanism or actuator results in better performance of the final exoskeleton device.

The literature shows many possible architectures for such devices, as listed in Section 2.1.3. However, current state-of-the-art compliant mechanism principles comply with the exoskeleton requirements only in a limited way. Further research is required to find a suitable mechanism architecture.

In this chapter, the focus is on a novel, energetically efficient mechanism for stiffness variation, which we call Pseudo-Linear Variable-Lever Variable-Stiffness Actuator or PLVL-VSA. The proposed stiffness variation mechanism can function as a stand-alone stiffness variation unit, or it can be integrated into a variable-stiffness actuator. Its primary advantage is efficient stiffness variation, which requires a lighter secondary stiffness variation motor and culminates in a lighter variable stiffness mechanism. Finally, a lighter variable stiffness mechanism results in a lighter exoskeleton device that uses it.
The following list summarizes the research effort:

- Develop a new mechanical stiffness variation principle and its underlying mathematical model.
- Design a prototype with a performance close to the requirements of the final application, i.e., an elbow exoskeleton.
- Perform extensive performance testing of the actuator prototype. Analyse and identify any faults of the proposed mechanism and find theoretical solutions.
- Develop an optimization method to achieve maximum utilization of the torque-deflection workspace of an actuator with variable stiffness given the torque limits of the geared motor.

The chapter begins with an explanation of the operational principle in Section 4.1, follows with the underlying mathematical model in Section 4.2 and concludes the first part with

theoretical results in Section 4.3. The sections that follow are dedicated to the prototype; PLVL-VSA in Section 4.4 and its improved version in Section 4.7.

4.1 Operation Principle

The proposed stiffness variation mechanism is based on a combination of a cam deflection and a variable lever mechanism. The essential components are shown in Fig. 4.1a.

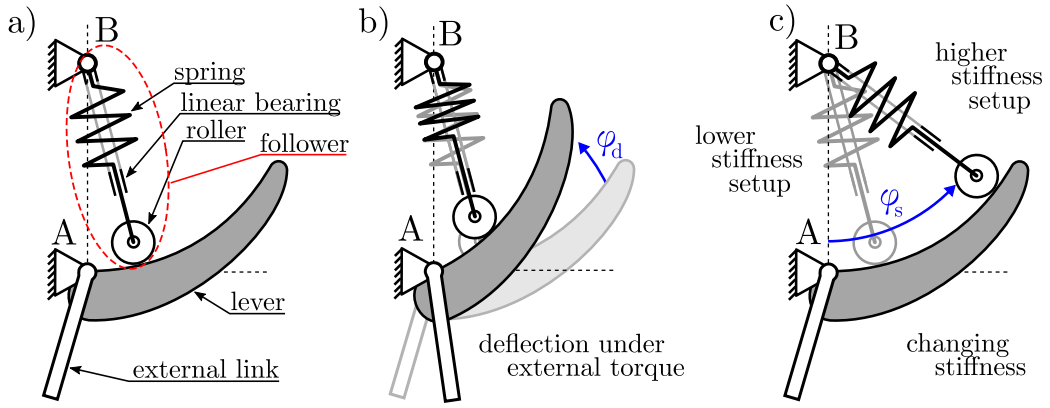


Figure 4.1: PLVL-VS actuator functional principle: a equilibrium position, **b** deflection under external torque and **c** stiffness variation.

In its basic form, the curved lever arm rotates and deflects around the pivot point A, thereby increasing its deflection angle (φ_d) and compressing the linear spring, see Fig. 4.1b. The curved lever is connected to the external link and provides the reaction torque there. Depending on the chosen design, the lever can be connected either directly to the external link for a one-way compression or indirectly for a bidirectional application. The follower can rotate around pivot B to change stiffness and is driven by a stiffness variation motor located directly at pivot B, see Fig. 4.1c. In order to retain the desired stiffness, the stiffness variation motor can be stopped at the appropriate angle – at a suitable position of the follower on the lever arm. A higher cam follower angle (φ_s) produces a longer effective torque arm between the spring contact point and the pivot A. The lever torque needed to compress the spring increases, resulting in a higher stiffness of the mechanism. This forms the basis for the proposed variable stiffness mechanism. The stiffness of the mechanism can be changed continuously and under all loads, as long as the load is below the peaks of both motors' gearboxes. While later in the results only a few follower angles are shown, the reader should not misunderstand that only these follower angles can be achieved.

Two motors of the mechanism are utilized similarly as in many other variable stiffness actuators. The first, hereafter referred to as the *position motor*, is placed at pivot A and either provides the desired torque or changes the equilibrium position of the external link. The second motor, hereafter referred to as *stiffness variation motor*, is placed at pivot B and can adjust the stiffness of the mechanism.

The lever arm has a circular arc shape, i.e., at zero deflection the radius between the pivot B and the contact at the circular arc is constant. Any other shape would result either in preload of the mechanism or in backlash/lift-off of the follower. Due to the arc shape, the spring system can ideally be turned without resistance at zero deflection, since the force/torque required to change the stiffness is applied perpendicularly to the load. Similarly to [97], most of the stiffness variation motor's power is used to vary the stiffness. This makes the stiffness variation energy-efficient and places the mechanism into

the category of preloadless mechanisms [41], where the stiffness is varied by changing the transmission ratio. Systems with energy-efficient stiffness variation employ a less powerful motor in comparison to the position motor and can save battery power and culminate in lighter final device.

The proposed concept has a strong resemblance to AwAS [97] and the derivation of PLVL-VSA in comparison to AwAS is shown in Fig. 4.2. The figure shows the transition from the linear stiffness variation principle using a ball-screw towards a rotational-based stiffness variation principle. Both mechanisms are still categorized as variable lever designs.

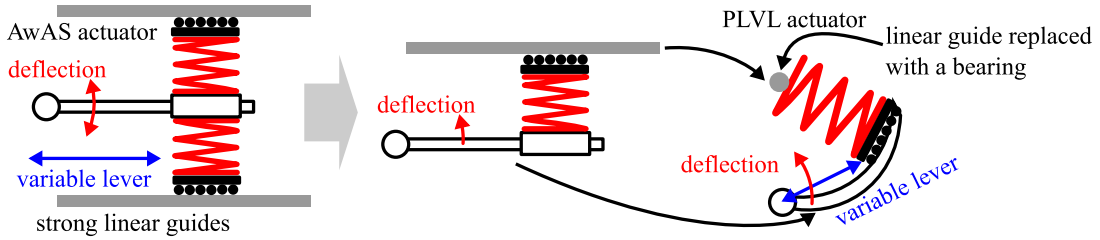


Figure 4.2: Rotational-based PLVL-VSA variable lever stiffness variation principle. The figure shows the derivation of PLVL-VSA in comparison to AwAS, i.e., the transition from the linear stiffness variation principle using a ball-screw (AwAS) towards a rotational-based stiffness variation principle (PLVL-VSA).

The proposed change results in a smaller mechanism area, since the long linear bearing is replaced through a rotational bearing. Other features are analysed later.

The proposed mechanism can only absorb compressive loads and is in principle unidirectional. When the load turns in the opposite direction, the lever arm loses contact with the cam roller. To achieve a bidirectional application, a special transmission mechanism is needed to change the bidirectional motion of the external link to a one-directional compression movement of the curved lever. The actual prototype uses a cable transmission mechanism to reverse the movement. In a previous study, a geared transmission was explored [63].

4.2 Mathematical Model

The system geometry is very straightforward, which means that a mathematical expression can be derived relating the deflection torque (τ_d) and the deflection angle (φ_d). This information is then used for design and control purposes. Fig. 4.3a shows the most important parameters affecting the model. R_s and R_b define the overall dimensions of the mechanism. Parameter R_b has been added to take into account for an additional bearing space at pivot A for future design iterations. The stiffness of the elastic element (k_int) used inside of the mechanism is important for the mechanism's overall properties. The actuator's state is determined based on angles φ_s and φ_d, which represent the stiffness variation motor rotation corresponding to the follower rotation and the angular deflection of the mechanism, respectively. Geometrically, the mechanism represents the interaction between a line (*line 1* in Fig. 4.3a) and a circle (*circle 1* in Fig. 4.3a), which is controlled by equations:

$$y = \tan\left(-\frac{\pi}{2} + \varphi_\mathrm{s}\right) x + (R_\mathrm{s} + R_\mathrm{b})\,, \tag{4.1}$$

$$R_\mathrm{s}^2 = (y - (R_\mathrm{s} + R_\mathrm{b}))^2 + x^2. \tag{4.2}$$

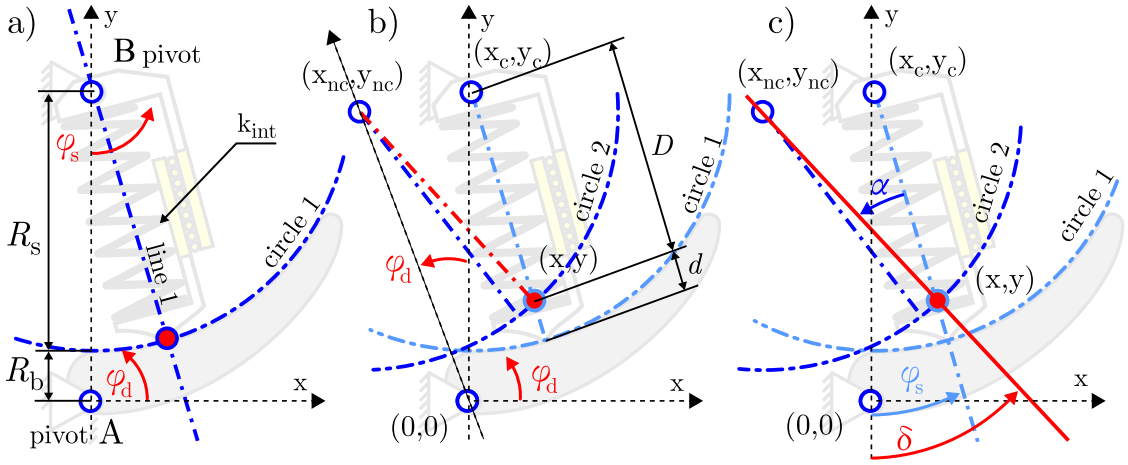


Figure 4.3: The flat-out simplified view of the proposed mechanism with its relevant parameters is shown in **a**. The deflection of the mechanism rotates the curved lever (*circle 1*), i.e., the arc profile in **b**. The red line in **c** is perpendicular to the deflected arc (*circle 2*) and goes through the center of the arc. From its inclination (δ), the pressure angle (α) can be calculated.

To calculate all torques, one must first calculate the intersection between the line (*line 1*) and the circle (*circle 1*) with coordinates (x, y) (see the red dot in Fig. 4.3) using equations (a is introduced to shorten them):

$$x(\varphi_d, \varphi_s, R_s, R_b) = (R_b + R_s)\sin(\varphi_s)\left(2\sin\left(\frac{\varphi_d}{2}\right)\sin\left(\frac{\varphi_d}{2} - \varphi_s\right) + a\right), \tag{4.3}$$

$$y(\varphi_d, \varphi_s, R_s, R_b) = (R_b + R_s)\cos(\varphi_s)\left(\cos\left(\varphi_d - \varphi_s\right) + \frac{\sin^2(\varphi_s)}{\cos\left(\varphi_s\right)} - a\right), \tag{4.4}$$

$$a = \sqrt{\frac{R_s^2}{(R_s + R_b)^2} - \left(\sin(\varphi_d - \varphi_s) + \sin(\varphi_s)\right)^2}. \tag{4.5}$$

The spring is the force-generating element, and it lies on the line with an inclination based on the cam follower angle (φ_s). The force (F_{spr}) is calculated from the compression (d) obtained through the distance (D) (see Fig. 4.3b):

$$D = \sqrt{(x - x_c)^2 + (y - y_c)^2}, \tag{4.6}$$

$$d = R_s - D, \tag{4.7}$$

$$F_{spr} = k_{int}\, d. \tag{4.8}$$

The *line 1* and the deflected *circle 2* geometry can be used to calculate the pressure angle (α) (note that $x_c = 0, y_c = R_s + R_b$) using equations:

$$x_{nc} = x_c\cos(\varphi_d) - y_c\sin(\varphi_d), \tag{4.9}$$

$$y_{nc} = y_c\cos(\varphi_d) + x_c\sin(\varphi_d), \tag{4.10}$$

$$\delta = \arctan\left(\frac{y - y_{nc}}{x - x_{nc}}\right) + \frac{\pi}{2}, \tag{4.11}$$

$$\alpha = \delta - \varphi_s. \tag{4.12}$$

Here, the new circle center coordinates (x_{nc}, y_{nc}) are calculated by the rotation/deflection (φ_d) of the original circle center (x_c, y_c). Variable δ stands for the inclination of a continuous line going through (x, y) and (x_{nc}, y_{nc}) that is perpendicular to the lever, i.e., it passes

through the center of the rotated circle, and is therefore required to calculate the pressure angle (α). $\pi/2$ in Eq. (4.11) represents the complementary angle. The deflection torque (τ_d) is determined using a vector cross product:

$$F = F_{\text{spr}}/\cos(\alpha), \tag{4.13}$$

$$\vec{F} = F\left[\cos\left(-\pi/2 + \varphi_{\text{s}} + \alpha\right), \sin\left(-\pi/2 + \varphi_{\text{s}} + \alpha\right), 0\right], \tag{4.14}$$

$$\vec{r} = [x, y, 0] \tag{4.15}$$

$$\vec{\tau}_{\text{d}} = \vec{r} \times \vec{F}. \tag{4.16}$$

The deflection torque derivative can be used to determine the theoretical stiffness of the mechanism (k_{theo}):

$$k_{\text{theo}} = \frac{d\tau_{\text{d}}}{d\varphi_{\text{d}}}. \tag{4.17}$$

In any state (φ_{s}, φ_{d}), the torque (τ_{s}) required to maintain a desired stiffness, i.e., angle φ_{s}, is calculated as:

$$F_{\text{din}} = F_{\text{spr}} \tan(\alpha), \tag{4.18}$$

$$\tau_{\text{s}} = F_{\text{din}}\, D. \tag{4.19}$$

F_{din} is the tangential force caused by the increasing pressure angle, because the loaded follower is not completely perpendicular to the lever. Finally, if information about the amount of stored elastic energy (E_{sys}) is required, the following equation can be used to calculate it:

$$E_{\text{sys}} = \int_0^{\varphi_{\text{d}}} \tau_{\text{d}} d\varphi_{\text{d}}. \tag{4.20}$$

4.3 Theoretical Analysis

To analyse the mathematical model, the parameters collected in Table 4.1 are used. The

Table 4.1: Mathematical model parameters.

Parameter	Value	Unit	Parameter	Value	Unit
R_{s}	50	[mm]	R_{b}	0	[mm]
k_{int}	72.6	[N/mm]	k_{lin}	0-49	[Nm/rad]
φ_{s}	0-80	[°]	φ_{d}	±20	[°]
$\tau_{\text{p,nom}}$	15	[Nm]	$\tau_{\text{s,nom}}$	5	[Nm]
$\tau_{\text{p,peak}}$	22.5	[Nm]	$\tau_{\text{s,peak}}$	6.3	[Nm]
t_{s}	0.15	[s]			

basic geometry is defined by the stiffness radius R_{s}. Parameter R_{b} is purely design-oriented and provides the flexibility for easier bearing placement on the pivot A. In both prototypes, the bearing of the arc lever was moved behind the plane of the follower mechanism, consequently R_{b} is equal to zero. Increasing the value of R_{b} opens up the possibility of a flatter future design where the bearing is placed in the plane of the tracking mechanism.

The torque limits of both motors resulting from their gearboxes are given in Table 4.1. The nominal and peak torques of the position motor are marked as ($\tau_{\text{p,nom}}, \tau_{\text{p,peak}}$)

and for the stiffness motor as $(\tau_{\mathrm{s,nom}}, \tau_{\mathrm{s,peak}})$. The reader should note that the theoretical results assume and evaluate the case where a position motor is located directly at Pivot A, which is not the case for both prototypes. To design a flat actuator, the position motor is relocated away from the axis and connected to the lever via a cable transmission. Fig. 4.4 shows the theoretical torque/deflection and stiffness/deflection properties calculated from the values in Table 4.1 for a set of different follower angles.

The size of the torque/deflection space of the mechanism is determined by the torque limits of the motor and its gearbox. In Fig. 4.4, the limits are marked with the red and black dashed lines in all graphs. They divide the torque/deflection space into four areas using the proposed model and numerical calculations. Blue and red colored areas (see Fig. 4.4a) represent the operation of the actuator below nominal and peak torques, respectively, for both motors used. The yellow area indicates where the torque required to maintain stiffness is higher than the stiffness motor's gearbox limit. Here, the stiffness motor can no longer adjust the stiffness and due to a high gearbox transmission, the gearbox can get damaged. The specific ways of taking this into account are explained in Section 4.5. Additional red dashed lines show how a potentially stronger stiffness motor affects and magnifies the peak operating range. Similarly, if the external torque is above the limit of the position motor (or its gearbox), depending on the type of gearbox and current limit set, it cannot move or is driven backwards. Since the motor can be back-driven in the event of an overload, the white area shown in Fig. 4.4a,b is theoretically not reachable.

Looking at the properties, two advantages can be observed. The first is the almost linear (pseudo-linear) torque/deflection characteristic, which is strongest in the operating range of the motor (see Fig. 4.4a,b). The pseudolinear expression is used to indicate that the mechanism is nonlinear in principle, but can be approximated as linear in the working

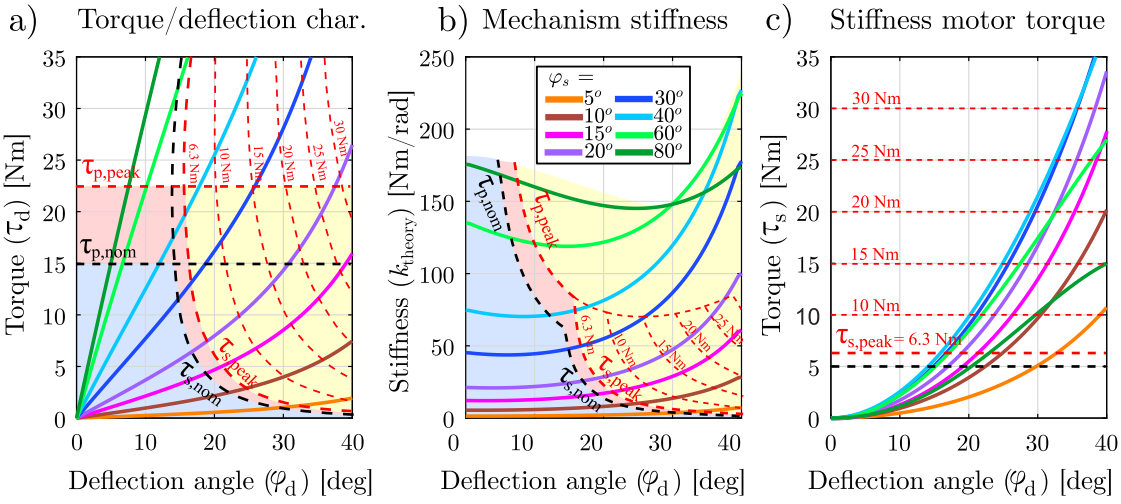


Figure 4.4: The torque/deflection properties of the proposed mechanism. The torque required for the deflection of the mechanism is shown in **a**. Its derivation or stiffness is shown in **b**. The torque required to maintain a given stiffness resulting from the tangential force is shown in **c**. The line colors represent a specific stiffness setup angle. The **black** and **red dashed lines** represent the nominal and peak torque for both motors. Additional **red dashed lines** represent the torque limits for stronger stiffness variation motors. The **blue**, **red** and **yellow areas** represent the below nominal, below peak and above actuator peak torque operation regions. Under the assumption that the position motor can be backdriven at loads above its current limit (gearbox peak torque), the **white areas** in **a** and **b** are theoretically not reachable.

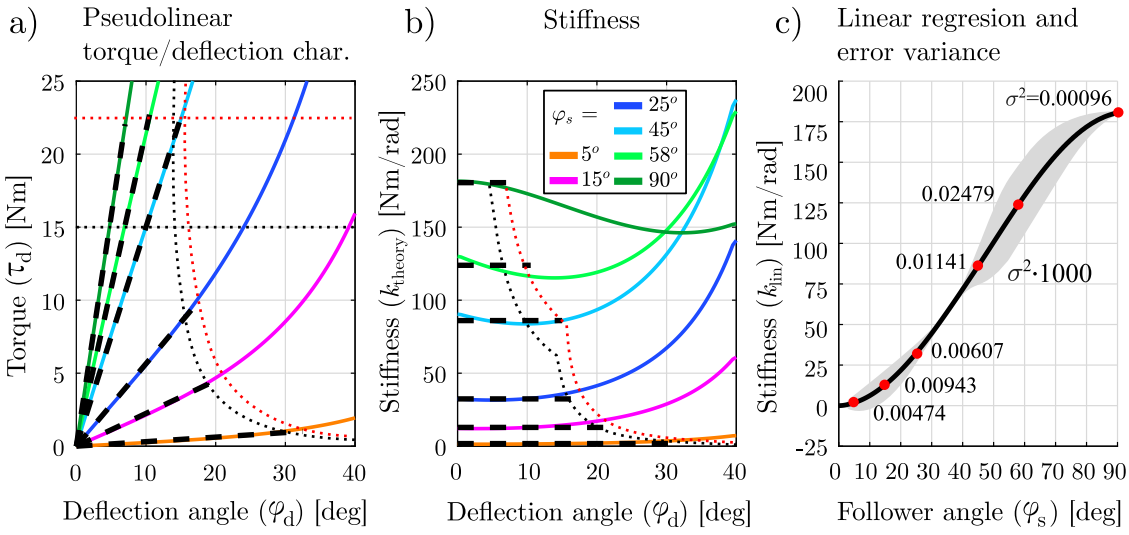


Figure 4.5: The pseudo-linear property of the mechanism. The external torque required to deflect the mechanism is shown in **a** for different cam follower angles. Its derivative, i.e., mechanism stiffness, is shown in **b**. The **black** and **red dotted lines** show the torque limits of both motors. The **black dashed lines** in **a** and **b** show the results of the linear regression. Based on the regression result, a relation between the cam follower angle and the resulting mechanism stiffness approximation can be constructed, shown in **c**. The **gray area** represents the linear regression error variance (scaled 1000x).

space with good accuracy. While linear regression can also be performed over peak motor conditions, because the actuator does not operate in this range, regression accuracy is improved by staying under peak conditions. See the linear regression results in Fig. 4.5a,b. In order to calculate the theoretical stiffness of the mechanism, the model requires the information of both the deflection (φ_d) and follower angle (φ_s). However, through linear regression in the area below the engine peak conditions, the model dimensions can be reduced. Each follower angle thus results in a linear equivalent stiffness of the mechanism. The linear stiffness is the same regardless of the deflection angle φ_d. To determine the stiffness of a progressive system, both φ_s and φ_d parameters need to be specified. The ability to use a linearized model facilitates mechanical design and allows the use of simpler control algorithms.

Torque-deflection properties in recognized designs, such as the MACCEPA [98] and the FSJ-Joint [96] are typically progressive (nonlinear), meaning that increased deflection increases the stiffness of the mechanism. Another example is the stiffness of an ankle prosthesis [167], which is also non-linear. The common reason why the progressive or stiffening stiffness characteristics of the mechanism is considered as an advantage is that it prevents the external link of the system from reaching its mechanical deflection limit and protects the device from mechanical damage. However, in these examples, the stiffness is determined with more than one parameter and depends on the stiffness setting parameter and the deflection of the mechanism, i.e., two or more parameters. Furthermore, the nonlinear properties also lead to a more unconventional and complex nonlinear control design resulting in longer control design times, as in [168, 169] where a VSA with nonlinear properties is used. Of course, the actual advantages depend on the nature of the chosen application. It is also expected that using progressive stiffness characteristics would not contribute greatly to the desired final exoskeleton application.

The regression is performed with the assumption that all the lines start at the origin.

As seen in Fig. 4.5c, a relation between the cam follower angle and the actual mechanism stiffness is thus created. In this specific case, a look-up table can be built to represent that relation to transform the cam follower angle to the actual stiffness and vice-versa. This look-up table can be then used for control purposes. Observe also that the linear regression of the theoretical model introduces only small errors, emphasized in Fig. 4.5c, which shows the linear regression error variance. The data had to be up-scaled 1000 times to appear on the plot.

The second mechanism advantage is the low stiffness variation torque (see Fig. 4.4c), which is far lower than the values for the position motor (see Fig. 4.4a). Thus, compared to the position motor, a less powerful motor can be used to vary the stiffness. Of course, it also depends on the desired speed of stiffness variation. However, observe that while initially the torque to hold the stiffness is small, with the increase of the deflection angle, the torque rapidly increases (see Fig. 4.4c), as the mechanism is losing its stiffness variation efficiency. This is an important feature, which needs to be considered when determining the parameters of the mechanism.

4.4 PLVL-VSA Prototype

The first implementation of the PLVL-VSA was a proof-of-concept prototype built with rapid prototyping technology in a previous study [63]. It can be seen in Fig. 4.6. Proof-of-

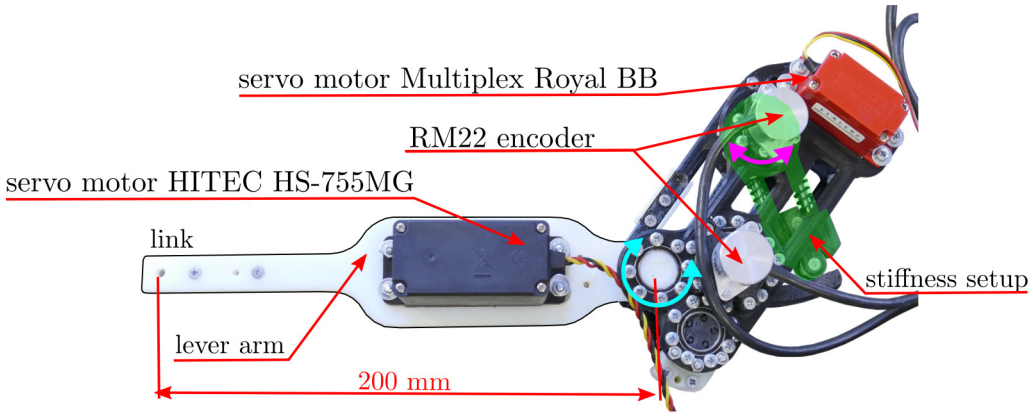


Figure 4.6: Proof-of-concept PLVL-VSA prototype from [63]. Some of its more important components are marked.

concept prototype was not suitable for an application use because of its high mechanical complexity, i.e., complicated special gears, and because its plastic components could only withstand low loads. This section presents the prototype implementation of the proposed stiffness variation concept in a new improved prototype. The new prototype has a more durable shape and is prepared for installation in an elbow exoskeleton device.

The main contribution of this section is a new implementation of the PLVL-VS principle, which features a reduced number, smaller variety and lower mechanical complexity of the various mechanical components. The PLVL concept of a spring-loaded cam follower and the curved lever leading to a lever mechanism with variable transmission remained unchanged. Instead of a gearbox from the proof-of-concept version, a steel cable transmission now extends the unidirectional cam mechanism and allows a bidirectional application. The new prototype uses more powerful motors and the entire actuator has specifications that come much closer to a practical application. Several experiments were designed to determine the characteristics of the prototype. Finally, the actuator benchmarks are compared

with the specifications of several other state-of-the-art actuators from the literature.

The target application of the proposed mechanism is the actuation of a wearable device, more specifically a 1 DoF elbow exoskeleton. However, the experimental focus of this section is on the compliant actuator and not on the exoskeleton device. One of the features required for the intended application is fast and efficient stiffness variation, thus the pretension-less and perpendicular stiffness variation is advantageous. The actuator should allow the possibility of a compact design. This is possible due to the rotational stiffness variation architecture and the additional parameters in the mathematical model. The non-standard parts used should be designed for practical manufacturing, in contrast to the complex gearbox of [63]. The device should integrate more sensors to allow monitoring of more parameters, including torque on the follower. In addition, it should allow self-calibration, which means that no other external measuring equipment is required to measure the actuators properties. Such an approach can be implemented through a redundant sensor architecture. The overall objective is to develop an actuator with a flat, lightweight and efficient structure suitable for a portable application. The proposed implementation of Pseudo-linear Variable-Ratio Lever Variable-Stiffness Actuator (PLVL-VSA) combines these features.

This section is organized as follows. The mechanism implementation is presented in Section 4.4.1. Section 4.4.2 that follows presents the experimental setup. The control algorithms used are presented in Section 4.4.3. The results and analysis are shown in Section 4.4.4.

4.4.1 Internal/External Mechanism

The proposed PLVL-VSA mechanism is shown in Fig. 4.7, with the flat-out mechanism drawings and the corresponding depictions of the CAD prototype. The cam and lever principle can be seen in Fig. 4.7a and the stiffness variation principle in Fig. 4.7b. The stiffness motor is located directly at the pivot point B and rotates the follower to change the stiffness. The lever arm deflects (φ_{d}) around the pivot point A and compresses the spring.

Since the PLVL principle only supports compressive loads, the pure compression action is converted into a bidirectional application, i.e., deflection in both directions, through an additional cable transmission. The additional cable transmission influences the performance of the final device. The mathematical model of the PLVL does not take cable transmission into account and only describes the internal mechanism. A distinction is therefore made between this basic mechanism, which is from now on called the *internal mechanism*, and the mechanism achieved by bidirectional transmission, which is subsequently called the *external mechanism*.

The cable implementation is schematically shown in Fig. 4.7c. The simplicity of implementation and the reduction of the total number of parts are two of its advantages. In the proposed arrangement, the position motor housing is rigidly mounted on a hollow pulley. The position motor axis runs through the hollow pulley and is attached to the external link. The rotation of the position motor shaft directly influences the equilibrium position of the external link. The pulley-motor assembly can then rotate and, due to the cable transmission, also deflect the curved lever which rotates around the pivot A. The complete prototype actuator is shown in Fig. 4.7d,e.

The final implementation of the cable transmission is explained in a detailed schematic diagram supported by a CAD model in Figure 4.8. To transmit the external torque over the cables, the cable is attached to a pulley with a cable holder (see Figure 4.8d). The cable is routed in both directions around the pulley to create additional friction and reduce the load on the point fixture. At the other end, the cable is passed over the circular-arc lever,

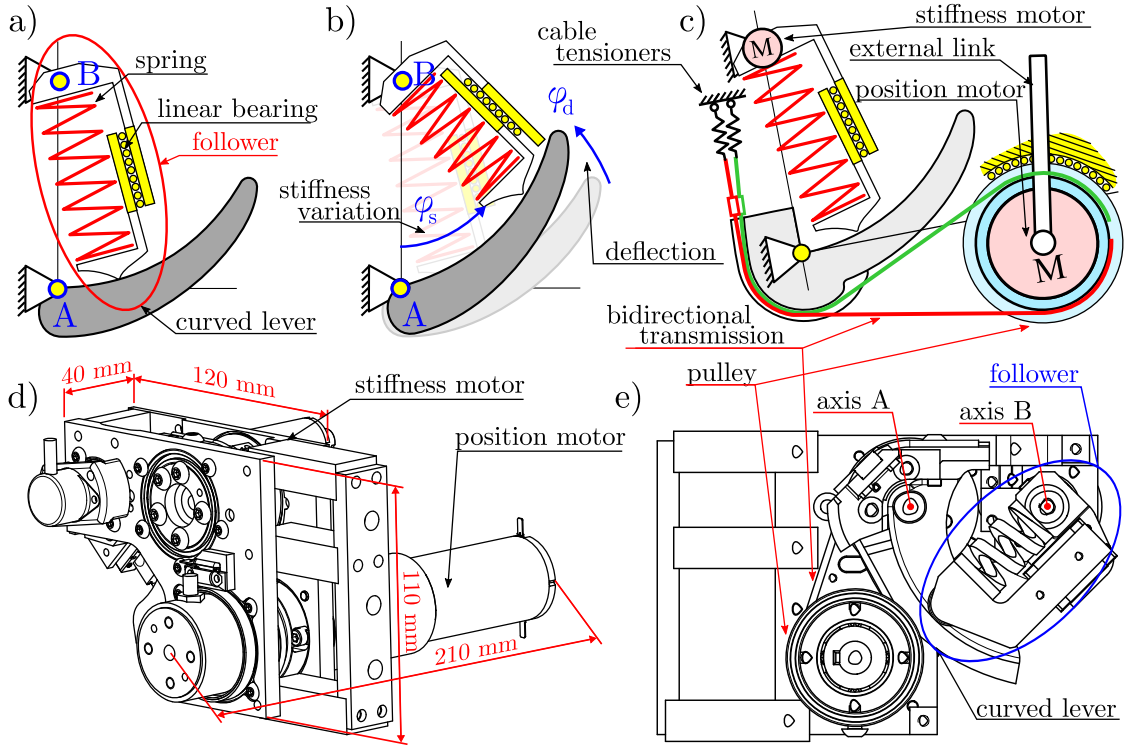


Figure 4.7: Several representations of the PLVL-VS mechanism. The flat-out representation of the internal mechanical components is shown in **a**. The compression motion is represented in **b** with a marked cam follower angle (φ_s) and a deflection angle (φ_d). A more detailed representation of the bidirectional VSA mechanism is shown in **c**. The CAD model of the VSA with dimensions is shown in **d** with its internal view in **e**.

but fixed to the mechanical housing by an elastic element. The elastic element between the housing and the cable provides the tension that reduces the non-linearity of the cable and ensures that the cable does not lift-off the pulley. The cable is also tensioned through a slight preload on the cam follower to additionally ensure that the follower does not lift-off. This small preload is presented later in Section 4.4.4.1. A blocking element mounted on the cable allows it to pull the curved lever.

While this mechanism seems rather complicated, the manufacture of its parts is less complicated than that of the custom gears from the previous study in [63].

4.4.2 Experimental Setup

The prototype was built not only to validate the proposed approach for stiffness variation, but also to later serve as an actuator for an exoskeleton. For this reason, experiments were carried out exploiting sensor redundancy and the fact that the actuator is a fully functional device and can provide monitoring data. Table 4.2 collects standard components that make up the VSA. To ensure sufficient actuation, Maxon motors are used due to their high power-to-weight ratio; an 80W version for position set-up and a 20W version for stiffness variation. Both motors use a planetary gear transmission. The ratio for the position motor is 113:1 and 172:1 for the stiffness variation motor. Note that the nominal and peak torques shown in Table 4.1 do not apply to the motors themselves, but to their planetary gear transmission. The position motor gearbox has 72% efficiency and 1° backlash, while the stiffness motor gearbox has 75% efficiency and 1.1° backlash. Each motor has its own dedicated Maxon ESCON 50/5 amplifier, which provides current feedback and the ability

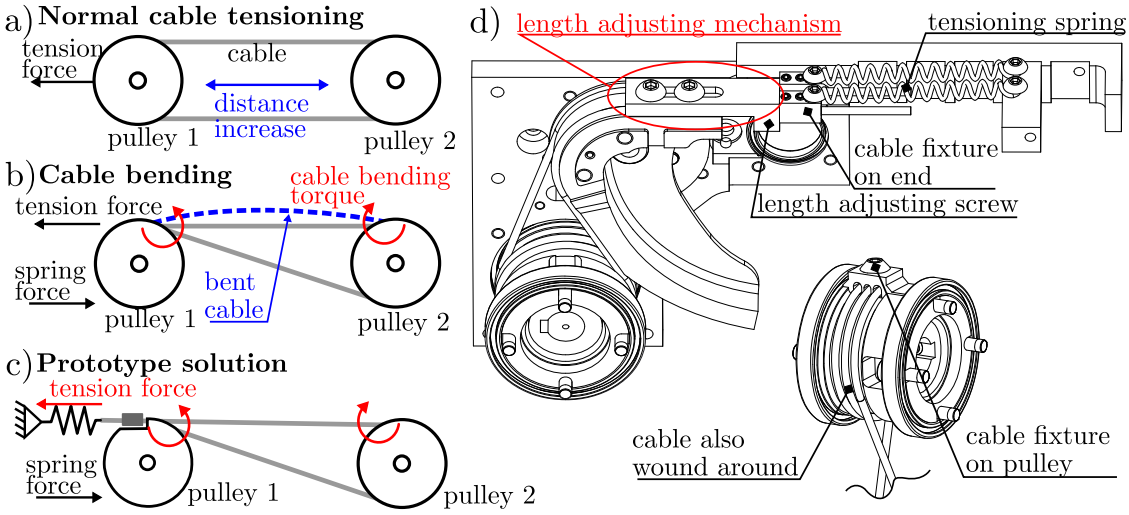


Figure 4.8: Cable transmission in-depth. A classic cable transmission is tensioned by increasing the distance between the pulleys, as shown in **a**. The prototype cable system is connected with both its ends onto the same side of the pulley (*pulley 1*), see **b**. Classic tensioning is therefore not possible and the internal bending moment in the rope also affects the mechanism load. The proposed tension solution is shown in **c**. The cable is tensioned by a spring connected to the mechanical housing. A CAD model representation of the actual prototype solution is shown in **d**.

Table 4.2: Actuator components.

Component	Description	Further data
Position motor	DCX35L GB KL 48V	Maxon 80W, 113:1
Stiffness motor	DCX22L GB KL 48V	Maxon 20W, 172:1
Motor amplifier	ESCON 50/5	one for each motor
Incremental encoders	4 encoders RLS	RM22, RoLin
Torque sensor	Tovey Engineering	RT-500, 55Nm
Controller	PCM-3362 PC-104	integrated circuit
Data acquisition	Sensoray 526	

to control the motor in either velocity or current input mode.

Fig. 4.9a shows the location of the mechanical components and Fig. 4.10 shows all the electronic system components. The experimental test configurations are shown in Fig. 4.9b,c. The prototype is mounted on an aluminum column, which allows a faster design cycle. The prototype system is fully sensored with 4 incremental encoders, one in front of the position motor gear, one after the stiffness motor gear, one at the arc lever and one at the external link. This results in sensor redundancy. A compact RT-500 reaction torque sensor with a rated torque of 55 Nm provides additional information about the external torque for validation purposes. Note that a compact commercial version of the actuator could be built with fewer sensors. The main controller consists of an integrated circuit (IC) PCM-3362 PC-104 with a Sensoray 526 data acquisition card. The Sensoray 526 provides 4 programmable counters for direct counting of incremental encoders and 8 A/D converters. The encoders can thus be directly counted on the PCM-3362 and accessed with low latency.

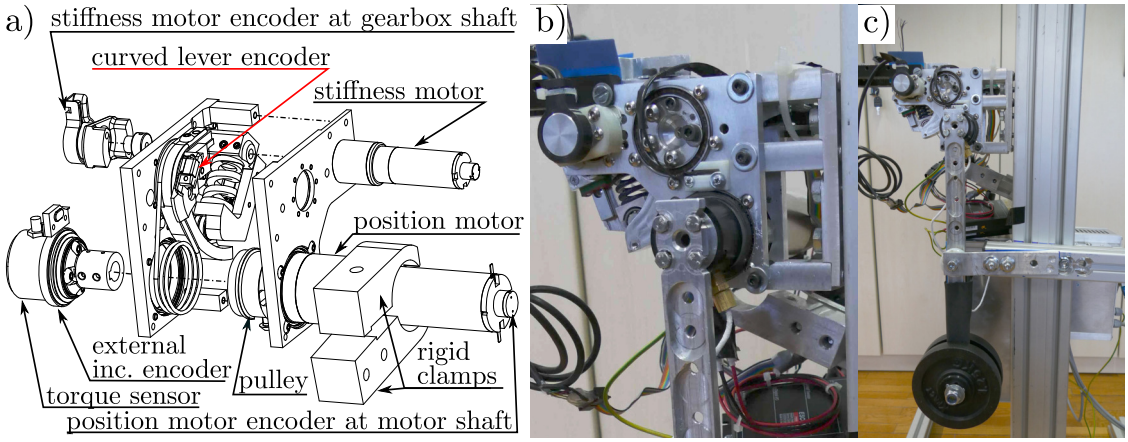


Figure 4.9: Exploded CAD model view of the experimental actuator is shown in **a**. Its actual implementation is shown in **b**. The experimental system where the external link is fixed to allow measurement of internal actuator properties is shown in **c**.

A/D converters allow for analysis of sensor data required for human-robot collaboration, like torque sensors for contact evaluation or EMG (Electromyography) electrodes for human biofeedback. The system is compatible with Simulink Real-Time™ software and provides real-time control at 1000Hz and synchronized data acquisition.

A 1000W power supply from MeanWell provides the necessary input power in the system. It is combined with an 8800 μF shunt regulator, which can store the return currents when the motors are braking. Reverse currents are enabled by 4-quadrant (4Q) operation of the Maxon ESCON 50/5 amplifiers. The shunt controller also protects the power supply, as any current that would flow back into it would overload it and force it to reset. During a power supply reset, the system loses all power until the power supply is able to recover.

4.4.3 Control Algorithms

Two experiments were performed to evaluate the device. The goal of the first is to measure the torque/deflection properties. The goal of the second one is to measure the rate of

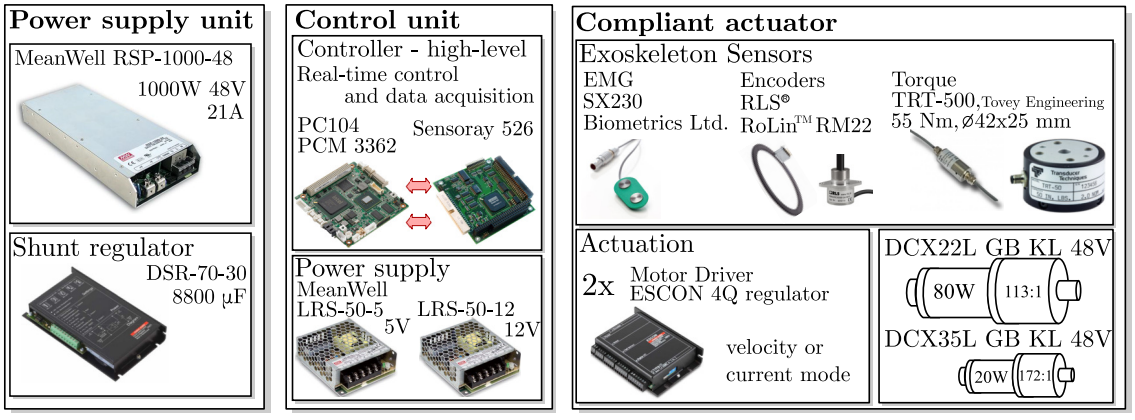


Figure 4.10: System electronics. The electronic system is subdivided into several units, among them: power supply unit, control unit and compliant actuator unit.

stiffness variation. The control of the position motor is different in each experiment. However, the control of the stiffness motor remained unchanged. All control algorithms are summarized in Table 4.3.

Table 4.3: Control algorithms.

Motor/**mode**	Control algorithm	
P. motor /**position**	$u_{\text{pos}} = K_{\text{p,ff}}\dot{\varphi}_{\text{p,des}} + \text{PD}(\varphi_{\text{p,des}} - \varphi_{\text{p,m}})$	(4.21)
P. motor /**torque**	$u_{\text{pos}} = \frac{1}{0.72}\left(\tau_{\text{des}}K_{\text{p,ff}} + \ddot{\tau}_{\text{des}}\frac{J_{\text{m}}}{K_{\text{s}}} + \text{PD}(\tau_{\text{des}} - \tau_{\text{ext}}) + \dot{\varphi}_{\text{p,m}}K_{\text{f}} + \ddot{\varphi}_{\text{p,ext}}J_{\text{m}}K_{\text{b}}\right)$	(4.22)
S. motor /**position**	$u_{\text{stiff}} = K_{\text{s,ff}}\dot{\varphi}_{\text{s,des}} + \text{PD}(\varphi_{\text{s,des}} - \varphi_{\text{s,m}})$	(4.23)

P. motor is the position motor and *S. motor* is the stiffness motor.

To control the position motor during torque/deflection characteristics measurements, a position feedback controller with a feedforward term with velocity as driver input was used (4.21). Here $K_{\text{p,ff}}$ is the feedforward term. The encoder position is read directly from the data acquisition card Sensoray 526 and transmitted to the IC PCM-3362 (integrated circuit). The position feedback loop is closed on the PCM-3362 IC. The PD regulator outputs the desired motor speed, which is transmitted directly to the motor driver via an analog signal ranging between ±10V. The same principle is also used to control the stiffness variation motor and its control block diagram is shown in Fig. 4.11. The position

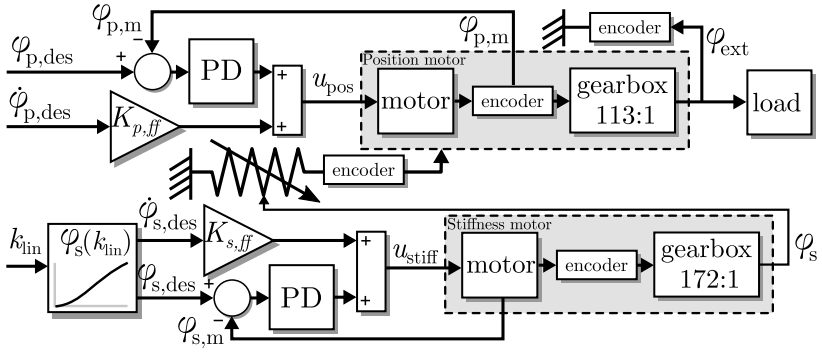


Figure 4.11: Position control block scheme. Block diagram of the position-based control for the position motor and for the stiffness variation motor. The position motor controller uses a PD regulator with a feedforward term. Both motor drivers accept speed as input.

motor controller does not account for the spring stiffness and is thus appropriate only for lower position motor speeds.

For the experiment on stiffness variation speed a torque control regulator from [40] and [94] with motor current as input to the motor driver was used. Due to the pseudo-linear behaviour of the proposed prototype, the same controller can be used as in [40] and [94]. In addition, the external link acceleration is used as feedback to take spring oscillations into account with an additional compensation term. In this case, $K_{\text{p,ff}}$ is the feed-forward term, J_{m} and $k_{\text{lin}}(\varphi_{\text{s,m}})$ represent the inertia and stiffness of the elastic element. Stiffness of

the elastic element is calculated based on the theoretical linear stiffness equivalent before the measurements, and replaced with an actual linear stiffness approximation after the experiments. K_f is the friction compensation term and K_b is the acceleration feedback term. During the experiment, the motor was commanded to maintain a certain torque while a rapid stiffness change command was given to the stiffness motor. The control block diagram is shown in Fig. 4.12.

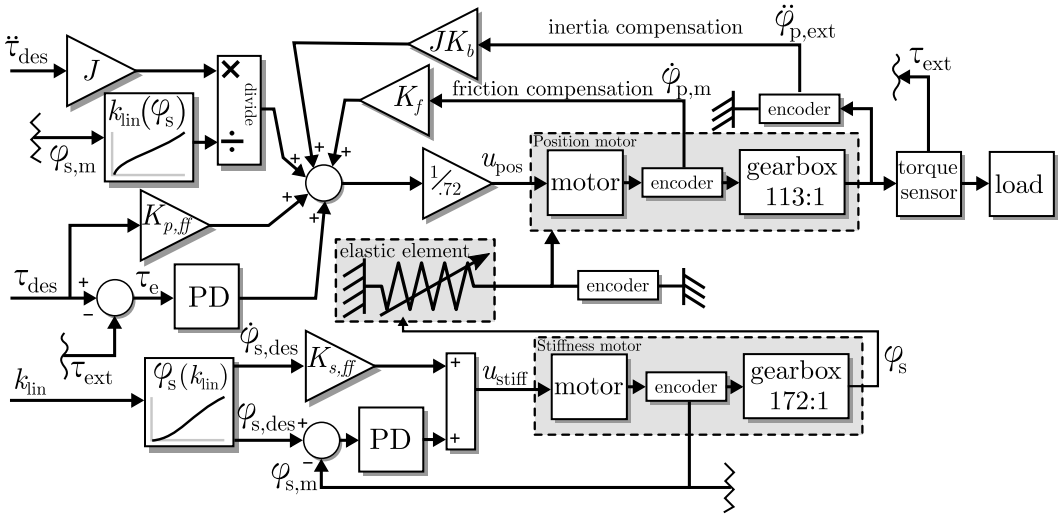


Figure 4.12: Torque control block scheme. Torque controller with feed-forward and compensation terms for the position motor. The stiffness variation motor employs a position-based controller with a feedforward term. The position motor driver accepts the motor current as input.

To control the position of the stiffness variation motor during both experiments, a simple position feedback regulator with a feedforward term (shown in Eq. (4.23)) was implemented, which uses the velocity as input to the motor driver. The stiffness variation motor regulators from Eq. (4.21) and Eq. (4.23) are the same. Here, $K_\mathrm{s,ff}$ is the feed forward term of the stiffness variation motor. More about the specific experiments is written in their respective result sections.

4.4.4 Results

4.4.4.1 Internal Mechanism Torque

The sensor redundancy was exploited to directly measure the torque/deflection characteristics of the internal mechanism and the torque required to maintain a given stiffness. For this particular measurement, the external link was fixed (see Fig. 4.9c), and the position motor performed motion using the position control. Since the external link is fixed, position motor movement directly compresses the internal mechanism, providing an easy way to rotate the deflection lever to a desired position.

The position motor was commanded to move slowly in one direction until either the current limit of the position motor (1.9A or approx. 15Nm) or the current limit of the stiffness motor (0.55A or approx. 4.3Nm), or the curved link deflection limit (predetermined angle $\varphi_d = 17^o$) was reached. The collected torque sensor data can now be compared with the movement of the curved lever to obtain the internal mechanical characteristics. Fig. 4.13a shows the results.

Note the moved origin phenomena in Fig. 4.13a. It is a consequence of the light preload,

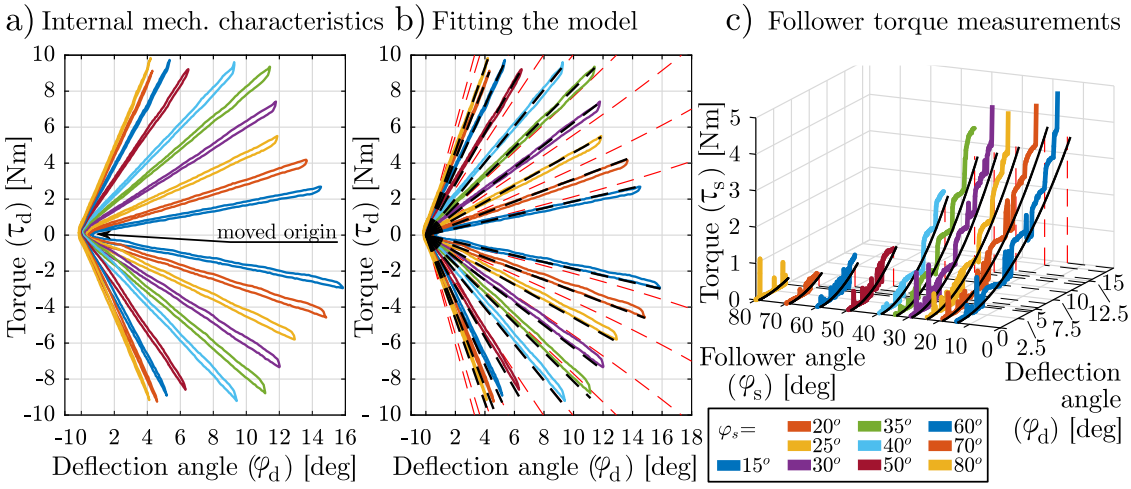


Figure 4.13: The measured relation between the torque and the deflection of the curved lever shown in **a** represents the internal mechanical properties for different follower angles. In **b** the theoretical model **dashed red** and a linear regression of the measurements **dashed black** are added to the initial measurements. The torque required to maintain a given stiffness, calculated on the basis of the motor current measurement, is in **c** compared to its theoretical model **(black line)**.

which prevents the cam follower from lifting and losing contact with the cam curve, since there is no load on the spring-loaded cam follower at zero deflection. In combination with the tensioning mechanism, this reduces the non-linearity effect of the steel cable in the external mechanism. As a result, however, the torque/deflection curves slightly miss the origin of the torque/deflection space in the internal mechanism. The slight preload should not be confused with preloadless stiffness variation [41, 97].

The data contain some discrepancies between the measurements and the pure mathematical model (see the red dotted lines in Fig. 4.13b). This is attributed to all the system nonlinearities that are also hard to model and are further elaborated in the discussion. In order to determine the actual linear properties of the internal mechanism, a linear regression is performed over the load phases of both directions. The results of the linear regression are shown in Fig. 4.13b in black dashed lines. The specific regression variance is shown later in Fig. 4.14c, where it is also compared to that of the mathematical model. The regression effectively establishes the relationship between the desired stiffness of the inner mechanism and the required cam follower angle to reach it.

The next important thing is the torque of the stiffness variation motor required to maintain the desired stiffness (see Fig. 4.13c). The torque of the stiffness motor nicely follows the mathematical model for different deflection angles. In this measurement, again, the experimental system is exploited and the motor current is used to approximate its torque. The current measurement and the fact that the motor is position-controlled can be attributed to different discrepancies seen between the theory and the actual measurements. Such effects, including bearing or gearbox nonlinearities, are not modelled and considered at this stage.

4.4.4.2 External Mechanism Torque

The main part of the external mechanism is the cable transmission, which allows a bidirectional application of the proposed VSA. To determine its characteristics, the torque sensor measurements are used in combination with the motion of the position motor. See Fig.

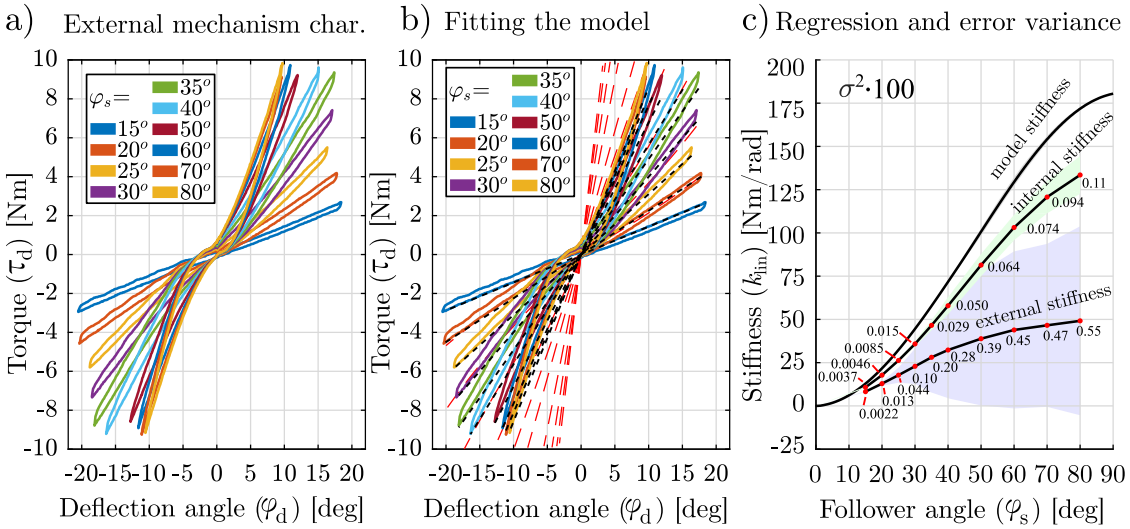


Figure 4.14: The torque required to deflect the VSA, i.e., the external mechanism, is represented in **a**. In **b**, the theoretical model **(red dashed lines)** and the linear regression lines **(black dashed lines)** are added to the measurements. The approximate resulting stiffness with respect to the cam follower angle is shown in **c** for different stages of the mechanism. These include the ideal theoretical relation, the internal mechanism and the external mechanism. The colored areas represent the linear regression error variance (scaled 100x).

4.14a for the results.

These measurements are influenced by the backlash of the position motor, the tension, the elastic deformation and bending of the steel cable, and the bearing friction. As can be seen in 4.14a, these effects culminate in a deflection torque that appears much less linear than the internal mechanism. One can also observe that the lines are not exactly symmetrical or centered again, especially at zero crossing. However, this depends on the calibration of the system. While the use of a cable transmission is generally quite simple, it increased the overall non-linearity of the system and its hysteresis. Such nonlinearities of cable transmission are common and also present in other types of VSAs using similar technologies [108].

A linear regression was performed to construct an approximated linear stiffness model of the external mechanism. It is shown in Fig. 4.14b in black dashed lines and the mathematical model in red dashed lines. The linear approximation still follows the measured data well. The collected results were used to construct a lookup table to be used for control and to transform the cam follower angle into the desired mechanical stiffness for the experiment in Section 4.4.4.3.

The error-variances of the linear regression are shown in Fig. 4.14c and allow the comparison of the linearity error between different stages of the mechanism. The stiffness of the mathematical model, the internal mechanism and the stiffness of the external mechanism are all marked on the diagram. It can be observed that the cable mechanism has reduced the stiffness range of the internal device from 0-130 Nm/rad to 0-49 Nm/rad as measured on the external mechanism. Similarly, one can observe in the error-variance that the linearity in the external mechanism is lower than in the internal mechanism. In the external mechanism, the regression error increases with higher stiffness or with higher loads.

4.4.4.3 Stiffness variation speed

An important feature is the efficient stiffness variation made possible by the preloadless mechanical principle. In the prototype, this feature is exploited for quick stiffness variation. However, it could also be utilised to use a smaller and lighter stiffness motor and thus reduce the overall weight of the device. For this experiment, a specific torque was commanded to the position motor using torque control as described in Table 4.3. Since the external link is fixed, the position motor torque loads the spring directly, simulating an external load. A step input is then commanded to the stiffness setup motor to achieve a stiffness change from 27Nm/rad to approximately 46Nm/rad. The results are shown in Fig. 4.15a for various external loads.

The cam follower angle used in earlier graphical representations is transformed here into its linear mechanism stiffness, which is approximated using the above linear regression results, i.e., the lookup table. The estimated stiffness is thus displayed on the left axis. The corresponding tracking angle is shown on the right axis. The change in stiffness was equally fast for all the cases, just below 0.15s. The external torque during a corresponding measurement is shown in Fig. 4.15b. The rapid follower rotation, i.e., the variation of the cam following angle, causes a disturbance of the external torque due to the inertia, mechanism's pressure angle and spring potential energy. However, the torque control of the position motor is capable of reducing this disturbance, as shown in Fig. 4.15b.

Fig. 4.15c shows the measured actuation current of the stiffness motor. The current of the stiffness motor is limited for reasons of hardware safety. The torque approximation is not precise and does not take into account the characteristics of the gearbox. A complex system for determining the exact torque would only slightly alter the torque limit. The limit is estimated at ∼5 Nm on the axis of the planetary gearbox, which is the specified nominal gearbox limit (see also Table 4.1).

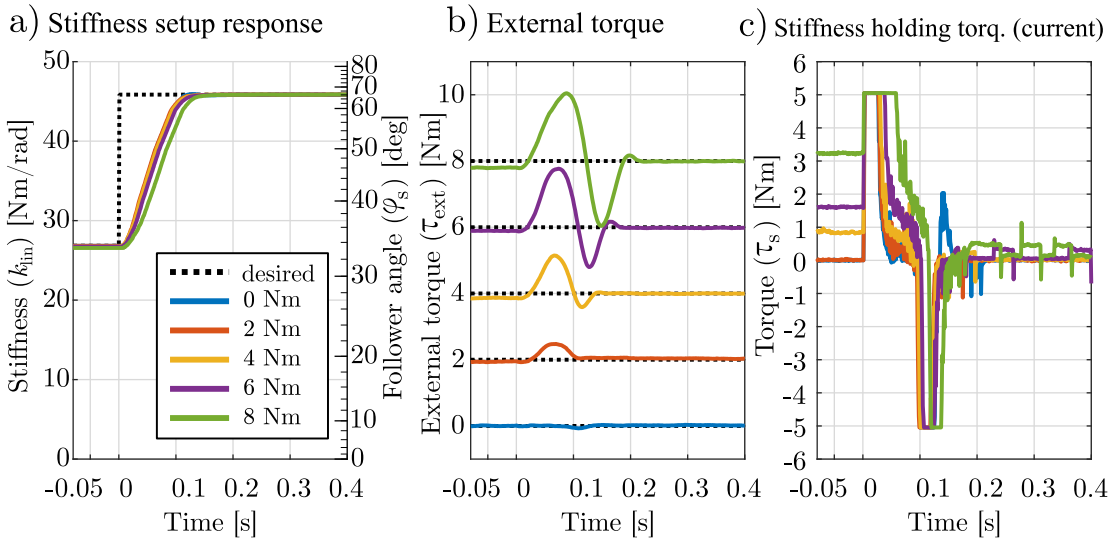


Figure 4.15: The stiffness variation response. The stiffness variation motor is commanded to perform a stiffness jump from 27 to 46 Nm/rad in **a** under various external loads. The equivalent follower angle is shown on the right axis. In **b** the corresponding external torque is displayed. The torque required to perform the jump on the velocity-based position-controlled motor is shown in **c**. The electric current of the motor is used to estimate its torque.

4.5 Discussion PLVL-VSA

4.5.1 Comparison to other VSAs

This section assesses the characteristics of the proposed actuator with respect to MACCEPA, FS-Joint and AwAS. These actuators have been selected for their frequent use in the literature. Their performance characteristics were collected from the literature in Table 4.4, their components in Table 4.5 and their geometric characteristics in Table 4.6. The reader should note that exact comparisons are difficult, if not impossible, due to the lack of available information and due to different actuator operation principles.

Table 4.4: Actuator comparison - part I - performance.

Actuator	Max. torque [Nm]	Spring used [N/mm]	Actuator stiffness [Nm/rad]	Max. elastic energy [J]	Defl. range [°]	Stiffness variation time [s]
MACCEPA [98, 105]	70	64.8	5-110	27.9	±60	2.6
FS-Joint [96, 110]	67	908	826	5.3	±15	0.33
AwAS [97]	80	80	30-1300	3.5	±14	4-6
PLVL-VSA	22.5	72.6	0*-49	3	±20	0.13

* Zero stiffness results in almost unobstructed external link movement inside the deflection range ±20°. It can be exploited for sensor calibration.

Also note that these actuators should be treated as research prototypes and are likely to be over-dimensioned, have redundant components, and may be designed for a specific application. For an accurate comparison, all these mechanisms would have to be constructed with the same motors and springs and then compared. Still, in Table 4.4, it can be observed that the FS-Joint implements a very stiff spring. Also, one can observe that the MACCEPA actuator has the largest deflection range and the ability to store the largest amount of elastic energy.

In Table 4.5, observe that the MACCEPA implements a more powerful stiffness vari-

Table 4.5: Actuator comparison - part II - components.

Actuator	Position motor **(power)**	Gearbox	Stiffness motor **(power)**	Gearbox
MACCEPA [98, 105]	Powermax 30 Maxon **(200W)**	(74x3.8):1 GP42C	Powermax 20 Maxon **(120W)**	(19x24):1 GP22HP
FS-Joint [96, 110]	Robodrive ILM 50x14 SP **(180W)**	80:1 HD CSD-25	Robodrive ILM 25x8 SP **(60W)**	1000:1 ?[a]
AwAS-I [97]	Emoteq, Inc., HT-02300 **(56W)**	50:1 HD[b]	Faulhaber, EN-1727C **(2.5W)**	(23x?[a]):1 Series 17/10
PLVL-VSA	Maxon DCX35L **(80W)**	113:1 GPX42 C	Maxon DCX22L **(20W)**	172:1 GPX26 C

[a] unknown/unspecified additional component
[b] unknown component, Harmonic Drive CSD-25-50-2A-GR is used

ation motor but still achieves a relatively slow stiffness variation (2.6s from 3% to 97% [105]). This is a direct consequence of the parallel stiffness variation mechanism. Observe also that the AwAS stiffness motor is the least powerful. Consequently, its stiffness variation is rather slow (4 - 6 s) but comparable to that of the MACCEPA. Using a perpendicular

way of stiffness variation, like in AwAS, enables a more efficient stiffness variation. Observe that the proposed prototype uses a low power motor and allows a very fast stiffness adaptation. However, this feature can also be used to reduce the stiffness motor torque and thus allow for a weaker motor.

In the last table, Table 4.6, the bare mechanism mass is introduced to reduce the

Table 4.6: Actuator comparison - part III - geometry.

Actuator	Mechanism dim. [cm]	Volume [cm^3]	Full mass [kg]	Position motor [kg]	Stiffness motor [kg]	Mechanism mass[d][kg]
MACCEPA [98, 105]	/	/	2.4	0.63	0.18+?[a]	1.6
FS-Joint [96, 110]	Ø9.5 x 12	851	1.4	0.39	0.25[c]	0.77
AwAS-I [97]	31 x 14 x 7	3038	1.8	0.79	0.07+?[a]	0.95
PLVL-VSA	12 x 11 x 4	528	1.9	0.85	0.20	0.85

[a] unknown/unspecified additional component
[c] unknown mass, Maxon motor planetary gearbox (GP32C) is used
[d] Mechanism mass = Full mass - Position motor - Stiffness motor

variability of mass data between the chosen mechanisms. It is calculated by subtraction of the combined mass of two motors with their gearboxes from the overall mass of the mechanism. However, the mass data are particularly difficult to compare and no explicit conclusions can be drawn in this respect. Note that AwAS has advantages, but you can see that its mechanism volume is quite high (see Table 4.6). Much space is taken up by the linear bearings rails, which must be sturdy enough to minimally deflect under load, and by the symmetrical spring arrangement, which also increases the overall size of the actuator. The PLVL-VSA perhaps most closely resembles the AwAS actuator. Contrary to the AwAS, it allows for a rotational-based stiffness variation. This replaces the long linear guides by rotary bearings and thus considerably reduces the overall size of the actuator.

The reader can see that a linear bearing is also used in the proposed PLVL-VSA design (see Fig. 4.7), but its role differs from that in AwAS because it does not have to carry the full spring load. It prevents the spring from moving tangentially or buckling and absorbs the tangential force caused by the pressure angle. In addition, only one compression spring is used, which further reduces the size and number of parts. As can be seen in Table 4.6, this results in a more compact actuator.

A cable transmission is then used to enable a bidirectional application and make the VSA-actuator fully functional. The actuator retains most of the advantages of the AwAS actuator, such as pseudolinear torque/deflection behavior and the variable-ratio lever stiffness variation principle. At higher deflections, a tangential force occurs which counteracts the stiffness of the motor movement, since the variation in stiffness is no longer entirely perpendicular. The same force is also shown in the AwAS actuator [97]. This can be avoided either by staying below a certain deflection, as with AwAS, or by staying above a certain stiffness, or by using a more powerful stiffness variation motor.

4.5.2 PLVL-VSA Analysis & Discussion

The proposed Pseudo-linear Variable-Lever Variable-Stiffness Actuator shows promising results, and a distinction to other relevant VSAs, namely the MACCEPA [107], the DLR FSJ [96] and the AwAS [97]. The presented results show that the internal mechanism

behaves as the model predicted. The full VSA includes the cable transmission, and its non-linearities pose some difficulties, if one desires accurate torque control combined with very accurate position control. However, this is a common feature of cable transmissions, bypassed through accurate models and frequent calibration [170]. For the proposed mechanism, the cable transmission is suitable for lower torques and lower stiffness settings. Fig. 4.14b,c shows that lower stiffness settings retain the (desired) linearity. In higher stiffness settings and higher torque loads, the nonlinearities and hysteresis increase.

The one-sided compression of the mechanism is problematic as it requires more components to arrive at a bidirectional mechanism. This can increase the size of the actuator. In the initial proof-of-concept prototype [63], this bidirectional mechanism was implemented with four gears and two deflection arms, making the mechanism bidirectional. Its curved lever required integrated gearing. Although the manufacture of such levers with 3D additive technologies is not difficult, the plastic material could only absorb low loads and led to relatively large elastic deformations, resulting in a large torque-hysteresis. Manufacturing the custom gears and geared levers from stronger materials would prove difficult. The cable solution is proved to be superior in this regard and the required components were easily manufactured out of aluminum. Overall, the cable transmission had no significant backlash in the bidirectional mechanism, although the planetary gearboxes of both motors had backlash. However, this backlash is specific to the motors and not to the compliant mechanism. Although friction and hysteresis were present, they appeared much more consistent than in previous proof-of-concept prototype in [63]. Their diagrams appear smooth and point to possible calibration and compensation with more precise mathematical models.

The cable transmission requires proper cable tension and minimal stretching of the cable. The latter can be accomplished by choosing a strong cable, which is thick and has a rigid strand configuration. However, since the pulley of the transmission is relatively small, choosing a thick, strong cable, increases its bending torque effect and consequently drastically increases the introduced nonlinearities. A 1.8 mm diameter stainless steel cable with a 7x7 strand geometry was used in the end. Some difficulties of the proposed case could be reduced by implementing pulleys of a larger diameter, if the application allows it. A contributing factor is also the friction in bearings. To reduce this effect, unsealed bearings were chosen with a larger safety factor or even double-row ball bearing types. This reduced the internal peak forces and therefore friction.

However, the current version and the proof-of-concept version from [63] have a common disadvantage, which needs to be considered. Namely, the slight discontinuity (nonlinearity) when crossing the zero deflection line. The discontinuity results from the no-load loading of the spring at zero deflection. Consequently, there is no force to push the cam roller and it can lift easily. The lift-off is possible due to the backlash resulting from the summation of the individual component tolerances, which leads either to a certain preload or a backlash of the cam roller. Theoretically a perfect contact within ideal tolerances is possible, but such a manufacture would be too expensive. To minimize or prevent this, a tuning mechanism has been implemented in the proof-of-concept prototype from [63] that allows a small manual movement of the spring to fine-tune and minimize the zero-cross discontinuity. The current version achieves this through a slight preload on the spring.

In the experimental evaluation, the torque sensor plays an important part. The actuator, however, is intended to function without it, since its removal can considerably decrease the cost of such a device. The presented implementation does have some drawbacks in that regard. The first stems from the cable non-linearities, which make the measurement of the compression at the external link not reliable at low torques. The second difficulty lies in the inability to infer the direction of the external load based on the elastic element compression measurement. The compression direction can be derived using other encoders. But, since

the external link encoder also measures the backlash in the position motor gearbox, smaller loads tend to oscillate around zero. This is why in the current case, the torque sensor is also used to determine the external load. However, with a more strategic placement of the position encoder sensor, a measurement devoid of position motor backlash could be achieved in future iterations.

The second common difficulty that still persists in the design of both mechanisms is the rising pressure angle. It is the main parameter that limits the usable range in the torque/deflection position motor space and torque space of the stiffness variation motor. The preferred working range depends on the capabilities of the position and stiffness variation motor and must be considered in the prototype design and control. For research purposes, this problem can be avoided by staying in stiffness settings above 15 Nm/rad. To reduce the device complexity, this was the option chosen during the experiments. However, to fully utilize the advantages of preloadless design, the first option is to sacrifice some stiffness variation speed and use a higher transmission ratio in the stiffness motor. Consequently, the torque/deflection area of the proposed mechanism, as marked in Fig. 4.4, would also increase. This can be achieved by implementing a worm gear transmission which would also make the stiffness setup mechanism non-backdrivable, meaning that no energy would be needed to hold a given stiffness.

Another way to keep the same motor and still achieve an increase of torque/deflection space is to exploit the external torque. One can use it to help the stiffness motor by an addition of a second spring connected between the curved lever and stiffness motor. This is theoretically explored in Section 4.7.

4.6 Elbow Exoskeleton

The proposed compliant actuator serves as a drive for an exoskeleton device. To this end, the PLVL-VSA actuator was mounted on an aluminium profile stand as seen in Fig. 4.16. A chair is positioned next to the exoskeleton, where the user can sit. A

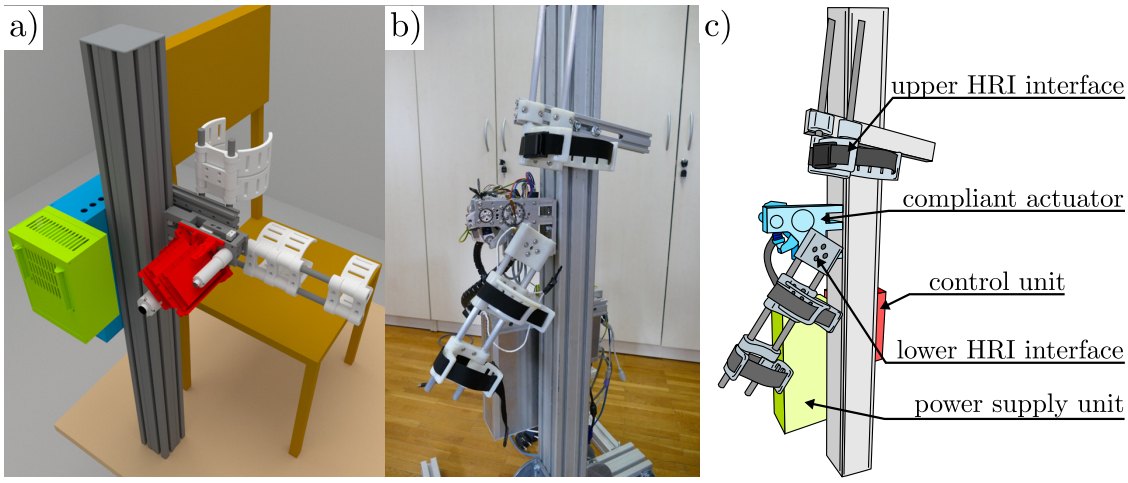


Figure 4.16: The modular exoskeleton system. The CAD model of the exoskeleton system is shown in **a**. A picture of the actual exoskeleton prototype in **b**. Image **c** shows a schematic representation of the exoskeleton where all its separate modules are marked.

human-robot interface (HRI), i.e., an exoskeleton frame, was designed and added to the compliant actuator. The frame is attached to the human arm by attachments which are a combination of rigid padding, i.e., hard straps, and normal belt straps, i.e., soft straps.

The rigid pads support and transmit torque or force from the exoskeleton frame to the user's arm, creating a rigid frame that can withstand high forces. On the other hand, the frame allows a certain mechanical flexibility, which is made possible by the rotation of the hard pads. This rotation allows the exoskeleton to adapt to different arm circumferences and also compensates for small misalignments between the exoskeleton joint axis and the human joint axis. The soft strap is routed through the hard strap and around the user's arm. In such a configuration, the pads allow some elastic movement of the human arm even when the arm is firmly strapped to the hard pads.

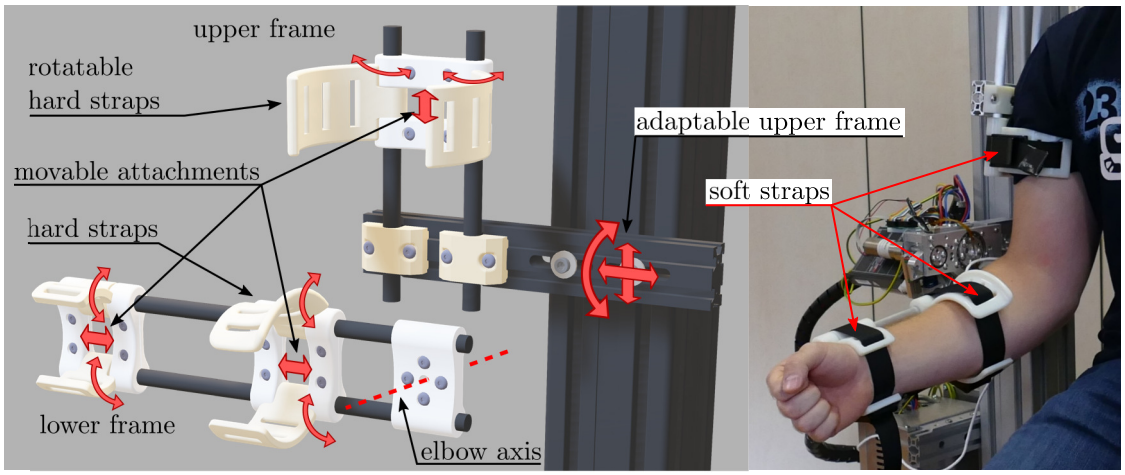


Figure 4.17: The elbow exoskeleton frame is split into the upper and lower exoskeleton frame. *Left* image shows the 3D rendered image. *Right* image shows the actual implementation.

The HRI allows manual movement of the attachments along the length of the forearm and upper arm to compensate for different arm lengths of the human user. This is possible due to a two-rod system, which holds and guides the rigid straps. The user can manually move the hard straps along the arm length to find the position, which is the most comfortable, functional and causes the least disturbance to the user's movement. The straps can then be blocked via screws at a certain translational position, which still allows their rotation around the axis of the respective aluminium rod. This adaptability through rotation of the hard pads and movement along the arm length makes the HRI adaptable to different geometries and, above all, reduces the number of iterations in the frame construction. Normally, a lot of effort and expensive equipment is required, like measuring and 3D scanning of the arm [171], that allows to find a comfortable configuration of the fastening straps for each user. These proposed features increase the comfort of the exoskeleton.

Fig. 4.17 shows the 3D rendered image and the actual implementation of the exoskeleton frame. The exoskeleton is split between the upper frame and the lower frame. The lower frame is attached directly to the actuator via a torque sensor, so that the axis of rotation of the actuator lies at the user's elbow joint. In the present frame configuration, the lower frame does not allow for pronation and supination of the forearm. The actuator combined with the lower frame can be moved up and down the aluminium stand until a suitable height is found. The upper frame can be manually moved in the elbow joint plane, rotated and then fixed to comfortably support the user's upper arm.

4.7 PLVL-VSA Modification & Parameter Optimization

The design values for the PLVL-VS actuator were determined empirically. The PLVL-VSA elbow exoskeleton targeted a torque of about 20Nm, which is sufficient for an elbow exoskeleton rehabilitation [172]. The stiffness range was determined to be in the range of 50 Nm/rad. An important feature of the PLVL-VSA is the mechanism's high stiffness variation efficiency. A drawback of the proposed design is the efficiency decrease at higher mechanism deflections. It is a drawback, because it limits the useful torque/deflection workspace of the mechanism.

This section proposes a modification, which reduces the stiffness variation torque and thus preserves stiffness variation efficiency even at higher mechanism deflections. It is the development continuation of the PLVL stiffness-variation principle. It also introduces an optimization method, which optimizes the torque/deflection space of the actuator and is a useful tool to achieve the desired deflection range given the properties of the position and stiffness variation motors. The bidirectional mechanism is not directly related to the efficiency of the variable stiffness mechanism in question and is omitted in this continuation. A real prototype was not built, however, it was extensively theoretically evaluated.

The section is organized as follows. Section 4.7.1 presents and establishes regions of the actuator torque/deflection space, which can be later optimized. The proposed mechanical modification is explained in Section 4.7.2. Section 4.7.3 presents the optimization method and process. The analysis of the results is performed in Section 4.7.4.

4.7.1 Torque/Deflection Space

The graph in Fig. 4.18 shows the amount of torque needed to compress the mechanism at different follower angles. The graphs are made with Eq. (4.16) and Eq. (4.19) from Section 4.2. The main advantage of the PLVL mechanism is the perpendicular stiffness variation

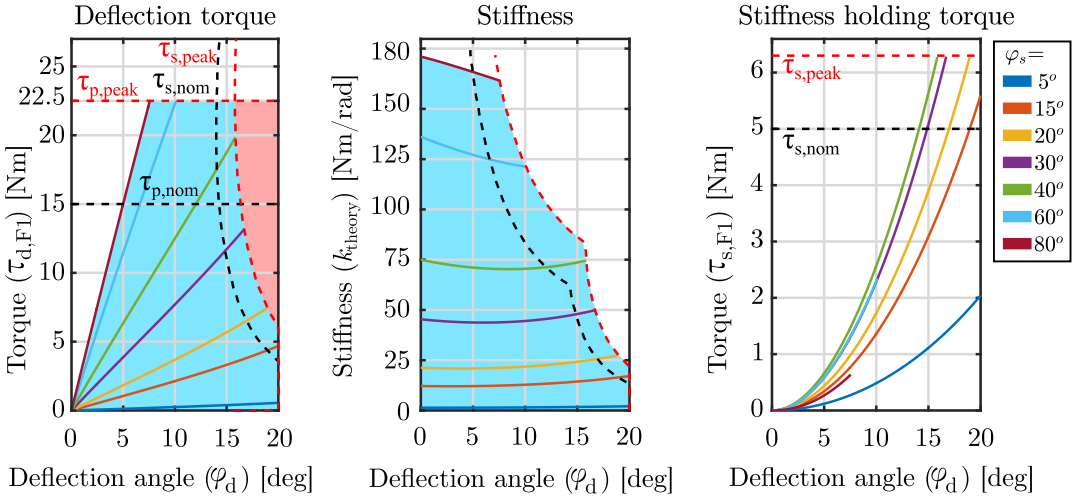


Figure 4.18: Torque-deflection characteristic shown in the *left* graph. The *middle* graph shows the corresponding derivative, i.e., the stiffness. The torque required to hold the follower at an angle is shown *right*. The BLUE region represents the below peak operation space of both motors. On the other hand, the RED region represents the area with the stiffness holding motor torques above its peak torque limit. The solid lines correspond to different follower angles as seen in the legend. The black and red dashed lines represent the nominal and peak torques of the position and stiffness varying motor gearboxes.

principle, because it results in a very energy-efficient stiffness variation. Consequently, most of the stiffness varying motor energy is used to vary the stiffness. In contrast, if the stiffness is varied in parallel with the elastic element, some energy is needed to overcome the spring pretension, as described in [104]. Thus, a stronger and therefore also a bigger motor is needed to achieve the same stiffness variation speed. An efficient stiffness variation not only saves electric energy, but also reduces overall weight, since the stiffness variation motor can be smaller. However, the stiffness variation efficiency changes through the deflection of the mechanism or through its stiffness variation φ_s.

The parameters used to construct the graphs are gathered in Table 4.7. The red

Table 4.7: Calculation parameters.

Variable	Name	Value	Unit
R_s	Cam parameter 1	50	[mm]
R_b	Cam parameter 2	0	[mm]
$k_{int,F1}$ [a]	Linear spring stiffness	72.6	[N/mm]
φ_d	Deflection angle range	$\pm$ 20	[^{o}]
φ_s	Stiff. follower angle	0 - 90	[^{o}]
P_s	Stiff. varying mot. power	20	[W]
$\tau_{s,nom}, \tau_{s,peak}$ [b]	Stiff. varying mot. limits	5, 6.3	[Nm]
P_p	Position motor power	80	[W]
$\tau_{p,nom}, \tau_{p,peak}$ [b]	Position motor limits	15, 22.5	[Nm]

[a] **F1** subscript serves to distinguish the original operation principle from the new proposed modifications, noted with a subscript **F2**.
[b] The values p,nom; p,peak; s,nom; and s,peak stand for position nominal, position peak, stiffness nominal and stiffness peak, respectively.

dashed and black dashed lines represent the limits and boundaries between the nominal and peak/maximum torque of the actuator motors. For practical reasons, they are calculated numerically. The numerical calculation is performed for 4.16 and 4.19 by increasing the φ_s for a small amount and then trimming the line with the torque limits of the respective motor gearboxes. The last untrimmed points of each torque/deflection curve are gathered and used to draw the respective dashed line. If motor/gearbox torque limits are used, which can be found in Table 4.7, the torque/deflection space (Fig. 4.18) is divided into several distinctly coloured areas.

In the BLUE area, both motors operate below their specified peak torques. The RED area occurs when the torque limit of the stiffness variation motor is mapped to the torque/deflection workspace. In the RED area, the torque requirements exceed the maximum torque capabilities of the stiffness variation motor. The position motor can be driven back above its maximum torque, which creates the WHITE area above the BLUE area and also makes it theoretically inaccessible.

Again, since the torque lines are nearly linear, i.e., pseudo-linear, they can be described by a linear approximation with sufficient accuracy. The behavior of the mechanism at each follower angle can therefore be sufficiently described with one parameter only, namely the equivalent linear stiffness. This property is regarded as an important advantage for our task, because it allows a simple comparison between possible modifications by using the equivalent stiffness as a base.

If the curved arm deviates from the equilibrium position, a tangential force results from the increasing pressure angle of the curve mechanism (F_{din}), seen in Eq. (4.18). The stiffness variation motor must overcome this force/moment to vary the stiffness. The increase in this force decreases the efficiency of the stiffness variation. At higher deflection

angles and lower follower angles, this force and problem becomes even clearer. We also refer to this problem as increasing follower torque, i.e., stiffness holding torque at lower follower angles and larger deflections, as it is directly linked to the torque required by the stiffness variation motor. The torque required to maintain the stiffness at some follower angles is shown in Fig. 4.18*right*. Observe that it rises almost exponentially as the deflection increases.

The same phenomenon of tangential force that reduces the efficiency of stiffness variation is also described in [173]. To reduce its effect, the authors limit the deflection of the mechanism to about ±15 degrees, where the follower torque is lower, to effectively reduce the tangential force.

The RED area, as shown in Fig. 4.18, appears because the stiffness motor has limited torque capabilities. Two things can happen when the actuator falls into this area where the torques are higher than the maximum gear torques of the stiffness variation motor. In the first case, the stiffness variation motor maintains its position due to the additional friction in its planetary gear (gear max. efficiency 75%), but does not move on command. The second case is when the follower torque is so high that the motor is driven back to a lower stiffness position. The deflection of the mechanism then reaches its maximum because the external torque remains unchanged and the stiffness decreased. Consequently the tangential force increase pushes the follower to the lowest position, and the mechanism cannot recover to its previous state until the external torque is present. This is considered worse than in the first case.

There are several ways to avoid this situation. It could be prevented by using a gear unit which cannot be driven backwards, e.g., a worm gear. However, due to the exponential torque increase, the maximum torque required is very high. A suitable worm gear would be large and would not improve the efficiency of the system. Another solution would be to use a ballscrew as a linear motor, which in its size is more tolerable to high forces and also has a higher mechanical efficiency. The required peaks are then provided by the motor, which can operate in its short-time range to provide the required peak torques. When using a planetary gearbox, the system is quite intolerable to high and fast intermittent peak torques, especially when the planetary gearbox is small. Another alternative is to use a more powerful stiffness variation motor, but this contradicts the original goals, since a larger motor increases the weight and price of the device.

While the above solutions would improve the functionality of the device, the energy efficiency of the stiffness variation would remain unchanged. Therefore, a modification is proposed using a second elastic element, which provides helping torque to the follower from the external deflection. Using it in this way, the same motor can remain and the torque requirements decrease. This modification is explored in the modified PLVL-VSA.

4.7.2 Proposed Modification & a New Mathematical Model

As seen in Fig. 4.19a, the prototype is dimensioned by two cam curve parameters (R_s and R_b), the same as in Section 4.4. One addition to the equations of the modified PLVL-VSA to the equations of the normal PLVL-VSA is in an added subscript F1 to represent them as normal PLVL mechanism equations. For example, parameter k_int of the original mechanism now becomes $k_\mathrm{int,F1}$, as seen in Fig. 4.19. The same is done for all other relevant parameters which remained the same between both mechanism instances. In the same way as using subscript F1, subscript F2 represents the effect of the second spring, i.e., the modification of the PLVL-VSA mechanism. The combined effect is then marked with subscript F1,F2.

The proposed modification is shown in Fig. 4.19b. The original mechanism is extended by the linear spring ($k_\mathrm{int,F2}$), which is connected to the follower at a distance of L_1. The

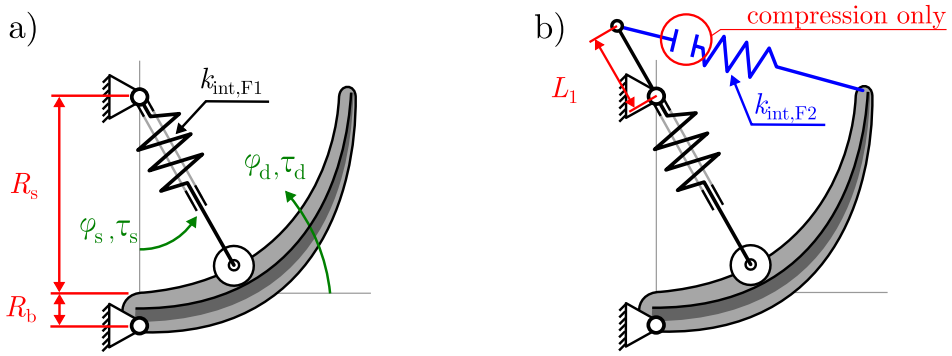


Figure 4.19: Flat view of the original mechanism with the essential parameters describing it in **a** and the modified one in **b**.

$k_{\text{int,F2}}$ and L_1 parameters are later selected for optimal performance. Deflection range of $\pm 20^o$ and a follower angle range of $0^o - 90^o$ is used in the analysis of the proposed prototype. The mathematical model data are taken over from normal PLVL-VSA, from Section 4.2. The data correspond to an actual physical prototype construction for testing of the PLVL variable stiffness mechanism. In the same way, the data from real motors and their nominal/peak gearbox is collected. All parameters used in this part are summarized in Table 4.7.

This second spring is attached at one end to the curved arm and connected at the other end to the follower via a free connection. This means that the spring can be compressed but not stretched. The stretching is prevented by the spring lift-off. This means that no negative deflection torque can occur when the follower rotates. This is also clearly marked in 4.19b as *compression only*. The second spring thus provides the torque required to compensate for the change in follower torque directly from the external deflection of the mechanism. The required follower torque is higher at lower follower angles, where the deflection of the mechanism is higher. In contrast, the follower torque is lower at higher follower angle setups and low deflections of the mechanism.

The analytical model of the original torque/deflection characteristic was derived in Section 4.2. This section evaluates, in theory, the potential benefits that the proposed modification would have on the existing actuator prototype. Therefore, in the modified model, the same parameters are used that were also used for the construction of the physical prototype PLVL-VSA. Because its mathematical model reliably described the actual properties of the actuator, and since the modification would require a partial redesign of the existing prototype, the modified version was analysed in theory and a real prototype was not designed and built.

The main relations are torque $\tau_{\text{d,F1}}(\varphi_{\text{d}}, \varphi_{\text{s}}, R_{\text{s}}, R_{\text{b}})$ Eq. (4.16) and the torque required to maintain a certain stiffness $\tau_{\text{s,F1}}(\varphi_{\text{d}}, \varphi_{\text{s}}, R_{\text{s}}, R_{\text{b}})$ Eq. (4.19). Both are dependent on the state variables φ_{d} and φ_{s}, and construction parameters R_{s} and R_{b}. For greater readability, the construction parameters R_{s} and R_{b} are henceforth omitted. The deflection torque and the follower torque contribution of the modification are thus written as $\tau_{\text{d,F2}}(\varphi_{\text{d}}, \varphi_{\text{s}})$ and $\tau_{\text{s,F2}}(\varphi_{\text{d}}, \varphi_{\text{s}})$. The combined effect or the superposition of both is then written with an index (F1, F2), or more precisely as $\tau_{\text{d,F1,F2}}(\varphi_{\text{d}}, \varphi_{\text{s}})$ and $\tau_{\text{s,F1,F2}}(\varphi_{\text{d}}, \varphi_{\text{s}})$.

Figure 4.20 shows a flat view of the mechanism with marked vectors and parameters that are helpful in deriving the mathematical model of the modified design. Vector $\vec{r}_{01}$ or the coordinates (x_1, y_1) are attached at the tip of the arc lever. Their value is calculated

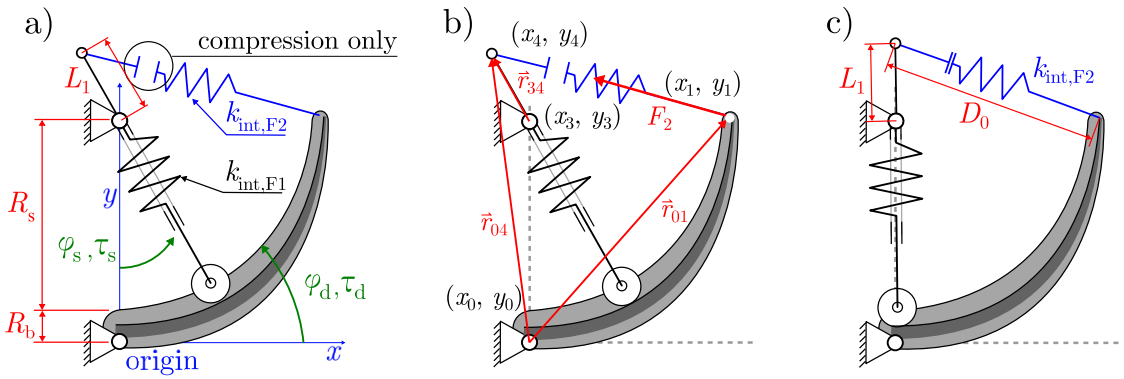


Figure 4.20: Flat view of the mechanism with parameters in **a** and model vectors for the calculation of $\tau_{\text{d,F2}}$ and $\tau_{\text{s,F2}}$ in **b**. The unloaded spring F2 is shown in **c**.

using Equations 4.3, 4.4 and 4.5 to get the (x, y) coordinates as follows:

$$x_{\text{temp}} = x(\varphi_d = 0,\ \varphi_s = 90^o,\ R_s = 50\text{mm},\ R_b = 0), \tag{4.24}$$
$$y_{\text{temp}} = y(\varphi_d = 0,\ \varphi_s = 90^o,\ R_s = 50\text{mm},\ R_b = 0). \tag{4.25}$$

The follower angle at that point is 90^o. The attachment point $(x_{\text{temp}}, y_{\text{temp}})$ rotates around the origin when the mechanism deflects and moves to:

$$x_1 = x_{\text{temp}} \cos(\varphi_d) - y_{\text{temp}} \sin(\varphi_d), \tag{4.26}$$
$$y_1 = y_{\text{temp}} \cos(\varphi_d) + x_{\text{temp}} \sin(\varphi_d). \tag{4.27}$$

This connecting point is essentially rigidly connected to the end of the cam lever and rotates with it. Vector $\vec{r}_{04}$ or coordinate (x_4, y_4) is calculated as:

$$x_4 = L_1 \cos(\pi/2 + \varphi_s), \tag{4.28}$$
$$y_4 = L_1 \sin(\pi/2 + \varphi_s) + R_s + R_b. \tag{4.29}$$

Point (x_4, y_4) rotates with the follower when the φ_s changes. It is assumed that the spring is unloaded at the follower angle of 0^o, and has a base length of D_0, as seen in Fig. 4.20c. Before calculating the spring force, the distance between coordinates (x_1, y_1) and (x_4, y_4) must be calculated. Let us define it as:

$$D_{14} = d((x_1, y_1), (x_4, y_4)). \tag{4.30}$$

D_0 is calculated in the same way:

$$D_0 = d((x_1, y_1), (x_4, y_4)), \tag{4.31}$$

however, in this case $\varphi_s = 0$ and $\varphi_d = 0$, as seen in 4.20c. With the current setup, the spring is not extended when the follower rotates, but lifts off. Therefore the size of the magnitude of the spring force is calculated as:

$$\text{F2} = \begin{cases} k_{\text{int,F2}}(D_0 - D_{14}) & \text{if } D_{14} < D_0, \\ 0 & \text{if } D_{14} \geq D_0, \end{cases} \tag{4.32}$$

representing the cases of compression and the corresponding force and the case of lift-off with a zero force. The direction of the vector $\vec{F}_2$ is then determined by the base vectors $\vec{r}_{04}$ and $\vec{r}_{01}$. The additional deflection torque due to the modification F2 is calculated as:

$$\vec{\tau}_{\text{d,F2}} = \vec{r}_{01} \times \vec{F}_2. \tag{4.33}$$

The third dimension is then the scalar value $\tau_{\mathrm{d,F2}}$. The contribution or reduction of the stiffness holding torque (follower torque) by modification F2 is calculated as:

$$\vec{\tau}_{\mathrm{s,F2}} = \vec{r}_{34} \times \vec{F}_2. \tag{4.34}$$

The third dimension is again the scalar value $\tau_{\mathrm{s,F2}}$. Vector $\vec{r}_{34}$ is calculated as:

$$x_{34} = L_1 \cos(\pi/2 + \varphi_{\mathrm{s}}), \tag{4.35}$$
$$y_{34} = L_1 \sin(\pi/2 + \varphi_{\mathrm{s}}). \tag{4.36}$$

The exact stiffness of the mechanism ($k_{\mathrm{theo,i}}$) is calculated in all cases via a derivative between the deflection torque and the deflection angle:

$$k_{\mathrm{theo,i}} = \frac{\mathrm{d}\tau_{\mathrm{d,i}}}{\mathrm{d}\varphi_d}, \quad \text{where } i \in \{\text{(F1), (F2), (F1,F2)}\}. \tag{4.37}$$

The summation of the contributions of both cases is straightforward both for the deflection torque ($\tau_{\mathrm{d,F1,F2}}$) and for the follower torque ($\tau_{\mathrm{s,F1,F2}}$):

$$\tau_{\mathrm{d,F1,F2}} = \tau_{\mathrm{d,F1}} + \tau_{\mathrm{d,F2}}, \tag{4.38}$$
$$\tau_{\mathrm{s,F1,F2}} = \tau_{\mathrm{s,F1}} + \tau_{\mathrm{s,F2}}. \tag{4.39}$$

4.7.3 Parameter Optimization

4.7.3.1 Optimization Goal & Cost Function

The optimization goal can be easily explained by the torque/deflection space of the drive shown in Fig. 4.21*left*. The ideal mechanism would have a stiffness in the range from 0 Nm/rad to infinity. In such a case it would fill the entire torque/deflection space. Due to mechanical and power limitations, the torque/deflection space is not completely filled and is divided into three areas (BLUE, RED and WHITE). The same areas are also briefly mentioned in Section 4.7.1. The goal of the optimization is to find a combination of L_1 and $k_{\mathrm{int,F2}}$ that reduces the RED region while keeping the BLUE functional region as large as possible. Note that the modification makes the WHITE region appear also below the torque/deflection lines and increases as the L_1 and $k_{\mathrm{int,F2}}$ values increase. In short, the BLUE area represents the normal operating area of the mechanism. The RED region represents the area in which the torque of the variable stiffness motor exceeds the limits of the transmission and in which the variable stiffness mechanism loses some of its functionality. The WHITE area represents the inaccessible area, either due to the backdrivability of the position motor or the addition of the spring, as shown later.

The maximum torque of the mechanism is limited by the maximum torque of the position motor gearbox (set at 22.5Nm). Parameters $\tau_{\mathrm{p,nom}}$, $\tau_{\mathrm{p,peak}}$, $\tau_{\mathrm{s,nom}}$ and $\tau_{\mathrm{s,peak}}$ represent the limits of the position motor and stiffness varying motor gearboxes. Their values can be found in Table 4.7. These parameters limit the torque/deflection space of the actuator. To calculate the boundary lines, torque/deflection lines and stiffness variation motor torques are calculated for a sufficiently small set of discrete follower angles. Each line is then numerically trimmed by the torque limits of both the position motor and the stiffness variation motor. The final lines, representing the boundaries, are then drawn as dashed in Fig. 4.21. The stiffness motor torque is then non-linearly transformed into the torque/deflection space, again by numerical means.

Since the operating principle of the mechanism is not completely perpendicular, the stiffness varying motor requires a certain torque to maintain its position. The RED area indicates where the torque required to maintain the desired stiffness exceeds the maximum

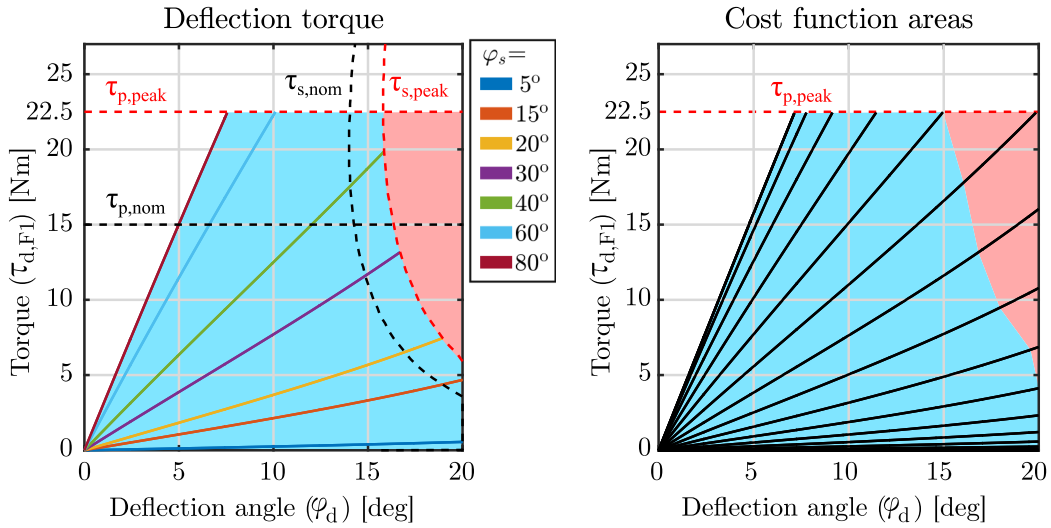


Figure 4.21: Theoretical torque/deflection space (*left*) and a low resolution numerical representation (*right*).

allowable torque of the stiffness varying motor gearbox. The WHITE areas are theoretically inaccessible and are therefore ignored.

The COST function is calculated as the difference between the size of the BLUE area and the size of the RED area as:

$$COST = A_{\mathrm{BLUE}} - n \cdot A_{\mathrm{RED}}, \tag{4.40}$$

In short, the larger the BLUE area compared to the ideal case, the better the COST. This way, increasing the BLUE area brings us closer to the ideal mechanism. Reducing the RED area reduces the peak torques of the stiffness variation motor. The cost function is indirectly influenced by the stiffness range, the amount of stored energy (area below the torque/deflection curves) and the stiffness variation torque. The first two should be maximized and the last one minimized. The working area is then limited by the torque limits of the gearboxes of the two motors used.

The ideal actuator would fill the entire working space and is limited by the maximum torque of 22.5Nm and the maximum deflection of 20°. This would mean that the mechanism would have a stiffness range from 0 Nm/rad to infinity, and would not be limited by the torque of the stiffness motor. Therefore, this size of the ideal case, multiplication of maximum torque and maximum deflection, is used to normalize the calculated ranges.

To calculate the surface, one can exploit the fact that the torque/deflection curve can be calculated at a certain follower angle. By using a small step for the follower angle, two neighbouring lines can be found. To calculate either the BLUE or the RED area, simply add the areas between these neighbouring torque/deflection lines. All lines are always trimmed with the gearbox limits.

For each discrete parameter set of $k_{\mathrm{int,F2}}$ and L_1, the theoretical model is used to calculate the torque/deflection lines within the nominal/peak torque limits. The BLUE and RED area sizes are then calculated as explained. The area values are then collected in a matrix and can be viewed in Fig. 4.22 as an area plot, where A_{BLUE} and A_{RED} represent the normalized BLUE and RED surface size, respectively. The values are normalized to the full area of:

$$A_{\max} = \max(\varphi_{\mathrm{d}}) \times \tau_{\mathrm{p,peak}}. \tag{4.41}$$

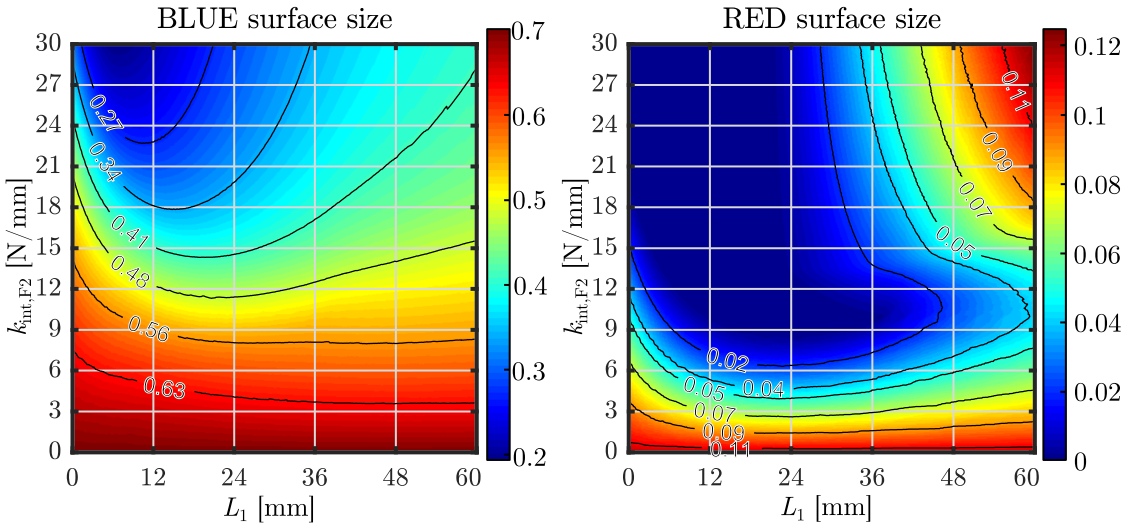


Figure 4.22: BLUE (left) and RED (right) area sizes for different $k_{\text{int,F2}}$ and L_1 parameter combinations.

The maximum values are $\max(\varphi_{\text{d}}) = 20^o$ and $T_{\text{p,peak}} = 22.5\text{Nm}$. The surface is then essentially compared to the ideal actuator, where the $COST$ value would be 1.

The proposed method to find the optimal combination of the parameters $k_{\text{int,F2}}$ and L_1 is essentially a brute force search through all discrete step combinations. Although other, more sophisticated optimization algorithms could also be used, in this case it is more valuable to take more time and search through the whole area to also visualize it later. Moreover, since only 2 parameters are optimized, brute force optimization is not computationally intensive. The search is performed for $L_1 = 0 - 60mm$ and $k_{\text{int,F2}} = 0 - 30N/mm$ in dense, discrete steps. The ranges have been determined empirically and since the purpose of this work is the extension of an existing VSA actuator, the parameter limits are defined in such a way that they are physically feasible.

With parameter n, the importance of both areas is weighted. Increasing n increases the influence of the RED area size in the cost value. The final n value is left to the designer. Consequently, the optimal solution is to move to larger $k_{\text{int,F2}}$ and L_1, as shown in Fig. 4.23. Empirical observations show that since the stiffness motor torque lines are mapped non-linearly into the torque deflection space, an endless increase in the n value does not improve the cost function endlessly, but begins to decrease it slowly. The final n value should be kept smaller rather than larger.

4.7.3.2 Cost Function Evaluation

Three n values are chosen arbitrarily, namely 1, 1.5 and 2. In Fig. 4.23, the cost function is calculated for these three different n values. In Fig. 4.23 the optimal value for all three cases is marked with a red circle. The peak values are 0.591 ($L_1 = 14.1$, $k_{\text{int,F2}} = 2.9$), 0.568 (16.6, 6.3) and 0.558 (17.0, 6.8), for $n = 1$, 1.5 and 2, respectively. The three peaks move with the change of n, meaning that the optimal combination of parameters also changes. The effect of the value n on the workspace is shown in Fig. 4.24. As seen in Fig. 4.24, the addition of a second spring actually reduces the size of the RED area, i.e., the state in which the torque required to maintain a certain stiffness exceeds the peak torque of the stiffness varying motor gearbox. However, this also affects the overall size of the BLUE area and therefore influences the stiffness of the actuator. The final value of parameter n

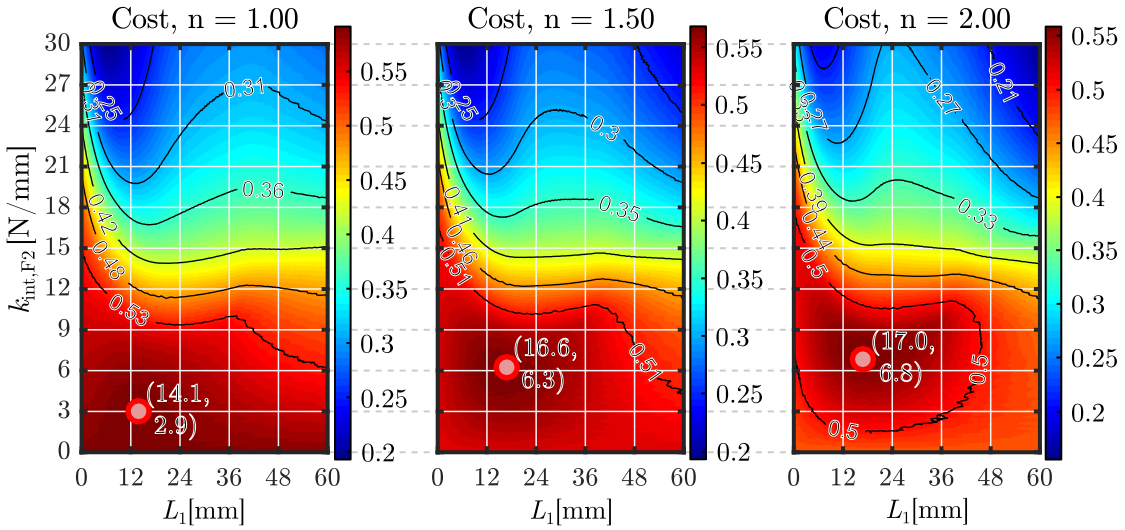


Figure 4.23: Parameter combinations and results. The cost at different $k_{\mathrm{int,F2}}$ and L_1 parameter combinations for different n values.

is left to the designer. In this case, $n = 1.5$ was chosen arbitrarily. The optimal values for $k_{\mathrm{int,F2}}$ and L_1 are therefore 6.3 N/mm and 16.6 mm, respectively. The choice of n is justified because the RED area is completely above the nominal torque limit of the position motor ($\tau_{\mathrm{p,nom}}$) of 15 Nm.

4.7.3.3 Linear Stiffness Approximation

Before proceeding with the comparison between the original and the modified mechanism, the concept of pseudolinearity needs to be revisited. The linear approximation is important in this case because it provides a baseline for the comparison between the two mechanisms. In the normal PLVL-VSA from Section 4.4, the pseudolinear property is exploited to replace the slightly curved torque/deflection curves with their respective linear approximations. Thus, each follower angle now represents a linear approximation of the stiffness. It is assumed that a linear approximation of the stiffness curves sufficiently describes the behavior of the mechanism. As a result, both the dimensionality and the complexity of the model are reduced. This not only simplifies the analysis, but also opens up equal conditions for the comparison between the original and the modified mechanism.

The torque/deflection workspace of the modified mechanism is shown in Fig. 4.25. As can be seen, the modified mechanism also exhibits pseudo-linearity, which is later exploited to represent the stiffness of the mechanism through its linear approximation. The linear approximation of each torque/deflection curve at discrete follower angle steps is calculated with a linear regression and the assumption that the lines start at the origin. The linear stiffness approximation can be easily calculated by taking the mean value of the exact mechanism stiffness, numerically calculated from deflection torque of the mechanism.

$$\vec{k}_{\mathrm{appr,F2}} = \mathrm{mean}(K_{\mathrm{F2}}(\vec{\varphi}_{\mathrm{d}},\, \vec{\varphi}_{\mathrm{s}} = j,\, R_{\mathrm{s}} = 0,\, R_{\mathrm{b}} = 50\mathrm{mm})), \tag{4.42}$$

where $\vec{\varphi}_{\mathrm{s}} = j$ is the vector containing the discrete values for follower angles.

The linear approximation of the modified mechanism can be seen in 4.26*left* for a few follower angles. The average value is only calculated in the BLUE area, where the torques of both motors are below the peak limits. The values above the peak limits are ignored. The same procedure is also used in the previous version from Section 4.4. A disadvantage

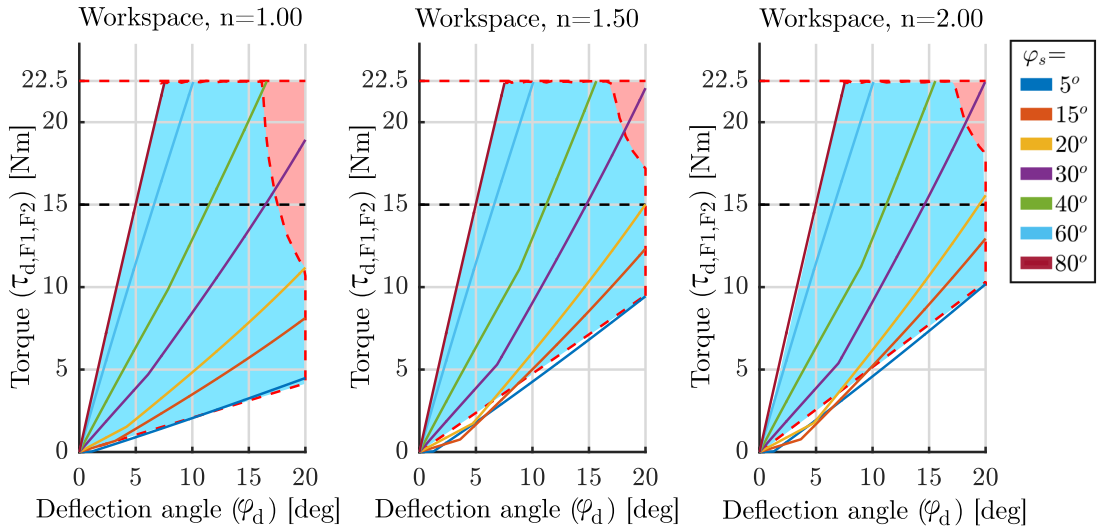


Figure 4.24: Torque/deflection working space change for different values of n.

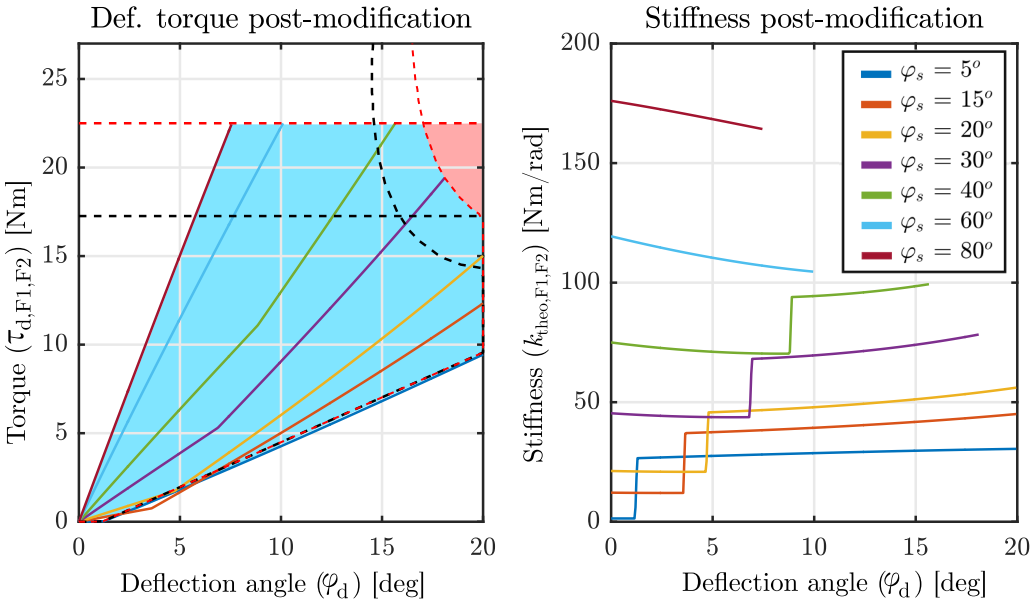


Figure 4.25: The torque-deflection graph of the modified mechanism (*left*) and its corresponding stiffness (*right*).

of the proposed modification is a discrete non-linearity, which occurs when the deflection arm comes into contact with the additional spring. This discrete action is captured in Eq. (4.32).

This also affects the stiffness of the mechanism and creates a non-linear jump. This is a disadvantage and a side effect of the proposed modification. In Fig. 4.27*right* the discrete step in the stiffness of the mechanism can be observed. However, as can be seen later in the more detailed analysis, the modification has other advantages.

By acquiring linear approximations of the stiffness for different follower angles, the relation between the follower angle and the stiffness of the resulting mechanism can be calculated. This is essentially done for case $F1$ as $\vec{k}_{\text{appr,F1}}$ and case $F1, F2$ as $\vec{k}_{\text{appr,F1,F2}}$. Two relations are created, one for the original mechanism and one for the modified mechanism.

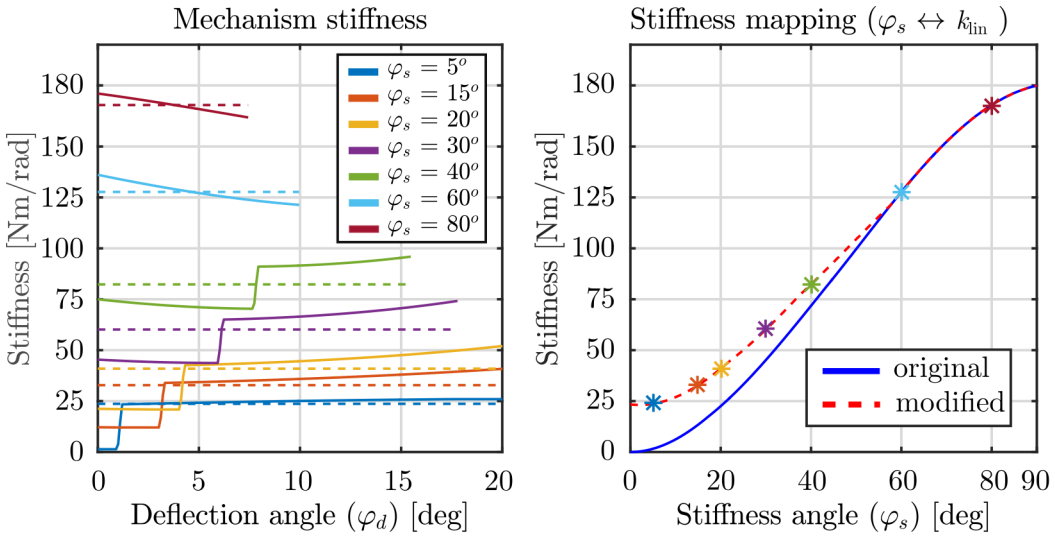


Figure 4.26: The linear approximation of the modified mechanism (*left*) and the stiffness map between both cases (*right*).

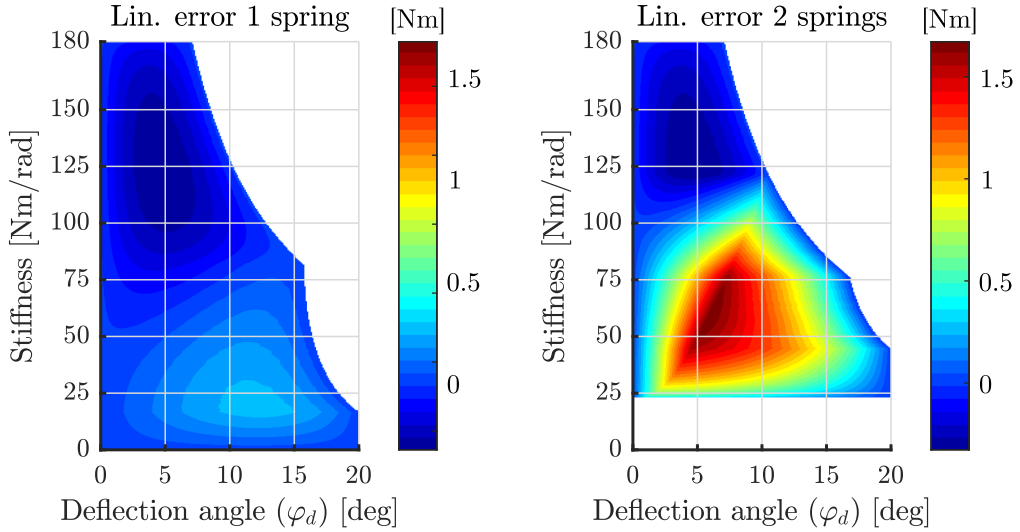


Figure 4.27: Difference between the actual stiffness and the linear approximation for pre- (*left*) and post- (*right*) modification.

The relations for both cases are shown in Fig. 4.26*right*.

One can clearly see that the stiffness of the modified mechanism is now different when using the follower angle as a baseline. Some of the lower stiffness levels are now inaccessible and the overall stiffness range has changed. The effect of the modification is stronger at lower stiffness levels. At higher stiffness levels, due to the rotation of the follower, there is no support from the second spring, as originally expected.

The mechanisms can be compared on the same ground by using the approximate values of linear stiffness rather than angles of the follower. The linearity error, i.e., the difference between the linear approximation and the actual mechanical stiffness, is shown in Fig. 4.27. It can be observed that the torque error of the first mechanism is relatively small. In the modified case, the error increases, however, it is still below reasonable levels.

4.7.4 Analysis and Discussion

This section examines how the addition of the second spring affects the torque and energy required to change the stiffness of the actuator. The additional spring lever has a certain amount of slack that allows the rotation of the follower if a different stiffness of the mechanism is required. This slack prevents the generation of negative torque and ensures that the spring can only be compressed. By increasing the follower angle, the slack is increased. The resulting behaviour is that the spring contributes much at lower follower angles, i.e., lower stiffness, and less at higher follower angles, i.e., higher stiffness. When the deflection link rotates, it first reduces the slack and then starts with the spring compression. The increase in the deflection torque and the resulting reduction in the torque required to maintain a given stiffness is shown in Fig. 4.28.

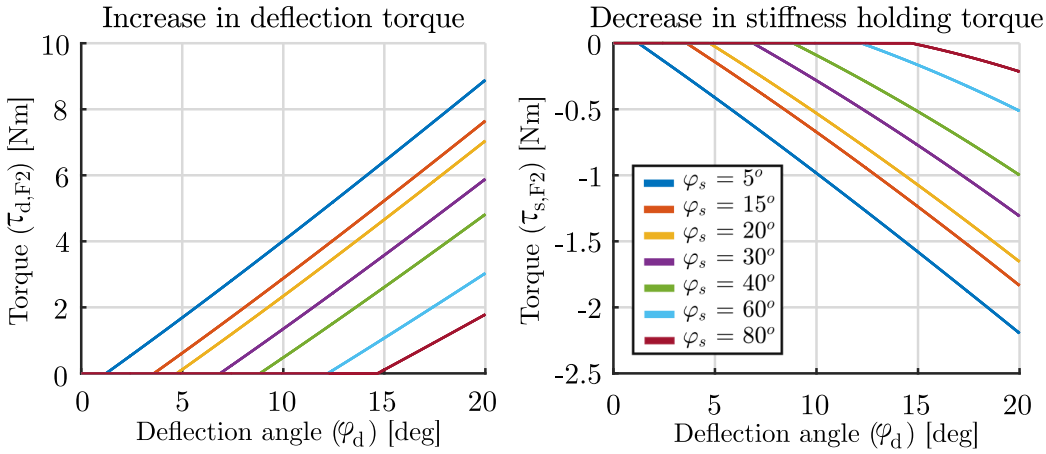


Figure 4.28: The increase of the deflection torque (*left*) and the resulting stiffness helping torque (*right*).

The proposed modification changes the overall stiffness of the mechanism. The relation between the linear stiffness equivalent and the follower angle is also changed. The stiffness of both mechanisms allows us to compare how the pre- and post- modification affects the mechanism on equal ground. The torque difference ($\Delta\tau_{s,F1,F2}$) of the stiffness varying motor between both cases is calculated as:

$$\Delta\tau_{s,F1,F2} = \tau_{s,F1,F2}(\varphi_d, \varphi_{s,F1,F2}(k)) - \tau_{s,F1}(\varphi_d, \varphi_{s,F1}(k)). \tag{4.43}$$

Here, $\tau_{s,F1,F2}$ represents the stiffness holding torque for the modified mechanism, while $\tau_{s,F1}$ represents the stiffness holding torque of the original mechanism. However, note that while the deflection angle is the same, the respective follower angle is calculated based on the linear stiffness k. The energy required to change from the minimum to a given stiffness is calculated by the following equation:

$$E_{s,i} = \int_{\varphi_{s,min}}^{\varphi_s} \tau_{s,i}\left(\varphi_{s,i}(k), \varphi_d\right) d\varphi_s, \quad \text{where } i \in \{(F1,F2), F1\}, \tag{4.44}$$

where $\tau_{s,i}$ and the deflection of the external link (φ_s) and the deflection of the external link (φ_d), in the case of the original mechanism ($i = F1$) and the modified version ($i = (F1,F2)$).

$\varphi_{s,i}(k)$ represents the relationship between the linear stiffness approximation and the follower angle. To compare everything on the same basis, the results for different follower angles (φ_s) must be converted to the equivalent stiffness as shown in Fig. 4.26*right*. The minimum stiffness ($\varphi_{s,min}$) is set to 23.2 Nm/rad as this is the minimum stiffness of the

modified mechanism. The difference between the energies required to change the stiffness in both cases is then calculated as:

$$\Delta E_{\mathrm{s,F1,F2}} = E_{\mathrm{s,F1,F2}}\left(\varphi_{\mathrm{s,F1,F2}}(k), \varphi_{\mathrm{d}}\right) - E_{\mathrm{s,F1}}\left(\varphi_{\mathrm{s,F1}}(k), \varphi_{\mathrm{d}}\right). \tag{4.45}$$

The stiffness variation energy results are presented in Fig. 4.29.

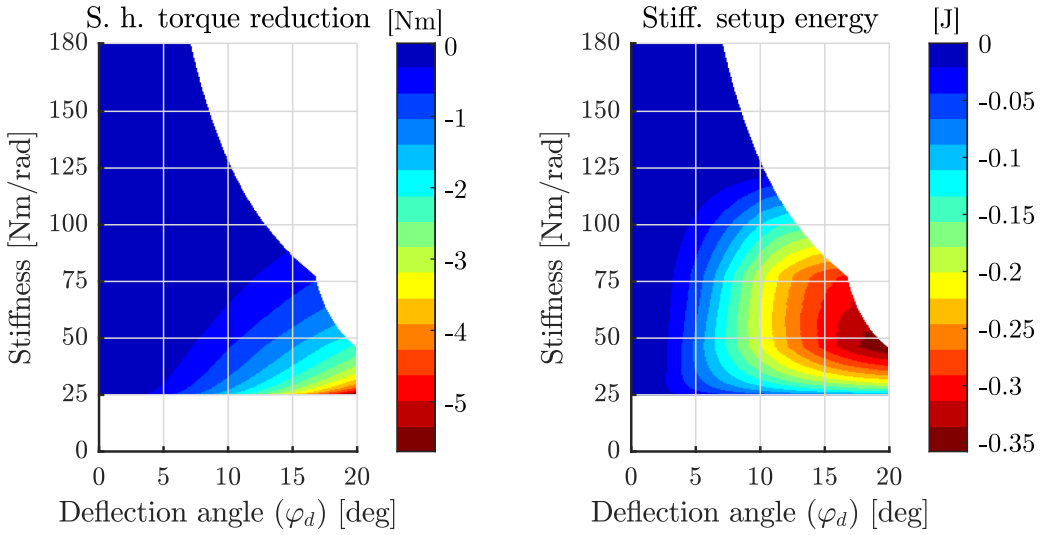


Figure 4.29: The difference between the two mechanical cases for the follower torque, i.e., the torque required to change the stiffness (*left*) and the energy required for this (E_{s}) (*right*).

The graphs show the overall picture over the entire deflection and stiffness range. From the results one can see in Fig. 4.29,*left* that the modification lowers the torque required to vary the stiffness at higher deflection angles of the mechanism and at the lower follower angles. However, at a higher stiffness it remains the same as in the original. Similarly it can be observed that at low follower angles, i.e., at lower stiffness, less energy is required to vary the stiffness again (Fig. 4.29,*right*).

Using the linear stiffness approximation, both mechanisms can be compared on the same graph, as shown in Fig. 4.30. It can be seen that the system still retains pseudo-linearity, which is favourable from the control point of view, however, the linearity of the lines decreased. The deflection range is limited to 20 deg, since the aim of this modification is to improve the PLVL-VS actuator from Section 4.4. The follower torque required to change the stiffness is shown in the right graph of Fig. 4.30.

As predicted, the new following torque is lower in critical cases due to the modifications. This shows that the proposed modification increases the performance of the unit while using the same motors as in the actual PLVL-VS actuator. Since the motors contribute a lot to the weight of the overall system, the small size of the motors also helps to keep the overall unit light, small and compact.

Another important aspect of the mechanism is the amount of elastic energy stored in the compressed mechanism. This stored elastic energy should not be confused with the energy needed to change a certain stiffness. In general, more stored energy means a higher possibility for more efficient movement of the external link. The amount of elastic energy stored in the device is compared both before and after the modification.

The stored **el**astic energy ($E_{\mathrm{el,i}}$) is calculated numerically according to the following

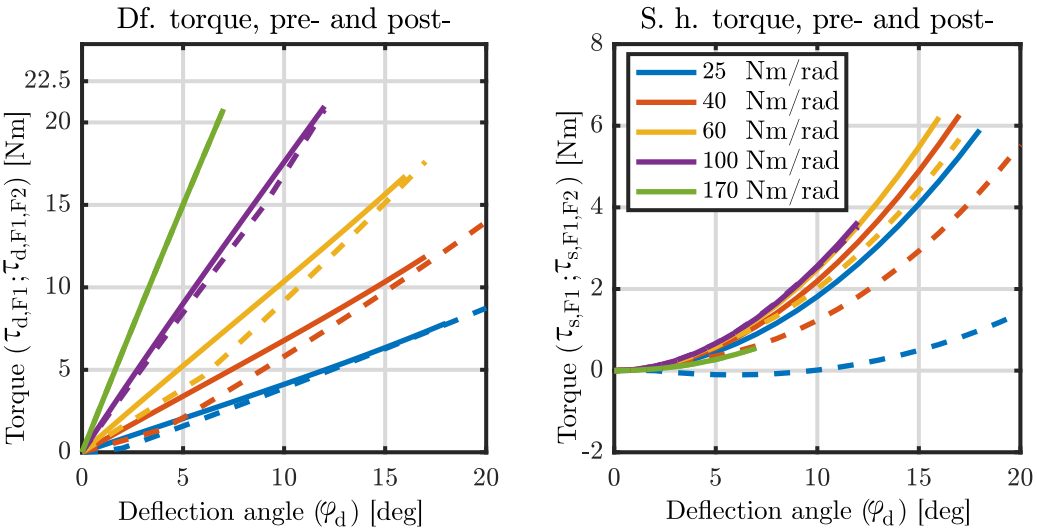


Figure 4.30: Comparison of the torque-deflection graph for different stiffness settings (*left*) and the torque required to maintain the given stiffness (*right*), for original and modified mechanisms. The solid lines represent the original mechanism and the dashed lines represent the modified mechanism.

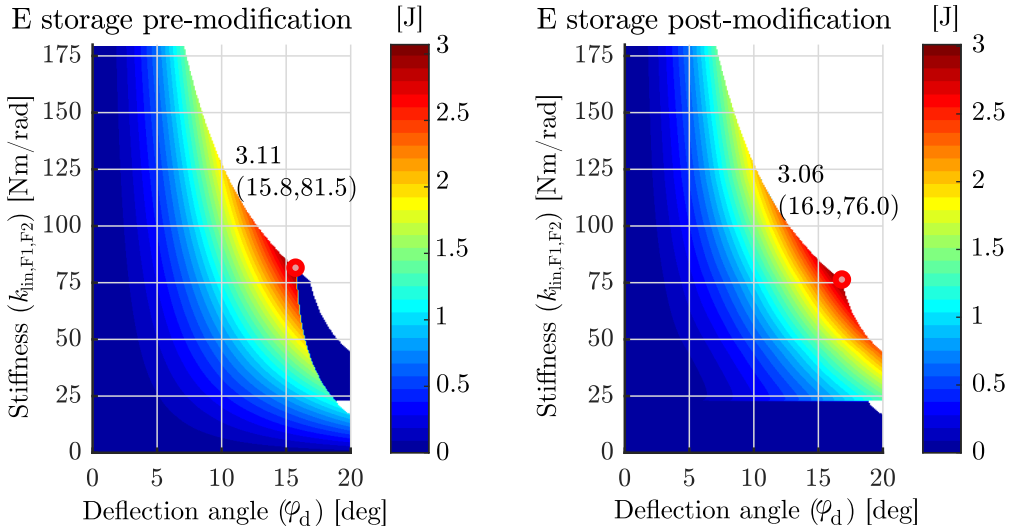


Figure 4.31: Graphs showing the elastic energy storage capacity (*left*) before and (*right*) after modification.

equation:

$$E_{\mathrm{el,i}} = \int_{\varphi_\mathrm{d}=0}^{\varphi_\mathrm{d}} \tau_{\mathrm{d,i}}\left(\varphi_{s,i}(k), \varphi_\mathrm{d}\right) \mathrm{d}\varphi_\mathrm{d}, \quad \text{where } i \in \{(\mathrm{F1,F2}), \mathrm{F1}\}\,. \tag{4.46}$$

$\tau_{\mathrm{d,i}}$ is the deflection torque dependent on the deflection of the external link φ_d and the stiffness of the device k, and on the follower angle φ_s. The results are shown in Fig. 4.31. The areas where the two workspaces do not overlap, i.e., where one mechanism version can reach it and the other cannot, are treated as areas where no elastic energy is stored. Areas where the workspace is unreachable for both versions are ignored, i.e., white in this case.

It can be seen that the amount of stored energy does not change noticeably at the maximum deflection of the mechanism of 20 degrees. The modified mechanism is able to

store more energy than the unmodified mechanism at stiffness levels below 75 Nm/rad. Since the workspaces between the two versions differ, a simple difference calculation between them is not sufficient and has therefore been omitted. For a higher elastic energy storage, the deformation range would have to be increased.

4.8 Chapter Conclusion

The PLVL-VS mechanism paves a way towards novel, energy-efficient stiffness variation methods. To summarize, the main features of the proposed principle are:

- an energy-efficient stiffness variation enabled through a perpendicular spring force principle,
- rotational stiffness variation architecture that allows a more compact and flatter actuator design,
- the pseudo-linear torque deflection behaviour allows the use of linear control design.

Due to the higher energy efficiency a fast or low-torque stiffness variation is possible. The motor required for the variation can be smaller and of lower power. Since the stiffness is not varied by preload, the internal forces are kept smaller, which allows a lighter, less rigid structure. The rotational stiffness variation mechanism is suitable for a more compact drive design, as opposed to a more elongated architecture from [97]. Mechanisms that use a parallel spring force configuration require internal springs with a high stiffness characteristic to achieve a reasonable external torque as they have less efficient force transmission. The option of using a motor with lower power requirements is practical, following the recent trend of actuator weight reduction and compact design. The pseudo-linear torque/deflection behaviour can be approximated as linear, which simplifies control design, eases the comparison between different architectures and allows for easier dimensioning of the final device.

The following features can be considered as possible disadvantages of the proposed principle:

- a zero deflection discontinuity when the direction of the external torque changes,
- the force required to change stiffness at higher deflection angles increases.

The first can be reduced with the correct controller tuning. The second disadvantage is common with VSAs and can be compensated by correct drive dimensioning. Modified version features a second spring and reduces the rising follower torque at lower stiffness and higher deflection angles, thereby reducing the impact of the second disadvantage. The resulting device requires less torque and energy to change its stiffness. The proposed modification extends the working range of the torque/deflection devices, maintaining a slightly smaller stiffness range but using the same motors. However, it also introduces a discrete nonlinearity and reduces the pseudolinearity of the torque-deflection graph. Although it is unclear how this discrete nonlinearity would affect the performance of an actual physical prototype, this has not been investigated at this stage. The modified configuration also suggests that there may be other more efficient variable stiffness mechanism architectures.

The proposed mathematical models have been verified and show a large coherence with the expected behavior of the physical prototype. The developed model can be used to either find a suitable combination of components or to find further solutions, i.e., new configurations. The optimization method proposed in Section 4.7.3 can be used to maximize the torque/deflection space by determining the proper mechanical spring and also other design parameters. Although there are drawbacks of the proposed implementation of the actuator that originated in its cable transmission, the results are encouraging and not detrimental to future exoskeleton applications.

The PLVL-VS actuator has been designed as a means for studying exoskeleton con-

trol algorithms. The properties of the above mechanism have been selected to facilitate such studies. It was integrated into an exoskeleton device to test its performance as an exoskeleton actuator. The overall exoskeleton focuses on performance but it is not as flexible, i.e., scalable as desired. The ultimate goal is to design a device that is fully portable, autonomous and scalable. Despite many advantages of the PLVL-VSA, such variable stiffness devices still bring an increased mechanical complexity and additional weight to the exoskeleton devices. However, with the proper exoskeleton design, the advantages of such mechanism can be amplified and the effects of the disadvantages mitigated. The research focus in the next chapter shifts toward the design of an exoskeleton aimed towards full autonomy, scalability and full-wearability in proper combination with the compliant mechanism.

The development of a novel stiffness variation principle, underlying mathematical model, optimization methods and several prototypes were critical steps in achieving goal **G2: Develop an efficient stiffness variation principle suitable for an exoskeleton application**. The research also confirmed hypothesis **H2: Using a novel architecture, an efficient variable stiffness actuator is possible that favourably conforms to factors such as mechanism's weight, volume and efficiency of stiffness variation.** Goal G2 and hypothesis H2 were reached and confirmed, respectively.

Chapter 5

Upper-Limb Exoskeleton

This chapter presents the research focused on goal **G3** and hypothesis **H3** of the thesis, both of which are concerned with the development of an upper-limb exoskeleton device. The exoskeleton application aims to reduce the effect of load-weight on the user's arm and to generate an additional torque to assist in the user's task. However, this work is focused on the development and testing of the underlying exoskeleton technology and not on the human-exoskeleton interaction aspect.

An exoskeleton device should be lightweight and mechanically adaptive to various user shapes to allow seemingly unimpeded movement. A lightweight structure adds minimal additional weight to the user and minimally increases the existing inertia of the user's limbs. While mechanically compliant actuation allows for and contributes to the mechanical adaptation of such devices, it also inadvertently introduces additional weight and increases inertia. To reduce the negative effects of integrating stiffness modification mechanisms, a new exoskeleton device is in development. The proposed exoskeleton device uses several approaches to solve or mitigate the difficulties of exoskeleton design:

- Modular design methods to reduce the variability of components and parts, and to lower manufacturing costs.
- Use of readily available electronic hardware components with open source software & hardware to ensure system scalability.
- Use of mathematical modelling and sensor fusion methods to improve the reliability of sensors.
- Use of Bowden cable transmission to transmit the force from the actuators to the joints, which:
  - ◇ shifts most of the mass towards the backpack,
  - ◇ ensures a more flexible and lighter exoskeleton frame,
  - ◇ enables external torque approximation through cable elongation measurements.

The current design aims at only 2 human joints, namely the vertical flexion/extension of the shoulder and the flexion/extension of the elbow. The operation of only the selected 2 joints is a good compromise between the necessary support for the user's tasks and the complexity of the exoskeleton's mechatronic system. The final mechatronic system includes mechanical, electronic and software design. It can potentially be extended to other joints of the upper and/or lower extremities. The primary goal, however, is to enable the implementation of variable stiffness technologies. In this respect, the proposed concept is convenient since:

- The potential additional weight of the variable stiffness units is not applied to the joints of the exoskeleton frame but to the exoskeleton backpack, so that the frame retains its light structure and inertia.
- Variable stiffness units suffer from increased mechanical complexity and higher weight,

but the flexibility of the cable design allows for less complex architectures and integration.
- Units with variable stiffness introduce additional inertia, which can be again reduced through the use of Bowden cables and component weight reallocation.

In this part, the proposed prototype of the exoskeleton is developed to support the integration of a variable stiffness mechanism, built and evaluated.
The following list summarizes the research effort:

- Develop a new exoskeleton prototype that has a lightweight frame, is fully wearable, and has its own battery power supply, allowing for complete autonomy. The lightweight frame structure is made possible by moving the exoskeleton actuators to the user's back using a Bowden cable transmission.
- Investigate the quality and feasibility of the various torque measurement methods:
  - ◇ Use mathematical modelling and sensor fusion tools to compensate for the effects of static and sliding friction of the Bowden cable.
  - ◇ Integrate a load cell that can measure the tension force of the Bowden cable.
  - ◇ Investigate the torque measuring method based on elongation measurement of the Bowden cable.
- Develop a concept for a compact integration of the PLVL-VSA stiffness variation mechanism.

5.1 Design Goals and Parameters

The design of the exoskeleton for the upper extremity aims for complete autonomy, scalability and full wearability. A fully wearable exoskeleton is considered to be one that is not connected to external computers or power sources with power conduits (in this case electrical wires, but could be pneumatic or hydraulic hoses). Its main function is to support the upper limbs. This is achieved either by reducing the effect of the user's arm weight or by generating additional torque to support the user's tool in the hand. The mechanical

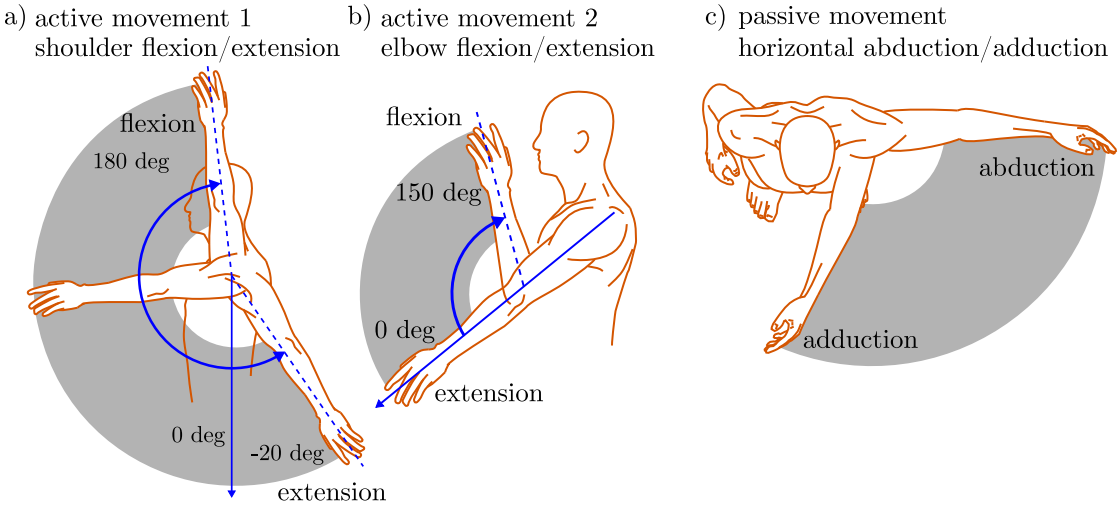
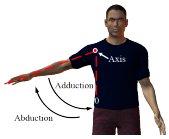
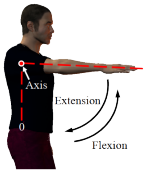
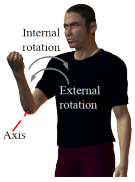
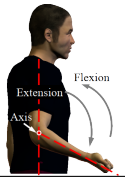
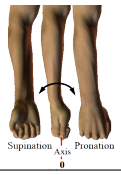


Figure 5.1: Exoskeleton range of movement. The first actuated movement shown in **a** is marked as *active movement 1* and includes the shoulder flexion and extension. **b** shows the *active movement 2*, which is the second actuated joint and comprises the elbow flexion and extension. Finally, shown in **c**, the mechanism allows horizontal abduction and adduction movement of the *passive* shoulder joint.

complexity of the proposed device was kept low enough to achieve the above objectives in the available time. Two brushless motors are used to actuate the 2 joints most commonly used for the given task. The two actuated joints are the shoulder *flexion* & *extension*, and the elbow *flexion* & *extension*, which are shown in Fig. 5.1a and 5.1b, respectively. The combination of the two joints allows gravity compensation of the user's upper and lower arm, reducing the muscle effort required to hold the arm. Additional torque can also reduce or eliminate the weight influence of any tools the user may be holding in his hands. In addition to the torques that compensate for gravity, additional torques can be generated to perform other tasks such as hammering, throwing, etc.

To increase the range of motion of the exoskeleton, additional passive joints are added to the exoskeleton frame. The horizontal abduction/adduction movement of the shoulder is recognized as important and is shown in Fig. 5.1c. To narrow down the requirements for the exoskeleton device, some human body factors relevant to the design have been

Table 5.1: Human motion parameters.

Axis of rotation	Comment/ source	ROM [°]	Vel. [°/s]	Acc. [°/s^2]	Torque [Nm]	P. [W]
vertical shoulder rotation, abduction, adduction 	ADL [172] average [174] isometric [175] max [176] average [176]	100 to -135 180 to 75[a] 0 to 135 142	71 0-48 238 113	103	20	25
horizontal shoulder rotation, flexion, extension 	ADL [172] average [174] isometric [175]	135 to -45 180 to 60 135 to -45	60 0	20 75.2-93.8	20	21
internal & external shoulder rotation, medial & lateral rotation 	ADL [172] average [174] isometric [175] peak [177] peak [177] peak [177]	-50 to 95 110 to 90 45 to 90	150 0-48 60 180 300	245	10 35-51.1 28.5-86.8 23.1-74.6 21.7-69.2	26
elbow flexion extension 	ADL [172] isometric [178] average [174]	0 to 135 0 to 146 5 to 145	91	116	20 72.5	32
forearm supination pronation 	isometric [178] average [174]	86 to 71 90 to 90			9.1	

[a] Different sources mark the range of rotation differently. For example, some consider shoulder rotation as positive in flexion and negative in extension, while others mark both movements as positive. ROM stands for range-of-motion.

compiled from the literature and are shown in Table 5.1. The exoskeleton design goals are summarized as:

- horizontal shoulder flexion/extension:
  - movement range from -20° to 180°,
  - minimal torque of 20 Nm,
  - velocities higher than 100°/s
  - and accelerations of 100°/s^2
- elbow flexion/extension:
  - movement range from 0° to 145°,
  - with minimal torque of 20 Nm,
  - velocities higher than 100°/s
  - and accelerations of at least 100°/s^2
- passive horizontal abduction/adduction stage,
- passive forearm pronation/supination stage.

The design of the final device is based on the above-mentioned specification, but also allows for future modifications to improve it. One example is the modular design principle, which allows a complete redesign of exoskeleton modules such as the actuation unit or the exoskeleton frame. An example of a non-modular design would be the integration of actuation units directly at the exoskeleton joints. Such a non-modular design requires additional power conduit routing through the exoskeleton joints and the exoskeleton frame, resulting in higher mechanical complexity. The proposed actuation unit also features a toothed belt transmission that allows for small changes in the transmission ratio via pulley replacement, thus allowing the exoskeleton joint velocity and torque ratio to be adjusted. The mechanical design is further elaborated in Section 5.2.

5.2 Mechanical Design of the Exoskeleton

The exoskeleton device is shown in Fig. 5.2 from different angles. The entire frame of the exoskeleton is attached to the side of a commercially available *hip orthosis* and the exoskeleton's actuation unit is attached to the back of the orthosis. The frame of the exoskeleton is attached via a passive ball joint so that its entire weight and the forces gen-

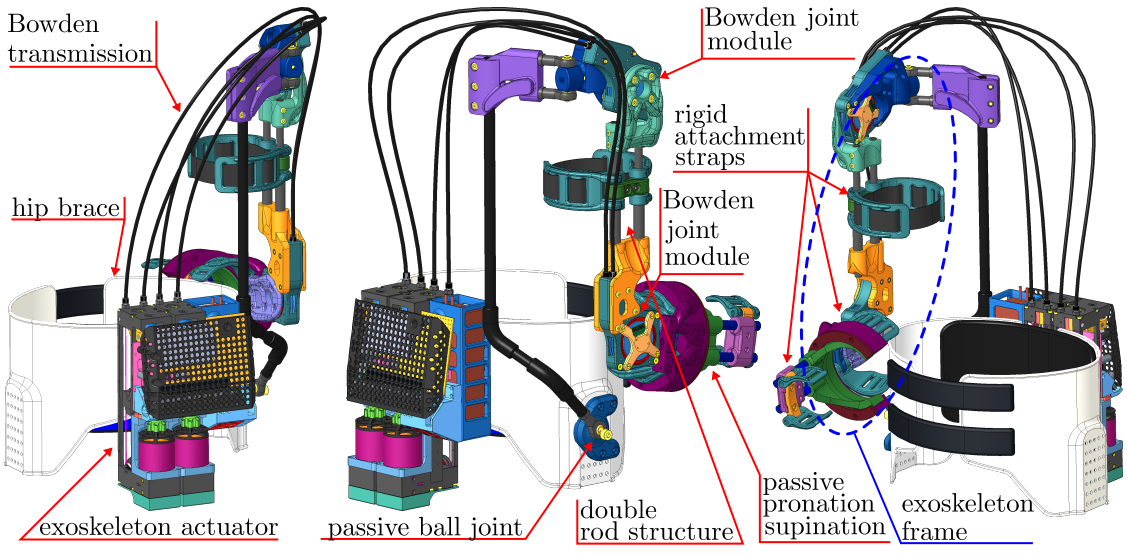


Figure 5.2: Exoskeleton device and its components shown in several perspectives.

erated are transferred to the hip orthosis and from there to the hip of the user. The frame is assembled using Bowden joint modules and links that also allow for manual length adjustment. All Bowden joint modules have the same structure, which reduces the variability of the exoskeleton components.

The power transmission from the motors to the joints of the exoskeleton is done by Bowden cables. The use of Bowden cable transmission is not a novelty in exoskeleton construction, as can be seen from the literature review in Section 2.2.2. However, there are several advantages to its use if the goal is a modular exoskeleton structure.

Most of the mass of the device is distributed to the user's back, resulting in a lightweight exoskeleton frame. The cables separate the exoskeleton actuator from the frame structure, meaning that both can be separated or even redesigned. Since the actuator components such as motors, power electronics and battery are now localized, cable routing and cooling design is simplified, resulting in a compact actuator unit. As researched in this chapter, cable stretch measurements can be used to estimate external torque, eliminating the need for load cell type sensors. This is a significant improvement because load cells are expensive, have a considerable weight, require electronic amplification, need to be compactly integrated into the design and are associated with chatter noise and thermal instability. The Bowden cable routing within the actuator unit opens up new ways to integrate variable stiffness architectures into a compact actuator unit. Despite the increased weight and mechanical complexity associated with compliant actuator structures, low actuator weight can be maintained. On the other hand, the use of Bowden cable actuation has one major disadvantage, namely relatively high friction, and therefore requires a stronger motor and more electrical power.

Figure 5.3 shows the Bowden cable transmission. It shows the realization of the cable transmission on the actuator side (Fig. 5.3a) and on the side of the Bowden joint module (Fig. 5.3b). The actual cable is continuously routed from the actuator unit to, and through, the Bowden joint and back to the actuator. On its way, the cable is led through Bowden cable sheaths placed between the actuator and the Bowden joint module. At the actuator, the cable's ends are rigidly connected to the ball screw nut. In the Bowden joint module, the cable is guided through the pulley in a special way. Observe in Fig. 5.3b how the cable is guided through the middle of the pulley to form a loop. This prevents possible slippage as the cable is held with sufficient friction. The cable then runs around the *redirection*

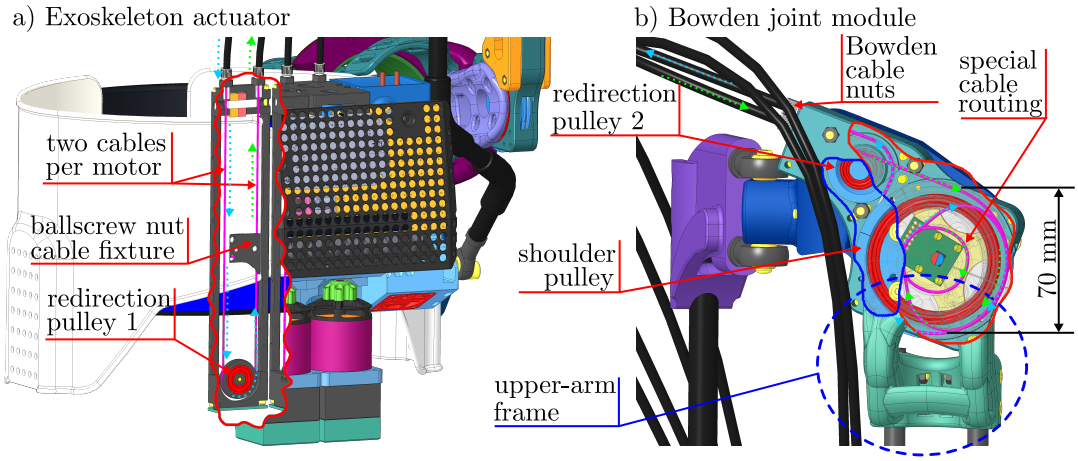


Figure 5.3: Bowden cable transmission and Bowden joint module. Figure **a** shows the cable routing at the actuator, while **b** shows the cable routing at the Bowden joint module. The cable routing direction is marked with *blue* and *green* arrows.

pulley 2, which places the two Bowden cable nuts closer together resulting in a compact Bowden joint module. Through the second Bowden cable sheath, the cable ends again at the actuator. It moves along the length of the actuator and is guided around *redirection pulley 1* to finally end up at the ball screw nut, where it is rigidly connected. During cable installation, after the cable has been attached to the ball screw nut, the screws of the Bowden cable sheath can be rotated to tension the Bowden cable. A total of four screws are used for each motor, and all four can be turned to reduce cable slack and tension the Bowden cable. Each Bowden joint module requires two Bowden cable sheaths and one cable.

In order to achieve a fully wearable exoskeleton device, i.e., one that can be worn by the user himself, a passive shoulder joint was developed and added. The proposed design of the passive joint is a compromise between ergonomic requirements and mechanical complexity.

It is shown in Fig. 5.4 in front, side and top views, to describe its range of motion. The kinematics of the human shoulder is complex [127] and the presented mechanism follows it only when it (the mechanism) is in the neutral position as shown in Fig. 5.4. The carbon

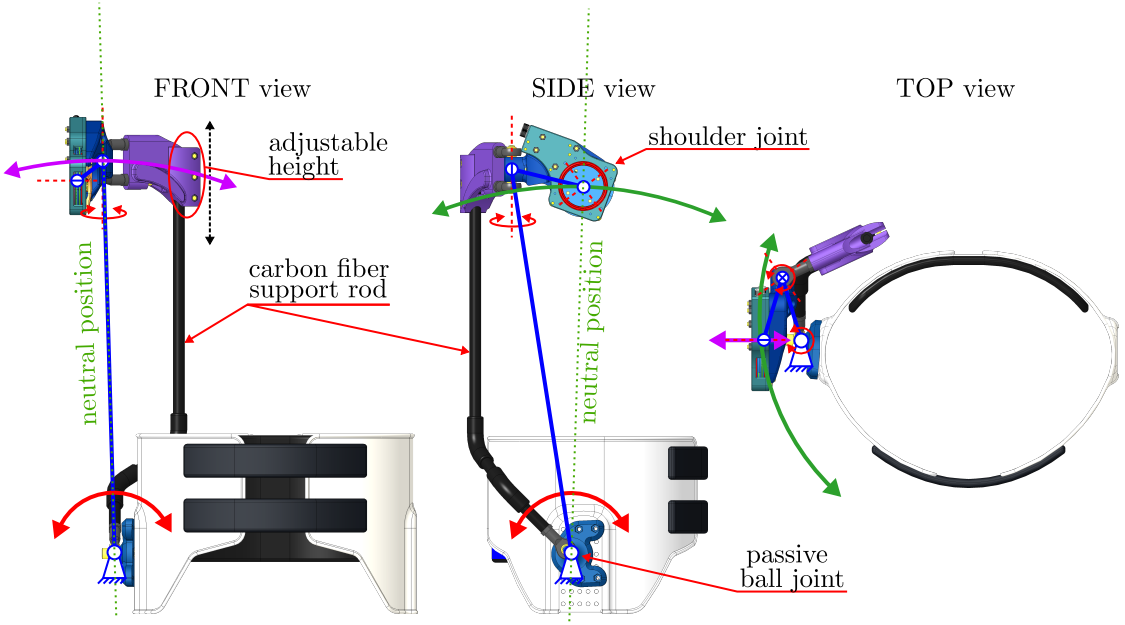


Figure 5.4: Shoulder passive joint of the exoskeleton is shown from different views and some of its movement directions are marked. The upper-limb exoskeleton frame is grounded using a carbon fibre-rod that is attached to the side of the hip orthosis using a passive ball joint.

fibre support rod is curved to allow negative horizontal shoulder rotation of the exoskeleton frame. A spherical ball joint is used to connect the carbon fiber tube onto the orthosis. Finally, the shoulder joint is mounted on the carbon fiber tube. This architecture allows for a spherical range-of-motion surface with a radius equal to the length of the carbon fiber rod whose center is on the ball joint. When the rod rotates away from its *neutral position*, the height of the shoulder joint decreases slightly, resulting in misalignment of the shoulder joint. To reduce the effects of this misalignment, the exoskeleton frame mounting brackets can compensate for it. They can rotate around the double bars of the double bar support structure of the frame to allow some movement despite the tight attachment to the user. The concept is the same as that of the exoskeleton elbow frame from Section 4.6. However, the design of the frame of the exoskeleton is not the focus of the present research.

In addition, the entire exoskeleton is modular, i.e., the frame can possibly be completely redesigned while retaining the existing actuator, electronics and sensor technology. The final exoskeleton prototype can be seen in Fig. 5.5.



Figure 5.5: Actual exoskeleton prototype shown *left* and a user wearing it shown *right*.

5.3 Design of Actuator Mechanics & Mechatronics

One of the main components of the actuator is the customized velocity reduction transmission system. The system combines a ball screw mechanism with a toothed belt transmission. Its inner workings are shown in Fig. 5.6. The figure shows a sectional view of the actuator module. A lever arm is used to integrate the load cell into the system. The lever arm ensures that only tensile or compressive forces are transmitted from the ball screw to the load cell. This mechanism is shown in several illustrations, including Fig. 5.6 and Fig. 5.9c. A more schematic representation of the architecture is shown in Fig. 5.7. The system consists of a Hacker A50-16L V4 brushless out-runner motor which serves as the main drive. These kind of motors are manufactured for use in a quad-copter drone aircraft. The selected motor can reach a temporary maximum output power of 1650W for 15s, which is much more than required for the selected application. However, as the actual requirements are unknown, partly due to the unknown level of cable friction and the effectiveness of fan cooling, a stronger motor was chosen to provide a safety margin.

A toothed belt drive is then used to connect the motor to the ball screw. The belt transmission not only protects the motor from vibration, but also allows small adjustments to the final transmission ratio by replacement of the toothed pulleys. Since the toothed belt pulleys were manufactured using 3D additive manufacturing, their teeth number can be easily adjusted to achieve the desired velocity and torque ratio. Since the exoskeleton is an experimental unit, this flexibility is an advantage. Use of plastic material for the pulleys is sufficient as the forces/moments directly at the motor are not large.

The toothed belt is directly connected to the ball screw drive. In this configuration, the screw rotates and the nut moves linearly. To improve the nut's resistance to non-axial

forces and torques, it is attached to a small linear motion guide bearing. The steel cable is then rigidly attached to the nut. Turning the ball screw clockwise or counter-clockwise moves the nut forward or backward. The respective cable movement results in the rotation of the external Bowden joint module pulley. Bi-directional movement of the ball screw nut results in bi-directional movement of the external link. However, the cable cannot be moved continuously, but only allows linear movement corresponding to the length of the ball screw. A limit switch is mounted at each end of the ball screw, which serves as an additional safety feature in case the ball screw nut reaches its hardware limit.

Each motor uses two AS5047D encoder circuits that allow simultaneous incremental or absolute mode. One of them is integrated in the Bowden joint module to provide absolute measurement of the position of the external link. This absolute measurement is used not only for control purposes, but also for the initial calibration of the system. The second AS5047D encoder is placed on the motor axis. Its incremental mode signal is used by the motor driver.

The system uses an integrated load cell that can measure the force on the ball screw to estimate the tensile force in the cable. A lever mechanism is used to transmit the forces of the ball screw to the load cell in a compact way. Its respective lever length is 19 mm between the grounded pivot and the ball screw and 51 mm between the grounded pivot and the load cell. See the schematic representation in Fig. 5.7. The lever lengths are chosen as a compromise between the compactness of the mechanism and the nominal load of the load cell. Three pivot points, one on the ground, the second on the ball screw and the third on the load cell, allow free rotation and ensure that only the ball screw's axial forces are transmitted to the load cell.

The above mechanical components of the upper arm exoskeleton are listed in Table 5.2. The final actuator prototype can be seen in Fig. 5.8. The majority of the more heavily loaded drive components are made of aluminium. Other components are manufactured using plastics and 3D additive manufacturing technologies. The Bowden joint module, for example, is mainly made of plastic with the exception of the metal bearings and is therefore very light.

The exoskeleton uses a 6S LiPo battery as the main power source with a nominal

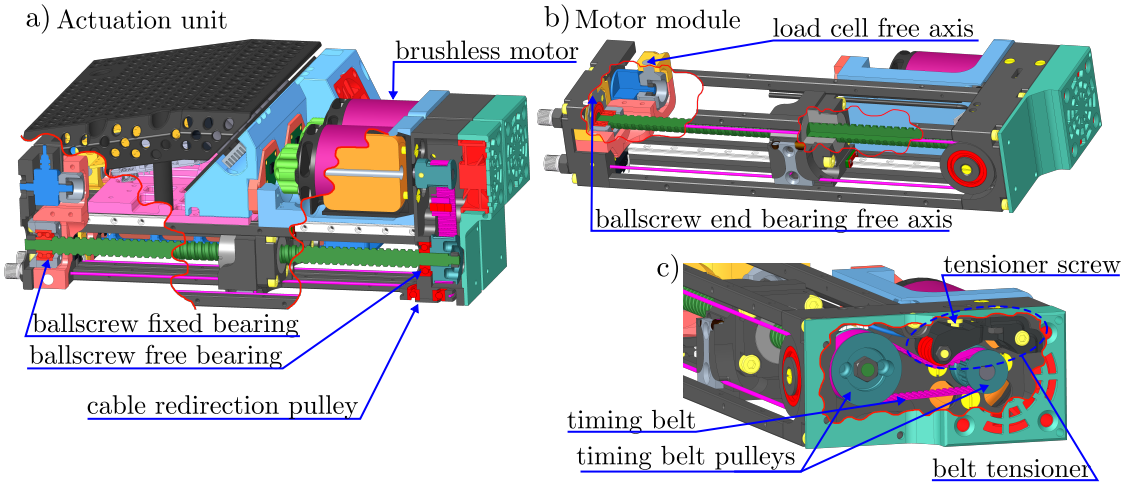


Figure 5.6: The actuator transmission system. **a** shows the operating unit with various cuts made to expose its inner workings. Several bearings that support the ball screw are shown. **b** shows the integrated load cell and the mechanism that prevents torque loads on the cell and **c** shows the timing belt transmission and its belt tensioning system.

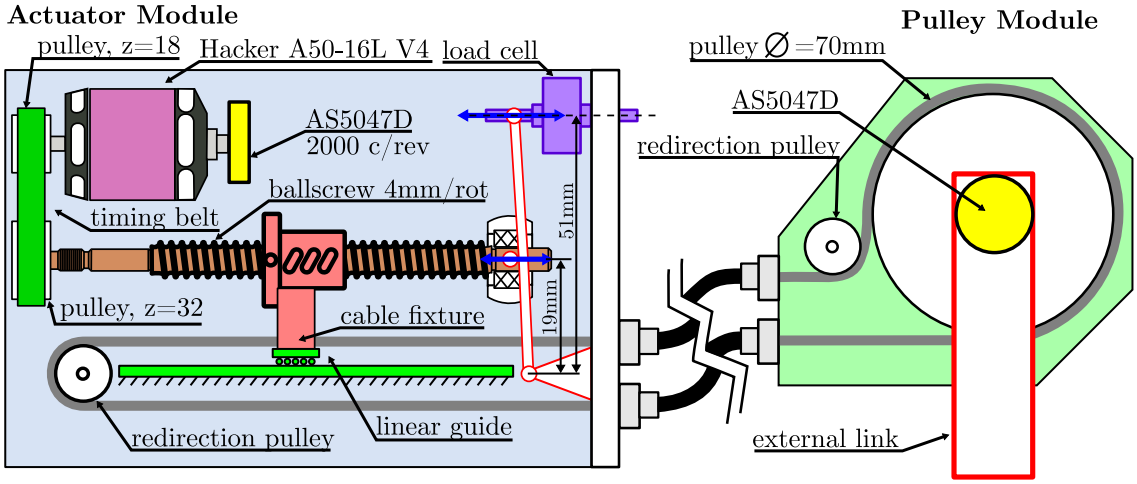


Figure 5.7: A schematic diagram of the mechanical system. The schematic shows different components and a simplified insight into the sensor placement, load cell integration and operation of the actuator transmission system.

Table 5.2: Mechanical components list.

Component	Identification	Properties
Brushless motor	Hacker A50-16L V4	– Power: max. 1650W (15s) – Idle Current @8.4V: 0.95A – Resistance (Ri): 0.031 Ohm – RPM/Volt: 265 RPM/V – Weight: 445g – Torque const. 0.035 Nm/A [179]
Ball screw HIWIN	R10-04T2-RSIT 240 240 0.052	– step -> 4 mm/rot – C_{dyn} = 1980N – C_0 = 2820N
Linear guide HIWIN	MGN05C2R200Z0HM	– Ratings: – M_x = 1.3Nm, M_y = 0.8Nm, M_z = 0.8Nm. – C_{dyn} = 540N, C_0 = 840N.
Load cell	500N DCE, LCM Systems	– Rated load 500N – excitation 10vdc – output 1.5mV/V at rated load
Encoder board	AS5047D	– 14-bit on-axis absolute position sensor – ABI incremental interface of 2000c/rev – requires a diametric magnet
Battery	TopFuel LiPo 20C-ECO-X	– 6S -> 22.2V, 3800mAh

voltage of 22.2V. A 1S LiPo battery cell corresponds to a nominal voltage of 3.7V. This information is important because it is one of the parameters that determines the maximum available velocity of the motor. The motors are selected on the basis of their velocity characteristics in combination with the battery. The selected motor has a velocity of 265 rpm/V ($\omega_{rpm,max}$), resulting in a maximum velocity of 5883 rpm at 22.2V. It is calculated

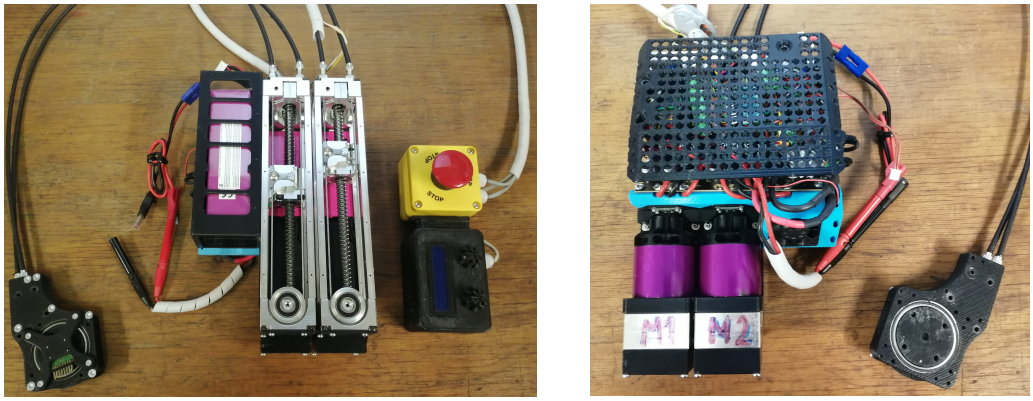


Figure 5.8: Actuator unit prototype. The back of the unit is shown *left* and its front is shown *right*.

as:

$$\omega_{\text{rpm,max}} = 265\text{rpm/V} \cdot 22.2\text{V} = 5883\text{rpm} = 35298\text{deg/s}. \tag{5.1}$$

The motor can thus theoretically achieve a rotation velocity of **5883rpm**. The selected battery allows a maximum current discharge of 20C. To obtain the discharge amperage, the battery's capacity is multiplied by its maximum discharge rate.

$$I_{\text{max,1m}} = 20\text{C}/2 \cdot 3800\text{mAh} \approx 38\text{A}, \tag{5.2}$$

where $I_{\text{max,1m}}$ is the maximum current allowed for one motor. The maximum discharge rate is halved, since two motors share one battery. One motor can use at most a current of **38A**.
Using this amperage value, the maximum theoretical power the battery can supply for one motor is calculated as:

$$P_{\text{max,1m,bat}} = 22.2\text{V} \cdot 38\text{A} = 843.6\text{W}. \tag{5.3}$$

843.6W is less than the maximum temporary (15s) power from the motor's technical data sheet, rated at 1650W.

Mechanical transmission of the system is slightly less straightforward. The motor's velocity is first reduced by the timing belt, which connects the motor's axis and the ball screw. Ball screw rotation then results in the linear motion of the cable. Finally, the cable's linear motion is converted back into the rotational movement of the pulley in the Bowden joint module. The full mechanical transmission ratio from the motor to the final pulley is calculated as:

$$n_{\text{m,p}} = 70\pi\text{mm} \,/\, 4\,\text{mm/rot} \cdot 32/18 \cdot 1\text{rot}^{-1} = 97.74 \tag{5.4}$$

where $n_{\text{m,p}}$ stands for motor-pulley transmission. 70πmm is the circumference of the pulley in the *Bowden joint module* and 4mm/rot is the transmission ratio of the ball screw. $32/18$ is the ratio of the toothed belt and 1rot^{-1} is the rotation of the motor.

The transmission ratio from the motor encoder to the external pulley angle is another important transmission ratio. It is calculated as:

$$n_{\text{e,p}} = 97.74 \cdot 2000\text{c/rot}/360\text{deg} = 543\text{c/deg}, \tag{5.5}$$

where $n_{\text{e,p}}$ is the transmission ratio, which describes how many encoder counts are required to rotate the external link by 1 degree. 2000c/rot is the encoder count/rotation number.

Finally, to calculate the ratio to achieve a movement of 1 degree, the results must be divided by 360 deg. Using the above transmission ratios, the maximum joint rotation and maximum joint torque can be calculated. The maximum joint velocity is based on the maximum velocity of the motor:

$$\varphi_{\mathrm{m,max}} = \omega_{\mathrm{rpm,max}}/n_{\mathrm{m,p}} = 35298\mathrm{deg/s}/97.74 = 361,14\mathrm{deg/s} \tag{5.6}$$

As for the maximum theoretical torque, it is calculated as:

$$\tau_{\mathrm{m,max}} = 0.035\mathrm{Nm/A} \cdot 38\mathrm{A} \cdot 97.74 = 130\mathrm{Nm}, \tag{5.7}$$

where 0.035Nm/A is the motor torque constant, 38A is the maximum battery discharge current and 97.74 is the previously calculated transmission ratio.

While the theoretical motor torque is now known, the cable is the last component that has to be checked for strength. It was chosen to be light and flexible, and therefore forms a compromise between strength and flexibility. It has a diameter of 1.5 mm and its minimum breaking load is about 1.3 kN. The equivalent maximum torque to achieve this load can be calculated with these specifications:

$$\tau_{\mathrm{c,max}} = 0.035\mathrm{m} \cdot 1300\mathrm{N} = 45.5\mathrm{Nm}. \tag{5.8}$$

$\tau_{\mathrm{c,max}}$ is the maximum allowable torque at the *Bowden joint module* in the present configuration. 0.035m stands for the radius of the Bowden joint module pulley.

The electronics of the exoskeleton system is based on several community-supported development platforms. Among them, BeagleBone Black (BBB) serves as the primary control board that runs the exoskeleton control algorithm. The BBB runs under an open source Linux distribution and thus supports custom software design. It has a 1 GHz processor unit with 512 MB RAM, which is sufficient computing power for the selected application. An integrated 4 GB flash memory distinguishes it against similar development boards. The memory can be used to store software and any measurement data. It also features multiple communication interfaces, which are exploited in this application. An additional microcontroller, called Teensy LC, is used to reduce the load on the BBB. The Teensy LC is a powerful microcontroller and features a 48MHz processor. In addition, it provides several communication interfaces and a 16-bit analog-to-digital converter. Finally, an open source and open hardware brushless motor driver, called Odrive v3.5, is used.

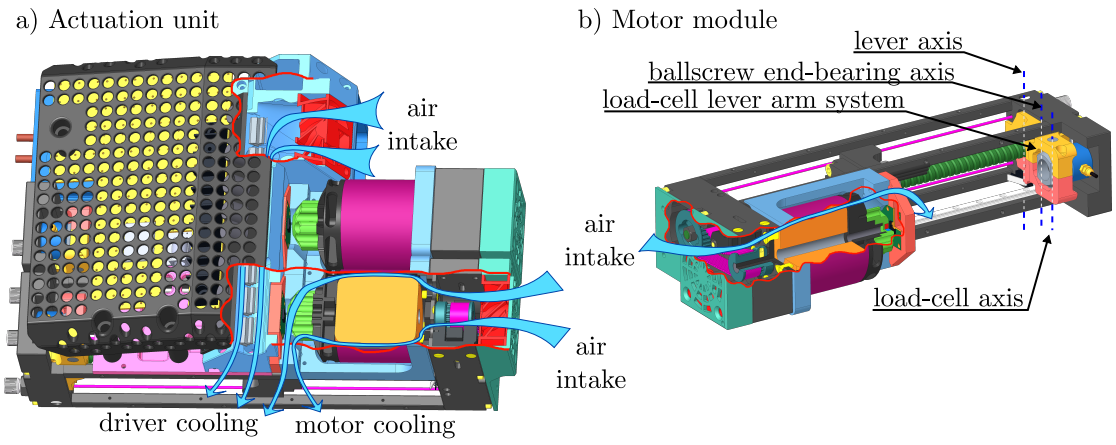


Figure 5.9: The cooling system. Picture **a** shows the implemented hardware cooling consisting of a cooling system for electronics and a cooling system for the motor. Figure **b** shows the separate *Motor module* and its cooling system.

One Odrive driver board can drive up to two brushless motors. It allows a continuous current of 40A per motor and a peak current of 100A. Additional cooling increases the amount of continuous current. For this reason, the proposed drive unit uses additional fans to improve its cooling. The actual implementation of cooling is shown in Fig. 5.9. An electric fan is used to cool the power circuit of the Odrive driver. Two additional fans are used, one for each motor, to blow air through the winding of the two motors to cool them.

Table 5.3 gathers a list of electrical components.

Table 5.3: List of electronic components.

Component	Identification	Properties
Motor driver	Odrive v3.5	– 24V version – 100A peak for each motor – 40A continuous per motor – 75A cont. with fan cooling
Controller	BeagleBone Black Wireless	– Octavo Systems OSD3358 1GHz ARM® Cortex-A8 – 512MB DDR3 RAM – 4GB 8-bit eMMC on-board flash storage – CAN, 2xSPI, 4xUART, 2xI2C, 65xGPIO, etc.
Microcontroller	Teensy LC	– Cortex-M0+ 48MHz – 2 SPI ports, 2 I2C, and 3 Serial ports – 16-bit Analog Input (12-bit use recommended)
Load cell amplifier	ICA2	– 3 Wire, 12V input voltage – 0.1 to 5.1V output

The mechatronic system of the exoskeleton uses the following sensors:

- 2 AS5047D encoders directly on the brushless motor axis operating in incremental mode,
- 3 AS5047D encoders attached to the exoskeleton joints and operating in absolute mode to measure the absolute rotation of the external links,
- 2 load cells that measure the force on the ball screw and indirectly the force in the cables,
- 4 limit switches that measure the end positions of the two ball screws,
- 1 safety switch button that sends two signals; to BBB, which tells that it is pressed; and to Odrive, which forces the driver into constant reset mode and essentially turns it off,
- current measurement on both motors by the Odrive driver,
- driver board temperature measurements,
- measurement of the battery voltage.

The electronic hardware with the corresponding communication interfaces is shown in Fig. 5.10. The BBB and the three AS5047D encoders attached to the exoskeleton joints communicate together through an SPI interface. The AS5047D enables various communication interfaces such as direct SPI, daisy-chain, incremental ABI, etc. In the actual exoskeleton implementation, the three absolute encoders are connected in a daisy-chain architecture, reducing the number of SPI communication interface lines required. For this purpose, a custom protocol was developed on the BBB that allows for daisy-chain communication

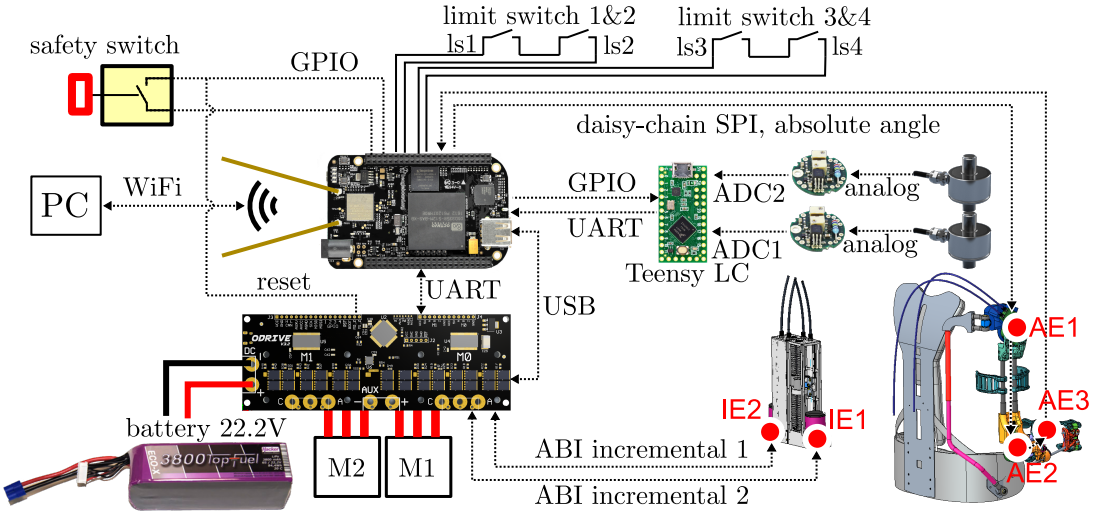


Figure 5.10: Electronic hardware schematics. The figure shows the electronic components and the corresponding communication interfaces. *IE1* and *IE2* stand for the incremental encoders. *AE1*, *AE2* and *AE3* stand for the absolute encoders.

with the sensors. The same encoders are also used as position sensors for the brushless motors. Their ABI incremental interface, i.e., the pulse output, is directly connected to the Odrive incremental encoder interface. Odrive uses this information to control the brushless motor and also to record the absolute position of the motor axis. Note that this absolute measurement at the motor's axis is zeroed at every system start up.

The communication between the BBB and Odrive is done via UART and USB interfaces. The slower USB connection is used to calibrate all Odrive-related parameters such as current limits, velocity limits, PID control parameters for the position control loop, etc. A slightly faster communication is then possible via the UART interface to transfer control input and feedback information. The frequency of the controller running on the BBB is 50 Hz, which is relatively low but sufficient for the exoskeleton tests. Currently, the BBB-Odrive UART connection is the communication bottleneck and could be improved through a better communication protocol, as the UART messages are very long. However, this would require a significant change in the software currently running on the Odrive.

Next, another UART interface is used for communication between BBB-Teensy LC. The Teensy LC is used to read out the two load cells. Their signal is first amplified by their respective analogue amplifier ICA2. It is then fed to the Teensy LC analog-to-digital converter. Since the Teensy LC works asynchronously with the BBB, its sensor readings can be read out much faster. The Teensy LC therefore uses a sliding average filter with 50 samples. Consequently, for each 50Hz loop of the BBB, the Teensy LC samples the load cells 50 times. This results in a much cleaner load cell signal, which is then transmitted via the UART interface using another custom communication protocol.

Finally the BBB has an integrated wireless network adapter. It is used to enable communication between the BBB and a personal computer. This communication line can be used either to program the BBB, to provide user input, or to stream data to the personal computer. While BBB allows for use of different programming languages, Python is the primary programming language in this project.

5.4 Control Design

5.4.1 Position Controller

The Odrive motor driver enables either position or current-based brushless motor control. To control the motors in position mode, the control algorithm shown in Fig. 5.11 is used. Since the BBB controller operates at a frequency of 50 Hz, this leads to jerky position

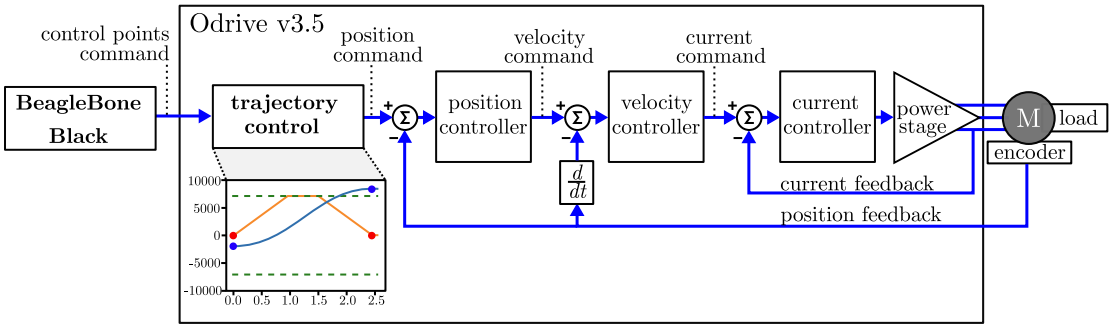


Figure 5.11: Upper-limb exoskeleton position controller. The schematic shows the position controller of the proposed system. It is built with a combination of the internal Odrive position controller and the trajectory mode. The diagram is partly adapted from [180] and [181].

control. For this reason the *Trajectory Control Mode* of the Odrive is used. Instead of direct position control data, the BBB sends trajectory control points at a frequency of 50 Hz. These are then interpolated by the Odrive using a trapezoidal velocity profile. The actual values used by the feedback controller and trajectory control parameters are recorded in Table 5.4. The shown position controller does not take into account cable

Table 5.4: Position controller parameters.

Parameter	Value 1	Unit 1	Value 2	Unit 2
K_P	30	counts/s		
K_I	0	A/(counts/s)		
K_D	0.001	A/counts/s^2		
velocity limit	75000	counts/s		
current limit	25	A		
trajectory mode: velocity limit	75000	counts/s	138.1	deg/s
trajectory mode: acceleration limit	100000	counts/s^2	184.2	deg/s^2
trajectory mode: deceleration limit	100000	counts/s^2	184.2	deg/s^2

elongation or other elastic deformations of the system. All control point commands are therefore used in a feedforward manner. This controller was used to control the system in the experiment to identify its properties. If the movements are slow, elastic deformations have no influence on the quality of the measurements. Later, the position controller was replaced by a current-based torque controller.

5.4.2 Torque Controller

The torque controller is somewhat more complex than the position controller. Due to the use of the Bowden cable transmission, the system is exposed to high friction. Since all sensors are located behind the Bowden cable transmission, they are all affected by the

friction nonlinearities, but to a different extent. The basis for the torque control algorithm has been adapted from [40]. Additional friction blocks were integrated into the SEA model to represent Bowden cable friction.

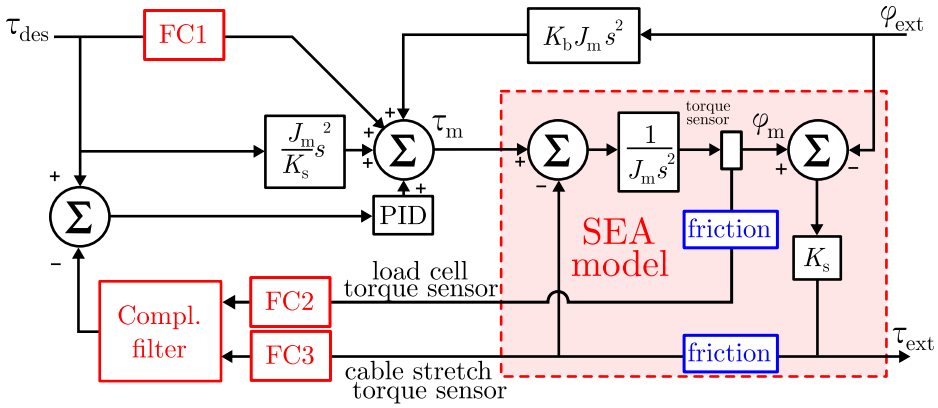


Figure 5.12: Torque control of the Series-Elastic Actuator. The friction due to the use of Bowden cables has been integrated into the SEA model. *FC1, FC2* and *FC3* blocks represent the place of mathematical friction compensation. Similarly, the *Complementary Filter* block shows the location where the two signals are blended together.

The proposed control algorithm is based on the feedback from two torque sensors estimators. The first torque sensor estimation is based on the signal from the load cell, which measures the force in the Bowden cable. Using the deflection pulley radius, the linear cable force is mathematically converted into its angular torque equivalent. The torque sensor signal based on the load cell is described by parameter τ_{lc}.

The second torque signal source is based on the measurement of the Bowden cable elongation. This is possible by using two rotary encoders. One of them is mounted directly on the motor axis and the other one directly on the exoskeleton joint. It is assumed that any deviation between them is primarily caused by cable elongation, and their behaviour is then modelled as a spring. In reality, this elastic deformation is a summation of the cable's deformation and the deformation of aluminium or plastic parts. Nevertheless, the phenomenon is repeatable and can be approximated by classical Hooke's law:

$$\tau_{el} = -K_{el} \cdot \Delta\varphi = -K_{el} \cdot (\varphi_{ext} - \varphi_m), \tag{5.9}$$

where τ_{el} is the corresponding spring torque.

K_{el} is the equivalent stiffness of the system, which takes into account the cable elongation and the elastic deformation of the components. φ_{ext} and φ_m are the angle measurements at the external exoskeleton joint and the motor axis, respectively. Value φ_m represents the motor axis rotation, which already accounts for the actuator transmission.

Both sensor signals are subject to system noise and different friction. It can therefore be assumed that noise and friction partially cancel each other out and a better approximation could be achieved if the information from both sensors was combined. Sensor fusion is used to investigate this preposition.

5.4.3 Stribeck+Coulomb Friction Model

Lastly, friction model is an important component of the torque controller. The use of Bowden cable transmission grants excellent ergonomics and wearability properties, which allow the user to move freely, since the actuation stages are allocated away from the end

effector. However, nonlinearities along the Bowden cable transmission will degrade control performance if not properly compensated [138, 139]. One of the main reasons for this is the static and dynamic friction that occurs between the cables and the Bowden sheath. Two other reasons are backlash and hysteresis [135]. The friction of a Bowden cable depends on its bending angle and can be successfully compensated [138]. However, in the present application, the bending angle does not change that significantly, so it is not included in the model.

A combination of Stribeck and Coulomb (Stribeck+Coulomb) friction model was used to model the friction. The Stribeck+Coulomb friction model is a well established method in friction modelling [182]. Although there are also other friction models [182], it is assumed that the Stribeck+Coulomb model approximates the friction of the Bowden cable sufficiently well. Stribeck+Coulomb friction model describes the relationship between frictional force and velocity as shown in Fig. 5.13.

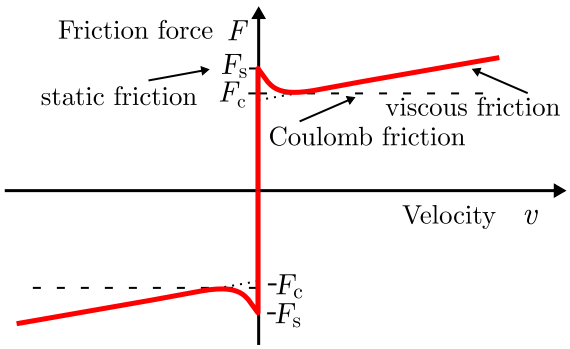


Figure 5.13: Stribeck+Coulomb friction model. The diagram shows the frictional force as a function of velocity. The friction model is composed of static, Coulomb and viscous friction.

The model consists of three types of friction; static friction (F_s), Coulomb friction (F_c), and viscous friction (F_v). The static friction occurs before the movement starts. As soon as the static friction is overcome, the system starts moving and the total friction decreases. Coulomb friction is constant as long as the system is in motion. Viscous friction occurs because layers of fluid move against each other. In the actual prototype, the Bowden cable is lubricated to reduce the total amount of friction. Furthermore, the Bowden sheath has an inner tube made of acetal or polyoxymethylene (POM) to further reduce the total friction between the cable and the Bowden sheath. When the steel cable slides on the POM, viscous friction also occurs. It is modelled as linear dependence on velocity. The static friction occurs when the velocity of the system is zero. Due to noise, the zero velocity state is extended to a slightly larger but still small margin, i.e., $|v(t)| < \alpha_{vm}$. The following equation applies:

$$F = \begin{cases} F_s & \text{if } 0^+ \leq v(t) < \alpha_{vm}, \\ -F_s & \text{if } -\alpha_{vm} < v(t) \leq 0^-. \end{cases} \tag{5.10}$$

The equation shows that it is not only important whether you are near zero velocity, but also whether this zero is positive (0^+) or negative (0^-). The negative or positive zero contains the additional information from which direction the zero was reached. If zero was reached from the positive or negative side, it is positive or negative, respectively. Otherwise, it is not known whether F_s at zero is positive or negative. If $|v(t)| \geq \alpha_{vm}$, then the Stribeck+Coulomb equation is used:

$$F_{scf} = \left[F_c + (F_s - F_c)\exp^{-|v(t)/v_s|^{\delta_{SCm}}}\right]\text{sign}(v(t)) + k_v v(t). \tag{5.11}$$

The equation contains parameters δ_{SCm} and v_{s} that describe the nonlinear curve that attenuates the effect of F_{s} when the velocity is close to zero. The parameter k_{v} adds viscous friction with increasing velocity. The final Stribeck+Coulomb friction equation is:

$$F_{\mathrm{SCm}} = \begin{cases} F_{\mathrm{s}} & \text{if } 0^{+} \leq v(t) < \alpha_{\mathrm{vm}}, \\ -F_{\mathrm{s}} & \text{if } -\alpha_{\mathrm{vm}} < v(t) \leq 0^{-}, \\ F_{\mathrm{scf}} & \text{if } |v(t)| \geq \alpha_{\mathrm{vm}}. \end{cases} \tag{5.12}$$

Since there are several sensor values, the effect of friction on a separate sensor is not the same. For this reason, an additional subscript parameter to $F_{\mathrm{sSCm},(.)}$, where (.) is either FF, LC or CE. In this case $F_{\mathrm{sSCm,FF}}$ for feedforward signal, $F_{\mathrm{sSCm,LC}}$ for the load cell-based external torque estimation and $F_{\mathrm{sSCm,CE}}$ for the cable-elongation-based external torque estimation. In the same manner, the nonsymmetric Stribeck+Coulomb model is given as $F_{\mathrm{nSCm},(.)}$. The difference between a symmetric and nonsymmetric model lies in the fact that the nonsymmetric model distinguishes between positive and negative velocity, and uses separate Stribeck+Coulomb parameters for them. While a symmetric version uses the same parameters for both the positive and negative velocities. A nonsymmetric model can additionally capture the nonsymmetry of the hardware. One example of this nonsymmetry are the different lengths of the Bowden cable for rotation of the system in one direction and in the other. As a result, the cables' stiffness levels are different.

5.4.4 Experimental System

Figure 5.14 shows the experimental system used to collect the necessary data to construct the mathematical models of friction. To perform the experiment, the shoulder joint of

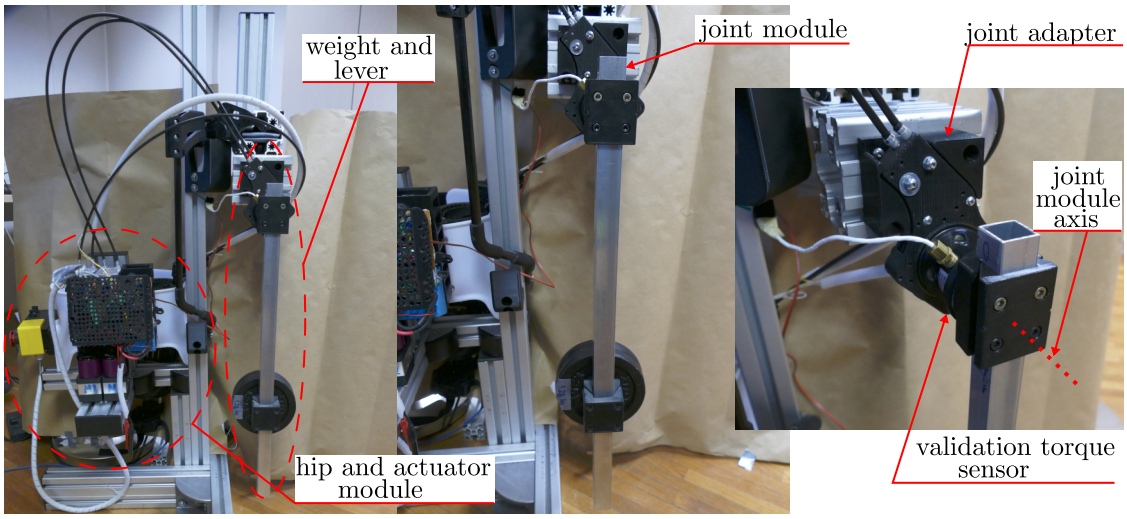


Figure 5.14: Experimental system. The Bowden joint module was removed from the exoskeleton's frame and mounted on an aluminium stand. A lever and a weight were mounted on the joint to allow the generation of an external torque. An additional torque sensor is used to validate the system.

the exoskeleton was removed from the frame and mounted on an aluminium stand. The main actuator of the exoskeleton, which is still attached to the hip orthosis, was lowered so that the Bowden cable sheath had a similar bending angle as in the actual application. This is important because the bending angle influences the amount of friction. A weight and a lever were mounted on the Bowden joint. An additional validation torque sensor

was mounted in between. The weights and the length of the lever were chosen so that a load of 10Nm is achieved when the lever is in the horizontal position ($\pm 90^{o}$). A second test setup is possible where the outer lever is rigidly fixed to prevent it from moving. In this configuration, the motor can apply torque but cannot move the lever. This is useful for tuning control parameters, to prevent chaotic oscillations of the lever if the controller becomes unstable.

Several measurements were carried out to collect data that sufficiently capture the characteristics of the system. The controller was in position-control mode, i.e., the motors are controlled in such a way that they overcome any friction. It is presented in Section 5.4.1. In its present form, the position controller does not take the elastic deformations of the system into account. However, due to the validation torque sensor this is not a problem. Several stops and starts of the entire system were performed to reduce the effects of the initial system calibration. Finally, the data was merged to facilitate the analysis.

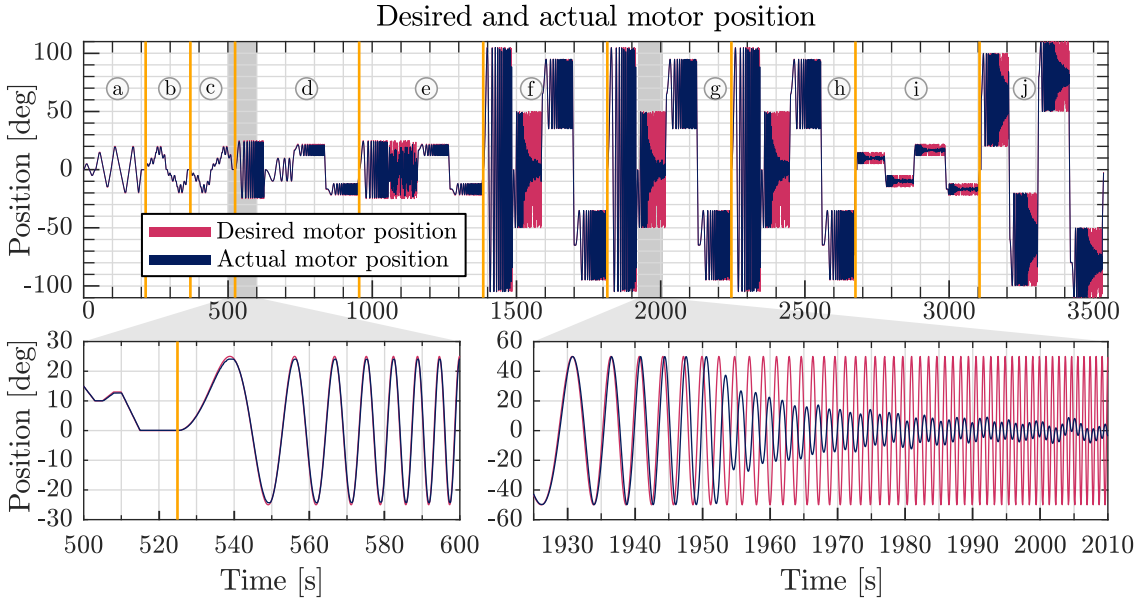


Figure 5.15: Position trajectory data, which shows the desired position of the motor and the actual motor position. The data is divided into several regions with vertical lines, indicating that the data represents multiple measurements.

The desired motor position and the actual motor position are shown in Fig. 5.15. Measured data is divided into several regions and marked with letters from a to j. The regions indicate the fact that several measurements have been made and that the data are merged, thus resulting in a total measurement time of 3535s. The external lever was fixed in the regions a, b, c, d, e and i. Higher external torque is easier to achieve when the external lever is fixed. The lever is free in regions f, g, h and j. Two 1.25 kg weights are attached to the lever at a distance from the respective axis to result in a combined load of 10Nm at $\pm 90^{o}$ position. In a, the lever is moved without the weights to measure the effects of friction and static friction at lower load levels. Only one of the two weights is used in g, and both weights are used in h and j measurements.

The respective external torque measurements are shown in Fig. 5.16. As can be seen in the left enlarged view between times 500s and 600s, the torque at the stitch between the measurements is not the same. The respective measurement stitches are marked via the orange vertical lines. This is due to the fact that the system is moved to the lowest position and the sensor readings are normalized to this value. Residual stiction friction

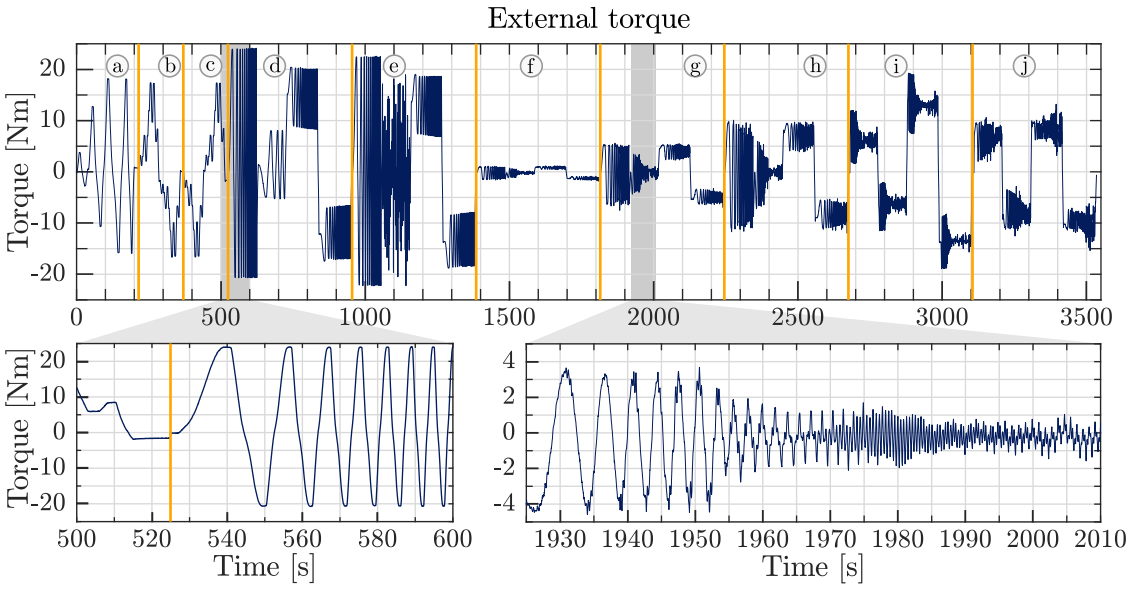


Figure 5.16: External torque data showing the actual external torque during each measurement.

may remain in the cables and prevent proper calibration. To counteract this, the system was recalibrated before each measurement.

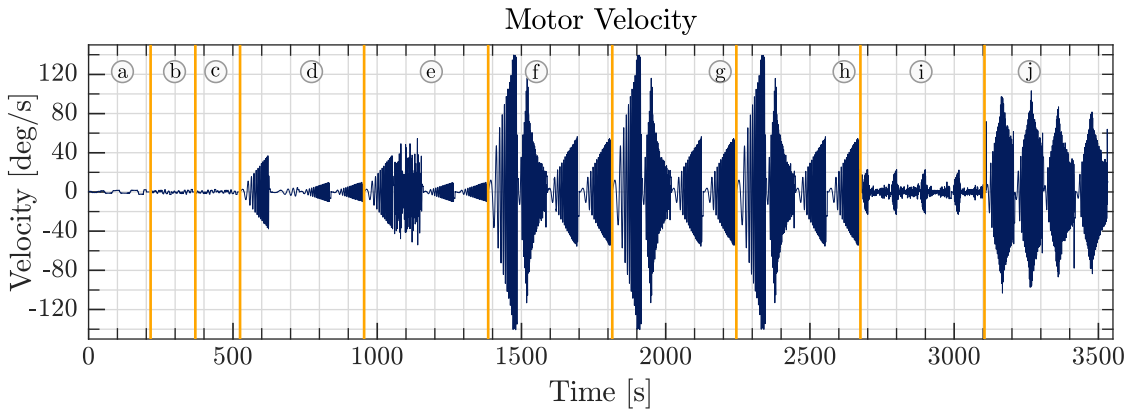


Figure 5.17: Motor velocity data showing the velocity of the motor.

Finally, velocity readings are shown in Fig. 5.17. The exoskeleton actuator data is used in combination with the validation torque sensor to fully describe the input and output signals of the system and identify the effects of friction. It is assumed that the selected friction model will be able to adequately capture the effect of friction in all cases, and that the chosen trajectory describes different torque/velocity states sufficiently well to derive it.

5.4.5 Friction Modelling & Compensation

System friction caused by Bowden cables is severe and poses a major problem, so effort is directed to reduce or mitigate the effects on control performance. The effect of friction is mitigated in a feed forward way. First, the friction is modelled by establishing a relation with motor velocity and desired torque. Secondly, this model is then applied to improve

the system performance. This section builds all three compensators shown in Fig. 5.12 in Section 5.4.2. The three models are:

FC1 that estimates the motor current needed for the motor to follow the desired torque given all the friction of the system.

FC2 that estimates the external torque using the integrated load cell mounted in between the motor and the Bowden cable. The load cell measures the forces on the ball screw and indirectly also the force in the cable that is influenced by the Bowden cable friction.

FC3 that estimates the external torque using the measurements of cable elongation, thus allowing for a relatively simple and inexpensive way of external torque approximation. The cable elongation can be approximated by position measurements both on the axis of the brushless motor and on the exoskeleton joint. The estimation is also affected by cable friction.

Figure 5.18 shows several 3-dimensional data plots of the experimental data gathered in previous Section 5.4.4. The surfaces shown are created through filtering of the data. As the data is collected in the time domain, it finally represents different areas of the X-axis and Y-axis of the respective surface plots with different densities. Both axes have been discretized. The motor velocity axis is sampled logarithmically (X-axis), while the other axis is sampled linearly (Y-axis). To build properly representative data, the measurements are averaged on the grid points shown below the surface plot. At each vertex, the data was averaged at a square shaped distance of half a step length from the adjacent sample point. Grid points without measurement were ignored. In all cases, a correlation between the axes exists which can be used to build a model. Three models are built, one for each compensation block (FC1, FC2 and FC3) in Fig. 5.12 in Section 5.4.2.

In **Fig. 5.18a**, the data captures the motor current in relation to external torque and motor velocity. As seen, both the velocity and external torque affect the required motor torque, i.e., current, to move the system. The relation between the motor current (I_m) with external torque (τ_ext) and motor velocity ($\dot{\varphi}_\mathrm{m}$) is described with the following equation:

$$\tau_\mathrm{m} \rightarrow I_\mathrm{m} \cdot k_\mathrm{a} = \tau_\mathrm{ext} + \tau_\mathrm{fr,FF}(\tau_\mathrm{ext}, \dot{\varphi}_\mathrm{m}). \tag{5.13}$$

Multiplication of the motor current I_m and the actuator torque constant k_a amounts to the torque the motor generates τ_m. This motor torque is equal to the summation of the external torque (τ_ext) and friction ($\tau_\mathrm{fr,FF}$). To move the Bowden joint with a desired torque, the motor needs to supply the desired torque and additional torque to overcome the friction. Friction $\tau_\mathrm{fr,FF}$ contains also other friction influences, like friction in bearings, etc. The equivalent motor torque is calculated using the k_a constant, i.e., actuator torque constant. k_a is not equivalent to the motor's torque constant, since it additionally also contains the transmission ratio of the system. Equation (5.13) shows the current required to reach a specific external torque. In this retrospect, the external torque is the desired torque ($\tau_\mathrm{ext} = \tau_\mathrm{des}$), and consequently, Eq. (5.13) is transformed into:

$$I_\mathrm{m} \cdot k_\mathrm{a} = \tau_\mathrm{des} + \tau_\mathrm{fr,FF}(\tau_\mathrm{des}, \dot{\varphi}_\mathrm{m}). \tag{5.14}$$

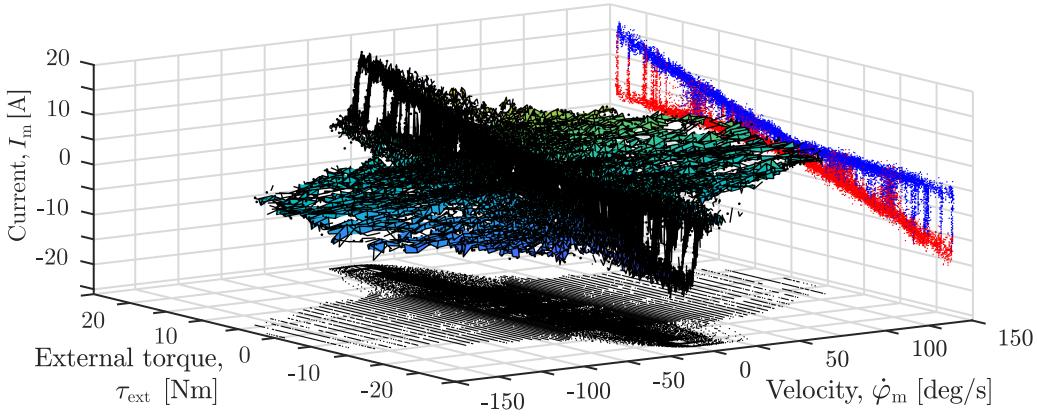
Current I_m can be calculated if the model of $\tau_\mathrm{fr,FF}$ and the k_a relation are known. Finally, the current estimate is calculated as:

$$I_\mathrm{m} \approx \frac{\tau_\mathrm{des} + F_\mathrm{nSCm,FF}(\tau_\mathrm{des}, \dot{\varphi}_\mathrm{m})}{k_\mathrm{a}}, \tag{5.15}$$

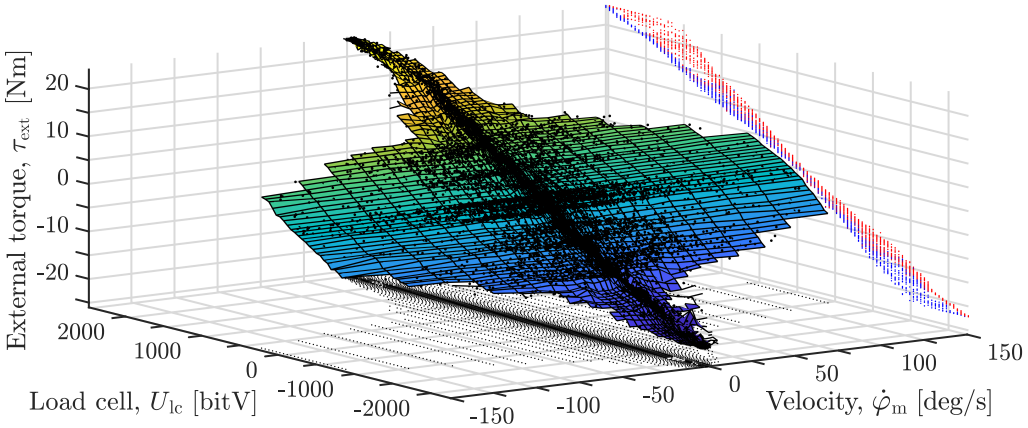
where $F_\mathrm{nSCm,FF}$ is the nonsymmetric Stribeck+Coulomb friction model.

Figures 5.18b,c show the correlation of the external torque with the load cell measurement and the cable elongation. Both also show the relation of the external torque

a) Motor current in relation to external torque and motor velocity



b) External torque in relation to load-cell reading and motor velocity



c) External torque in relation to cable elongation and motor velocity

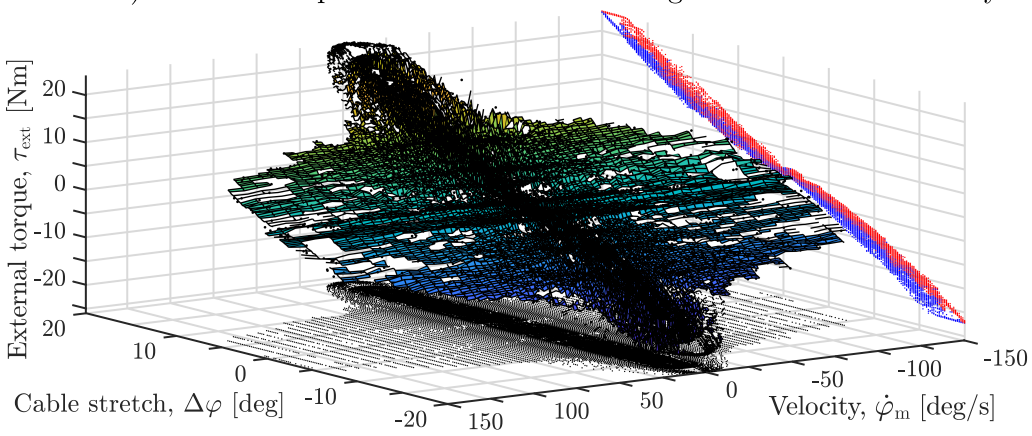


Figure 5.18: Experimental data plots. **a** shows the motor current in relation to external torque and motor velocity. **b** shows the external torque measurement in relation to load cell reading and motor velocity. **c** shows the external torque in relation to cable elongation and motor velocity. The black points at the bottom present the sampling grid that was used to create the filtered surface plot. Black dots are not drawn in areas without the data. The data is also projected onto the side plane, where blue dots stand for positive velocity data and negative velocity data.

to velocity. In both cases, exploiting the correlation and building a model allows future estimation of external torque based on the load cell measurements and cable elongation.

In **Fig. 5.18b**, the following equation describes the relation between the external torque, the load cell measurements and motor velocity:

$$\tau_{\mathrm{lc}} \rightarrow U_{\mathrm{lc}} \cdot n_{\mathrm{lc}}(U_{\mathrm{lc}}) = \tau_{\mathrm{ext}} + \tau_{\mathrm{fr,LC}}(\tau_{\mathrm{ext}}, \dot{\varphi}_{\mathrm{m}}). \tag{5.16}$$

The sensor signal (U_{lc}) is partly influenced by the friction of the Bowden cable, and a friction model is required to improve the signal quality. The load cell torque equivalent (τ_{lc}) is calculated by multiplying the load cell sensor reading (U_{lc}) with a transmission ratio ($n_{\mathrm{lc}}(U_{\mathrm{lc}})$). This ratio is, as seen later, not constant but dependent on U_{lc}. It is influenced by the material and electrical properties of the cell, the parameters of the amplifier circuit and by the mechanical transmission ratio. The final goal is to estimate the external torque, by using a model of $\tau_{\mathrm{fr,LC}}$ and by finding the relation $n_{\mathrm{lc}}(U_{\mathrm{lc}})$. Same as before, by using the symmetric Stribeck+Coulomb model ($F_{\mathrm{sSCm,LC}}$) to approximate $\tau_{\mathrm{fr,LC}}$. External torque estimate is then calculated as:

$$\tau_{\mathrm{ext,LC}} \approx U_{\mathrm{lc}} \cdot n_{\mathrm{lc}}(U_{\mathrm{lc}}) - F_{\mathrm{nSCm,LC}}. \tag{5.17}$$

where $F_{\mathrm{nSCm,LC}}$ is the nonsymmetric Stribeck+Coulomb friction model.

In **Fig. 5.18c**, the following equation describes the relation between the external torque, cable elongation measurement and motor velocity:

$$\tau_{\mathrm{ce}} \rightarrow K_{\mathrm{ce}}(\Delta\varphi) \cdot \Delta\varphi = \tau_{\mathrm{ext}} + \tau_{\mathrm{fr,CE}}(\tau_{\mathrm{ext}}, \dot{\varphi}_{\mathrm{m}}). \tag{5.18}$$

The deformation torque of the cable (τ_{ce}) is calculated by multiplying the cable elongation ($\Delta\varphi$) with the cable stiffness ($K_{\mathrm{ce}}(\Delta\varphi)$). This is then equal to the external torque (τ_{ext}) and any friction captured in $\tau_{\mathrm{fr,CE}}$. The $\Delta\varphi$ deformation is calculated as:

$$\Delta\varphi = \varphi_{\mathrm{m}} - \varphi_{\mathrm{ext}}. \tag{5.19}$$

While stiffness ($K_{\mathrm{ce}}(\Delta\varphi)$) is formulated as the stiffness of the cable, the term actually includes any mechanical transmission and elastic deformation of other components. The deformation torque is then equal to the external load and friction. Similar as before, the goal is to create a model that allows estimation of the external torque, taking into account the cable elongation and motor velocity. The external torque can be estimated using the following equation:

$$\tau_{\mathrm{ext,CE}} \approx K_{\mathrm{ce}}(\Delta\varphi) \cdot \Delta\varphi - F_{\mathrm{nSCm,CE}}, \tag{5.20}$$

where $F_{\mathrm{nSCm,CE}}$ is the nonsymmetric Stribeck+Coulomb friction model.

To find the three final nonsymmetric Stribeck+Coulomb friction models ($F_{\mathrm{nSCm,FF}}$, $F_{\mathrm{nSCm,LC}}$ and $F_{\mathrm{nSCm,CE}}$) and their corresponding parameters (k_{a}, $n_{\mathrm{lc}}(U_{\mathrm{lc}})$, $K_{\mathrm{ce}}(\Delta\varphi)$), a two-step **optimization process** is performed. The above nonsymmetric Stribeck+Coulomb friction models are optimized to best approximate the data from Fig. 5.18. The friction models are built using the Stribeck+Coulomb model specified in Section 5.4.3. Since the external torque also has an influence on the friction, a 2-dimensional Stribeck+Coulomb model is built. The axis opposite to the velocity is divided into equal pieces, and each of these pieces is then approximated using the Stribeck+Coulomb model. This essentially creates a table with Stribeck+Coulomb friction parameters that depend on the Y-axis, which is either the desired torque (Fig. 5.18a), load cell measurement (Fig. 5.18b) or cable stretch measurement (Fig. 5.18c). The final friction model contains separate Stribeck+Coulomb parameters for positive and negative motor velocity to account for nonsymmetric hardware characteristics. To calculate values between two discrete Y-axis values, we first calculate the resulting friction at the adjacent Stribeck+Coulomb curves at a given motor velocity. The friction value between them is then determined by linear interpolation. At the edges, the parameters are extrapolated using the two neighbouring curves.

Although the friction surface could also be approximated by other, more general approximation methods like neural networks or Gaussian-mixture models [183], this is not practical in the given situation for two reasons. The first problem is that the X-Y space is not completely filled or represented due to the limited power of the actuator. Actuator performance is limited due to both hardware limitations and safety reasons. Data is primarily missing at the corners of the X-Y space in Fig. 5.18, where the required motor power to achieve the torque/velocity state is the greatest. The second problem, which also affects the execution of the optimization, is the fact that the Bowden cables of the exoskeleton are not of equal length. As a result, the friction data on the velocity axis, i.e., its absolute value, are not symmetrical. Combined with the lack of data, i.e., the data is sometimes missing asymmetrically, which means that for a given Y-axis measurement, positive velocity data can be represented more than negative velocity data or vice versa. In such a situation, the optimization would give more weight to areas with more data, which eventually leads to a poor friction model for some data blocks of the external torque axis. For these two reasons, the data can still be well modelled and also safely extrapolated by exploiting the Stribeck+Coulomb model and combining it with the proposed optimization steps. In contrast, methods like neural networks or Gaussian mixture models are general approximation methods and do not contain an underlying mathematical friction model, which makes extrapolation of the data difficult.

The optimization is carried out in two steps. A symmetric Stribeck+Coulomb model is fitted to the data in the **first step** of the optimization. It is used to account for a possible nonsymmetric lack of velocity data that would result in bad estimates of k_a, $n_\mathrm{lc}(U_\mathrm{lc})$ and $K_\mathrm{ce}(\Delta\varphi)$. The problem arises because the estimates k_a, $n_\mathrm{lc}(U_\mathrm{lc})$ and $K_\mathrm{ce}(\Delta\varphi)$ are not completely independent with friction models $F_\mathrm{nSCm,FF}$, $F_\mathrm{nSCm,LC}$ and $F_\mathrm{nSCm,CE}$, as all contain elements that can scale the data. The symmetric Stribeck+Coulomb model does not distinguish between negative and positive velocity values and can thus offer a better estimation. Both the symmetric and the nonsymmetric Stribeck+Coulomb model are based on equations from Section 5.4.3. The only difference is that the nonsymmetric model performs a sign check on the velocity and then takes either the Stribeck+Coulomb parameter set for negative velocities or the one for positive velocities.

The **first step** of optimization is trying to optimize the following vectors:

$$\vec{x}_\mathrm{FF1,i} = [F_\mathrm{c,i}, F_\mathrm{s,i}, v_\mathrm{s,i}, k_\mathrm{v,i}, \delta_\mathrm{SCm,i}, k_\mathrm{a,i}]\,, \tag{5.21}$$

$$\vec{x}_\mathrm{LC1,i} = [F_\mathrm{c,i}, F_\mathrm{s,i}, v_\mathrm{s,i}, k_\mathrm{v,i}, \delta_\mathrm{SCm,i}, n_\mathrm{lc,i}]\,, \tag{5.22}$$

$$\vec{x}_\mathrm{CE1,i} = [F_\mathrm{c,i}, F_\mathrm{s,i}, v_\mathrm{s,i}, k_\mathrm{v,i}, \delta_\mathrm{SCm,i}, K_\mathrm{ce,i}]\,, \tag{5.23}$$

where i indicates a specific discrete Y-axis chunk of data. Each vector, i.e., model, is optimized separately. The first 5 parameters of the vector are the symmetric Stribeck+Coulomb parameters, while the last account for k_a, n_lc and K_ce in Eq. (5.15), (5.17) and (5.20), respectively. Matlab® *fmincon* constrained optimization function with multi-start property is used to find a global minimum of the above parameters. Parameters of vector in Eq. (5.21) are empirically constrained to lie between [0, 0, 0, 0, 0, 1] and [20, 1, 15, 25, 20, 5]. Parameters of vector in Eq. (5.22) are empirically constrained to lie between [0, 0, 0, 0, 0, -2] and [20, 20, 20, 20, 20, 2]. And, parameters of vector in Eq. (5.23) are empirically constrained to lie between [0, 0, 0, 0, 0, -10] and [100, 100, 100, 100, 100, 10]. Optimization tries to minimize the following *cost* functions:

$$cost_\mathrm{FF1,i} = \mathrm{MSE}\left(I_\mathrm{m,i} \cdot k_\mathrm{a,i}\,,\, \tau_\mathrm{ext,i} + F_\mathrm{sSCm,FF,i}\right), \tag{5.24}$$

$$cost_\mathrm{LC1,i} = \mathrm{MSE}\left(U_\mathrm{lc,i} \cdot n_\mathrm{lc,i}\,,\, \tau_\mathrm{ext,i} + F_\mathrm{sSCm,LC,i}\right), \tag{5.25}$$

$$cost_\mathrm{CE1,i} = \mathrm{MSE}\left(K_\mathrm{ce,i}(\Delta\varphi) \cdot \Delta\varphi\,,\, \tau_\mathrm{ext,i} + F_\mathrm{sSCm,CE,i}\right), \tag{5.26}$$

where i stands for each discrete Y-axis chunk of relevant data.

The resulting symmetric Stribeck+Coulomb models and relations k_{a}, n_{lc} and K_{ce} are shown in Fig. 5.19. In Figure 5.19a, $k_{\mathrm{a,i}}$ is assumed to remain constant independent of

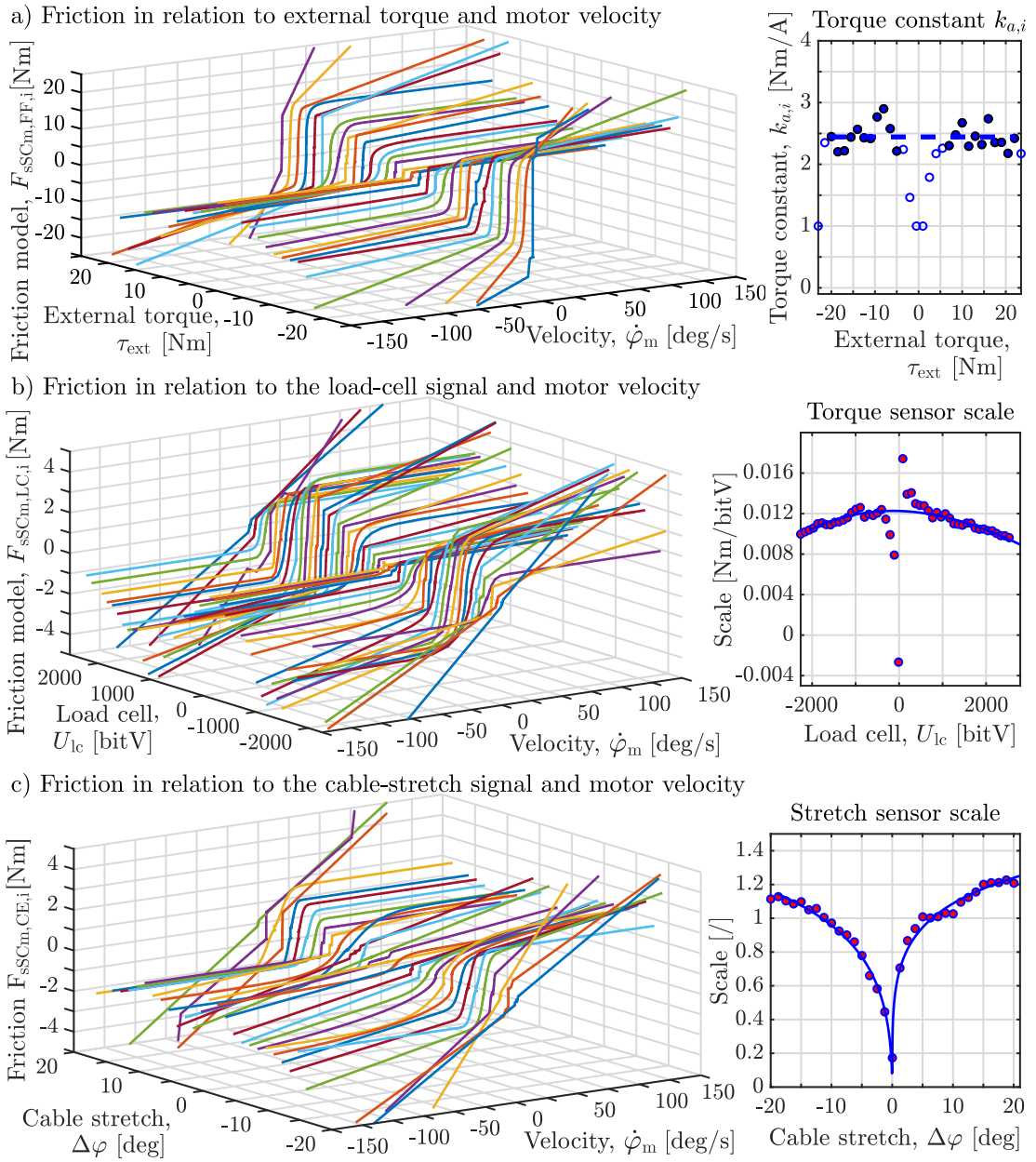


Figure 5.19: The respective symmetric Stribeck+Coulomb friction curves and the scale parameters. **a** shows the symmetric Stribeck+Coulomb friction curves $F_{\mathrm{sSCm,FF,i}}$,*left* and the parameter $k_{\mathrm{a,i}}$,*right*. **b** shows the symmetric Stribeck+Coulomb friction curves $F_{\mathrm{sSCm,LC,i}}$,*left* and the parameter $n_{\mathrm{lc,i}}$,*right*. **c** shows the symmetric Stribeck+Coulomb friction curves $F_{\mathrm{sSCm,CE,i}}$,*left* and the parameter $K_{\mathrm{ce,i}}$,*right*.

the external torque values. Since it combines the torque constant of the motor and the transmission of the system, it should be independently of the external torque. As shown in Fig. 5.19a,*right*, it remains relatively constant throughout the external torque, as expected. Due to missing measurement data, the values only deviate at the positive and negative limit of the external torque axis. It also deviates close to zero, because when the external

torque is close to zero, the current is also close to zero, as can be seen in Eq. (5.13). As I_{m} gets closer to zero, the actual $k_{\mathrm{a,i}}$ values become hard to determine, also because of the measurement noise. The final $k_{\mathrm{a}} = 2.44$ is calculated as the average of the $k_{\mathrm{a,i}}$ values. The first 10% and the last 10% and the middle 20% of the points are excluded for the reasons mentioned above, i.e., only the filled blue points in Fig. 5.19a,*right*, are used for approximation. This value differs from the theoretical $k_{\mathrm{a,th}}$, which is calculated as:

$$k_{\mathrm{a,th}} = k_{\mathrm{I}} \cdot n_{\mathrm{m,p}} = 0.035\mathrm{Nm/A} \cdot 97.74 = 3.42, \tag{5.27}$$

where $k_{\mathrm{I}} = 0.035\mathrm{Nm/A}$ and the transmission ratio is $n_{\mathrm{m,p}} = 97.74$. The motor torque constant is adapted from [179]. The optimization results indicate that the actual motor torque constant is probably different. These types of motors often do not come with accurate data about their internal characteristics, which is one of the reasons why they are less expensive.

As observed in Fig. 5.19b,*right*, it can be seen that $n_{\mathrm{lc}}(U_{\mathrm{lc}})$ is approximated with a polynomial function. The $n_{\mathrm{lc}}(U_{\mathrm{lc}})$ relation is approximated as:

$$n_{\mathrm{lc}}(U_{\mathrm{lc}}) = 2.5883\text{e-}14 \cdot {U_{\mathrm{lc}}}^3 - 4.5479\text{e-}10 \cdot {U_{\mathrm{lc}}}^2 - 1.2692\text{e-}7 \cdot U_{\mathrm{lc}} + 0.0123. \tag{5.28}$$

Finally, as observed in Fig. 5.19c,*right*, it can be seen that $K_{\mathrm{ce,i}}(\Delta\varphi)$ cannot be approximated with a constant value. It was approximated with the following equation:

$$K_{\mathrm{c}}(\Delta\varphi) = 0.602 \log((-x)^{0.592} + 1) \cdot \mathrm{heaviside}(-x) + 0.954 \log(x^{0.326} + 1) \cdot \mathrm{heaviside}(x). \tag{5.29}$$

Using the above relation, parameter K_{c} can be calculated to either be used for control purposes or to scale the data for the second optimization step.

The respective Stribeck+Coulomb parameter values for the symmetric model for all three compensators are shown in Fig. 5.20. Since k_{a}, n_{lc} and K_{ce} have been additionally approximated post first optimization step, the calculated symmetric Stribeck+Coulomb models are not correct any more. However, the calculation of symmetrical model parameters is not in vain, since they are used as starting points in the nonsymmetrical model optimization.

For the **second step** of optimization, k_{a}, n_{lc} and K_{ce} are first used to transform the data. The resulting motor current data $I_{\mathrm{m}}(\tau_{\mathrm{ext}}, \dot{\varphi}_{\mathrm{m}})$ are thus converted into motor torque data $\tau_{\mathrm{m}}(\tau_{\mathrm{ext}}, \dot{\varphi}_{\mathrm{m}})$, since:

$$\tau_{\mathrm{m}}(\tau_{\mathrm{ext}}, \dot{\varphi}_{\mathrm{m}}) = I_{\mathrm{m}}(\tau_{\mathrm{ext}}, \dot{\varphi}_{\mathrm{m}}) \cdot k_{\mathrm{a}}. \tag{5.30}$$

Equation (5.13) becomes:

$$\tau_{\mathrm{m}} = \tau_{\mathrm{ext}} + \tau_{\mathrm{fr,FF}}(\tau_{\mathrm{ext}}, \dot{\varphi}_{\mathrm{m}}). \tag{5.31}$$

In the same way, the load cell data is transformed using the $n_{\mathrm{lc}}(U_{\mathrm{lc}})$ relation, since:

$$\tau_{\mathrm{lc}} = U_{\mathrm{lc}} \cdot n_{\mathrm{lc}}(U_{\mathrm{lc}}). \tag{5.32}$$

Equation (5.16) becomes:

$$\tau_{\mathrm{lc}} = \tau_{\mathrm{ext}} + \tau_{\mathrm{fr,LC}}. \tag{5.33}$$

And finally, the cable stretch data is also transformed using the $K_{\mathrm{ce}}(\Delta\varphi)$ relation from Eq. (5.18), since:

$$\tau_{\mathrm{ce}} = K_{\mathrm{ce}}(\Delta\varphi) \cdot \Delta\varphi. \tag{5.34}$$

The measurement data is transformed into:

$$\tau_{\mathrm{ce}} = \tau_{\mathrm{ext}} + \tau_{\mathrm{fr,CE}}. \tag{5.35}$$

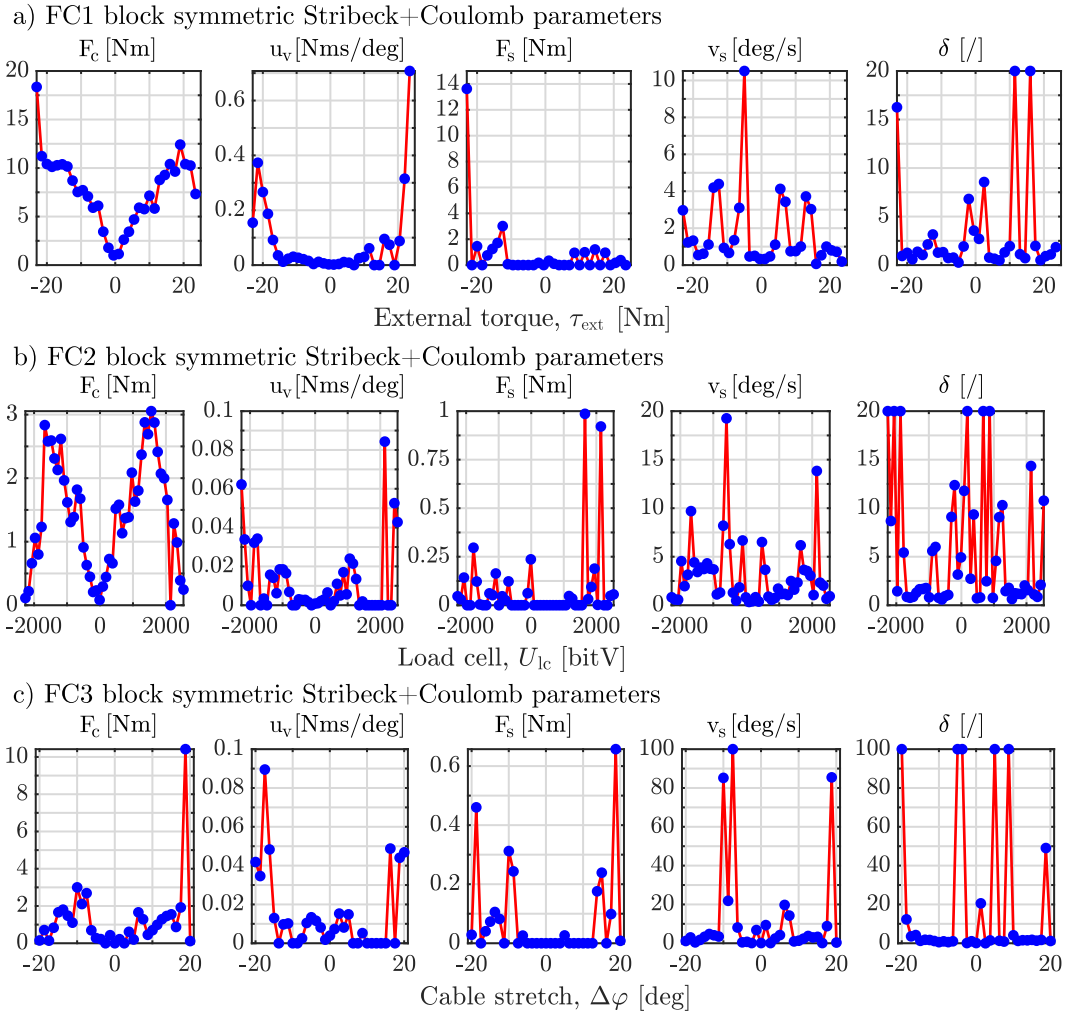


Figure 5.20: Values of the symmetric Stribeck+Coulomb friction model for each discrete value of external torque. For Fig. 5.19a,*left* in **a**, for Fig. 5.19b,*left* in **b** and Fig. 5.19c,*left* in **c**.

The second step of optimization finds nonsymmetric Stribeck+Coulomb models to approximate the frictions $\tau_{\mathrm{fr,FF}}$, $\tau_{\mathrm{fr,LC}}$ and $\tau_{\mathrm{fr,CE}}$ in Equations (5.31), (5.33) and (5.35). The respective nonsymmetric Stribeck+Coulomb models are $F_{\mathrm{nSCm,FF}}$, $F_{\mathrm{nSCm,LC}}$ and $F_{\mathrm{nSCm,CE}}$. The optimization vectors for the second step of optimization are:

$$\vec{x}_{\mathrm{FF2,i}} = \left[F^{-}_{\mathrm{c,i}}, F^{-}_{\mathrm{s,i}}, v^{-}_{\mathrm{s,i}}, k^{-}_{\mathrm{v,i}}, \delta^{-}_{\mathrm{SCm,i}}, F^{+}_{\mathrm{c,i}}, F^{+}_{\mathrm{s,i}}, v^{+}_{\mathrm{s,i}}, k^{+}_{\mathrm{v,i}}, \delta^{+}_{\mathrm{SCm,i}}\right], \tag{5.36}$$

$$\vec{x}_{\mathrm{LC2,i}} = \left[F^{-}_{\mathrm{c,i}}, F^{-}_{\mathrm{s,i}}, v^{-}_{\mathrm{s,i}}, k^{-}_{\mathrm{v,i}}, \delta^{-}_{\mathrm{SCm,i}}, F^{+}_{\mathrm{c,i}}, F^{+}_{\mathrm{s,i}}, v^{+}_{\mathrm{s,i}}, k^{+}_{\mathrm{v,i}}, \delta^{+}_{\mathrm{SCm,i}}\right], \tag{5.37}$$

$$\vec{x}_{\mathrm{CE2,i}} = \left[F^{-}_{\mathrm{c,i}}, F^{-}_{\mathrm{s,i}}, v^{-}_{\mathrm{s,i}}, k^{-}_{\mathrm{v,i}}, \delta^{-}_{\mathrm{SCm,i}}, F^{+}_{\mathrm{c,i}}, F^{+}_{\mathrm{s,i}}, v^{+}_{\mathrm{s,i}}, k^{+}_{\mathrm{v,i}}, \delta^{+}_{\mathrm{SCm,i}}\right]. \tag{5.38}$$

The positive and negative sign in the superscript classifies the parameters either to the negative or positive velocity. Again, Matlab® *fmincon* constrained optimization function with multi-start property is used to find a global minimum of the above parameters. The parameter values for vector Eq. (5.36) are constrained between [0, 0, 0, 0, 0, 0, 0, 0, 0, 0] and [20, 1, 15, 25, 20, 20, 1, 15, 25, 20]. The parameter values for vector Eq. (5.37) are constrained between [0, 0, 0, 0, 0, 0, 0, 0, 0, 0] and [20, 20, 20, 20, 20, 20, 20, 20, 20, 20]. And finally, the parameter values for vector Eq. (5.38) are constrained between [0,

0, 0, 0, 0, 0, 0, 0, 0, 0] and [100, 100, 100, 100, 100, 100, 100, 100, 100, 100]. Symmetric Stribeck+Coulomb parameter values are used as the starting point of optimization.

Optimization tries to minimize the following *cost* functions:

$$cost_{\mathrm{FF2,i}} = \mathrm{MSE}\left(\tau_{\mathrm{m,i}}\,,\ \tau_{\mathrm{ext,i}} + F_{\mathrm{nSCm,FF,i}}\right), \tag{5.39}$$

$$cost_{\mathrm{LC2,i}} = \mathrm{MSE}\left(\tau_{\mathrm{ext,i}}\,,\ \tau_{\mathrm{lc,i}} - F_{\mathrm{nSCm,LC,i}}\right), \tag{5.40}$$

$$cost_{\mathrm{CE2,i}} = \mathrm{MSE}\left(\tau_{\mathrm{ext,i}}\,,\ \tau_{\mathrm{ce,i}} - F_{\mathrm{nSCm,CE,i}}\right), \tag{5.41}$$

where i stands for each discrete Y-axis chunk of relevant data. The respective costs are minimized by finding the best approximation $F_{\mathrm{nSCm,FF,i}}$, $F_{\mathrm{nSCm,LC,i}}$ and $F_{\mathrm{nSCm,CE,i}}$.

The resulting nonsymmetric Stribeck+Coulomb parameters can be seen in Fig. 5.21. As expected, the values of the nonsymmetric parameters differ depending on the sign of

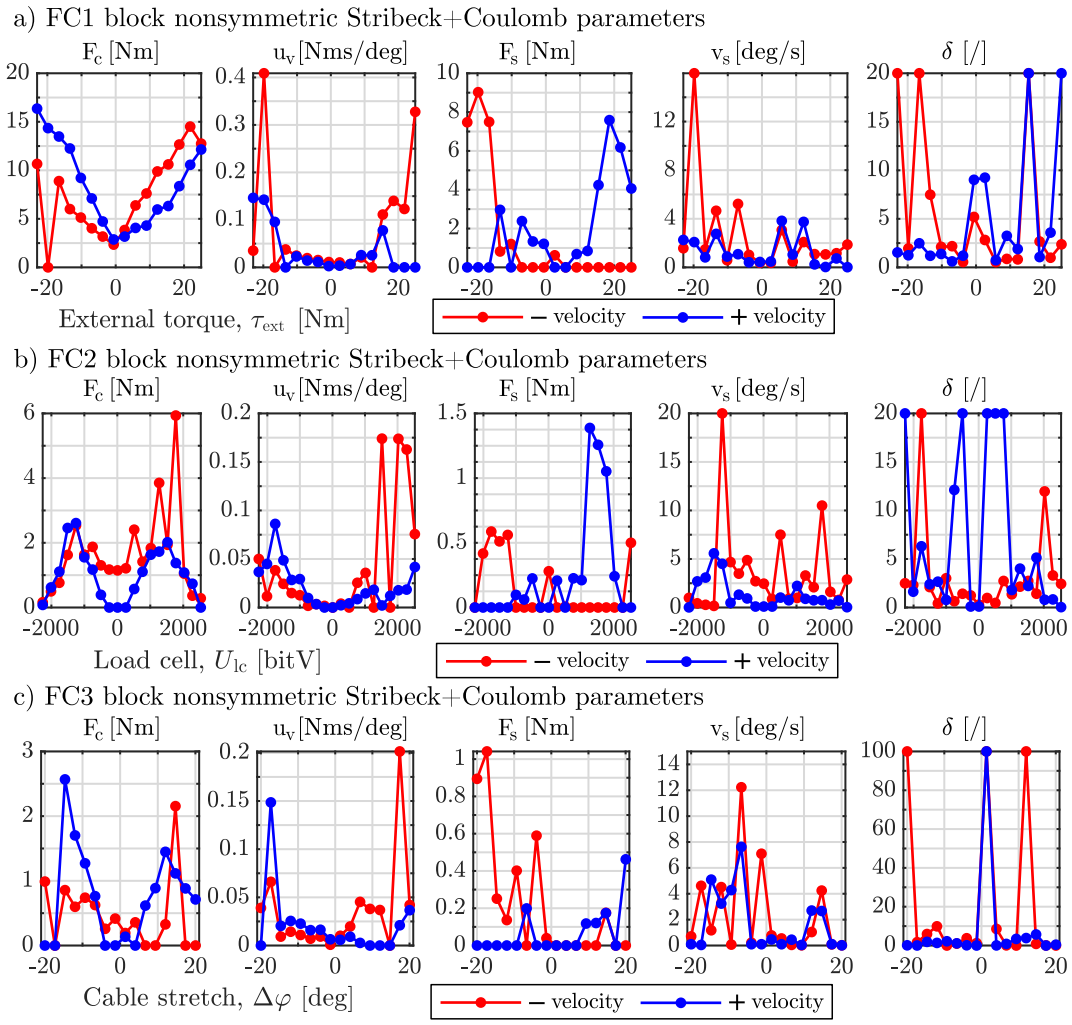


Figure 5.21: Values of the nonsymmetric Stribeck+Coulomb friction models. a shows $F_{\mathrm{nSCm,FF,i}}$, **b** shows $F_{\mathrm{nSCm,LC,i}}$ and **c** shows $F_{\mathrm{nSCm,CE,i}}$ models.

the motor velocity, and the proposed nonsymmetric model is able to capture this effect. The resulting Stribeck+Coulomb curves that correspond to the nonsymmetric parameters from Fig. 5.21 are shown in Fig. 5.22. Due to the lack of data, the curves are sometimes approximated in a strange way. For example, observe the red curve (second from negative direction of external torque) in 5.22a. However, for the given case and region, the friction

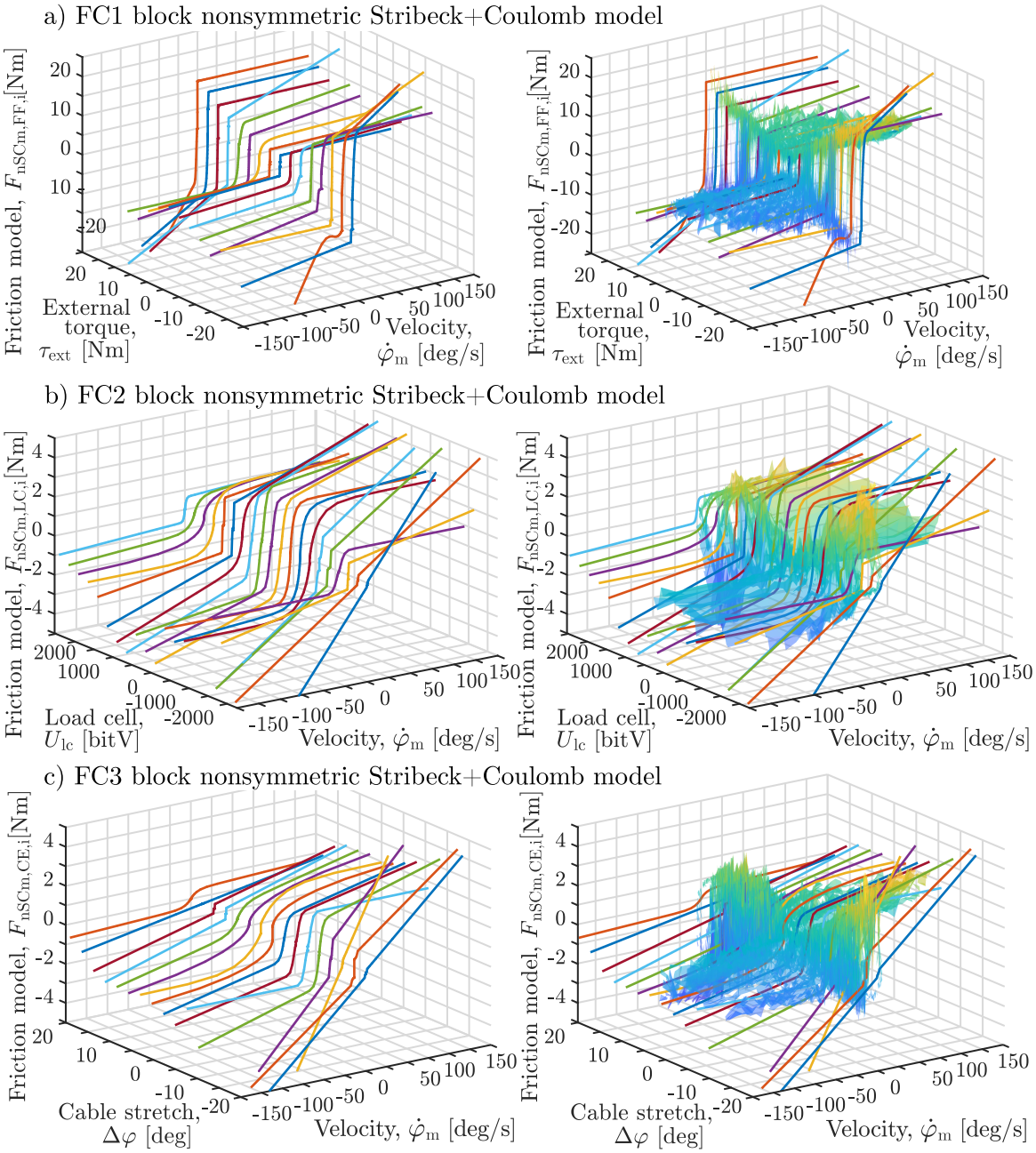


Figure 5.22: Stribeck+Coulomb curves for the nonsymmetric model. Curves for $F_{\mathrm{nSCm,FF,i}}$ are shown in **a**, for $F_{\mathrm{nSCm,LC,i}}$ are shown in **b** and for $F_{\mathrm{nSCm,CE,i}}$ in **c**. **a**, **b** and **c** show the bare curves in the *left* figure. Transparent surface data from Fig. 5.18 is added on top of the curves in the *right* figure.

models are nonetheless sufficient. For the motor current estimation, the MSE error between the actual value and the prediction drops from **7.476** to **1.621** when the optimally approximated friction model is applied. This denotes both that the influence of the friction is big and that the model improves the prediction. Similarly, the MSE between the actual external torque and the prediction of the two estimators:

- ◇ drops from **2.144** to **0.634** for the load cell-based external torque estimator,
- ◇ drops from **1.440** to **0.729** for the cable stretch-based external torque estimator.

Finally, the required feed-forward current is calculated as:

$$I_{\mathrm{m}} \approx \frac{\tau_{\mathrm{des}} + F_{\mathrm{nSCm,FF}}(\tau_{\mathrm{des}}, \dot{\varphi}_{\mathrm{m}})}{k_{\mathrm{a}}}, \tag{5.42}$$

where $F_{\mathrm{nSCm,FF}}$ is the nonsymmetric Stribeck+Coulomb friction model. The load cell-based external torque estimate is calculated as:

$$\tau_{\mathrm{ext,LC}} \approx U_{\mathrm{lc}} \cdot n_{\mathrm{lc}}(U_{\mathrm{lc}}) - F_{\mathrm{nSCm,LC}}, \tag{5.43}$$

where the nonsymmetric Stribeck+Coulomb model $F_{\mathrm{nSCm,LC}}$ is used in combination with the $n_{\mathrm{lc}}(U_{\mathrm{lc}})$ polynomial relation. And, the cable stretch-based external torque is calculated as:

$$\tau_{\mathrm{ext,CE}} \approx K_{\mathrm{ce}}(\Delta\varphi) \cdot \Delta\varphi - F_{\mathrm{nSCm,CE}}, \tag{5.44}$$

The constructed nonsymmetric Stribeck+Coulomb friction models are used to perform the final confirmation experiment in Section 5.5.2, as shown in the control algorithm in Fig. 5.12.

5.5 Experimental Results

5.5.1 Signal Comparison & Sensor Fusion

To improve the quality of the overall external torque estimation, the sensor readings from the load cell-based estimation and from the cable stretch-based estimation can be combined using sensor fusion methods to arrive at a better estimate. One of the easiest ways to combine two signals is with a **Complementary Filter**. The complementary filter blends two sources of data in a complementary manner as:

$$\tau_{\mathrm{compl}} = p \cdot \tau_{\mathrm{ext,LC}} + (1 - p) \cdot \tau_{\mathrm{ext,CE}}, \tag{5.45}$$

where value p lies between 0 and 1. The final signal is a mixture of both and often the combined signal quality increases because, for example, the noise is cancelled out. One of its advantages is the simplicity of implementation and easy optimization of p value. As a disadvantage, the filtering is not robust and if one of the input signals fails, the filter also fails. Another more known fusion method is the Kalman Filter [184]. However, while the Kalman Filter features a very robust way of sensor fusion, it comes with a higher mathematical complexity and requires a more complex tuning of its parameters. This is why at this stage, the complementary filter was chosen over the Kalman Filter.

The optimal p value from Eq. (5.45) can be found by iteration until p is found that results in minimal mean-square error between the external torque measurement and the equivalent complementary signal. In short, the following cost function is minimized:

$$cost_{\mathrm{compl}}(p) = \mathrm{MSE}\left(\tau_{\mathrm{ext}}\,,\, \tau_{\mathrm{compl}}(p)\right). \tag{5.46}$$

Results are shown in Fig. 5.23. Fig. 5.23,*left* shows the search for optimal p value. The fusion of both signals decreases the MSE error between the actual external torque estimate and the signal from the complementary filter. The optimal p value was found to be 0.54, which means that the ratio of the load cell signal is slightly larger compared to the cable stretch-based estimate.

Figure 5.23,*right* shows the comparison of MSE values between all the signals. It can be seen that using friction compensation improves the signals in all cases. The MSE of the raw load cell-based signal is 2.144 and is much higher than the raw cable stretch-based

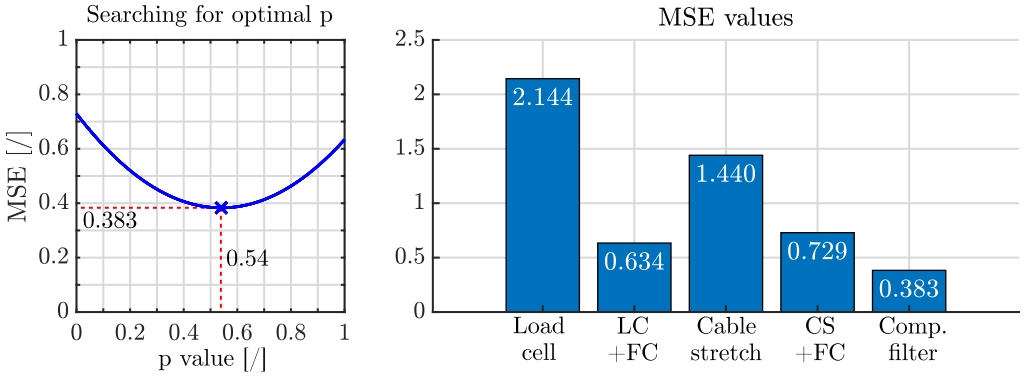


Figure 5.23: Calibration of the complementary filter and comparison between sensor signals. *Left* image shows the MSE values from Eq. (5.45) for different p values and also marks the optimal ratio. *Right* image gathers the MSE values for the above sensors. It shows the load cell-based signal and the effect of friction compensation (LC+FC) next to it. Cable stretch-based external torque estimation and the effect of friction compensation (CS+FC) is shown besides it. Finally, the MSE of the complementary filter is shown.

estimate. One reason for this is because the load cell captures a higher amount of friction. It was also observed that the load cell also measures a slight wobbling of the ball screw. Nevertheless, the use of the friction compensation model greatly reduces the error of the external torque estimate. The cable stretch-based estimate is lower than the load cell-based one. Part of the discrepancy between the actual measurements and the estimated ones can be attributed to the difficulties in system calibration. One difficulty is that for the cable stretch measurement two sensors are required to measure cable elongation, one attached to the exoskeleton joint and the other to the motor shaft. In the present configuration the exoskeleton joint is equipped with an absolute encoder. However, the rotation of the motor

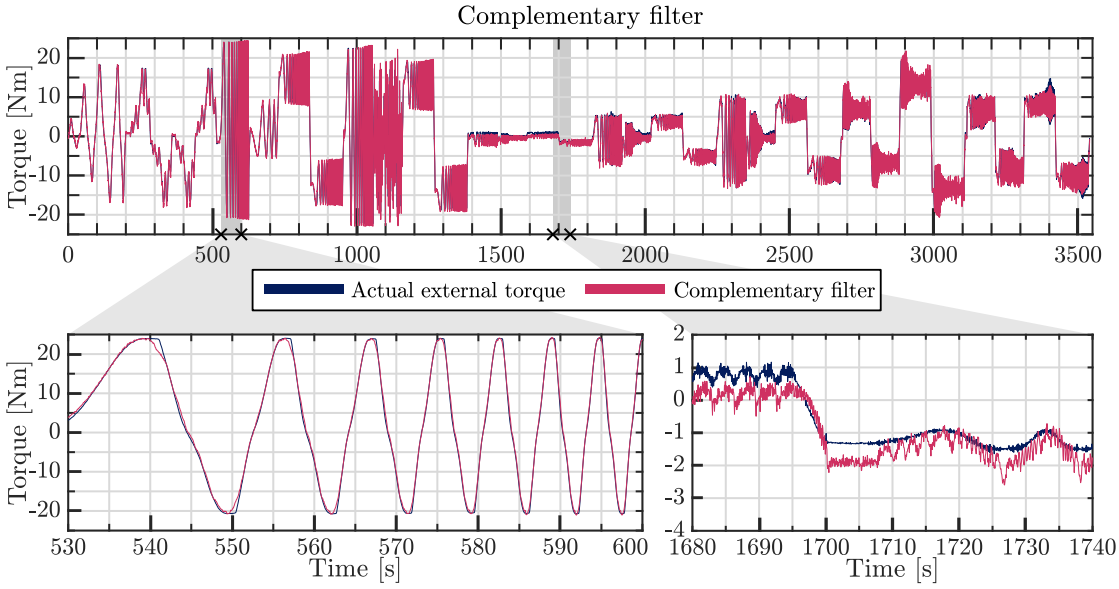


Figure 5.24: Comparison between the complementary signal and actual external torque measurements. Both signals are shown on the same graph. Two enlarged views are added for a clearer representation.

axis is measured by an incremental encoder. Consequently, the initial system calibration leads to a certain uncertainty in the cable elongation measurements.

The quality of the cable stretch-based external torque estimation increases when the friction compensation model is applied. However, the improvement is not as drastic as in the load cell estimate. This points to the fact that the Stribeck+Coulomb model could still be improved to better capture the system nonlinearities. Furthermore, there might also be other factors that affect the amount of friction in the system.

Finally, the complementary filter achieves the lowest MSE value, pointing at the fact that the signals can complement each other. The complementary filter signal is also shown in Fig. 5.24. The figure shows the actual torque measurements and compares them with the complementary filter signal. Overall, it follows the desired torque well when the system is moving and when the loads are high. Some discrepancies occur when the frictional force changes direction, i.e., at the peak of the measurements. It can be seen that friction modelling and sensor fusion methods manage to capture the friction model and derive it from the original signal to improve the quality of the external torque signal estimation.

5.5.2 Final Algorithm Implementation

To confirm the effect of each control element on the performance of the final controller, the controller was commanded to follow a torque curve consisting of a square wave and a sine wave. The external lever arm was fixed during the experiment, which means that every movement of the motor stretched the cable until the desired torque was reached. The external torque is then measured with the validation torque sensor mounted between the lever and the Bowden cable pulley.

The experiment evaluates the effect of the PID controller, the feed-forward elements and two external torque estimation sources, where one is based on the integrated load cell measurement and the other on the cable stretch measurement. When both torque estimation sources are used, the final sensor information is merged via the complementary filter at a ratio of $(0.54, 0.46)$ in favour of the load cell. While the PID controller usually consists of only three elements, the mention of the PID controller in this case also includes the forward acceleration and feedback acceleration elements. Controller block diagram is shown in Fig. 5.12 in Section 5.4.2. All five controller parameters are tuned empirically and their values are listed in Table 5.5. The experimental trajectory is run through 20 times,

Table 5.5: Controller parameters.

Parameter	Value	Comment
PID, K_P	0.8	proportionate gain
PID, K_D	0.02	derivative gain
PID, K_I	0	integration gain
$K_\mathrm{b} \cdot J_\mathrm{m}$	-0.125	acceleration feedback
$J_\mathrm{m}/K_\mathrm{s}$	0.0005	feedforward acceleration

with some of the control elements being either activated or deactivated during each run. In this way the effect of friction compensation can be clearly observed. The performance of the controller is evaluated by estimating the error between the desired and actual torque curve using the mean square error difference. The test results are summarized in Table 5.6. The table shows the mean squared error (MSE) numerically and graphically for each test run and also shows which elements of the controller have been enabled or disabled. The following observations can be made:

Table 5.6: Controller performance.

No.	PID	Load cell TS	Load cell TS+FC	Cable Stretch TS	Cable Stretch TS+FC	Feed-Forward	Feed-Forward +FC	MSE
1	■	■						15.293
2	■	■	■					13.324
3	■			■				16.059
4	■			■	■			15.273
5						■		26.516
6						■	■	25.285
7	■	■		■				15.025
8	■	■		■		■		7.792
9	■	■		■		■	■	5.582
10	■	■	■	■	■			14.489
11	■	■	■	■	■	■		7.027
12	■	■	■	■	■	■	■	**4.841**
13	■	■				■		7.817
14	■	■				■	■	5.507
15	■	■	■			■		6.775
16	■	■	■			■	■	**4.817**
17	■			■		■		8.682
18	■			■		■	■	5.709
19	■			■	■	■		7.421
20	■			■	■	■	■	**5.209**

The black squares (■) indicate the control element used in the given measurement. The PID stands for the proportional-integral-derivative controller and the acceleration feedforward and feedback. TS stands for torque sensor. FC stands for friction compensation. MSE stands for mean squared error.

- ◇ Use of feed-forward torque improves the controller performance in all cases, except in No. 5 and 6, where desired torque is fed forward without the PID controller element.
- ◇ The best result (no. 16) uses the load cell-based external torque estimation as feedback and the desired torque as feedforward. Both feedback and feedforward elements also use friction compensation.
- ◇ The use of external torque approximation based on cable strain, either in combination with the load cell-based approximation (no. 12) or as a stand-alone measurement (no. 20), gives a quality comparable to the load cell-based approximation (no. 16).

Fig. 5.25 shows the desired torque trajectory and three best cases.

The controller successfully tracks the trajectory, however, the trajectory is associated with various artefacts that also exhibit repeatable behaviour. Nevertheless, in light of the large amounts of friction, the system performs well. Observe that the sole use of the PID controller in combination with the feedforward and feedback of acceleration is not sufficient to ensure good trajectory tracking. During tuning of the PID controller, more aggressive PID parameters improved trajectory tracking. However, while the controller seemed to work well initially, the controller became unstable at some random wave of the squared signal. This is partly due to the stochastic nature of friction. The friction follows the mathematical model, but it can happen that the friction is slightly less than expected, which reduces the damping effect and leads to unstable controller behaviour. For this very reason, a less aggressive controller combined with feed-forward friction modelling gives better results. Looking at the magnified square wave from Fig. 5.25, the controller responses between the two peaks of the square wave profile are different, although the square wave remains the same. The reason can either lie in the hardware or in the quality

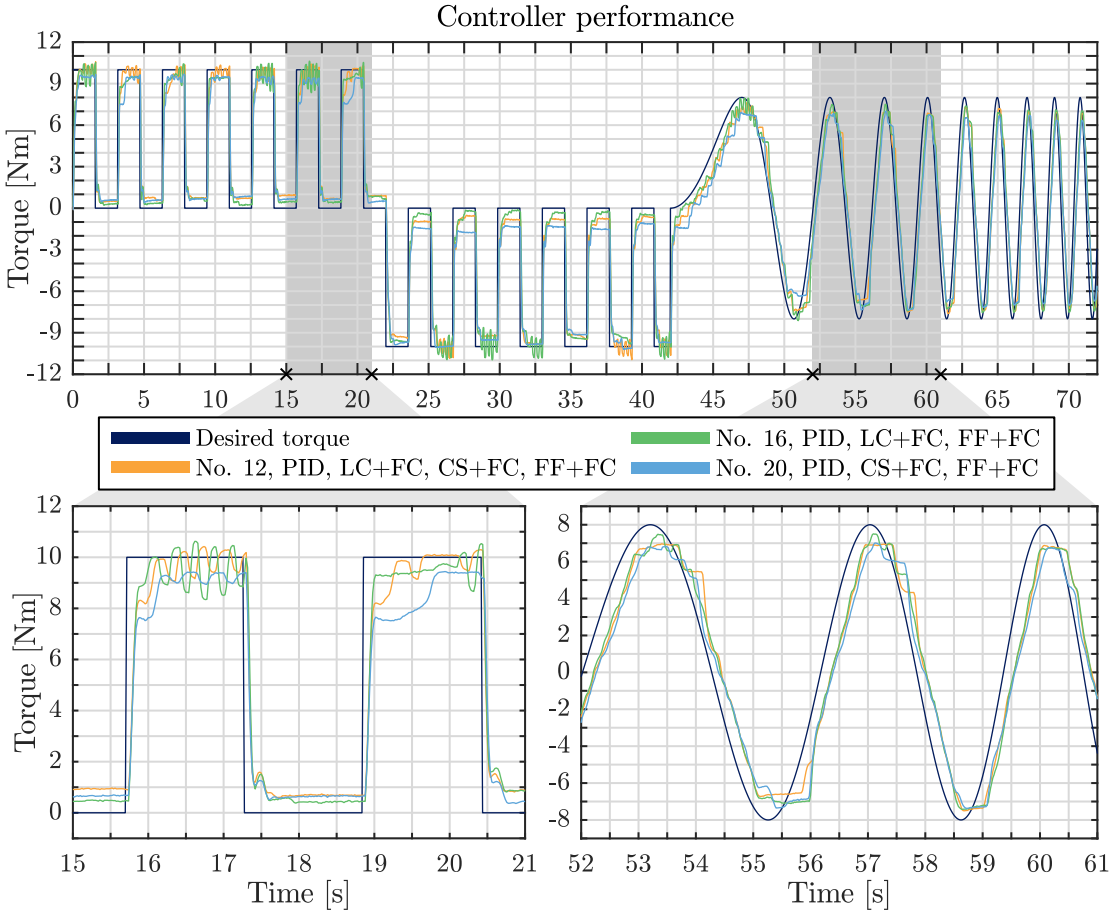


Figure 5.25: Final algorithm test. The graph shows the desired torque curve and the actual external torque for the three best cases (no. 12, 16 and 20) from Table 5.6.

of the friction model. The friction model has discrete properties, and consequently this can lead to small oscillations when the motor velocity is close to zero. Observe some oscillations in one peak and no oscillations in the other square wave peak. This again points to the unpredictable nature of friction compensation and shows that PID control elements should not be too aggressive. Presumably the quality of the controller could be improved by approximating a smoother friction model and using hardware solutions to reduce friction in the Bowden cables.

The cable stretch-based approximation is shown to produce external torque approximation of comparable quality. Lower precision and unreliability of the signal can be attributed to the fact that only the external link allows for absolute angle measurements, while the motor features only relative angle measurements. The equilibrium position of the cable was therefore estimated using the validation torque sensor at each system start-up and undoubtedly led to a certain inaccuracy of the cable stretch measurement. The results could be improved by using a second absolute encoder measurement. However, due to the high transmission ratio of the motor, the system would have to be extensively modified to allow such measurements. During the experiment it was also observed that the Bowden joint module deformed significantly under the external load. The external torques were high and peaked at about 20Nm. The cable stretch-based estimation could have become inaccurate as the modules got worn out due to large torque peaks. Nevertheless, the results point at the potential of the device and the measurement methods. To improve the results,

the next design iteration should therefore also include the reinforcement of the Bowden joint module.

5.6 Mechanically Compliant Exoskeleton

Although the proposed exoskeleton is mechanically compliant due to the elongation of the Bowden cable and possible elastic deformation of the components, it is not the ultimate goal of the design. The final goal is an exoskeleton device which is mechanically compliant with built-in variable stiffness mechanisms. Its stiffness can thus be adapted to any task. Due to increased complexity and time constraints, variable stiffness compliance has not been implemented at this stage. At this point only the concept is presented and briefly analysed.

The proposed design of the device and actuation system is favourable for the integration of variable stiffness compliance. There are several reasons for the above:

- ◇ The additional weight due to the introduction of a variable stiffness mechanism is placed on the user's back and the exoskeleton frame remains lightweight.
- ◇ Additional sensors and additional motors are localized on the actuation unit, which requires shorter electrical cables and makes it easier to design a cooling system.
- ◇ The possibility of cable routing and the use of redirection pulleys allows special architectures for easier integration of variable stiffness units, resulting in a smaller final actuator.

Normally, the variable stiffness units (VS) are integrated into the joints of the exoskeleton. Since these VS units are associated with additional weight and mechanical complexity, the mass and inertia of the exoskeleton joints increase. Similarly, additional components require more electrical conduits that have to be routed through the exoskeleton frame. As mentioned above, shifting all power components to the user's back with Bowden cables is advantageous in this area.

A concrete schematic example of the potential variable stiffness mechanism integration into the proposed device is shown in Fig. 5.26. Keeping the same underlying exoskeleton

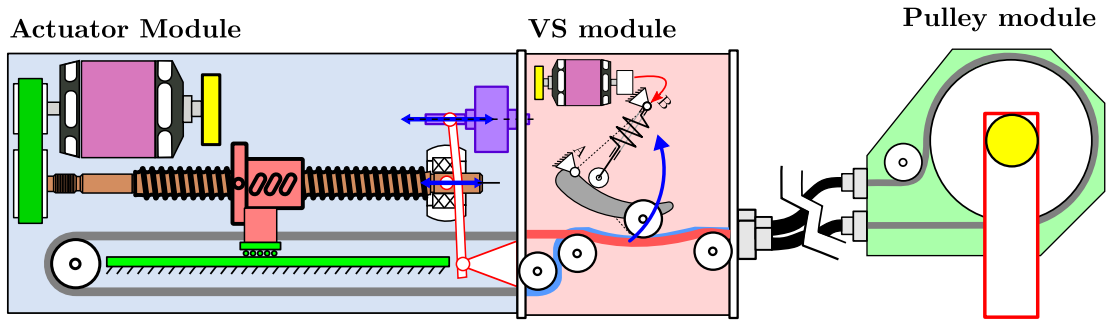


Figure 5.26: A schematic diagram of a novel actuator with variable stiffness. The proposed actuator unit of the upper limb exoskeleton remains the same. A variable stiffness unit is added above it to allow for mechanical compliance with stiffness variation.

actuation unit, the new unit with variable stiffness is simply mounted on the existing construction. For this variable stiffness unit, the developed PLVL-VSA concept can be used directly. One difference to the existing mathematical model of the PLVL-VSA is that in this case the elasticity of the cable must also be incorporated into it.

The proposed variable stiffness concept based on Bowden cables offers another advantage over many other modern variable stiffness architectures. The advantage is explained

through the MACCEPA actuator, which is shown in Fig. 5.27. Note that although MACCEPA is used as a reference, the assumptions are true for many other VS architectures. Looking at the MACCEPA, it can be seen that its position motor (M1 in Fig. 5.27) is fixed

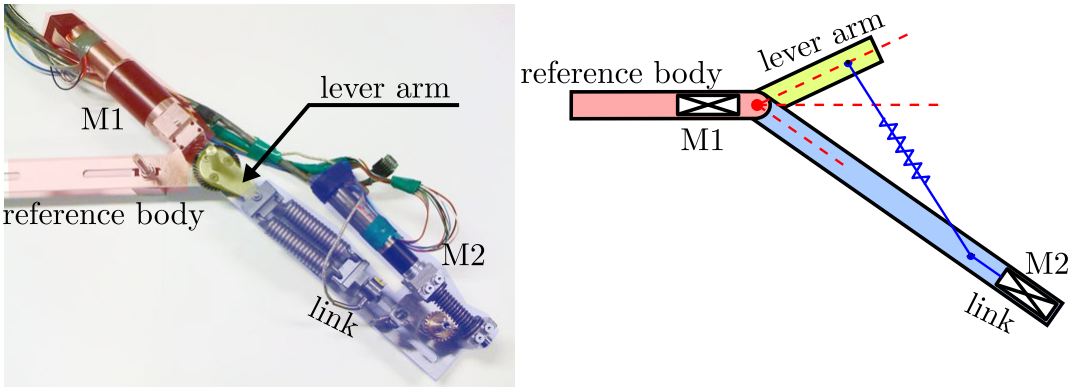


Figure 5.27: Analysis of MACCEPA actuator. The actual prototype is shown *left* and its schematic representation *right*. The original figures are adapted from [105].

to the reference body. If the motor M1 changes the equilibrium position of the system, it must move the *lever arm* and *link*. A passive elastic element couples the *lever arm* and *link* together. In Fig. 5.27, they are coloured *blue* and *yellow*.

However, when the motor moves the blue link, it also has to move the entire stiffness modification mechanism and its corresponding motor M2 that is attached onto it. It follows that the motor M1 must also overcome the inertia of the *blue* link as it moves. The inertia of the *blue* link is increased by the weight of the stiffness variation mechanism mounted on it. Depending on the sophistication of the stiffness variation mechanism, this weight is either higher or lower.

Unlike the MACCEPA example, the proposed system does not have the same problem. Its stiffness variation mechanism is mounted on the actuator. The movement of the cable to change the equilibrium position and therefore the movement of the external link does not require the movement of the stiffness variation mechanism base. This is considered an advantage because the *equilibrium* or *position* motor has reduced overall inertia.

5.7 Chapter Conclusion

The proposed exoskeleton device for the upper limbs paves the way for a novel mechanically compliant exoskeleton device. Its overall design meets the requirements of previous research studies. The ultimate goal is the construction of a mechanically compliant exoskeleton device with variable stiffness actuation. Although this adaptive compliance has many advantages, it also brings increased mechanical complexity and weight. For this very reason, the proposed exoskeleton device uses a Bowden cable transmission to distribute the actuation components to the user's back. The result is an exoskeleton frame that is light and has minimal inertia.

The same concept is also suitable for the integration of variable stiffness actuation. The same as with the position motors, the VS units are also integrated on the back of the user. The addition of the mechanically compliant units increases the weight but does not affect the lightness of the exoskeleton frame and maintains its inertia. Keeping the exoskeleton inertia low is an important feature. The final exoskeleton (frame included) weighs 7 kg without the mass of the battery (0.7 kg), where its frame weights about 1.8 kg. As stated

before, the VS units are not yet featured in the current exoskeleton prototype, however, the prototype design foresees such upgrades.

The proposed exoskeleton device has two actuators and both are attached to the back of the user. Via the Bowden cable transmission, the motors transfer their power to two Bowden joint modules. These are separate units equipped with a pulley. The connections of the exoskeleton frame can thus be connected to these Bowden joint modules and pulleys to finally obtain an exoskeleton device. Additional passive degrees of freedom increase the working range of the exoskeleton device.

The use of Bowden cables has the above-mentioned advantages, but also deteriorates the system performance due to the introduced nonlinearities. In this thesis, the effect of these nonlinearities is reduced through mathematical modelling of friction and through sensor fusion methods. It is shown that the measurement of cable stretch can be used to approximate the external torque. As a result, load cells become obsolete, which cannot only reduce the overall weight of the device, but also reduce its cost. Load cells are often costly and require specialized electronic circuits for signal amplification.

The development of the upper-arm exoskeleton was a critical step in achieving goal **G3: Develop an exoskeleton device that exploits the benefits of variable stiffness actuators** and confirming hypothesis **H3: An upper body exoskeleton design that conforms with the integration of variable stiffness compliant actuators (VSA) is possible.** Goal G3 and hypothesis H3 were reached and confirmed, respectively.

Chapter 6

Future Work and Conclusion

The research work began with the design, construction and testing of the passive ankle exoskeleton device. Its prototype and tests showed that it helps users even without the use of heavy motors and batteries. This is an important feature, as many currently commercially available devices are very heavy and allow for a limited battery time. Furthermore, the assistance of the passive device ranged between 7% to 15% in flat ground walking. Contrary to that, many commercially available devices struggle to achieve such performance with motors.

The core of the passive ankle exoskeleton is formed by the mechanically compliant technology. An elastic element with a certain stiffness is required for proper operation. The two user-oriented studies emphasized the potential of the device and the need for ergonomic design, proper exoskeleton kinematics and lightweight construction. During the user-oriented tests it was shown that the optimal stiffness is not immediately known. The cumbersome replacement of the passive elastic elements to change the stiffness of the mechanisms showed the need for a variable stiffness mechanism technology, which would enable on-the-fly stiffness variation. Therefore the research that followed was focused on such compliant technologies.

There are many architectures with variable stiffness, but many are associated with energetic inefficiency, complex mechanical design and increased weight. The exoskeleton system can only remain lightweight and energy-efficient if the compliant technology presented has such properties. For this purpose, a novel mechanically compliant actuator with efficient stiffness variation was developed. The properties of the novel mechanism were rigorously analysed and confirmed. Among other properties, a high speed of stiffness variation stood out. The PLVL-VSA drive was finally implemented into an elbow exoskeleton device.

However, despite its energy-efficient design that contributes to a lower final device mass, the PLVL-VSA device is still accompanied with nonnegligible weight. This impacts an exoskeleton device that exploits it primarily by increasing its link inertias, overall weight of the device and power requirements. To take this into account, a new exoskeleton device was developed. It is based on modular design techniques, which means that its exoskeleton frame can be redesigned without affecting its actuation unit. The device uses a Bowden cable transmission to distribute the heavy motors to the user's back so that the exoskeleton frame remains light. The Bowden cable transmission also provides opportunity for novel architectures for the integration of mechanically compliant mechanisms, reducing the effect of the additional weight that this compliant technology brings.

Overall, all three prototype designs can be researched further. For example, the passive ankle exoskeleton showed great potential, but its technology has not yet been studied in detail. The question remains as to what the optimal stiffness is and which parameters it depends on. Using the proposed variable stiffness mechanism to adjust stiffness during

walking could help to answer this question. Mechanical modifications or upgrades are also possible, that would improve its ergonomic design, which is one of the current passive exoskeleton prototype weaknesses.

Further research is also possible in the field of variable stiffness compliance. New techniques that were developed enable the search for new, more efficient architectures. These can be used either for the passive ankle exoskeleton or for the upper limb exoskeleton. Many potential synergies are also possible between these two devices. The construction of energy-efficient, lighter and compact units with variable stiffness would also have a more positive impact on the exoskeleton devices. Currently, the integration of mechanically compliant elements is associated with higher system complexity and additional weight.

Finally, the exoskeleton of the upper limbs offers room for many improvements. First, its software can be improved without major hardware upgrades. Due to the communication bottleneck of BBB-Odrive, the control frequency is limited to 50 Hz and would improve the quality of the control system if increased. The next bigger step is to find mechanical ways to reduce the friction in the Bowden cables. This would significantly improve the quality of the sensor signals and the efficiency of the proposed system. The exoskeleton actuator can be upgraded with a variable stiffness mechanism and transform the existing actuator into a variable stiffness actuator. Finally, the ergonomic properties of the exoskeleton frame were not studied in detail. Its structure can be improved with more ergonomic and compact design.

Our research has certainly answered some questions, but opened up many new ones.

References

[1] Eurostat Statistics Explained, *Disability statistics, eurostat (european commission)*, https://ec.europa.eu/eurostat/statistics-explained/index.php/Disability_statistics, visited on 20th March 2020.

[2] Eurostat (European Commission), *Ageing Europe - Looking at the lives of older people in the EU: 2019 edition*. Publications Office of the European Union, 2019. DOI: 10.2785/811048.

[3] Statistični urad Republike Slovenije, *Prebivalstvena piramida slovenija 1971-2080*, https://www.stat.si/PopPiramida/Piramida2.asp, visited on 20th March 2020.

[4] A. Gray, "Population ageing and health care expenditure," *Ageing Horizons*, vol. 2, pp. 15–20, 2005, (visited on 20th March 2020). [Online]. Available: https://www.ageing.ox.ac.uk/download/15.

[5] Eurostat Statistics Explained, *Population structure and ageing*, https://ec.europa.eu/eurostat/statistics-explained/index.php/Population_structure_and_ageing, visited on 20th March 2020.

[6] E. Stevens, E. Emmett, Y. Wang, C. McKevitt, and C. Wolfe, *The Burden of Stroke in Europe - report*. Stroke Alliance for Europe, 2017.

[7] D. P. Ferris, "The exoskeletons are here," *Journal of NeuroEngineering and Rehabilitation*, vol. 6, no. 1, 2009, ISSN: 1743-0003. DOI: 10.1186/1743-0003-6-17.

[8] S. Viteckova, P. Kutilek, and M. Jirina, "Wearable lower limb robotics: A review," *Biocybernetics and Biomedical Engineering*, vol. 33, no. 2, pp. 96–105, 2013. DOI: 10.1016/j.bbe.2013.03.005.

[9] L. M. Mooney, E. J. Rouse, and H. M. Herr, "Autonomous exoskeleton reduces metabolic cost of human walking during load carriage," *Journal of NeuroEngineering and Rehabilitation*, vol. 11, no. 1, p. 80, 2014. DOI: 10.1186/1743-0003-11-80.

[10] A. M. Dollar and H. Herr, "Lower extremity exoskeletons and active orthoses: Challenges and state-of-the-art," *IEEE Transactions on Robotics*, vol. 24, no. 1, pp. 144–158, 2008. DOI: 10.1109/tro.2008.915453.

[11] D. P. Ferris, G. S. Sawicki, and A. Domingo, "Powered lower limb orthoses for gait rehabilitation," *Topics in spinal cord injury rehabilitation*, vol. 11, no. 2, p. 34, 2005. DOI: 10.1310/6GL4-UM7X-519H-9JYD.

[12] Ekso Bionics Holdings Inc., *Ekso Bionics Releases its Upgraded EksoPulse Platform, Advanced Cloud-Based Analytics for Robotic Exoskeleton-Assisted Rehabilitation*, https://ir.eksobionics.com/press-releases/detail/676/ekso-bionics-releases-its-upgraded-eksopulse-platform, visited on 20th March 2020.

[13] J. Babič, T. Petrič, K. Mombaur, I. Kingma, J. Bornmann, J. González-Vargas, S. Baltrusch, N. Šarabon, and H. Houdijk, "SPEXOR: Design and development of passive spinal exoskeletal robot for low back pain prevention and vocational reintegration," *SN Applied Sciences*, vol. 1, no. 3, 2019. DOI: 10.1007/s42452-019-0266-1.

[14] Bioservo Technologies AB, *Applications for Ironhand*, https://www.bioservo.com/professional/ironhand-applications, visited on 20th March 2020.

[15] Global Market Insights, Inc, *Exoskeleton market to surpass $3.5bn by 2026: Global market insights, inc.* https://www.globenewswire.com/news-release/2018/12/19/1669201/0/en/Exoskeleton-Market-to-surpass-3-5bn-by-2026-Global-Market-Insights-Inc.html, visited on 20th March 2020.

[16] ResearchAndMarkets.com, *Global exoskeletons market study 2018-2026: Recent trends & growth prospects for leading exoskeleton developers & researchers*, https://www.globenewswire.com/news-release/2019/08/29/1908598/0/en/Global-Exoskeletons-Market-Study-2018-2026-Recent-Trends-Growth-Prospects-for-Leading-Exoskeleton-Developers-Researchers.html, visited on 20th March 2020.

[17] Exoskeleton Report LLC, *Exoskeleton Catalog*, http://exoskeletonreport.com/product-category/exoskeleton-catalog/, visited on 20th March 2020.

[18] S. Mohammed and Y. Amirat, "Towards intelligent lower limb wearable robots: Challenges and perspectives - state of the art," pp. 312–317, 2009. DOI: 10.1109/robio.2009.4913022.

[19] R. Jimenez-Fabian and O. Verlinden, "Review of control algorithms for robotic ankle systems in lower-limb orthoses, prostheses, and exoskeletons," *Medical engineering & physics*, vol. 34, no. 4, pp. 397–408, 2012. DOI: 10.1016/j.medengphy.2011.11.018.

[20] J. Zhang, C. C. Cheah, and S. H. Collins, "Experimental comparison of torque control methods on an ankle exoskeleton during human walking," *2015 IEEE International Conference on Robotics and Automation (ICRA)*, pp. 5584–5589, 2015. DOI: 10.1109/icra.2015.7139980.

[21] A. Gams, T. Petrič, T. Debevec, and J. Babič, "Effects of robotic knee exoskeleton on human energy expenditure," *IEEE Transactions on Biomedical Engineering*, vol. 60, no. 6, pp. 1636–1644, 2013. DOI: 10.1109/TBME.2013.2240682.

[22] D. Ferris and C. Lewis, "Robotic lower limb exoskeletons using proportional myoelectric control," *2009 Annual International Conference of the IEEE Engineering in Medicine and Biology Society*, pp. 2119–2124, 2009. DOI: 10.1109/iembs.2009.5333984.

[23] J. Zhang, P. Fiers, K. A. Witte, R. W. Jackson, K. L. Poggensee, C. G. Atkeson, and S. H. Collins, "Human-in-the-loop optimization of exoskeleton assistance during walking," *Science*, vol. 356, no. 6344, pp. 1280–1284, 2017. DOI: 10.1126/science.aal5054.

[24] M. Kim, Y. Ding, P. Malcolm, J. Speeckaert, C. J. Siviy, C. J. Walsh, and S. Kuindersma, "Human-in-the-loop bayesian optimization of wearable device parameters," *PLOS ONE*, vol. 12, no. 9, X. Hu, Ed., e0184054, 2017. DOI: 10.1371/journal.pone.0184054.

[25] S. Galle, P. Malcolm, W. Derave, and D. D. Clercq, "Adaptation to walking with an exoskeleton that assists ankle extension," *Gait & Posture*, vol. 38, no. 3, pp. 495–499, 2013. DOI: 10.1016/j.gaitpost.2013.01.029.

[26] S. M. Cain, K. E. Gordon, and D. P. Ferris, "Locomotor adaptation to a powered ankle-foot orthosis depends on control method," *Journal of NeuroEngineering and Rehabilitation*, vol. 4, no. 1, 2007. DOI: 10.1186/1743-0003-4-48.

[27] C. Walsh, D. Paluska, K. Pasch, W. Grand, A. Valiente, and H. Herr, "Development of a lightweight, underactuated exoskeleton for load-carrying augmentation," *Proceedings 2006 IEEE International Conference on Robotics and Automation ICRA*, pp. 3485–3491, 2006. DOI: 10.1109/robot.2006.1642234.

[28] Y. Ding, I. Galiana, A. T. Asbeck, S. M. M. D. Rossi, J. Bae, T. R. T. Santos, V. L. de Araujo, S. Lee, K. G. Holt, and C. Walsh, "Biomechanical and physiological evaluation of multi-joint assistance with soft exosuits," *IEEE Transactions on Neural Systems and Rehabilitation Engineering*, vol. 25, no. 2, pp. 119–130, 2017. DOI: 10.1109/tnsre.2016.2523250.

[29] A. T. Asbeck, S. M. D. Rossi, I. Galiana, Y. Ding, and C. J. Walsh, "Stronger, smarter, softer: Next-generation wearable robots," *IEEE Robotics & Automation Magazine*, vol. 21, no. 4, pp. 22–33, 2014. DOI: 10.1109/mra.2014.2360283.

[30] G. Grioli, S. Wolf, M. Garabini, M. Catalano, E. Burdet, D. Caldwell, R. Carloni, W. Friedl, M. Grebenstein, M. Laffranchi, D. Lefeber, S. Stramigioli, N. Tsagarakis, M. van Damme, B. Vanderborght, A. Albu-Schaeffer, and A. Bicchi, "Variable stiffness actuators: The user's point of view," *The International Journal of Robotics Research*, vol. 34, no. 6, pp. 727–743, 2015. DOI: 10.1177/0278364914566515.

[31] A. Albu-Schaffer, O. Eiberger, M. Grebenstein, S. Haddadin, C. Ott, T. Wimbock, S. Wolf, and G. Hirzinger, "Soft robotics," *IEEE Robotics & Automation Magazine*, vol. 15, no. 3, pp. 20–30, 2008. DOI: 10.1109/mra.2008.927979.

[32] M. del Carmen Sanchez-Villamañan, J. Gonzalez-Vargas, D. Torricelli, J. C. Moreno, and J. L. Pons, "Compliant lower limb exoskeletons: A comprehensive review on mechanical design principles," *Journal of NeuroEngineering and Rehabilitation*, vol. 16, no. 1, 2019. DOI: 10.1186/s12984-019-0517-9.

[33] R. M. Alexander, "Three uses for springs in legged locomotion," *The International Journal of Robotics Research*, vol. 9, no. 2, pp. 53–61, 1990. DOI: 10.1177/027836499000900205.

[34] G. S. Sawicki, C. L. Lewis, and D. P. Ferris, "It pays to have a spring in your step," *Exercise and Sport Sciences Reviews*, vol. 37, no. 3, pp. 130–138, 2009. DOI: 10.1097/jes.0b013e31819c2df6.

[35] B. Vanderborght, A. Bicchi, E. Burdet, D. Caldwell, R. Carloni, M. Catalano, G. Ganesh, M. Garabini, M. Grebenstein, S. Haddadin, M. Laffranchi, D. Lefeber, F. Petit, N. Tsagarakis, M. V. Damme, R. V. Ham, L. C. Visser, and S. Wolf, "Variable impedance actuators: Moving the robots of tomorrow," *2012 IEEE/RSJ International Conference on Intelligent Robots and Systems*, pp. 5454–5455, 2012. DOI: 10.1109/iros.2012.6385433.

[36] C. B. Cunningham, N. Schilling, C. Anders, and D. R. Carrier, "The influence of foot posture on the cost of transport in humans," *Journal of Experimental Biology*, vol. 213, no. 5, pp. 790–797, 2010. DOI: 10.1242/jeb.038984.

[37] D. W. Haldane, M. M. Plecnik, J. K. Yim, and R. S. Fearing, "Robotic vertical jumping agility via series-elastic power modulation," *Science Robotics*, vol. 1, no. 1, eaag2048, 2016. DOI: 10.1126/scirobotics.aag2048.

[38] D. E. Lieberman and D. M. Bramble, "The evolution of marathon running," *Sports Medicine*, vol. 37, no. 4, pp. 288–290, 2007. DOI: 10.2165/00007256-200737040-00004.

[39] P. J. Darlington, "Group selection, altruism, reinforcement, and throwing in human evolution.," *Proceedings of the National Academy of Sciences*, vol. 72, no. 9, pp. 3748–3752, 1975. DOI: 10.1073/pnas.72.9.3748.

[40] G. Pratt and M. Williamson, "Series elastic actuators," *Proceedings 1995 IEEE/RSJ International Conference on Intelligent Robots and Systems. Human Robot Interaction and Cooperative Robots*, vol. 1, pp. 399–406, 1995. DOI: 10.1109/iros.1995.525827.

[41] S. Wolf, G. Grioli, O. Eiberger, W. Friedl, M. Grebenstein, H. Hoppner, E. Burdet, D. G. Caldwell, R. Carloni, M. G. Catalano, D. Lefeber, S. Stramigioli, N. Tsagarakis, M. V. Damme, R. V. Ham, B. Vanderborght, L. C. Visser, A. Bicchi, and A. Albu-Schaffer, "Variable stiffness actuators: Review on design and components," *IEEE/ASME Transactions on Mechatronics*, vol. 21, no. 5, pp. 2418–2430, 2016. DOI: 10.1109/tmech.2015.2501019.

[42] R. Ham, T. Sugar, B. Vanderborght, K. Hollander, and D. Lefeber, "Compliant actuator designs," *IEEE Robotics & Automation Magazine*, vol. 16, no. 3, pp. 81–94, 2009. DOI: 10.1109/mra.2009.933629.

[43] J. Saldien, K. Goris, B. Vanderborght, J. Vanderfaeillie, and D. Lefeber, "Expressing emotions with the social robot probo," *International Journal of Social Robotics*, vol. 2, no. 4, pp. 377–389, 2010. DOI: 10.1007/s12369-010-0067-6.

[44] B. Kim and A. D. Deshpande, "Design of nonlinear rotational stiffness using a noncircular pulley-spring mechanism," *Journal of Mechanisms and Robotics*, vol. 6, no. 4, p. 041009, 2014. DOI: 10.1115/1.4027513.

[45] B. Vanderborght, B. Verrelst, R. V. Ham, M. V. Damme, D. Lefeber, B. M. Y. Duran, and P. Beyl, "Exploiting natural dynamics to reduce energy consumption by controlling the compliance of soft actuators," *The International Journal of Robotics Research*, vol. 25, no. 4, pp. 343–358, 2006. DOI: 10.1177/0278364906064566.

[46] B. Ugurlu, C. Doppmann, M. Hamaya, P. Forni, T. Teramae, T. Noda, and J. Morimoto, "Variable ankle stiffness improves balance control: Experiments on a bipedal exoskeleton," *IEEE/ASME Transactions on Mechatronics*, vol. 21, no. 1, pp. 1–1, 2015. DOI: 10.1109/tmech.2015.2448932.

[47] D. Popov, I. Gaponov, and J.-H. Ryu, "Towards variable stiffness control of antagonistic twisted string actuators," *2014 IEEE/RSJ International Conference on Intelligent Robots and Systems*, pp. 2789–2794, 2014. DOI: 10.1109/iros.2014.6942944.

[48] L. Flynn, J. Geeroms, R. Jimenez-Fabian, B. Vanderborght, N. Vitiello, and D. Lefeber, "Ankle–knee prosthesis with active ankle and energy transfer: Development of the CYBERLEGs alpha-prosthesis," *Robotics and Autonomous Systems*, vol. 73, pp. 4–15, 2015. DOI: 10.1016/j.robot.2014.12.013.

[49] M. Grebenstein, A. Albu-Schaffer, T. Bahls, M. Chalon, O. Eiberger, W. Friedl, R. Gruber, S. Haddadin, U. Hagn, R. Haslinger, H. Hoppner, S. Jorg, M. Nickl, A. Nothhelfer, F. Petit, J. Reill, N. Seitz, T. Wimbock, S. Wolf, T. Wusthoff, and G. Hirzinger, "The DLR hand arm system," *2011 IEEE International Conference on Robotics and Automation*, vol. 1, pp. 3175–3182, 2011. DOI: 10.1109/icra.2011.5980371.

[50] H. Vu, R. Pfeifer, F. Iida, and X. Yu, "Improving energy efficiency of hopping locomotion by using a variable stiffness actuator," *IEEE/ASME Transactions on Mechatronics*, vol. 21, pp. 1–1, 2015. DOI: 10.1109/tmech.2015.2428274.

[51] A. S, M. S, and P. V, "Modeling and application of series elastic actuators for force control multi legged robots," *Journal of Computing*, vol. 1, pp. 26–33, 1 Dec. 20, 2009. arXiv: 0912.3956v1 [cs.RO].

[52] K. Isik, S. He, J. Ho, and L. Sentis, "Re-engineering a high performance electrical series elastic actuator for low-cost industrial applications," *Actuators*, vol. 6, no. 1, p. 5, 2017. DOI: 10.3390/act6010005.

[53] S. H. Collins, M. B. Wiggin, and G. S. Sawicki, "Reducing the energy cost of human walking using an unpowered exoskeleton," *Nature*, vol. 522, no. 7555, pp. 212–215, 2015. DOI: 10.1038/nature14288.

[54] B. Vanderborght, A. Albu-Schaeffer, A. Bicchi, E. Burdet, D. Caldwell, R. Carloni, M. Catalano, O. Eiberger, W. Friedl, G. Ganesh, M. Garabini, M. Grebenstein, G. Grioli, S. Haddadin, H. Hoppner, A. Jafari, M. Laffranchi, D. Lefeber, F. Petit, S. Stramigioli, N. Tsagarakis, M. V. Damme, R. V. Ham, L. Visser, and S. Wolf, "Variable impedance actuators: A review," *Robotics and Autonomous Systems*, vol. 61, no. 12, pp. 1601–1614, 2013. DOI: 10.1016/j.robot.2013.06.009.

[55] N. L. Tagliamonte, F. Sergi, D. Accoto, G. Carpino, and E. Guglielmelli, "Double actuation architectures for rendering variable impedance in compliant robots: A review," *Mechatronics*, vol. 22, no. 8, pp. 1187–1203, 2012. DOI: 10.1016/j.mechatronics.2012.09.011.

[56] M. Dežman, T. Debevec, J. Babič, and A. Gams, "Effects of passive ankle exoskeleton on human energy expenditure: Pilot evaluation," *Advances in Intelligent Systems and Computing*, pp. 491–498, 2016. DOI: 10.1007/978-3-319-49058-8_53.

[57] M. Dežman, J. Babič, and A. Gams, "Qualitative assessment of a clutch-actuated ankle exoskeleton," *Advances in Service and Industrial Robotics*, pp. 778–786, 2017. DOI: 10.1007/978-3-319-61276-8_82.

[58] M. Dežman, T. Debevec, J. Babič, and A. Gams, "Vpliv pasivnega gleženjskega eksoskeleta na energijsko porabo človeka pri hoji," *SI robotika*, M. Munih, Ed., p. 307–316, 2017.

[59] M. Dežman, T. Debevec, J. Babič, and A. Gams, "Passive ankle exoskeleton: Design and practical evaluation," *Proceedings: part 1, 9th Jožef Stefan International Postgraduate School Students' Conference*, p. 140–148, 2016.

[60] M. Dežman, "Ankle helping boot for easy walking and rehabilitation," *Proceedings of the 11th International Technology Transfer Conference*, Š. Stres, R. Blatnik, F. Podobnik, and U. Mrgole, Eds., p. 19, 2018.

[61] M. Dežman, J. Babič, and A. Gams, "Ankle exoskeleton with a quasi-passive clutch," *Proceedings - 9th Jožef Stefan International Postgraduate School Students' Conference*, p. 38, 2017.

[62] M. Dežman and A. Gams, "Rotatable cam-based variable-ratio lever compliant actuator for wearable devices," *Mechanism and Machine Theory*, vol. 130, pp. 508–522, 2018. DOI: 10.1016/j.mechmachtheory.2018.09.006.

[63] M. Dežman and A. Gams, "Pseudo-linear variable lever variable stiffness actuator: Design and evaluation," *2017 IEEE International Conference on Advanced Intelligent Mechatronics (AIM)*, vol. 1, pp. 785–790, 2017. DOI: 10.1109/aim.2017.8014113.

[64] M. Dežman and A. Gams, "Podajni aktuator PLVL-VSA z mehansko spremenljivo togostjo," *Proceedings of the Twenty-sixth International Electrotechnical and Computer Science Conference ERK 2017*, p. 221–224, 2017.

[65] M. Dežman and A. Gams, "Optimization and analysis of the modified PLVL-variable stiffness actuator," *International Journal of Mechanics and Control*, vol. 20, no. 1, pp. 22–33, 2019, ISSN: 15908844.

[66] M. Dežman and A. Gams, "Extending the workspace of the PLVL-variable stiffness actuator," *International Conference on Robotics in Alpe-Adria Danube Region*, pp. 291–299, 2018. DOI: 10.1007/978-3-030-00232-9_30.

[67] M. Dežman and A. Gams, "Extending the workspace of pseudo-linear variable-lever variable stiffness actuator," *Robotics: proceedings of the 20th International Multiconference Information Society - IS 2017*, str. 23–26, 2017.

[68] M. Dežman and A. Gams, "Elbow assistance exoskeleton to facilitate high level control design," *Proceedings - 10th Jožef Stefan International Postgraduate School Students' Conference and 12th Young Researchers' Day*, p. 40, 2018.

[69] M. Dežman, T. Asfour, A. Ude, and A. Gams, "Designing an upper body exoskeleton," *Book of abstracts: science of the future how to stay up-to-date with your research!, 11th Jožef Stefan International Postgraduate School Students' Conference and 13th Young Researchers' Day*, p. 43, 2019.

[70] M. Dežman, "Lightweight and cost-effective upper-arm exoskeleton," *Proceedings of the 12th International Technology Transfer Conference*, Š. Stres, L. Pal, F. Podobnik, D. Odić, and R. Blatnik, Eds., p. 39, 2019.

[71] T. J. Roberts and E. Azizi, "Flexible mechanisms: The diverse roles of biological springs in vertebrate movement," *Journal of Experimental Biology*, vol. 214, no. 3, pp. 353–361, 2011. DOI: 10.1242/jeb.038588.

[72] S. Standring, *Gray's Anatomy : the Anatomical Basis of Clinical Practice*. London: Elsevier Health Sciences UK, 2008, ISBN: 9780702042072.

[73] D. G. Thelen, "Adjustment of muscle mechanics model parameters to simulate dynamic contractions in older adults," *Journal of Biomechanical Engineering*, vol. 125, no. 1, pp. 70–77, 2003. DOI: 10.1115/1.1531112.

[74] Y. K. Jun Ueda, *Human Modelling for Bio-inspired Robotics*. Elsevier LTD, Oxford, Sep. 1, 2016, 280 pp., ISBN: 0128031379. [Online]. Available: https://www.ebook.de/de/product/25720795/jun_ueda_yuichi_kurita_human_modelling_for_bio_inspired_robotics.html.

[75] K. Kroemer, *Engineering physiology : bases of human factors engineering/ ergonomics*. S.l: SPRINGER, 2020, ISBN: 9783030406264.

[76] H. Höppner, "Analysis of human intrinsic stiffness modulation and its use in variable-stiffness robots," Ph.D. dissertation, Technische Universität München, 2016.

[77] A. Bicchi, G. Tonietti, M. Bavaro, and M. Piccigallo, "Variable stiffness actuators for fast and safe motion control," *Springer Tracts in Advanced Robotics*, pp. 527–536, 2005. DOI: 10.1007/11008941_56.

[78] D. J. Braun, V. Chalvet, T.-H. Chong, S. S. Apte, and N. Hogan, "Variable stiffness spring actuators for low-energy-cost human augmentation," *IEEE Transactions on Robotics*, vol. 35, no. 6, pp. 1435–1449, 2019. DOI: 10.1109/tro.2019.2929686.

[79] A. Q. Keemink, H. van der Kooij, and A. H. Stienen, "Admittance control for physical human–robot interaction," *The International Journal of Robotics Research*, vol. 37, no. 11, pp. 1421–1444, 2018. DOI: 10.1177/0278364918768950.

[80] H. Chang, S. J. Kim, and J. Kim, "Feedforward motion control with a variable stiffness actuator inspired by muscle cross-bridge kinematics," *IEEE Transactions on Robotics*, vol. 35, no. 3, pp. 747–760, 2019. DOI: 10.1109/tro.2019.2900567.

[81] D. Braun, M. Howard, and S. Vijayakumar, "Optimal variable stiffness control: Formulation and application to explosive movement tasks," *Autonomous Robots*, vol. 33, no. 3, pp. 237–253, 2012. DOI: 10.1007/s10514-012-9302-3.

[82] S. Haddadin, T. Laue, U. Frese, S. Wolf, A. Albu-Schäffer, and G. Hirzinger, "Kick it with elasticity: Safety and performance in human–robot soccer," *Robotics and Autonomous Systems*, vol. 57, no. 8, pp. 761–775, 2009. DOI: 10.1016/j.robot.2009.03.004.

[83] A. Zhakatayev, M. Rubagotti, and H. A. Varol, "Energy-aware optimal control of variable stiffness actuated robots," *IEEE Robotics and Automation Letters*, vol. 4, no. 2, pp. 330–337, 2019. DOI: 10.1109/lra.2018.2890439.

[84] M. Grimmer, M. Eslamy, S. Gliech, and A. Seyfarth, "A comparison of parallel- and series elastic elements in an actuator for mimicking human ankle joint in walking and running," *2012 IEEE International Conference on Robotics and Automation*, vol. 1, pp. 2463–2470, 2012. DOI: 10.1109/icra.2012.6224967.

[85] R. Bischoff, J. Kurth, G. Schreiber, R. Koeppe, A. Albu-Schaeffer, A. Beyer, O. Eiberger, S. Haddadin, A. Stemmer, G. Grunwald, and G. Hirzinger, "The KUKA-DLR lightweight robot arm - a new reference platform for robotics research and manufacturing," *ISR 2010 (41st International Symposium on Robotics) and ROBOTIK 2010 (6th German Conference on Robotics)*, pp. 1–8, 2010.

[86] G. Mathijssen, D. Lefeber, and B. Vanderborght, "Variable recruitment of parallel elastic elements: Series–parallel elastic actuators (SPEA) with dephased mutilated gears," *IEEE/ASME Transactions on Mechatronics*, vol. 20, no. 2, pp. 594–602, 2015. DOI: 10.1109/tmech.2014.2307122.

[87] D. Kaneishi, R. P. Matthew, and M. Tomizuka, "Active/passive switching control framework for assistive devices with variable stiffness actuator," *2019 American Control Conference (ACC)*, pp. 5240–5246, 2019. DOI: 10.23919/acc.2019.8814676.

[88] N. G. Tsagarakis, D. G. Caldwell, F. Negrello, W. Choi, L. Baccelliere, V. Loc, J. Noorden, L. Muratore, A. Margan, A. Cardellino, L. Natale, E. M. Hoffman, H. Dallali, N. Kashiri, J. Malzahn, J. Lee, P. Kryczka, D. Kanoulas, M. Garabini, M. Catalano, M. Ferrati, V. Varricchio, L. Pallottino, C. Pavan, A. Bicchi, A. Settimi, A. Rocchi, and A. Ajoudani, "WALK-MAN: A high-performance humanoid platform for realistic environments," *Journal of Field Robotics*, vol. 34, no. 7, pp. 1225–1259, 2017. DOI: 10.1002/rob.21702.

[89] L. Colasanto, N. G. Tsagarakis, and D. G. Caldwell, "A compact model for the compliant humanoid robot COMAN," *2012 4th IEEE RAS & EMBS International Conference on Biomedical Robotics and Biomechatronics (BioRob)*, vol. 1, pp. 688–694. 2012. DOI: 10.1109/biorob.2012.6290765.

[90] A. Parmiggiani, G. Metta, and N. Tsagarakis, "The mechatronic design of the new legs of the iCub robot," *2012 12th IEEE-RAS International Conference on Humanoid Robots (Humanoids 2012)*, 2012. DOI: 10.1109/humanoids.2012.6651563.

[91] N. Vitiello, T. Lenzi, S. Roccella, S. M. M. D. Rossi, E. Cattin, F. Giovacchini, F. Vecchi, and M. C. Carrozza, "NEUROExos: A powered elbow exoskeleton for physical rehabilitation," *IEEE Transactions on Robotics*, vol. 29, no. 1, pp. 220–235, 2013. DOI: 10.1109/tro.2012.2211492.

[92] D. Maeda, K. Tominaga, T. Oku, H. T. T. Pham, S. Saeki, M. Uemura, H. Hirai, and F. Miyazaki, "Muscle synergy analysis of human adaptation to a variable-stiffness exoskeleton: Human walk with a knee exoskeleton with pneumatic artificial muscles," *2012 12th IEEE-RAS International Conference on Humanoid Robots (Humanoids 2012)*, vol. 1, pp. 638–644, 2012. DOI: 10.1109/humanoids.2012.6651587.

[93] M. Xiloyannis, E. Annese, M. Canesi, A. Kodiyan, A. Bicchi, S. Micera, A. Ajoudani, and L. Masia, "Design and validation of a modular one-to-many actuator for a soft wearable exosuit," *Frontiers in Neurorobotics*, vol. 13, p. 39, 2019. DOI: 10.3389/fnbot.2019.00039.

[94] A. Calanca, R. Muradore, and P. Fiorini, "Impedance control of series elastic actuators: Passivity and acceleration-based control," *Mechatronics*, vol. 47, pp. 37–48, 2017. DOI: 10.1016/j.mechatronics.2017.08.010.

[95] G. Tonietti, R. Schiavi, and A. Bicchi, "Design and control of a variable stiffness actuator for safe and fast physical human/robot interaction," *Proceedings of the 2005 IEEE International Conference on Robotics and Automation*, pp. 526–531, 2005. DOI: 10.1109/robot.2005.1570172.

[96] S. Wolf, O. Eiberger, and G. Hirzinger, "The DLR FSJ: Energy based design of a variable stiffness joint," *2011 IEEE International Conference on Robotics and Automation*, vol. 1, pp. 5082–5089, 2011. DOI: 10.1109/icra.2011.5980303.

[97] A. Jafari, N. G. Tsagarakis, B. Vanderborght, and D. G. Caldwell, "A novel actuator with adjustable stiffness (AwAS)," *2010 IEEE/RSJ International Conference on Intelligent Robots and Systems*, vol. 1, pp. 4201–4206, 2010. DOI: 10.1109/iros.2010.5648902.

[98] R. V. Ham, B. Vanderborght, M. V. Damme, B. Verrelst, and D. Lefeber, "MACCEPA, the mechanically adjustable compliance and controllable equilibrium position actuator: Design and implementation in a biped robot," *Robotics and Autonomous Systems*, vol. 55, no. 10, pp. 761–768, 2007. DOI: 10.1016/j.robot.2007.03.001.

[99] S. Wang, W. van Dijk, and H. van der Kooij, "Spring uses in exoskeleton actuation design," *2011 IEEE International Conference on Rehabilitation Robotics*, vol. 1, pp. 1–6, 2011. DOI: 10.1109/icorr.2011.5975471.

[100] N. G. Tsagarakis, I. Sardellitti, and D. G. Caldwell, "A new variable stiffness actuator (CompAct-VSA): Design and modelling," *IEEE/RSJ International Conference on Intelligent Robots and Systems (IROS)*, vol. 1, pp. 378–383, 2011. DOI: 10.1109/iros.2011.6095006.

[101] F. Petit, W. Friedl, H. Hoppner, and M. Grebenstein, "Analysis and synthesis of the bidirectional antagonistic variable stiffness mechanism," *IEEE/ASME Transactions on Mechatronics*, vol. 20, no. 2, pp. 684–695, 2015. DOI: 10.1109/tmech.2014.2321428.

[102] M. G. Catalano, G. Grioli, F. Bonomo, R. Schiavi, and A. Bicchi, "VSA-HD: From the enumeration analysis to the prototypical implementation," *2010 IEEE/RSJ International Conference on Intelligent Robots and Systems*, vol. 1, pp. 3676–3681, 2010. DOI: 10.1109/iros.2010.5649774.

[103] M. G. Catalano, G. Grioli, M. Garabini, F. Bonomo, M. Mancini, N. Tsagarakis, and A. Bicchi, "VSA-CubeBot: A modular variable stiffness platform for multiple degrees of freedom robots," *2011 IEEE International Conference on Robotics and Automation*, vol. 1, pp. 5090–5095, 2011. DOI: 10.1109/icra.2011.5980457.

[104] B. Vanderborght, N. G. Tsagarakis, R. V. Ham, I. Thorson, and D. G. Caldwell, "MACCEPA 2.0: Compliant actuator used for energy efficient hopping robot chobino1d," *Autonomous Robots*, vol. 31, no. 1, pp. 55–65, 2011. DOI: 10.1007/s10514-011-9230-7.

[105] P. Cherelle, V. Grosu, P. Beyl, A. Mathys, R. V. Ham, M. V. Damme, B. Vanderborght, and D. Lefeber, "The MACCEPA actuation system as torque actuator in the gait rehabilitation robot ALTACRO," *2010 3rd IEEE RAS & EMBS International Conference on Biomedical Robotics and Biomechatronics*, vol. 1, pp. 27–32, 2010. DOI: 10.1109/biorob.2010.5627030.

[106] German Aerospace Center, *VIACTORS homepage VSA data sheets*, visited on 20th March 2020. [Online]. Available: http://www.viactors.org/VSA%20data%20sheets.htm.

[107] B. Vanderborght, N. Tsagarakis, C. Semini, R. V. Ham, and D. Caldwell, "MACCEPA 2.0: Adjustable compliant actuator with stiffening characteristic for energy efficient hopping," *IEEE International Conference on Robotics and Automation (ICRA)*, vol. 1, pp. 544–549, 2009. DOI: 10.1109/robot.2009.5152204.

[108] R. Furnemont, G. Mathijssen, T. van der Hoeven, B. Brackx, D. Lefeber, and B. Vanderborght, "Torsion MACCEPA: A novel compact compliant actuator designed around the drive axis," *2015 IEEE International Conference on Robotics and Automation (ICRA)*, vol. 1, pp. 232–237, 2015. DOI: 10.1109/icra.2015.7139005.

[109] A. Jafari, N. G. Tsagarakis, and D. G. Caldwell, "AwAS-II: A new actuator with adjustable stiffness based on the novel principle of adaptable pivot point and variable lever ratio," *2011 IEEE International Conference on Robotics and Automation*, vol. 1, pp. 4638–4643, 2011. DOI: 10.1109/icra.2011.5979994.

[110] S. Wolf and G. Hirzinger, "A new variable stiffness design: Matching requirements of the next robot generation," *2008 IEEE International Conference on Robotics and Automation*, vol. 1, pp. 1741–1746, 2008. DOI: 10.1109/robot.2008.4543452.

[111] K. L. Richards, *Design Engineer's Handbook*. CRC Press, 2012. DOI: 10.1201/b12714.

[112] H. V. Quy, L. Aryananda, F. I. Sheikh, F. Casanova, and R. Pfeifer, "A novel mechanism for varying stiffness via changing transmission angle," *2011 IEEE International Conference on Robotics and Automation*, pp. 5076–5081, 2011. DOI: 10.1109/icra.2011.5980097.

[113] M. K. VUKOBRATOVIC, "WHEN WERE ACTIVE EXOSKELETONS ACTUALLY BORN?" *International Journal of Humanoid Robotics*, vol. 04, no. 03, pp. 459–486, 2007. DOI: 10.1142/s0219843607001163.

[114] J. L. Pons, "Witnessing a wearables transition," *Science*, vol. 365, no. 6454, pp. 636–637, 2019. DOI: 10.1126/science.aaw9407.

[115] H. Kazerooni, "A review of the exoskeleton and human augmentation technology," *ASME 2008 Dynamic Systems and Control Conference, Parts A and B*, pp. 1539–1547, 2008. DOI: 10.1115/dscc2008-2407.

[116] R. A. R. C. Gopura, K. Kiguchi, and D. S. V. Bandara, "A brief review on upper extremity robotic exoskeleton systems," *2011 6th International Conference on Industrial and Information Systems*, pp. 346–351, 2011. DOI: 10.1109/iciinfs.2011.6038092.

[117] N. Li, L. Yan, H. Qian, H. Wu, J. Wu, and S. Men, "Review on lower extremity exoskeleton robot," *The Open Automation and Control Systems Journal*, vol. 7, no. 1, 2015. DOI: 10.2174/1874444301507010441.

[118] R. Bogue, "Exoskeletons and robotic prosthetics: A review of recent developments," *Industrial Robot: An International Journal*, vol. 36, no. 5, pp. 421–427, 2009. DOI: 10.1108/01439910910980141.

[119] H. Herr, "Exoskeletons and orthoses: Classification, design challenges and future directions," *Journal of NeuroEngineering and Rehabilitation*, vol. 6, no. 1, 2009. DOI: 10.1186/1743-0003-6-21.

[120] R.-J. Wang and H.-P. Huang, "AVSER active variable stiffness exoskeleton robot system: Design and application for safe active-passive elbow rehabilitation," *2012 IEEE/ASME International Conference on Advanced Intelligent Mechatronics (AIM)*, pp. 220–225, 2012. DOI: 10.1109/aim.2012.6266034.

[121] M. Cestari, D. Sanz-Merodio, J. Arevalo, and E. Garcia, "ARES, a variable stiffness actuator with embedded force sensor for the ATLAS exoskeleton," *Industrial Robot: An International Journal*, vol. 41, no. 6, pp. 518–526, 2014. DOI: 10.1108/ir-06-2014-0350.

[122] D. Rodriguez-Cianca, M. Weckx, R. Jimenez-Fabian, D. Torricelli, J. Gonzalez-Vargas, M. Sanchez-Villamañan, M. Sartori, K. Berns, B. Vanderborght, J. L. Pons, and D. Lefeber, "A variable stiffness actuator module with favorable mass distribution for a bio-inspired biped robot," *Frontiers in Neurorobotics*, vol. 13, p. 20, 2019. DOI: 10.3389/fnbot.2019.00020.

[123] R. C. Browning, J. R. Modica, R. Kram, and A. Goswami, "The effects of adding mass to the legs on the energetics and biomechanics of walking," *Medicine & Science in Sports & Exercise*, vol. 39, no. 3, pp. 515–525, 2007. DOI: 10.1249/mss.0b013e31802b3562.

[124] S. O. Schrade, K. Dätwyler, M. Stücheli, K. Studer, D.-A. Türk, M. Meboldt, R. Gassert, and O. Lambercy, "Development of VariLeg, an exoskeleton with variable stiffness actuation: First results and user evaluation from the CYBATHLON 2016," *Journal of NeuroEngineering and Rehabilitation*, vol. 15, no. 1, 2018. DOI: 10.1186/s12984-018-0360-4.

[125] H. K. Yap, J. H. Lim, F. Nasrallah, J. C. H. Goh, and R. C. H. Yeow, "A soft exoskeleton for hand assistive and rehabilitation application using pneumatic actuators with variable stiffness," *2015 IEEE International Conference on Robotics and Automation (ICRA)*, pp. 4967–4972, 2015. DOI: 10.1109/icra.2015.7139889.

[126] A. Sutrisno and D. J. Braun, "Enhancing mobility with quasi-passive variable stiffness exoskeletons," *IEEE Transactions on Neural Systems and Rehabilitation Engineering*, vol. 27, no. 3, pp. 487–496, 2019. DOI: 10.1109/tnsre.2019.2899753.

[127] B. Kim and A. D. Deshpande, "An upper-body rehabilitation exoskeleton harmony with an anatomical shoulder mechanism: Design, modeling, control, and performance evaluation," *The International Journal of Robotics Research*, vol. 36, no. 4, pp. 414–435, 2017. DOI: 10.1177/0278364917706743.

[128] E. Trigili, S. Crea, M. Moise, A. Baldoni, M. Cempini, G. Ercolini, D. Marconi, F. Posteraro, M. C. Carrozza, and N. Vitiello, "Design and experimental characterization of a shoulder-elbow exoskeleton with compliant joints for post-stroke rehabilitation," *IEEE/ASME Transactions on Mechatronics*, vol. 24, no. 4, pp. 1485–1496, 2019. DOI: 10.1109/tmech.2019.2907465.

[129] ExoskeletonReport.com, *ReWalk 6.0*, https://exoskeletonreport.com/product/rewalk/, visited on 5th February 2020.

[130] ExoskeletonReport.com, *Indego*, https://exoskeletonreport.com/product/indego/, visited on 2nd February 2020.

[131] ExoskeletonReport.com, *Ekso GT*, https://exoskeletonreport.com/product/ekso-gt/, visited on 2nd February 2020.

[132] Y. He, D. Eguren, T. P. Luu, and J. L. Contreras-Vidal, "Risk management and regulations for lower limb medical exoskeletons: A review," *Medical Devices: Evidence and Research*, vol. Volume 10, pp. 89–107, 2017. DOI: 10.2147/mder.s107134.

[133] A. T. Asbeck, K. Schmidt, and C. J. Walsh, "Soft exosuit for hip assistance," *Robotics and Autonomous Systems*, vol. 73, pp. 102–110, 2015. DOI: 10.1016/j.robot.2014.09.025.

[134] J. Bae, C. Siviy, M. Rouleau, N. Menard, K. Odonnell, I. Geliana, M. Athanassiu, D. Ryan, C. Bibeau, L. Sloot, P. Kudzia, T. Ellis, L. Awad, and C. J. Walsh, "A lightweight and efficient portable soft exosuit for paretic ankle assistance in walking after stroke," *2018 IEEE International Conference on Robotics and Automation (ICRA)*, pp. 2820–2827, 2018. DOI: 10.1109/icra.2018.8461046.

[135] B. K. Dinh, M. Xiloyannis, L. Cappello, C. W. Antuvan, S.-C. Yen, and L. Masia, "Adaptive backlash compensation in upper limb soft wearable exoskeletons," *Robotics and Autonomous Systems*, vol. 92, pp. 173–186, 2017. DOI: 10.1016/j.robot.2017.03.012.

[136] G. Lee, Y. Ding, I. G. Bujanda, N. Karavas, Y. M. Zhou, and C. J. Walsh, "Improved assistive profile tracking of soft exosuits for walking and jogging with off-board actuation," *2017 IEEE/RSJ International Conference on Intelligent Robots and Systems (IROS)*, pp. 1699–1706, 2017. DOI: 10.1109/iros.2017.8205981.

[137] L. Cappello, A. Pirrera, P. Weaver, and L. Masia, "A series elastic composite actuator for soft arm exosuits," *2015 IEEE International Conference on Rehabilitation Robotics (ICORR)*, pp. 61–66, 2015. DOI: 10.1109/icorr.2015.7281176.

[138] U. Jeong and K.-J. Cho, "Feedforward friction compensation of bowden-cable transmission via loop routing," *2015 IEEE/RSJ International Conference on Intelligent Robots and Systems (IROS)*, pp. 5948–5953, 2015. DOI: 10.1109/iros.2015.7354223.

[139] P. Letier, A. Schiele, M. Avraam, M. Horodinca, and A. Preumont, "Bowden cable actuator for torque-feedback in haptic applications," *2006 Proceedings Eurohaptics Conference*, 2006.

[140] S. Lemerle, G. Grioli, A. Bicchi, and M. G. Catalano, "A variable stiffness elbow joint for upper limb prosthesis," *2019 IEEE/RSJ International Conference on Intelligent Robots and Systems (IROS)*, pp. 7327–7334, 2019. DOI: 10.1109/iros40897.2019.8970475.

[141] R. Chin, E. T. Hsiao-Wecksler, E. Loth, G. Kogler, S. D. Manwaring, S. N. Tyson, K. A. Shorter, and J. N. Gilmer, "A pneumatic power harvesting ankle-foot orthosis to prevent foot-drop," *Journal of NeuroEngineering and Rehabilitation*, vol. 6, no. 1, p. 19, 2009. DOI: 10.1186/1743-0003-6-19.

[142] M. Plooij, G. Mathijssen, P. Cherelle, D. Lefeber, and B. Vanderborght, "Lock your robot: A review of locking devices in robotics," *IEEE Robotics & Automation Magazine*, vol. 22, no. 1, pp. 106–117, 2015. DOI: 10.1109/mra.2014.2381368.

[143] S. Diller, C. Majidi, and S. H. Collins, "A lightweight, low-power electroadhesive clutch and spring for exoskeleton actuation," *2016 IEEE International Conference on Robotics and Automation (ICRA)*, pp. 682–689, 2016. DOI: 10.1109/icra.2016.7487194.

[144] M. H. Rahman, M. Saad, J.-P. Kenné, and P. S. Archambault, "Control of an exoskeleton robot arm with sliding mode exponential reaching law," *International Journal of Control, Automation and Systems*, vol. 11, no. 1, pp. 92–104, 2008. DOI: 10.1007/s12555-011-0135-1.

[145] G. Elliott, G. S. Sawicki, A. Marecki, and H. Herr, "The biomechanics and energetics of human running using an elastic knee exoskeleton," *2013 IEEE 13th International Conference on Rehabilitation Robotics (ICORR)*, pp. 1–6, 2013. DOI: 10.1109/icorr.2013.6650418.

[146] W. van Dijk, H. van der Kooij, and E. Hekman, "A passive exoskeleton with artificial tendons: Design and experimental evaluation," *2011 IEEE International Conference on Rehabilitation Robotics*, pp. 1–6, 2011. DOI: 10.1109/icorr.2011.5975470.

[147] Ekso Bionics Holdings Inc., *EksoWorks Exoskeleton*, http://eksobionics.com/eksoworks/, visited on 20th March 2020.

[148] Lockheed Martin, *Fortis Exoskeleton*, https://www.lockheedmartin.com/en-us/products/exoskeleton-technologies/industrial.html, visited on 20th March 2020.

[149] P. Maurice, S. Ivaldi, J. Babic, J. Camernik, D. Gorjan, B. Schirrmeister, J. Bornmann, L. Tagliapietra, C. Latella, D. Pucci, and L. Fritzsche, "Objective and subjective effects of a passive exoskeleton on overhead work," *IEEE Transactions on Neural Systems and Rehabilitation Engineering*, vol. 28, no. 1, pp. 152–164, 2020. DOI: 10.1109/tnsre.2019.2945368.

[150] S. Alabdulkarim and M. A. Nussbaum, "Influences of different exoskeleton designs and tool mass on physical demands and performance in a simulated overhead drilling task," *Applied Ergonomics*, vol. 74, pp. 55–66, 2019. DOI: 10.1016/j.apergo.2018.08.004.

[151] K. Huysamen, T. Bosch, M. de Looze, K. S. Stadler, E. Graf, and L. W. O'Sullivan, "Evaluation of a passive exoskeleton for static upper limb activities," *Applied Ergonomics*, vol. 70, pp. 148–155, 2018. DOI: 10.1016/j.apergo.2018.02.009.

[152] Otto Bock Holding GmbH and Co. KG, *Exoskeletons make jobs more ergonomic*, https://www.ottobock.com/media/ottobock-corporate/newsroom/media/files/paexo-ottobock.zip, visited on 20th March 2020.

[153] G. Elliott, A. Marecki, and H. Herr, "Design of a clutch–spring knee exoskeleton for running," *Journal of Medical Devices*, vol. 8, no. 3, 2014. DOI: 10.1115/1.4027841.

[154] W. van Dijk and H. V. der Kooij, "XPED2: A passive exoskeleton with artificial tendons," *IEEE Robotics & Automation Magazine*, vol. 21, no. 4, pp. 56–61, 2014. DOI: 10.1109/mra.2014.2360309.

[155] A. J. van den Bogert, "Exotendons for assistance of human locomotion," *BioMedical Engineering OnLine*, vol. 2, no. 1, p. 17, 2003. DOI: 10.1186/1475-925x-2-17.

[156] G. Aguirre-Ollinger, "Learning muscle activation patterns via nonlinear oscillators: Application to lower-limb assistance," *2013 IEEE/RSJ International Conference on Intelligent Robots and Systems*, pp. 1182–1189, 2013. DOI: 10.1109/iros.2013.6696500.

[157] R. Ronsse, N. Vitiello, T. Lenzi, J. van den Kieboom, M. C. Carrozza, and A. J. Ijspeert, "Human–robot synchrony: Flexible assistance using adaptive oscillators," *IEEE Transactions on Biomedical Engineering*, vol. 58, no. 4, pp. 1001–1012, 2011. DOI: 10.1109/tbme.2010.2089629.

[158] D. P. Ferris, J. M. Czerniecki, and B. Hannaford, "An ankle-foot orthosis powered by artificial pneumatic muscles," *Journal of Applied Biomechanics*, vol. 21, no. 2, pp. 189–197, 2005. DOI: 10.1123/jab.21.2.189.

[159] D. P. Ferris, K. E. Gordon, G. S. Sawicki, and A. Peethambaran, "An improved powered ankle–foot orthosis using proportional myoelectric control," *Gait & Posture*, vol. 23, no. 4, pp. 425–428, 2006. DOI: 10.1016/j.gaitpost.2005.05.004.

[160] K. Gui, H. Liu, and D. Zhang, "A practical and adaptive method to achieve EMG-based torque estimation for a robotic exoskeleton," *IEEE/ASME Transactions on Mechatronics*, vol. 24, no. 2, pp. 483–494, 2019. DOI: 10.1109/tmech.2019.2893055.

[161] X. Li, Y.-H. Liu, and H. Yu, "Iterative learning impedance control for rehabilitation robots driven by series elastic actuators," *Automatica*, vol. 90, pp. 1–7, 2018. DOI: 10.1016/j.automatica.2017.12.031.

[162] Q. Wu, B. Chen, and H. Wu, "Neural-network-enhanced torque estimation control of a soft wearable exoskeleton for elbow assistance," *Mechatronics*, vol. 63, p. 102 279, 2019. DOI: 10.1016/j.mechatronics.2019.102279.

[163] J. Gunasekara, R. Gopura, T. Jayawardane, and S. Lalitharathne, "Control methodologies for upper limb exoskeleton robots," *2012 IEEE/SICE International Symposium on System Integration (SII)*, pp. 19–24, 2012. DOI: 10.1109/sii.2012.6427387.

[164] T. Proietti, V. Crocher, A. Roby-Brami, and N. Jarrasse, "Upper-limb robotic exoskeletons for neurorehabilitation: A review on control strategies," *IEEE Reviews in Biomedical Engineering*, vol. 9, pp. 4–14, 2016. DOI: 10.1109/rbme.2016.2552201.

[165] H. B. Menz, M. Auhl, S. Ristevski, N. Frescos, and S. E. Munteanu, "Evaluation of the accuracy of shoe fitting in older people using three-dimensional foot scanning," *Journal of Foot and Ankle Research*, vol. 7, no. 1, 2014. DOI: 10.1186/1757-1146-7-3.

[166] G. G. Berntson and J. T. Cacioppo, "Heart rate variability: Stress and psychiatric conditions," *Dynamic Electrocardiography*, pp. 57–64, 2004. DOI: 10.1002/9780470987483.ch7.

[167] M. K. Shepherd and E. J. Rouse, "Design of a quasi-passive ankle-foot prosthesis with biomimetic, variable stiffness," *2017 IEEE International Conference on Robotics and Automation (ICRA)*, pp. 6672–6678, 2017. DOI: 10.1109/icra.2017.7989788.

[168] T. Wimbock, C. Ott, A. Albu-Schaffer, A. Kugi, and G. Hirzinger, "Impedance control for variable stiffness mechanisms with nonlinear joint coupling," *2008 IEEE/RSJ International Conference on Intelligent Robots and Systems*, pp. 3796–3803, 2008. DOI: 10.1109/iros.2008.4651079.

[169] F. Patrick Petit, *Analysis and control of variable stiffness robots*, 2014.

[170] J. F. Veneman, R. Ekkelenkamp, R. Kruidhof, F. C. van der Helm, and H. van der Kooij, "A series elastic- and bowden-cable-based actuation system for use as torque actuator in exoskeleton-type robots," *The International Journal of Robotics Research*, vol. 25, no. 3, pp. 261–281, 2006. DOI: 10.1177/0278364906063829.

[171] S. M. F. Reimer, T. C. Lueth, and L. T. D'Angelo, "Individualized arm shells towards an ergonomic design of exoskeleton robots," *2014 IEEE International Conference on Systems, Man, and Cybernetics (SMC)*, pp. 3958–3965, 2014. DOI: 10.1109/smc.2014.6974550.

[172] T. Nef, M. Mihelj, and R. Riener, "ARMin: A robot for patient-cooperative arm therapy," *Medical & Biological Engineering & Computing*, vol. 45, no. 9, pp. 887–900, 2007. DOI: 10.1007/s11517-007-0226-6.

[173] A. Jafari, N. G. Tsagarakis, and D. G. Caldwell, "A novel intrinsically energy efficient actuator with adjustable stiffness (AwAS)," *IEEE/ASME Transactions on Mechatronics*, vol. 18, no. 1, pp. 355–365, 2013. DOI: 10.1109/tmech.2011.2177098.

[174] R. A. R. CHANDRA, "Development and control of upper-limb exoskeleton robots," Ph.D. dissertation, School of Science and Engineering, Saga University, Japan, 2009.

[175] J. C. Otis, R. F. Warren, S. I. Backus, T. J. Santner, and J. D. Mabrey, "Torque production in the shoulder of the normal young adult male: The interaction of function, dominance, joint angle, and angular velocity," *The American Journal of Sports Medicine*, vol. 18, no. 2, pp. 119–123, 1990. DOI: 10.1177/036354659001800201.

[176] J. García-Alsina, C. G. Almazan, J. M. Mesquida, and E. P. Cobo, "Angular position, range of motion and velocity of arm elevation: A study of consistency of performance," *Clinical Biomechanics*, vol. 20, no. 9, pp. 932–938, 2005. DOI: 10.1016/j.clinbiomech.2005.05.005.

[177] G. J. Soderberg and M. J. Blaschak, "Shoulder internal and external rotation peak torque production through a velocity spectrum in differing positions," *Journal of Orthopaedic & Sports Physical Therapy*, vol. 8, no. 11, pp. 518–524, 1987. DOI: 10.2519/jospt.1987.8.11.518.

[178] A. Gupta and M. K., "Robotic exoskeletons for upper extremity rehabilitation," *Rehabilitation Robotics*, 2007. DOI: 10.5772/5171.

[179] S. Wang, C. Meijneke, and H. van der Kooij, "Modeling, design, and optimization of mindwalker series elastic joint," *2013 IEEE 13th International Conference on Rehabilitation Robotics (ICORR)*, pp. 1–8, 2013. DOI: 10.1109/icorr.2013.6650381.

[180] ODrive Community, *ODrive Documentation - Control*, https://docs.odriverobotics.com/control.html, visited on 3rd February 2020.

[181] ODrive Community, *ODrive Documentation - Trajectory Mode*, https://docs.odriverobotics.com/, visited on 3rd February 2020.

[182] H. Olsson, K. Åström, C. C. de Wit, M. Gäfvert, and P. Lischinsky, "Friction models and friction compensation," *European Journal of Control*, vol. 4, no. 3, pp. 176–195, 1998. DOI: 10.1016/s0947-3580(98)70113-x.

[183] C. M. Bishop, *Pattern Recognition and Machine Learning (Information Science and Statistics)*. Berlin, Heidelberg: Springer-Verlag, 2006, ISBN: 0387310738.

[184] G. Welch, G. Bishop, *et al.*, *An introduction to the Kalman filter*. Citeseer, 1995.

Bibliography

Publications Related to the Thesis

Original Scientific Article

M. Dežman and A. Gams, "Optimization and analysis of the modified PLVL-variable stiffness actuator," *International Journal of Mechanics and Control*, vol. 20, no. 1, pp. 22–33, 2019, ISSN: 15908844.

M. Dežman and A. Gams, "Rotatable cam-based variable-ratio lever compliant actuator for wearable devices," *Mechanism and Machine Theory*, vol. 130, pp. 508–522, 2018. DOI: 10.1016/j.mechmachtheory.2018.09.006.

Published Scientific Conference Contribution

M. Dežman and A. Gams, "Extending the workspace of the PLVL-variable stiffness actuator," *International Conference on Robotics in Alpe-Adria Danube Region*, pp. 291–299, 2018. DOI: 10.1007/978-3-030-00232-9_30.

M. Dežman and A. Gams, "Pseudo-linear variable lever variable stiffness actuator: Design and evaluation," *2017 IEEE International Conference on Advanced Intelligent Mechatronics (AIM)*, vol. 1, pp. 785–790, 2017. DOI: 10.1109/aim.2017.8014113.

M. Dežman, J. Babič, and A. Gams, "Qualitative assessment of a clutch-actuated ankle exoskeleton," *Advances in Service and Industrial Robotics*, pp. 778–786, 2017. DOI: 10.1007/978-3-319-61276-8_82.

M. Dežman and A. Gams, "Extending the workspace of pseudo-linear variable-lever variable stiffness actuator," *Robotics: proceedings of the 20th International Multiconference Information Society - IS 2017*, str. 23–26, 2017.

M. Dežman and A. Gams, "Podajni aktuator PLVL-VSA z mehansko spremenljivo togostjo," *Proceedings of the Twenty-sixth International Electrotechnical and Computer Science Conference ERK 2017*, p. 221–224, 2017.

M. Dežman, T. Debevec, J. Babič, and A. Gams, "Vpliv pasivnega gleženjskega eksoskeleta na energijsko porabo človeka pri hoji," *SI robotika*, M. Munih, Ed., p. 307–316, 2017.

M. Dežman, T. Debevec, J. Babič, and A. Gams, "Effects of passive ankle exoskeleton on human energy expenditure: Pilot evaluation," *Advances in Intelligent Systems and Computing*, pp. 491–498, 2016. DOI: 10.1007/978-3-319-49058-8_53.

M. Dežman, T. Debevec, J. Babič, and A. Gams, "Passive ankle exoskeleton: Design and practical evaluation," *Proceedings: part 1, 9th Jožef Stefan International Postgraduate School Students' Conference*, p. 140–148, 2016.

Published Scientific Conference Contribution Abstract

M. Dežman, T. Asfour, A. Ude, and A. Gams, "Designing an upper body exoskeleton," *Book of abstracts: science of the future how to stay up-to-date with your research!, 11th Jožef Stefan International Postgraduate School Students' Conference and 13th Young Researchers' Day*, p. 43, 2019.

M. Dežman and A. Gams, "Elbow assistance exoskeleton to facilitate high level control design," *Proceedings - 10th Jožef Stefan International Postgraduate School Students' Conference and 12th Young Researchers' Day*, p. 40, 2018.

M. Dežman, "Lightweight and cost-effective upper-arm exoskeleton," *Proceedings of the 12th International Technology Transfer Conference*, Š. Stres, L. Pal, F. Podobnik, D. Odić, and R. Blatnik, Eds., p. 39, 2019.

M. Dežman, "Ankle helping boot for easy walking and rehabilitation," *Proceedings of the 11th International Technology Transfer Conference*, Š. Stres, R. Blatnik, F. Podobnik, and U. Mrgole, Eds., p. 19, 2018.

M. Dežman, J. Babič, and A. Gams, "Ankle exoskeleton with a quasi-passive clutch," *Proceedings - 9th Jožef Stefan International Postgraduate School Students' Conference*, p. 38, 2017.

Radio or Television Broadcast

R. Dacinger, R. Kamnik, Z. Matjačić, and M. Dežman, "Eksoskeleti," *Ugriznimo znanost*, 2017.

Other Publications

Published Scientific Conference Contribution

M. Dežman, T. Asfour, A. Ude, and A. Gams, "Exoskeleton arm pronation/supination assistance mechanism with a guided double rod system," *IEEE-RAS 19th International Conference on Humanoid Robots(HUMANOIDS 2019)*, pp. 590–595, 2019.

Editor

P. Jovičević Klug, M. Dežman, K. Bačnik, R. Novak, T. Turk Dermastia, Ž. Marinko, A. Kikaj, A. Jurov, and M. Topole, Eds., *Book of abstracts - 12th Jožef Stefan International Postgraduate School Students' Conference and 14th Young Researchers' Day*, Ljubljana: Jožef Stefan International Postgraduate School, Jožef Stefan Institute, 2020.

M. Topole, T. Turk Dermastia, M. Dežman, B. Škrlj, A. Jurov, K. Bačnik, J. Masten, Ž. Marinko, P. Jovičević Klug, R. Pahič, I. Rybkin, J. Černilogar, and A. Kikaj, Eds., *Book of abstracts: science of the future how to stay up-to-date with your research!, 11th Jožef Stefan International Postgraduate School Students' Conference and 13th Young Researchers' Day*, Ljubljana: Jožef Stefan International Postgraduate School, Jožef Stefan Institute, 2019.

M. Dežman, A. Pecman, K. Bačnik, J. Masten, M. Topole, M. Bergant, M. Cevzar, A. Jurov, B. Škrlj, and T. Turk Dermastia, Eds., *Proceedings - 10th Jožef Stefan International Postgraduate School Students' Conference and 12th Young Researchers' Day*, Ljubljana: Jožef Stefan International Postgraduate School, Jožef Stefan Institute, 2018.

Biography

The author of this thesis was born on April 4th 1991 in Ljubljana, Slovenia. He graduated in 2013 from the Faculty of Mechanical Engineering at the University of Ljubljana with a Bachelor's degree in Mechanical Engineering. He continued his studies at the same faculty and graduated from the Master's program in Mechatronics and Laser Technologies in 2015. In the same year, the author was employed at the Department for Automation, Biocybernetics and Robotics at the Jožef Stefan Institute under the Slovenian Research Agency Young Researcher program. The author continues his education and research at the same institution to this day.

Between October 2018 and March 2019, the author visited the High-Performance Humanoid Technologies Lab at the Karlsruhe Institute of Technology to facilitate future cooperation between the two institutions. The author's applied research culminated in several innovative physical prototypes, which were also submitted to several innovation competitions. In addition, the authors' research results were published in journal articles and at several scientific conferences. The author also cooperated intensively with the Student Council of the Jožef Stefan International Postgraduate School and also co-organized several annual student conferences of the Jožef Stefan International Postgraduate Schools.

Other achievements are written below.

Conferences and Workshops

May 2020: Co-organized the *"12th Jožef Stefan International Post-graduate School Students Conference"* online conference.

January 2020: Held a 3-day workshop titled *"Controlling a 2-DoF upper arm exoskeleton"* at the 2020 Wearable Robots Winter School in Obertauern, Austria.

April 2019: Co-organized and attended with a contribution (abstract, poster, elevator pitch) the *"11th Jožef Stefan International Post-graduate School Students Conference"* in Planica, Slovenia.

June 2018: Attended with a contribution (article and oral presentation) the *"27th International Conference on Robotics in Alpe-Adria-Danube Region, RAAD 2018"* in Patras, Greece.

May 2018: Co-organized and attended with a contribution (abstract, poster, elevator pitch) the *"10th Jožef Stefan International Post-graduate School Students Conference"* in Piran, Slovenia.

October 2017: Attended with a contribution (article and oral presentation) the *"20th International Multiconference Information Society"* conference in Ljubljana, Slovenia.

September 2017: Attended with a contribution (article and oral presentation) the *"International Electrotechnical and Computer Science Conference (ERK 2017)"* in Portorož, Slovenia.

July 2017: Attended with a contribution (article, oral presentation and poster presentation) the *"IEEE/ASME International Conference on Advanced Intelligent Mechatronics (AIM 2017)"* in Munich, Germany.

June 2017: Attended with a contribution (article and oral presentation) the *"26th International Conference on Robotics in Alpe-Adria-Danube Region, RAAD 2017"* in Turin, Italy.

April 2017: Attended with a contribution (extended abstract, poster, elevator pitch) the *"9th Jožef Stefan International Post-graduate School Students Conference"* in Ljubljana, Slovenia.

June 2016: Attended with a contribution (oral presentation) the *"25th International Conference on Robotics in Alpe-Adria-Danube Region, RAAD 2016"* in Belgrade, Serbia.

May 2016: Attended with a contribution (extended abstract, poster, elevator pitch) the *"8th Jožef Stefan International Post-graduate School Student Conference"* in Ljubljana, Slovenia

Awards

April 2019: Special Jury Mention in the competition *"9th MANUS® competition for plastic plain bearing applications"* for the Upper-Arm Exoskeleton Prototype.

November 2018: Awarded a 4 month long scholarship for a short research visit in Germany, funded by the *"Deutscher Akademischer Austauschdienst"* (DAAD).

May 2018: Received the *"The best overall presentation of the Information and Communication Technologies study program"* award at the *"10th Jožef Stefan International Post-graduate School Students Conference"* in Piran, Slovenia.

Competitions

February 2019: Competed in the *"9th MANUS® competition for plastic plain bearing applications"* with the Upper-Arm Exoskeleton Prototype.

October 2018: Competed in the public call for the *"Best innovation in 2018 at the public research organizations (PROs)"* at the International Technology Transfer Conference – ITTC with the Quasi-Passive Ankle Exoskeleton.

April 2018: Competed at the public call *"Rektorjeva nagrada za naj inovacijo v Univerzi v Ljubljani 2018"*, i.e. "Rectors award for the best innovation in the University of Ljubljana 2018" with the Compliant Actuator.

October 2017: Competed in the public call for the *"Best innovation in 2017 at the public research organizations (PROs)"* at the International Technology Transfer Conference – ITTC with the Compliant Actuator.

Research visits

October 2018 – March 2019: Research visit at the High-Performance Humanoid Technologies Lab of Prof. Dr. Tamim Asfour, to design an upper-limb exoskeleton.

Memberships

October 2017 - September 2018 *Jožef Stefan International Postgraduate School* student-council vice-president and the student-council representative of the "Information and Communication Technologies" study program.

October 2018 - September 2019 *Jožef Stefan International Postgraduate School* student-council member and the student-council representative of the "Information and Communication Technologies" study program.

DECLARATION

I, the undersigned Miha Dežman, declare herewith that:

- The submitted Master Thesis/Doctoral Dissertation has been prepared by myself based on my own research and using the sources listed, under the supervision of supervisor Andrej Gams and co-supervisor ;
- This Master Thesis/Doctoral Dissertation has not been submitted either in whole or in part for obtaining any other degree at another university or faculty;
- I have followed the Regulations on Master and Doctoral Studies, the IPS instructions for writing and submitting the Master Thesis/Doctoral Dissertation and the instructions for stating the IPS affiliation in publications related to Master Thesis/Doctoral Dissertation, and I take full responsibility for their implementation;
- I declare my own responsibility for ensuring that previously copyrighted material used in this work, beyond fair use, has been reproduced with written permission of the copyright owner;
- I am fully aware that plagiarism – presenting the work of others either in cited form, as literal paraphrasing or in graphic form with which the thoughts of others or their ideas are presented as my own – is punishable by law (Copyright and Related Rights Act (UL RS, No.16/07-UPB3, 68/08, 85/10 Skl.US: U-I-191/09-7, Up-916-16)) and as a demeanour also sanctioned by IPS according to its Regulations;
- I agree with public access to this Master Thesis/Doctoral Dissertation in specialised libraries and on the IPS homepage.

Signature of the candidate:



I, the undersigned supervisor Andrej Gams, declare herewith that I have examined the Master Thesis/Doctoral Dissertation and approve that it is prepared in accordance with the IPS criteria regarding the content, language and template, and that it is appropriate to proceed to the IPS Senate.

Signature of the supervisor:



In Ljubljana, on 4.5.2020